Simultaneous Modelling of the Morphological and Spectral Features of the Pulsar Wind Nebula HESS J1825–137 in TeV γ rays

Julia Brucker

Simultaneous Modelling of the Morphological and Spectral Features of the Pulsar Wind Nebula HESS J1825−137 in TeV γ rays

Simultane Modellierung der morphologischen und spektralen Eigenschaften des Pulsarwindnebels HESS J1825–137 in TeV-Gammastrahlung

Der Naturwissenschaftlichen Fakultät
der Friedrich-Alexander-Universität Erlangen-Nürnberg
zur Erlangung des Doktorgrades Dr. rer. nat.

vorgelegt von
Julia Natalie Brucker
aus Dachau

Als Dissertation genehmigt von der Naturwissenschaftlichen Fakultät
der Friedrich-Alexander-Universität Erlangen-Nürnberg

Tag der mündlichen Prüfung: 18. Februar 2013

Vorsitzender der Promotionkommission:	Prof. Dr. Johannes Barth
Erstberichterstatter:	Prof. Dr. Christian Stegmann
Zweitberichterstatter:	Prof. Dr. Jörn Wilms

Zusammenfassung

In der vorliegenden Dissertation wird eine detaillierte Studie der TeV-Gammastrahlenquelle HESS J1825–137 präsentiert, die zur Quellklasse der Pulsarwindnebel zählt. Genauer gesagt handelt es sich bei HESS J1825–137 um einen der prominentesten Vertreter der sogenannten „entwickelten Pulsarwindnebel“, die aufgrund ihres fortgeschrittenen Alters mehrere Entwicklungsstufen durchlaufen haben. Im Vergleich zu jungen Pulsarwindnebeln – die im TeV-Gammastrahlungs Licht gewöhnlich „klecksartig“ erscheinen und bei denen der Schwerpunkt der emittierten Strahlung im Zentrum der Emissionsregion liegt – weisen die entwickelten TeV-Pulsarwindnebel oft sehr spezielle Erscheinungsformen auf: Die Emissionsregionen sind stark ausgedehnt und häufig asymmetrisch und der Pulsar, der die Teilchen freisetzt welche die TeV-Gammastrahlung emittieren, befindet sich in vielen Fällen abseits des Zentrums der Emissionsregion. Mit seiner stark asymmetrischen Morphologie, einem Durchmesser von über 1.2° und einem Pulsar der sich am nördlichen Ende der Emissionsregion befindet, stellt HESS J1825–137 sozusagen einen Prototypen der entwickelten Pulsarwindnebel dar. Die Eigenschaft, die ihn allerdings aus der Masse der Gammastrahlen emittierenden Pulsarwindnebeln hervorhebt, ist, dass er einer von nur zwei Pulsarwindnebeln ist, für die im TeV-Gammastrahlenbereich eine energieabhängige Morphologie nachgewiesen werden konnte.

Eine Besonderheit von der Beobachtung von Pulsarwindnebeln im Gammastrahlungsbereich ist, dass sich durch die Gammastrahlung sowohl Teilchen beobachten lassen, die erst vor kurzem vom Pulsar an den Nebel abgegeben wurden, als auch Teilchen, die bereits vor mehreren tausend Jahren emittiert wurden. In anderen Worten: das heutige Gammastrahlenbild zeigt sozusagen die integrierte Geschichte des Pulsarwindnebels. Die zuvor beschriebenen besonderen Eigenschaften der entwickelten Pulsarwindnebel sind folglich das Resultat der Entstehungsgeschichte des Nebels. Deswegen kann man die TeV-Gammastrahlungs-Beobachtungen nutzen um Rückschlüsse auf die Entwicklung des Pulsarwindnebels zu ziehen. Zu diesem Zweck wurde im Rahmen dieser Arbeit ein Modell entwickelt, dessen Ziel es ist die Entstehung der besonderen räumlichen und spektralen Eigenschaften von HESS J1825–137 nachzuvollziehen. Angelehnt an gängige Pulsarwindnebel Modelle wurde simuliert wie sich die Stärke der Teilchenemission des Pulsars während seiner bisherigen Lebenszeit entwickelt hat, wie sich die Teilchen im Raum ausgebreitet und welche Energieverluste sie erlitten haben und schlussendlich wie die heutige Gesamtteilchenverteilung aussieht. Aus letzterer ließ sich unmittelbar die erwartete Gammastrahlen-Emission berechnen. Die Besonderheit des hier vorgestellten Modells ist, dass es sowohl für die die Berechnung von Energiespektren der Gamma-Photonen in beliebigen Teilregionen der Emissionsregion, als auch für die Berechnung von Himmelskarten genutzt werden kann.

Durch Vergleich der Vorhersagen des Modells mit gemessenen Daten ließen sich die Modellparameter optimieren. In dieser Arbeit lag das Hauptaugenmerk darauf, die mit dem H.E.S.S. Teleskop gemessenen TeV Gammastrahlungs-Daten von HESS J1825–137 besonders gut wiederzugeben. Der verwendete TeV-Datensatz umfasste nahezu die doppelte Beobachtungszeit und wurde mit einer sensitiveren Analysemethode untersucht als es in

der vorhergegangenen H.E.S.S. Veröffentlichung zu HESS J1825–137 der Fall war. Mit Hilfe einer Durchmusterung des Modell Parameter Raumes sowie eines zusätzlichen Minimierungsverfahrens wurden zehn verschiedene Kombinationen an Modell Parametern bestimmt, die die TeV-Energiespektren von zwölf ausgewählten Teilbereichen der Emissionsregion – denen schon in der vorausgegangenen H.E.S.S. Veröffentlichung eine herausragende Rolle zugeschrieben wurde – besonders gut reproduzieren konnten. In detaillierten Studien wurde untersucht, wie für die ausgewählten Parametersätze die Modell Vorhersagen für die Energiespektren im TeV-, GeV- und Röntgenbereich sowie für die Morphologien der H.E.S.S. Himmelskarten aussehen und wie sich diese im Vergleich zu tatsächlich gemessenen Daten verhalten. Abschließend wurde zukünftige Verbesserungsmöglichkeiten an dem ausgewählten Optimierungsverfahren untersucht, mit dem Ziel sowohl die spektralen als auch die morphologischen Eigenschaften der TeV-Gammastrahlungsquelle bestmöglich zu berücksichtigen.

Abstract

In the thesis at hand an in-depth study of the TeV γ-ray source HESS J1825–137 is presented, which belongs to the pulsar wind nebulae source class. More specifically, HESS J1825–137 is one of the most prominent representatives of the so-called "evolved pulsar wind nebulae", which due to their advanced age have passed multiple evolutionary stages. In comparison to young pulsar wind nebulae, which usually appear blob-like and centre-filled in TeV γ rays, the evolved TeV-nebulae often exhibit very peculiar forms of appearance: The emission regions are vastly extended and often asymmetric and the pulsar – which emits the particles that generate the TeV γ rays – is located offset to the centre of the emission region in many cases. With its strongly asymmetric morphology, its diameter of more than 1.2° and a pulsar which is located at the northern limb of the emission region, HESS J1825–137 can be considered an archetype of the class of evolved pulsar wind nebulae. Beyond that, HESS J1825–137 stands out from the plenitude of γ-ray emitting pulsar wind nebulae because the source is one of only two pulsar wind nebulae for which an energy-dependent morphology could be established in TeV γ rays.

A special feature of the observation of pulsar wind nebulae in γ rays is, that the TeV γ rays give indirect access to particles that have been injected into the nebula recently, but at the same time also to particles which have been emitted a few thousand years ago. Or in other words: the present γ-ray image sort of shows the integrated history of the pulsar wind nebula. Consequently, the special features of the evolved pulsar wind nebula as described above are the result of the evolutionary history of the nebula. Therefore, the TeV γ-ray observations can be used to draw conclusions on the evolution of the pulsar wind nebula. For this purpose a model aiming to reproduce the formation of the unique spatial and spectral features of HESS J1825–137 was developed within this thesis. On the basis of well-established pulsar wind nebula models, it was simulated how the particle emission of the pulsar has evolved within its previous lifetime, how the particles have spread into space, which energy losses they have undergone and finally how the present-day distribution of all particles ever emitted looks like. From the latter the expected γ-ray emission could be derived directly. What makes the presented model rather special is that it can be used to compute both, the energy spectra of γ rays from arbitrary subregions of the total emission region as well as sky maps.

Comparing the predictions of the model to measured data, it was possible to optimise the model parameters. In this work the primary focus was on reproducing the TeV γ-ray data of HESS J1825–127 obtained with the H.E.S.S. telescopes. The used TeV data set comprised almost twice the amount of live time and was analysed with higher sensitivity than in the previous H.E.S.S. publication dedicated to HESS J1825–137. By means of a scan of the parameter space and an additional minimisation procedure ten model parameter sets were selected which reproduced the TeV energy spectra of twelve subregions of the emission region – which had already played an important role in the previous H.E.S.S. publication – particularly well. For the selected parameter sets it was investigated how the model predictions for the energy spectra in the TeV-, GeV- and X-ray range as well as for the morphologies of the H.E.S.S. sky maps look like and whether they

are consistent with observational data. Finally, future improvements of the optimisation procedure were studied with the objective of considering the spectral and spatial features of the investigated source in the best possible way.

Contents

1. Introduction

Our knowledge of the Universe, in particular of the different types of celestial objects, has been gained in various ways. One approach is the optical astronomy, i.e. the most traditional form of astronomy, which has been pursued for more than 5000 years. While the stars were originally observed with the naked eye, the invention of optical telescopes resulted in a rapid progress in the exploration of the sky. By means of the new techniques a multitude of celestial objects was detected and most notably could be studied in detail using photography, photometry, spectroscopy and polarimetry. In doing so, first conclusions on the physical processes occurring in celestial objects were drawn. These studies revealed that the prevalent astronomical sources of visible light are objects with temperatures between 1000 K and 100 000 K, which emit thermal radiation, e.g. stars, galaxies and gas / dust nebulae. During the first third of the 20th century the energy range of the electromagnetic radiation in which astronomical objects could be observed was extended to include infrared and radio wavelengths. However, a further extension of the observable wavelength range for ground-based telescopes was – at least for the time being – prevented by the opaqueness of the Earth's atmosphere (see Fig. 1.1).

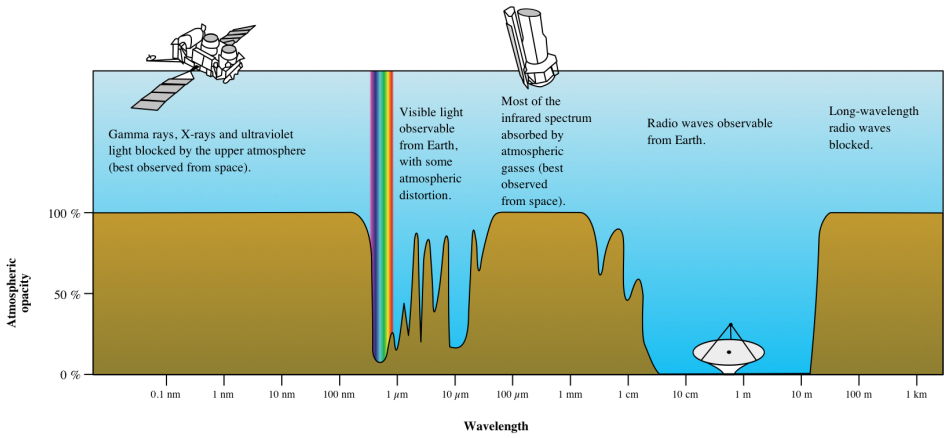

Figure 1.1.: Chart of the opacity of the Earth's atmosphere for different wavelengths of electromagnetic radiation, courtesy NASA / JPL-Caltech. In addition, the best suited instruments for observations are indicated.

Besides the electromagnetic radiation other types of radiation exist, which can be used to gain information about celestial objects. These include an intense flux of charged and neutral cosmic particles which continuously hit the Earth's atmosphere. These cosmic rays (CRs), which have been discovered by Victor Hess in 1912, are predominantly composed of protons and nuclei, but also comprise electrons, positrons, neutrons, neutrinos etc.

As we know today, the energy of these particles can be as high as 10^{20} eV. Thus these particles provide clear indications that there are explosive non-thermal emission processes in the Universe. It is, however, rather difficult to identify the origins of the cosmic rays. The problem with the charged particles is that they are randomly deflected in galactic and intergalactic magnetic fields and therefore have lost the information on their original direction when they hit the Earth. Neutral particles on the other hand have the disadvantage of short livetimes and/or of challenging detectability. As a result, even today – 100 years after the first discovery of the cosmic rays – the puzzle about their origin and the acceleration mechanisms is not entirely solved.

Due to the presented problems a great part of the scientific findings concerning the sources of cosmic rays is again based on observation of electromagnetic radiation. These observations take advantage of the fact that highly energetic protons and electrons emit photons via different processes. One of these processes is the decay of π^0-particles produced in hadronic interactions. Others are for instance the synchrotron radiation in local magnetic fields and the inverse-Compton (IC) scattering of highly energetic electrons on background photons. These non-thermal processes emit photons over the entire electromagnetic spectrum, from radio up to energies of several PeV. They are, however, especially well observable at high energies, i.e. in X-rays and γ rays, as the photon spectra in these energy ranges are dominated by the non-thermal processes. Thus, the start of space flights was a first milestone in the search for cosmic-ray sources, as X-ray detectors could finally be lifted above the shielding atmosphere. Photons with even higher energies, so called very high energy (VHE, $E \geq 10^{11}$ eV) photons, are, however, not accessible for satellites, as the fluxes at these energies are small and require large detection areas which can not be provided by spacecraft. In order to observe these photons an indirect detection method was invented at the end of the last century, which uses the Earth's atmosphere as a detector. When the VHE γ rays hit the atmosphere, they generate a distinct signal that can be detected and analysed by ground-based telescopes, see Sec. 4.1. Currently, there are three operating experiments of this type, i.e. imaging atmospheric Cherenkov telescopes (IACTs), which are spread over the globe to cover the full sky. Having detected more than 130 VHE γ-ray sources within the last ten years, H.E.S.S.[1], MAGIC[2] and VERITAS[3] proved to be extremely successful. An up-to-date overview of the observable TeV sources and their location in the Universe is presented in Fig. 1.2. One notices immediately that the TeV sources are not spread evenly over the sky. Instead, most of them cluster along the Galactic Plane. This spatial distribution is reflected by the classification of the TeV sources as extragalactic or galactic. The former are extremely strong γ-ray emitters, e.g. active galactic nuclei (AGN) and starburst galaxies. However, because of their large distances to the Earth they are only visible as point sources for current TeV experiments. This is not the case for the Galactic TeV sources, as shown in Figure 1.3. The image gives an impression of a section of the Milky Way as seen by the H.E.S.S. experiment and reveals a plenitude of types and forms of appearance. Typical Galactic TeV emitters are pulsar wind nebulae (PWNe), supernova remnants (SNRs), star clusters

[1] http://www.mpi-hd.mpg.de/hfm/HESS
[2] http://magic.mppmu.mpg.de
[3] http://veritas.sao.arizona.edu

and binary systems.

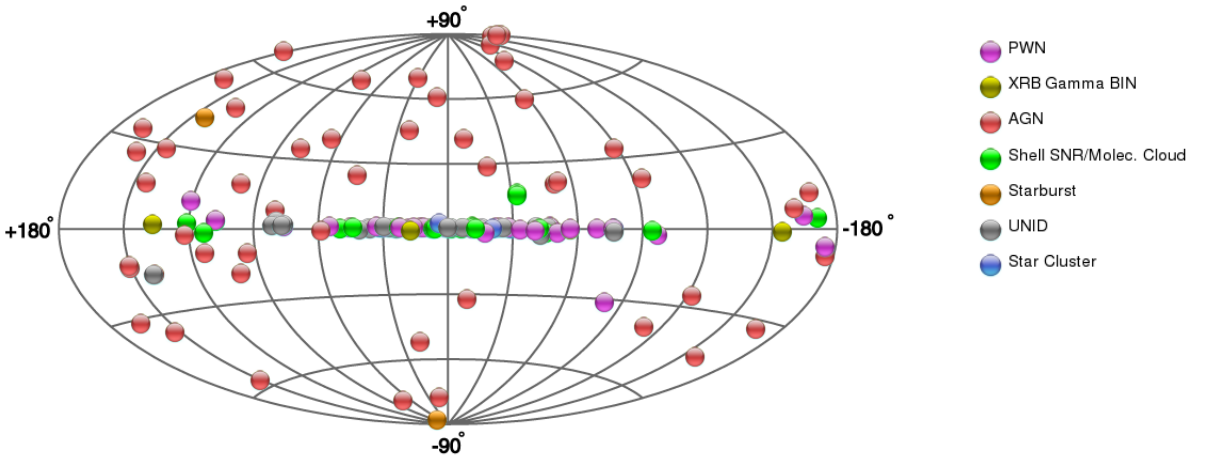

Figure 1.2.: VHE γ-ray sources and their location on the sky, illustrated in Galactic coordinates. The figure was taken from the online catalog for TeV astronomy (TeVCat, [WH12]) and captures the state of September 2012. Generally, extragalactic and galactic sources are distinguished. While the former spread evenly over the sky, the latter cluster along the Galactic Plane. The colours of the markers represent the respective sources classes. The extragalactic sources comprise active galactic nuclei (red) and starburst galaxies (orange), the galactic sources pulsar wind nebulae (purple), supernova remnants (green), star clusters (blue) and binary systems (yellow). Sources which have not been identified yet are marked with grey dots.

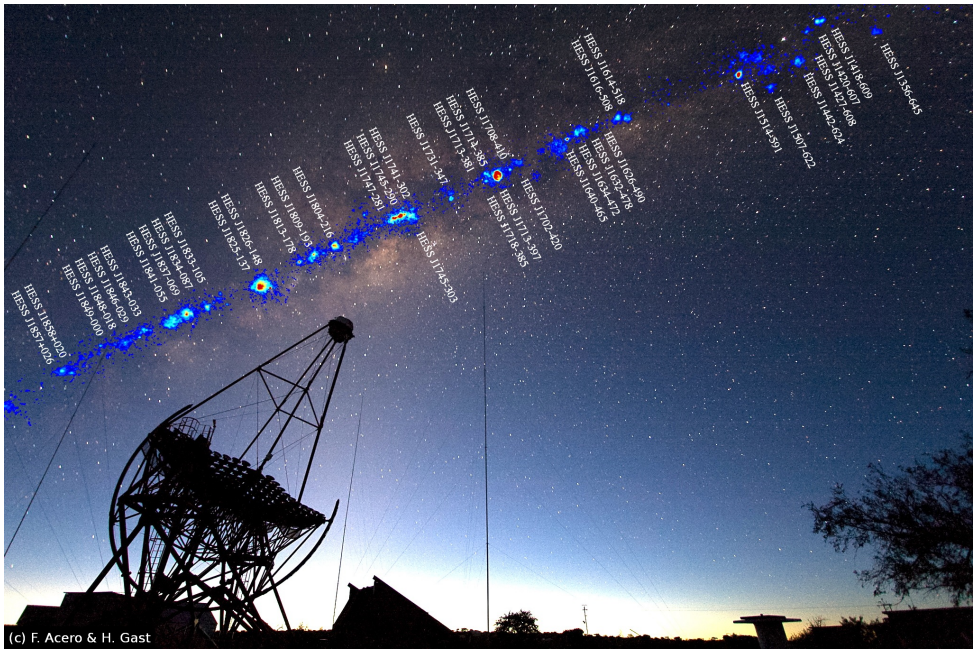

Figure 1.3.: The Milky Way in VHE γ rays as seen by H.E.S.S., credit H. Gast & F. Acero, © H.E.S.S. Collaboration

In Fig. 1.4 an overview of the abundances of the different Galactic VHE γ-ray sources is given. Besides a large number of unidentified sources, which have not been assigned to a specific source type yet, the PWNe form the most abundant group. They are followed by the SNRs – which in the figure are subdivided into SNRs with directly observable shell and SNRs, that are only visible due to their interaction with molecular clouds – and by star clusters. The rarest class is formed by the binary systems. Depending on the energy range in which the source has been discovered, this class can even be subdivided into X-ray and γ-ray binaries. With only one representative, viz. HESS J0632+057, the γ-ray binaries are truly unique. In the course of my work as Ph.D. student I have contributed to the identification of this source, i.e. we have presented first hints to its transient nature [H$^+$09]. The details of this work and an overview of the current status of research on this subject are presented in App. A.

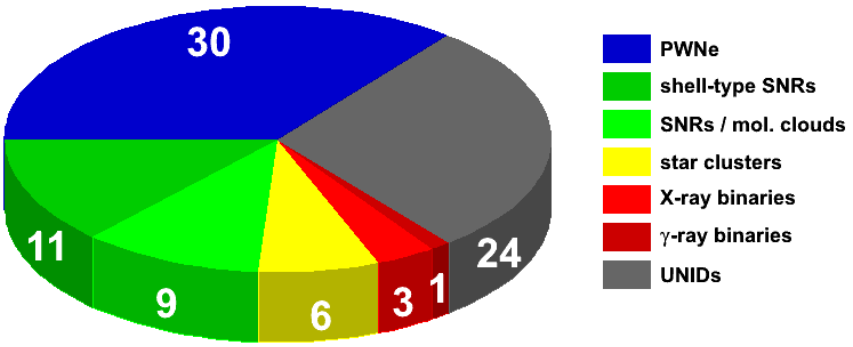

Figure 1.4.: Pie chart of Galactic VHE γ-ray sources, compiled using TeV Cat as of September 2012. Sorted by descending frequency, there are: pulsar wind nebulae, supernova remnants interacting with molecular clouds, shell-type supernova remnants, star clusters and binary systems. The latter are subdivided in X-ray binaries (XRB) and Gamma-ray binaries, depending on the energy range in which they have been discovered. Sources which have not been identified yet are summarised as unidentified sources (UNID).

The main focus of this work, however, is dedicated to the study of PWNe, or more precisely to the study of one of the most prominent representatives: HESS J1825–137. Pulsar wind nebulae are nebulae of highly energetic particles which are powered by pulsars. The latter come into existence in supernova explosions at the final stage of stellar evolution, when the mass of the progenitor star is too high for a white dwarf to be stable, but too low for a black hole to be created. Due to the conservation of angular momentum and magnetic flux the newly formed compact object is rotating extremely fast and is surrounded by an extraordinarily strong magnetic field. In this violent environment charged particles are accelerated to very high energies and they form a particle wind, which in turn feeds the pulsar wind nebula. In current models it is usually assumed that the accelerated particles in the pulsar wind nebula are predominantly leptons, viz. electrons and positrons. Interacting with the strong magnetic fields these leptons emit synchrotron radiation which is well observable in X-rays. In addition, the particles can also upscatter ambient photons to very high energies. Theoretical calculations show that the synchrotron

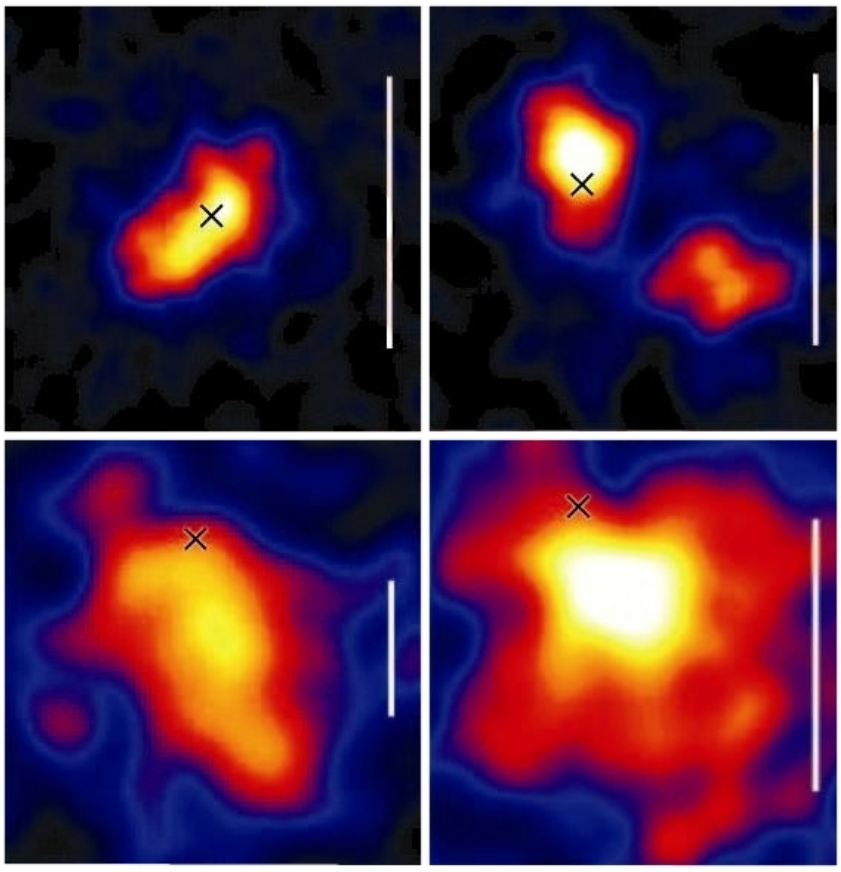

Figure 1.5.: Sky maps of extended PWNe as observed with H.E.S.S., taken from [HH09]. Clockwise from top left the presented sources are: MSH 15–5*2*, the K3 / Rabbit PWN, HESS J1825–137 and Vela X. All these PWNe belong to the class of evolved PWNe and exhibit TeV morphologies that are far more extended than the point spread function of the VHE telescopes (in the order of 0.1°). In the images the white bar indicates a size of 0.5°. Besides the different sizes, the shapes and the location of the VHE source with respect to the corresponding pulsar (indicated by black crosses) vary.

radiation is generated by young and highly energetic leptons, while the VHE photons can still be generated by older and even by cooled lepton populations. In accordance with this assumption TeV observation of PWNe often reveal significantly extended sources. Four prominent examples of evolved PWNe are presented in Fig. 1.5. These four images give a first impression of the variety of sizes, shapes and arrangements. While X-ray observations predominantly allow to study the spatial distributions of the magnetic fields within the PWNe, the VHE γ-ray observations provide insights in the spatial distribution of the charged particles themselves. By studying the spatial and spectral distributions of the γ rays, and thus of the emitting charged particles, conclusions on the evolution of the PWN can be drawn.

In this thesis we will study in detail the TeV γ-ray source HESS J1825–137. A first glimpse of HESS J1825–137 is presented in the bottom right sky map of Fig. 1.5. HESS J1825–137 is one of the most extended TeV γ-ray sources. Due to the asymmetry of the emission region and due to the offset location of the corresponding pulsar the identification of HESS J1825–137 as a PWN was fraught with difficulties. The final identification only succeeded by means of an approach which at this time was unique in TeV astronomy: the verification of an energy-dependent morphology. While γ rays with energies between 0.2 TeV and 0.8 TeV are found at high distances to the pulsar, the most energetic γ rays, i.e. with energies above 2.5 TeV, originate in the immediate vicinity of the pulsar. In this work the analysis of an enlarged TeV data set is presented. Moreover, a model is developed which is targeted on reproducing the unique spatial and spectral distribution of the γ rays within HESS J1825–137 by simulating the evolution of the PWN. In detailed studies it is investigated how the parameters can be optimized to reproduce the TeV γ-ray emission. Although the modelling is primarily oriented towards the TeV γ ray emission, the model predictions for other wavelengths, viz. X-rays and GeV γ rays, are also compared to measured data.

The structure of this thesis is the following: In Chapter 1 the present state of knowledge about PWNe is introduced. Emphasis is placed on the structure and the evolution of PWNe, as well as on the radiation mechanisms, which allow us to study PWNe in X-rays and γ rays. In the second chapter published observations of HESS J1825–137 in various energy ranges and the emerging conceptions are presented. In addition, already existing models are introduced which aim to explain the features of HESS J1825–137. Since the modelling of the TeV γ-ray data requires an in-depth understanding of the imaging properties of the observing telescopes, the imaging atmospheric Cherenkov technique and its challenges are studied in Chapter 3. Taking the H.E.S.S. telescopes as example, the data analysis procedure is presented and finally a considerably enlarged H.E.S.S. data set of HESS J1825–137 is evaluated. To investigate the unique TeV features of HESS J1825–137 a new model was developed and is introduced at the beginning of Chapter 4. Subsequently, an optimisation procedure for the model parameters is presented in detail and the model predictions for the X-ray and GeV γ-ray regime are computed and compared with observational data. Finally, it is discussed how the optimisation procedure may be improved in the future.

2. Pulsar Wind Nebulae

Pulsar wind nebulae belong to the class of objects which come into existence when the evolution of a star is terminated by a supernova explosion. Hence, they form a subclass of supernova remnants. In contrast to the class of shell-type supernova remnants, in X-rays and γ rays pulsar wind nebulae exhibit a blob-like form and often a centre-filled structure. Therefore, they are also referred to as "plerions", a denotation that derives from the ancient Greek word "pleres", which can be translated as "full" or "covered" [WP78]. But how are these blobs formed?

In brief, our current understanding of PWNe is the following: When at the end of the evolution of a massive star the gas pressure can no longer counterbalance the gravitational pressure, then the star collapses and the outer layers of the progenitor star are ejected in a supernova explosion. The blast wave expands into the interstellar medium and a supernova shell is formed, which can be observed at several wavelengths. In case that the mass of the progenitor star has been high enough, a neutron star may form. Due to the conservation of the angular momentum and the magnetic flux the compact object usually rotates rapidly and is surrounded by a strong magnetic field. As a result of the rotation electromagnetic waves are emitted and may be detected by a distant observer as a pulsed signal. Moreover, particles are accelerated in the strong electric fields and give rise to a magnetized outflow, the so called pulsar wind. Thus, the neutron star continuously dispenses its rotational energy and serves as a central engine of the pulsar wind nebula. When the pulsar wind catches up with the slower flow in the nebula a termination shock forms. At this termination shock the flow of the particles is decelerated, but the energies of the particles are even boosted [Sla08]. Downstream of the shock a bubble of highly energetic particles and magnetic fields forms. This PWN is confined by the inertia of the supernova ejecta and the pressure of the interior of the SNR. The PWN is a strong emitter of electromagnetic radiation, as the highly energetic particles emit photons in non-thermal processes. A schematic representation of a typical PWN is presented in Fig. 2.1(a).

A verification of the assumed structure by observational data is presented in Fig. 2.1(b). This image shows a sky map which has been produced from X-ray observations of SNR G 21.5-0.9 with the Chandra telescope. In the centre of the image we can see the pulsar, which is surrounded by the PWN. Moreover, the connection to the supernova remnant is approved, as the PWN is located in the centre of the supernova shell. Such SNRs, for which the shell and the PWN are observed, are called composite SNRs. Observations of this kind are sometimes made for rather young PWNe, but one should note, that they are not the norm. Especially in older systems, the emission of the shell may be too weak to be traceable. Moreover, the SNR and the PWN often expand into heterogeneous media and thus develop in an asymmetric way. Such an asymmetric development may even

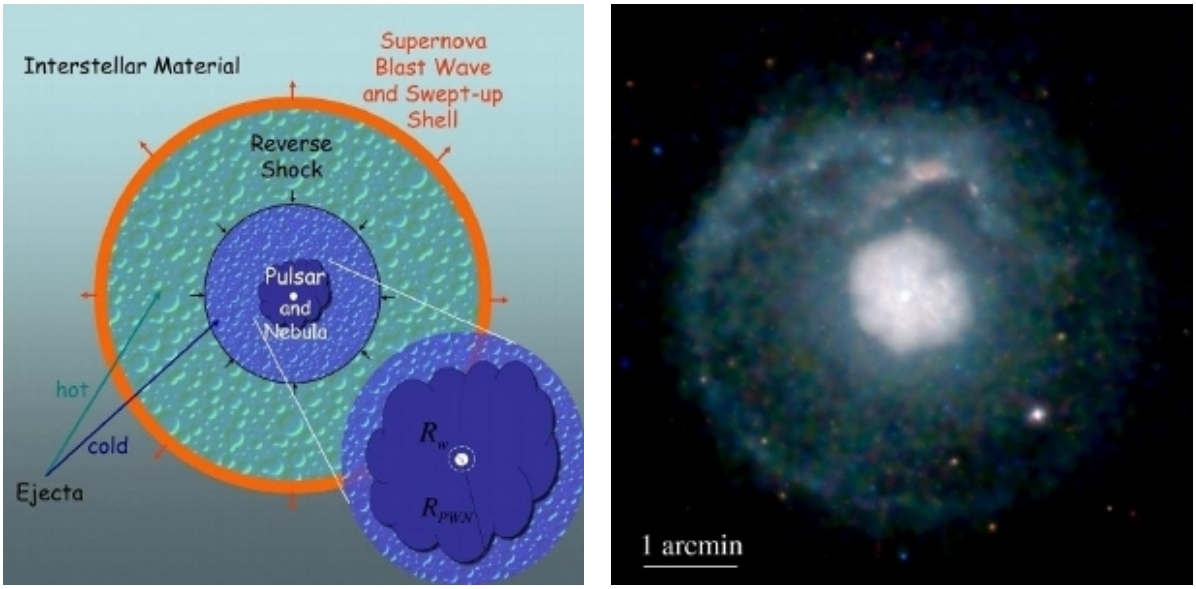

(a) Schematic representation of a composite PWN (b) Chandra X-ray image of SNR G 21.5–0.9

Figure 2.1.: Schematic representation and observational data of a pulsar wind nebula inside a supernova shell, [GS06] and references therein. (a) Schematic representation of our current knowledge of PWNe inside supernova remnants. The supernova blast wave, which has its seeds in the supernova explosion, spreads out into the interstellar medium and can be observed as swept-up shell. At the same time a pulsar, which came into existence in the supernova explosion, continuously powers a wind of charged particles and a wind nebula is formed at the centre of the remnant (see enlarged section). Under certain circumstances a reverse shock is generated, which can strongly influence the evolution of the pulsar wind nebula. (b) The X-ray image shows the composite SNR G 21.5–0.9 as observed with the Chandra telescope. Clearly visible are the shell of the supernova remnant (with a diameter of $\approx 5'$) and the PWN (diameter $\approx 1.5'$), which evolves in the centre of the SNR. The young pulsar PSR J1833–1034 is located at the centre of the PWN.

be amplified, when the system is old enough that a reverse shock could arose from the supernova shell. If such a shock hits the PWN, it is crushed and may even be displaced. Last but not least, pulsars often gain a kick during the supernova explosion and therefore move with supersonic velocities. This also distorts the symmetric appearance presented in Fig. 2.1.

Besides these typical forms of appearance, the energy distribution of the detected photons is especially characteristic for PWNe. PWNe represent a very violent environment: there are highly energetic particles and extremely strong magnetic fields. Due to the magnetic fields charged particles predominantly emit synchrotron radiation, but they can also upscatter background photons, e.g. photons from the cosmic microwave background (CMB), via IC scattering. The emitted photons can be observed over a broad range of wavelengths from radio to VHE γ rays. In Fig. 2.2, for instance, the spectral energy distribution (SED) of the photons from the most famous and best studied PWN, the Crab Nebula, is presented. Clearly visible is a double hump structure which is generally

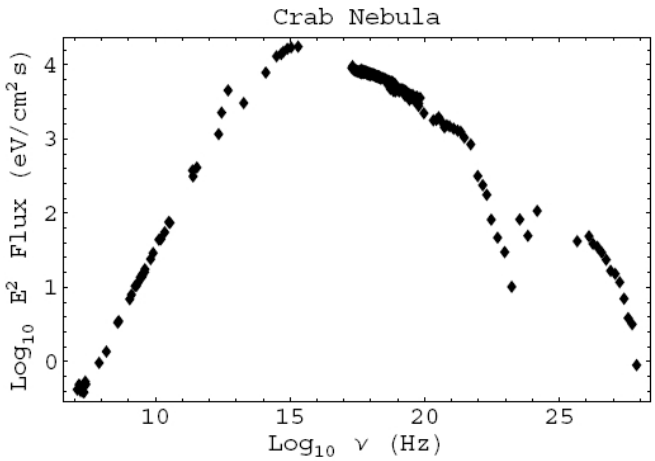

Figure 2.2.: Spectral energy distribution of the Crab Nebula, [KLP09] and references therein. Via non-thermal processes the charged particles in the pulsar wind nebula emit photons from radio over infrared, optical and X-ray up to TeV energies. The SED exhibits a characteristic double hump structure which is ascribed to synchrotron and IC emission.

ascribed to the synchrotron and the IC emission. A similar spectral energy distribution is observed from other PWNe. However, it should be noted that the specific structure depends again on several factors. The precise shape is influenced by the spectrum of the emitting particles, the strength of the magnetic fields, the target photons, the age of the system, etc.

While the differences in the forms of appearance and the shapes of the SEDs may complicate the identification of PWNe, they allow us to draw conclusions on the emitting particle populations, on the acceleration and transportation mechanisms, on the photon emission processes, etc. Our current understanding of these processes will be presented in this chapter. At first the constituents of the PWN will be studied: the pulsar, the unshocked wind, the termination shock and finally the nebula itself. As the PWN HESS J1825–137 is a middle-aged PWN with an age of about 20 kyr the evolution of PWNe is examined in the second section. Afterwards, typical assumptions in the modelling of PWNe are introduced. In particular, the relevant photon emission processes are investigated. Finally, at the end of the chapter, we will have a closer look at the multifarious TeV observations of PWNe with H.E.S.S.

2.1. Composition

Pulsar wind nebulae are characterised by the complex interplay of several constituents. This section presents what various observations have taught us about these constituents. As a start the pulsar as the engine of the PWN will be of particular interest. Thus, the first subsection deals with the creation of pulsars, their features and the question how they generate pulsar winds. Afterwards, some concepts regarding the acceleration of particles to extremely high energies and the evolution of the wind nebula will be presented.

2.1.1. The Pulsar

The name "pulsar" is a contraction of "pulsating star" and was established for a source class that was discovered by chance by the Ph.D. student Jocelyn Bell and her supervisor Anthony Hewish in 1967. They monitored the scintillation of celestial radio sources, when Bell noticed a distinct signal that consisted of an extremely regular series of radio pulses and that reappeared four minutes earlier each day. Hewish concluded that the signal is of celestial origin and he even suggested that it might be connected with a very compact neutron star, a star type which had only been discussed theoretically at this time [H$^+$68]. Indeed, the concept of a neutron star as an endpoint of the stellar evolution had been introduced by Walter Baade and Fritz Zwicky in 1934 [BZ34], but for a long time the observability of these objects has been considered unlikely. A first hint that neutron stars are nevertheless traceable was provided a few months before the discovery of the pulsars by Franco Pacini, who proposed that rapidly rotating neutron stars with strong dipolar magnetic field can power nebulae like the Crab Nebula [Pac67]. Without being aware of this publication it was, however, Thomas Gold who shortly after the discovery of the pulsars suggested rotating neutron stars as the engine of the pulsating sources [Gol68]. Joining their efforts, Pacini and Gold soon established the basis of our present understanding of pulsars [Pac68, Gol69]. In this understanding neutron stars emerge from the gravitational collapse of a massive star accompanied by a supernova explosion. Due to the conservation of the angular momentum and the magnetic flux a neutron star is born with a rotation period in the order of milliseconds and a dipolar magnetic field of about 10^{12} G. In general, the rotation axis and the magnetic axis are not aligned. In the co-rotating magnetosphere, a narrow beam of electromagnetic radiation is created. Due to the rotation the signal from the pulsar can only be detected when the beam points directly to a distant observer. In the remaining time of the rotation period the source appears dark, i.e. no signal is detected. Thus, a characteristic pulsed signal is created. While the pulses are extremely regular, a slow-down of the rotation is expected as rotational energy is lost due to magnetic dipole radiation. Observational evidence for this rotation-powered pulsar model was provided by the detection of very short rotation periods, e.g. for the two very prominent pulsars the Crab pulsar [SR68] and the Vela pulsar [LVM68] with periods of 33 ms and 89 ms, respectively. Moreover, Radhakrishnan et al. showed that the positioning angle of the plane of polarisation of the radio waves from the Vela pulsar changed during the pulse phase just as it would be expected in simple models of beamed emission [R$^+$69]. And finally, the slow down of the rotation was detected for the Crab pulsar by Richards and Comella [RC69].

Characteristics of Pulsars

Today more than 2000 pulsars are known (compare for instance the ATNF pulsar catalogue[4], [M$^+$05]). These pulsars do not only emit pulses in the radio regime, but also in

[4] http://www.atnf.csiro.au/research/pulsar/psrcat

several other wavelengths. For the Crab pulsar, for instance, pulsed emission has been detected over 19 orders of magnitudes up to γ rays above 25 GeV [A$^+$08b]. This observability in the different wavelengths, as well as the shapes and the arrival times of the pulses, allow conclusions on the emission processes of the radiation. We will later have a closer look at these processes, but will first proceed with our overview of the known pulsar population.

Measured rotation periods and their time derivatives are in the order of 1 ms to 10 s and 10^{-21} to 10^{-12}, respectively [LGS05]. However, when we look at the distribution of the pulsars in a P-$\dot{P}$-diagram, it becomes evident that there are actually two populations: one that rotates very fast and shows hardly any slow-down and one with slower rotation periods and higher slow-down rates. The first group, the so called millisecond pulsars, supposedly are recycled pulsars, which have been part of a binary system. Due to accretion from a companion star angular momentum was transferred to the pulsar and resulted in an increase of the rotation frequency. At the same time millisecond pulsars have magnetic fields which are only in the order of 10^9 G. Therefore, they are unlikely to generate strong pulsar winds or even pulsar wind nebulae. Indeed, PWNe that emit VHE γ-ray emission have only been detected for the second group, the rotation-powered pulsars. Their rotation periods are in the order of 10 ms to 10 s and the period derivatives range from 10^{-18} to 10^{-12}.

Distances to radio emitting pulsars can be derived rather well from the dispersion measure [TC93]. This technique takes advantage of the dependency of the propagation velocity in the ionised interstellar medium on the radio frequency of the photon. In simplified terms: more energetic photons are less influenced in their propagation and will therefore arrive earlier than less energetic photons. Therefore, the differences in the arrival times of pulses observed at different wavelengths can be used to draw conclusions on the amount of traversed matter. As the propagation of the radio waves is predominantly influenced by free electrons, models of the distribution of the electron density in the Galaxy, e.g. [CL02], are needed to convert the dispersion measure into an estimate of the distance of the pulsar. The largest part of the observed galactic pulsars is situated along the Galactic Plane in a layer with a thickness of about 1 kpc and a radius of about 10 kpc, [LGS05] p. 93 f.

Due to the long baselines in radio astronomy the positions of radio pulsars on the sky can be determined with an accuracy in the order of a tenth of an arcsecond. Thereby, different methods based on direct interferometry or timing analysis are applied. The latter takes advantage of the dependency of the arrival times of the pulses on the orbital motion of the Earth around the Sun, [LGS05] p. 50 ff. Observations taken over the course of several years can be used to derive the position and a potential proper motion very accurately. Concerning the proper motion of pulsars, Gunn & Ostriker were the first to notice that pulsars are moving with much higher velocities than their progenitor stars [GO70]. This observation was confirmed by several other authors, amongst others by Hobbs et al. who conducted a statistical study of the proper motions of 233 pulsars. This study revealed that the mean 3-D pulsar birth velocity is in the order of 400 km s^{-1} [H$^+$05]. The high velocities are usually thought to arise from asymmetries in the explosive formation processes of pulsars which can give a kick to the newly born compact star.

Formation and Structure of Neutron Star

The understanding of pulsars, their pulsed emission and winds is directly linked to the properties of the underlying neutron stars. Thus, this subsection is dedicated to their formation and structure: At the end of the stellar evolution when the fusion processes no longer balance the gravitational pressure, massive stars collapse under their own gravity. Depending on the mass of the progenitor star three different final states are distinguished: white dwarfs, neutron stars and black holes. Neutron stars are generated when the progenitor star has a mass between six and fifteen solar masses ($M_\odot = 2 \times 10^{33}\,\mathrm{g}$) [LGS05]. When the fusion processes fade, the atoms get compressed and the electron degeneracy pressure balances the gravitational pressure. At first this transformation proceeds in a controlled way and for white dwarfs with masses smaller than 1.4 solar masses, i.e. the Chandrasekhar limit, the electron degeneracy pressure is enough to keep the compact star stable. However, when this limit is exceeded the electron degeneracy pressure no longer suffices and the inverse β-decay process takes place, in which protons and electrons transform into neutrons and neutrinos. Moreover, the outer envelope of the progenitor star is blown off in the supernova explosion and approximately $10^{51}\,\mathrm{erg}$ are released almost instantaneously. The newly formed neutron star is stabilised by strong repulsive neutron-neutron interactions, as well as by the neutron degeneracy pressure. Due to the degeneracy the equation of state is dominated by pressure and density, whereas temperature no longer plays an important role. By means of the standard general-relativity equation of hydrostatic equilibrium predictions about the pressure and the density of neutron stars can be made. They are, however, subject to uncertainties, as the matter in the neutron star is in a state that can not be observed on Earth. Consequently several different predictions for the equation of state exist, compare for instance [LP01]. Default assumptions on the size and the mass of a neutron star are a radius of about 10 km and a mass of 1.4 solar masses. This corresponds to a mean density in the order of $6.7 \times 10^{14}\,\mathrm{g\,cm^{-3}}$, which exceeds the density of nuclear matter $\rho_\mathrm{n} = 2.7 \times 10^{14}\,\mathrm{g\,cm^{-3}}$.

Despite the uncertainties in the equation of state, the internal structure of a neutron star is well predicted. An overview of the structure is given in [Lat04] and will briefly be summarised in the following. Basically five major regions are distinguished: the atmosphere, the envelope, the crust and the outer and the inner core. The atmosphere and the envelope are extremely thin and contain only a tiny fraction of the total mass, but they influence the transport of the thermal energy and the final thermal photon spectrum emitted by the neutron star. The crust is expected to have a thickness of 1 to 2 km. Due to the comparatively small pressure, nuclei exist in the crust. At the outer limb of the crust there are mainly iron nuclei, whereas with increasing depth neutron-rich heavy nuclei prevail. When the density gets higher than the neutron drip density of $4 \times 10^{11}\,\mathrm{g\,cm^{-3}}$, a neutron fluid starts to coexist with the nuclei. In the outer core, where the density is higher than in nuclear matter, the neutron fluid dominates and contains only a small fraction of protons, electrons and muons. The neutron fluid in the outer core and and in the crust is expected to behave like a superfluid. In addition the protons may form a superconductor [BPP69]. Observational evidence for the existence of the superfluid was given by the detection of glitches, i.e. sudden increases in the rotation rate, cf. [AI75, LEV92]. In the inner core

densities as high as 5 to 10 times the nuclear density are expected, favouring the existence of exotic states of matter, e.g. a solid core of mesons or kaons, or even deconfined quark matter.

Magnetosphere

A simple estimate of the magnetic field strength for a young pulsar can be derived from the assumption that the magnetic flux is conserved during the formation process of the pulsar. After the gravitational collapse the mass is concentrated in a significantly smaller volume, whereas the magnetic field strength is amplified to a multiple of its original value. Thus the magnetic dipole field of neutron stars belongs to the strongest magnetic fields in the Universe: for young pulsars it is in the order of 10^{12} G and even for older ones it is still in the order of 10^{10} G, [LGS05] p. 21. The high level of stability of the magnetic field over time is ascribed to the super-conductive component inside the neutron star. For the sake of completeness it should be mentioned that a small subclass of pulsars with higher magnetic fields than the quoted ones exist, [LGS05] p. 140. These so called magnetars exhibit magnetic field strengths in the order of 10^{14} G to 10^{15} G and rotation periods in the range of 6 s to 12 s. It is assumed that such extremely high magnetic field strengths are generated when neutron stars are born with initial periods smaller than 10 ms. For such fast rotating neutron stars dynamo action in the ionised gas may drastically amplify the original magnetic field [KDT03]. However, since the spin-down time of the magnetars is relatively short, i.e. 10^3 yr to 10^5 yr, the number of observable magnetars is much smaller than the number of rotation-powered pulsars.

While the high magnetic field strength in rotation-powered pulsars is not expected to have significant influence on the inner structure of the neutron star, its influence increases in the vicinity of the surface and it becomes the dominant factor outside of the neutron star [Rud71]. Accordingly, the sphere surrounding the pulsar is called magnetosphere, see Fig. 2.3. As the magnetosphere is the region where the highly energetic emission originates, we will have a closer look at it in the following. The basis of our present understanding of the pulsar magnetosphere was provided by Goldreich and Julian in 1969 [GJ69]. Although they analysed the simplified case of an aligned rotator, i.e. a neutron star with aligned rotation axis and magnetic dipole moment, they derived basic concepts which are still valid today. Goldreich and Julian showed that the rotating neutron star must be surrounded by a dense high-energy plasma. If this was not the case, i.e. if the neutron star was surrounded by vacuum, the electric forces along the magnetic field lines would be much higher than the corresponding gravitational forces on surface charges of the neutron star. Thus the charges would be torn out from the neutron star. As the matter inside the neutron star and in the magnetosphere is assumed to be an excellent electrical conductor no net electric field is sustained. The induced electrical field is given by $\vec{E} = -\frac{1}{c}(\vec{\Omega}\times\vec{r})\times\vec{B}$, where $\vec{\Omega}$ denotes the angular velocity of the pulsar and $\vec{B}$ the magnetic field. From this equation the net charge density can be derived: $n_{\mathrm{GJ}} = n_- - n_+ = \frac{\vec{\Omega}\cdot\vec{B}}{2\pi ec}$. As a result, regions with positive and negative net charges are formed in the magnetosphere.

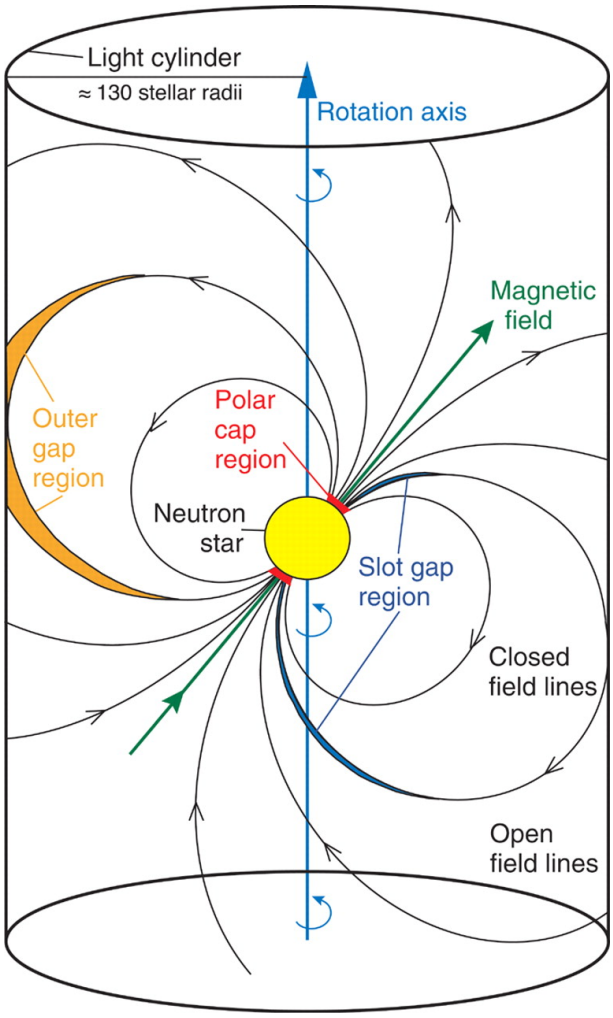

Figure 2.3.: Schematic representation of the magnetosphere of a pulsar, taken from [A+08b]. The environment of the pulsar that is dominated by the extremely strong dipolar magnetic field is called the magnetosphere. The magnetosphere is bordered by the light cylinder. Outside the light cylinder co-rotating particles would have to move with velocities greater than the velocity of light. As a result closed and open magnetic field lines arise and vacuum gaps are formed, in which particles are accelerated. These vacuum gaps comprise the polar caps, slot gaps and outer gaps.

In the strong magnetic field the charged particles move along the magnetic field lines. In doing so they are forced to co-rotate with the neutron star. In regard to the co-rotation an essential zone of the magnetosphere can be defined: the light cylinder (see Fig. 2.3). Particles within the light cylinder have velocities smaller than the velocity of light, particles outside would have to move faster. This has consequences on the course of the magnetic field lines and the motion of the particles. While the magnetic field lines within the light cylinder are closed, the magnetic field lines which intersect the light cylinder are open, as they bend away from their original direction when reaching the light cylinder. Moreover, the plasma which is located within the region encompassed by the closed magnetic field lines is static, whereas the particles in areas with open field lines are able to leave the magnetosphere.

Particle Acceleration and Pulsed Emission

The sources of the pulsed electromagnetic emission and of the particle wind are supposed to be located in the dynamic regions of the magnetosphere. Primarily two regions are distinguished: the polar caps and the outer gaps, see Fig. 2.3. The polar caps are located on top of the magnetic poles, where the open field lines intersect the surface of the neutron star. The outer gaps are located further outside in the magnetosphere, in the close vicinity to the light cylinder. They are directly attached to the closed field lines and are bounded by the null surface, i.e. the boundary layer where the net charge is zero. In common theories the polar caps are associated with the coherent radio emission observable from pulsars, while the outer gaps are more usually linked to the high-energy radiation in X-rays and γ rays, [LGS05] p. 213. The non-thermal component must originate from subregions of the magnetosphere which exhibit significant charge depletion. Only then electric fields with strong components along the magnetic field lines can form which are necessary to accelerate the charged particles and enables them to produce the observed photons. The prevailing emission mechanism thereby is synchrotron-curvature radiation. The exact origin of the highly energetic emission in the magnetosphere has long been discussed. Several models exist which associate the emission with the polar caps (e.g. [RS75, Bar04]), as well as with an enhancement of the polar caps, the so called slot gaps (e.g. [AS79, Har08]) and finally the outer gaps (e.g. [CHR86, T$^+$08]). The predictions of these models differ primarily for the high energy range, i.e. the energy range above several GeV. This is due to the fact that the emitted γ rays initiate electromagnetic particle cascades in the magnetosphere via pair production, [LGS05] p. 233 ff. In the close vicinity to the star surface the γ-ray absorption is dominated by the strong magnetic field, i.e. magnetic pair production, while it is based on photon-photon pair production in the vicinity to the light cylinder. As a consequence the models predict different cut-offs for the photon spectrum. In the polar cap models the cut-off is expected at several GeV, while the outer gap models allow pulsed γ-ray emission even higher than 10 GeV [A$^+$08b]. In 2008 the MAGIC telescope was the first imaging atmospheric Cherenkov telescope that measured pulsed emission at energies over 25 GeV [A$^+$08b]. This observation strongly favoured the outer gap scenario. However, the detailed study of the photons in the energy range

between 20 GeV and 400 GeV revealed several unexpected features. Therefore, today it is even discussed that the pulsed GeV emission might be emitted in regions outside the light cylinder, i.e. in the pulsar wind [ABK12].

2.1.2. The Magnetised Particle Wind

The particles which are generated and / or accelerated in the magnetosphere represent an important component of the pulsar wind. Due to the study of the photon emission from pulsars and PWNe and in particular their spectral distribution very soon a theory was established that ascribed the observed photons primarily to a population of relativistic electrons and positrons, e.g. [RG74, AA96]. In the following we will also act on this assumption. For the sake of simplicity we will generally use the term electrons, even when electrons as well as positrons are meant. It should be noted, however, that a contribution from a hadronic component is also conceivable, e.g. [Bed07]. In particular, an ion outflow in equatorial regions is predicted in several models, which might play an important role in acceleration processes, see [GS06] and references therein.

The particles which leave the magnetosphere of the pulsar along the open magnetic field lines as well as the electromagnetic radiation form the basis of the unshocked pulsar wind, see Fig. 2.4. In general, it is assumed that the pulsar wind near the light cylinder is dominated by the Poynting flux, while the particle component is significantly weaker [KC84b]. Quantitatively, this can be described by the magnetisation parameter (σ), which is defined as the ratio of electromagnetic and particle energy flux [GS06]:

$$\sigma \equiv \frac{F_{\mathrm{E}\times\mathrm{B}}}{F_{\mathrm{particles}}} = \frac{B^2}{4\pi\rho\Gamma c^2}. \tag{2.1}$$

In this context B is the magnetic flux density, ρ the particle density and Γ the Lorentz factor of the pulsar wind. According to Aharonian et al. the latter is assumed to be in the order of 10^4 to 10^7 in the unshocked pulsar wind [AB03].

Despite the high magnetic flux density Aharonian et al. do not expect synchrotron emission from the unshocked wind, as the magnetic field is frozen into the plasma and thus moves synchronously with the particles. Instead, Aharonian et al. suggest that γ-ray emission might be observable from the unshocked wind, due to IC scattering of the leptons on thermal photons from the neutron star or non-thermal photons from the magnetosphere. However, up to now no γ rays from the unshocked pulsar wind could be verified with absolute certainty. The reason for this is not that there are no γ rays, but that the angular resolution of the current experiments detecting GeV and TeV photons is insufficient to resolve such small structures as the unshocked wind, which extend on scales smaller than 0.1 pc. Nevertheless, such observations would be highly appreciated as the physics of the unshocked wind is discussed controversially.

In particular, it is known from different observations and well established magnetohydrodynamic simulations that the magnetisation parameter which is in the order of 10^4 near the light cylinder takes a value of $\ll 0.01$ at the termination shock, which confines the unshocked pulsar wind, e.g. [KC84a]. The conversion of the Poynting flux to the kinetic

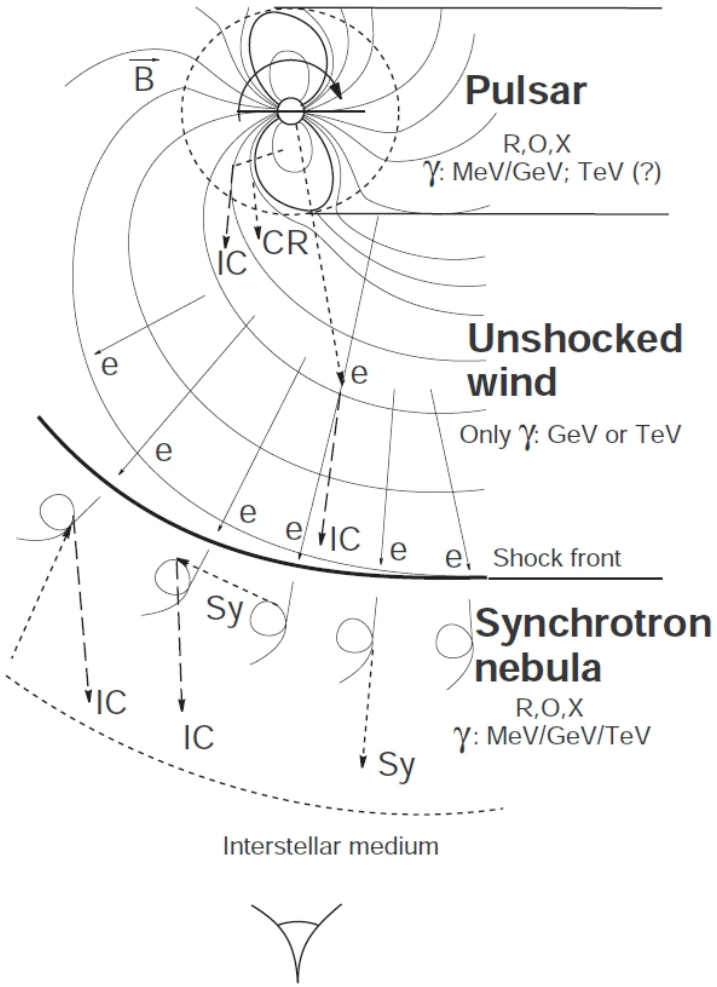

Figure 2.4.: Schematic representation of a pulsar wind nebula (taken from [AB03]), indicating the different emission regions and the respective emission wavelengths: radio (R), optical (O), X-rays (X) and γ rays (γ). For the γ rays it is specified, whether they are emitted in the MeV, GeV or even in the TeV energy range. From the central engine of the PWN, the pulsar and its magnetosphere, pulsed emission on the basis of synchrotron-curvature radiation is observed in the energy range from radio up to at least GeV energies. In the unshocked wind the synchrotron emission is suppressed and therefore only γ rays from the IC scattering are expected. Finally, in the pulsar wind nebula synchrotron radiation and IC scattering both contribute to the observed emission and therefore photons from radio up to TeV energies are detected.

energy of the bulk motion has to take place somewhere between the light cylinder and the termination shock. The exact location and the physical processes involved, however, are unclear. On the one hand there are theoretical models which predict a gradual acceleration over the total extension of the unshocked wind (e.g. [LK01]) and on the other hand there are models which assume distinct acceleration zones close to the light cylinder (e.g. [Vla04, ABK12]). An interesting possibility to probe the nature of the unshocked pulsar winds may be the study of binary systems, q.v. App. A. In these close systems the unshocked pulsar wind interacts with the dense photon field of a companion star and may thus reveal hints to its true nature [CDH08].

2.1.3. The Termination Shock

The termination shock separates the unshocked wind from the pulsar wind nebula, see Fig. 2.4. This shock is formed due to the interaction of the supernova remnant, the pulsar wind nebula and the pulsar wind: When the pulsar wind nebula expands into the slowly moving ejecta from the supernova explosion, the Nebula is over-pressured and drives a shock into the ejecta, thus the PWN is confined. In the same way a shock is formed when the relativistic pulsar wind inflates the confined PWN. This shock occurs at a radius where the pressure of the relativistic outflow is equal to the pressure of the nebula [RG74]. As this shocks terminates the relativistic flow of the pulsar wind it is called termination shock. According to Gaensler & Slane [GS06] the radius of the termination shock r_s is equal to

$$r_\mathrm{s} = \sqrt{\frac{\dot{E}}{4\pi\omega c P_\mathrm{PWN}}}, \tag{2.2}$$

where P_PWN is the pressure in the PWN and ω is the equivalent filling factor of an isotropic wind. For young PWNe like the Crab Nebula this equation predicts radii in the order of 0.1 pc.

Observational evidence for termination shocks has been provided, among others, by X- ray observations of PWNe. For instance, in Fig. 2.5 the Chandra observations of the Crab Nebula are shown (in blue). An underluminous area surrounding the pulsar is visible, which is bordered by a distinct ring feature, i.e. the termination shock. This feature materialises as the particles upstream of the shock do not emit synchrotron radiation, but downstream of the shock they do. How can this be explained? As has been stated before, it is generally assumed that in the cold, unshocked wind the magnetic field is frozen into the plasma and moves with the particles. However, when the particles cross the termination shock, they are accelerated and in particular their directions are randomised. Thus downstream of the termination shock synchrotron emission is predicted – and indeed observed – over the total electromagnetic wavelength range. From the observed X-ray emission from regions close to the termination shock conclusions on the Lorentz factors of the accelerated leptons can be drawn. These observations have hinted to an efficient acceleration mechanism which is able to boost the energy of the particles by a factor $\geq 10^3$ [Sla08].

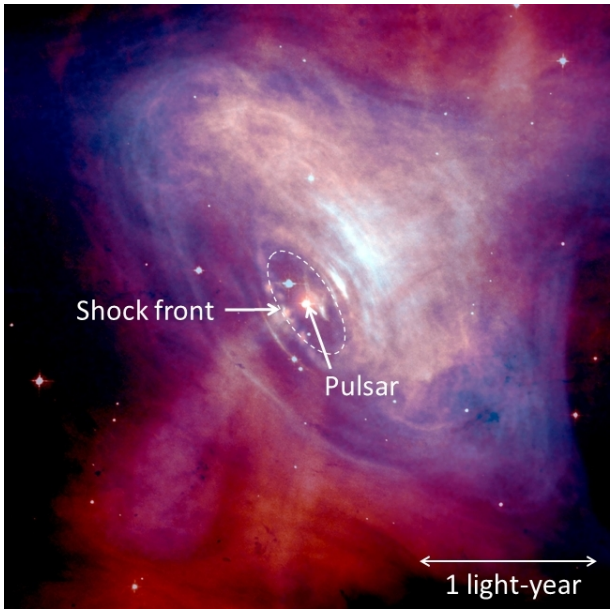

Figure 2.5.: In this composite image of the Crab Nebula data from X-ray (blue) and optical (red) observations are superimposed, see [Feu12] and references therein. Several features of the Nebula can be observed: the termination shock as a distinct inner ring, jet-like structures along the rotation axes and the X-ray torus indicating the toroidal magnetic field.

So far no definitive answer to the question of the contributing acceleration mechanisms has been provided, but one mechanism that certainly plays an important role is the Fermi acceleration. This mechanism has first been presented by Fermi in 1949 [Fer49]. Back then Fermi considered the stochastic acceleration of charged particles which are reflected between magnetic mirrors, e.g. irregularities in magnetic fields, that move with a velocity v. Fermi was able to show that the particles gain an average energy of $\langle \Delta E/E \rangle \propto (v/c)^2$ per collision, e.g. [Lon94], p. 348. Due to this proportionality this process is often referred to as second order Fermi acceleration. All in all, this acceleration results in a particle spectrum that can be described by a power law, with a power-law index that depends on ambient conditions. However, plausible assumptions on the velocities of such mirrors, the number of collisions and the consideration of ionisation losses revealed that the process is not very efficient. Therefore, the acceleration of charged particles to extremely high energies in astrophysics is today usually ascribed to an advancement of the second order Fermi acceleration. In the enhanced scenario the acceleration of the particles in strong supersonic shocks is considered, e.g. [Lon94] p. 351 ff.: Thereby, it is assumed that the shock propagates through the interstellar medium with velocity U and that there are fluxes of highly energetic particles upstream and downstream of the shock. The velocities of the particles are much higher than the supersonic velocity of the shock and due to turbulences and inhomogeneities an isotropic velocity distributions is expected on both sides of the shock front. In a relativistic scenario it can be shown that the mean energy a particle gains by traversing the shock front is in the order of $\langle \Delta E/E \rangle \propto U/c$. In comparison to the second order Fermi acceleration the energy gain is increased and due to the proportionality to (U/c), it is called first order Fermi acceleration. The particle

loss rate in the shock scenario is determined by the particles downstream of the shock which move away from the acceleration area. This rate, however, is rather small as the shock propagates non-relativistically. Balancing the energy gains and the particle losses the differential energy spectrum of the particles can be derived, which is well described by a power law with index -2 ($\mathrm{d}N/\mathrm{d}E \propto E^{-2}$).

While the first-order Fermi acceleration is the acceleration mechanism that is considered responsible for electrons with energies $\gtrsim 1$ TeV, other mechanisms are supposed to prevail for the 100 MeV to 1 TeV energy range [KLP09]. Among these are the resonant absorption of cyclotron waves and magnetic reconnection. The former has been proposed by Amato & Arons [AA04], who considered the influence of ions as constituents of the pulsar wind. At the termination shock front the ions emit cyclotron waves, which can be absorbed by the electrons and the positrons and thus contribute to their acceleration. In case of the magnetic reconnection it is assumed that the pulsar wind possesses a wave-like alternating structure due to its origin in an oblique rotator and due to the emitted electromagnetic waves. Such a wind is referred to as striped wind. When the striped wind reaches the termination shock, the alternating fields annihilate and the released energy is transferred to the particles [PL07].

2.1.4. The Nebula

Together with the injected magnetic fields the accelerated and isotropised electrons that have passed the termination shock form the pulsar wind nebula. From the observational point of view the nebula is the most prominent component of the pulsar-wind-nebula system. The nebula is far more extended and significantly brighter than the pulsar or the pulsar wind. As was shown in Fig. 2.2 for the Crab Nebula, the photon spectra of typical PWNe extend over several orders of magnitude from radio up to TeV energies. The photons with energies below the GeV regime are mainly generated via synchrotron emission, those with higher energies via IC emission. An overview of these emission processes will be presented in Sec. 2.4.3. For the moment, however, we will continue with the study of the observable features of PWNe, of which an extensive overview is given in [GS06]. In the radio regime the observed flux density S_ν is usually well described by a power law $S_\nu \propto \nu^{\alpha_\mathrm{r}}$, where α_r is called the "spectral index" and is typically in the order of $-0.3 \lesssim \alpha_\mathrm{r} \lesssim 0$. In a similar way the differential energy spectra in the X-ray regime $\frac{\mathrm{d}N}{\mathrm{d}E}$ can also be reproduced by power laws: $\frac{\mathrm{d}N}{\mathrm{d}E} \propto E^{\alpha_\mathrm{x}}$, where α_x is the "photon index" and usually takes a value of $-2.5 \lesssim \alpha_\mathrm{x} \lesssim -1.5$. Such a photon distribution can not be explained by a single electron population whose energy distribution is described by a power law. Instead, at least one spectral break is required in the energy spectrum of the electrons. Such a break may arise from various acceleration mechanisms in the termination shock, as has been mentioned in the previous section. Another possibility is that cooling processes have altered the energy distribution of the electrons. This is especially expected to occur in the case of older PWNe.

That cooling effects play an important role in the evolution of the PWN is also visible in Fig. 2.5. In this composite image of the Crab Nebula the X-ray emission is presented in

blue, while the optical emission is shown in red. It is clearly visible that the lower energetic optical component can still be detected at larger distances to the pulsar, whereas the X-ray component is more compact. This observation can be explained in the following way: While the electrons move away from the pulsar they lose energy. Close to the pulsar they have enough energy to produce X-ray photons, but further away their energy does only allow the generation of less energetic photons. As long as we consider only synchrotron emission the following behaviour is expected: The lower the energy of the considered photons, the larger the size of the observable PWN.

However, the observed distribution of the synchrotron photons does not only depend on the spatial distribution of the particles but also on the distribution of the magnetic fields. This is why we can see a kind of torus in the X-ray image of the Crab Nebula, see Fig. 2.5. Indeed, MHD calculations have shown that the magnetic field of the rotating pulsar outside of the light cylinder has a toroidal shape and thus it is not surprising that this spatial distribution is also observable in the emitted synchrotron photons. Moreover, the magnetic field may also give rise to jet-like structures along the spin axis of the pulsar as the toroidal magnetic field causes an increased equatorial pressure [GS06]. Other structures that are occasionally visible in PWN observations are wisp-like structures in the nebula or filaments at the forward shock of the PWN. Such structures, however, are well below the spatial resolution of the TeV observations considered here, and therefore the interested reader is referred to [GS06].

VHE γ-ray observatories have opened a new observational window for the study of PWNe. In contrast to radio and X-ray observations the detected photons are no longer generated via synchrotron radiation, but via IC emission. Thus complementary information is gained. While the synchrotron emission depends on the spatial distribution of the electrons and the magnetic fields, the IC emission depends on the distribution of the electrons and the target photon fields. Usually the distribution of the latter is assumed to be rather smooth across the emission region and therefore the VHE γ-ray observations can be used to track the distribution of the emitting electrons. Moreover, even cooled electrons can still generate TeV photons via IC scattering. Therefore, TeV PWNe are often quite extended and source regions that were formerly difficult to observe can now be accessed. Furthermore, VHE γ-ray observations are well suited for the study of evolved PWNe, i.e. PWNe which are older than $\approx 10\,\mathrm{kyr}$ and which have accumulated electron populations of different ages. By their observation information on the evolution of PWNe can be gained.

2.2. Evolution

The evolution of a PWN is strongly influenced by the interaction with the surrounding supernova remnant, see Fig. 2.1. A compact summary of the different evolutionary stages can be found in [GS06] and will be summarised in the following. Accordingly, four different phases are distinguished: the expansion into unshocked ejecta, the interaction with a reverse shock from the SNR, the development inside a Sedov SNR and finally the escape

of the pulsar into the interstellar gas.

In the first stage the blast wave of the SNR expands freely into the interstellar medium and at the same time the PWN starts to evolve from the pulsar which is located close to the centre of the SNR. At this early stage the PWN is surrounded by slowly moving ejecta from the supernova explosion. As a result, the nebula is highly over-pressured and a shock is formed that confines the nebula. Assuming a spherically symmetric case Chevalier [Che77] derived the following equation for the age-dependent radius of the PWN:

$$R_{\mathrm{PWN}} \approx 1.1\,\mathrm{pc} \left(\frac{\dot{E}_0}{10^{38}\,\mathrm{erg\,s^{-1}}}\right)^{1/5} \left(\frac{E_{\mathrm{SN}}}{10^{51}\,\mathrm{erg}}\right)^{3/10} \left(\frac{M_{\mathrm{ej}}}{10\ M_\odot}\right)^{-1/2} \left(\frac{t}{10^3\,\mathrm{yr}}\right)^{6/5}. \quad (2.3)$$

In the formula $\dot{E}_0$ is the initial spin-down luminosity of the pulsar, which is assumed to be almost constant within the first $\sim 1000\,\mathrm{yr}$ of the pulsar's lifetime (see Eq. 2.13), and E_{SN} and M_{ej} are the kinetic energy and the mass released in the supernova explosion.

As time goes on the SNR sweeps up more and more mass from the interstellar medium. When the swept-up mass is in the order of the mass ejected in the supernova explosion a reverse shock is formed. This formation proceeds as follows: When the mass ahead of the shock is decelerated, the mass from behind crashes into it, is therefore abruptly stopped and a new shock front is created. At the beginning the reverse shock moves in the same direction as the forward shock, but eventually starts to move inwards. In doing so the reverse shock decelerates and heats up the expanding supernova ejecta, see Fig. 2.1. The time that the reverse shock needs to reach the centre of the SNR, if no pulsar is present, was predicted by Reynold and Chevalier [RC84] for an ambient medium with number density n_0:

$$t_{\mathrm{Sedov}} \approx 7\,\mathrm{kyr} \left(\frac{M_{\mathrm{ej}}}{10\ M_\odot}\right)^{5/6} \left(\frac{E_{\mathrm{SN}}}{10^{51}\,\mathrm{erg}}\right)^{-1/2} \left(\frac{n_0}{1\,\mathrm{cm^{-3}}}\right)^{-1/3}. \quad (2.4)$$

In the case that a PWN is present inside the SNR, the nebula gets compressed by the reverse shock at $t < t_{\mathrm{Sedov}}$, which is in the order of a few thousand years. Thereby the pressure inside the PWN increases until it becomes sufficient to revive the expansion of the PWN. Subsequently, reverberations arise, during which the nebula alternately expands and contracts.

When the interior of the SNR has been heated by the reverse shock, the SNR enters the Sedov Taylor phase, i.e. the stage of its evolution in which the energy is conserved and the expansion takes place adiabatically. In this environment the PWN resumes its expansion when the oscillations have faded. The expansion of the nebula now proceeds subsonically and depends on the spin-down luminosity of the pulsar: Assuming again a spherically symmetric expansion the radius of the PWN can be described by $R_{\mathrm{PWN}} \propto t^{11/15}$ in the case that the spin-down luminosity is still equal to $\dot{E}_0$ [v+01], but is better represented by $R_{\mathrm{PWN}} \propto t^{3/8}$ when the spin-down luminosity has already decreased and $n = 3$ [RC84].

In general, however, it is not expected that the evolution of the PWN proceeds symmetrically. Indeed there are several factors which may cause asymmetries: For instance, SNRs frequently expand into inhomogeneous media. As a consequence the expansion of the SNR will not be spherically symmetric and neither will be the reverse shock, see Fig. 2.6.

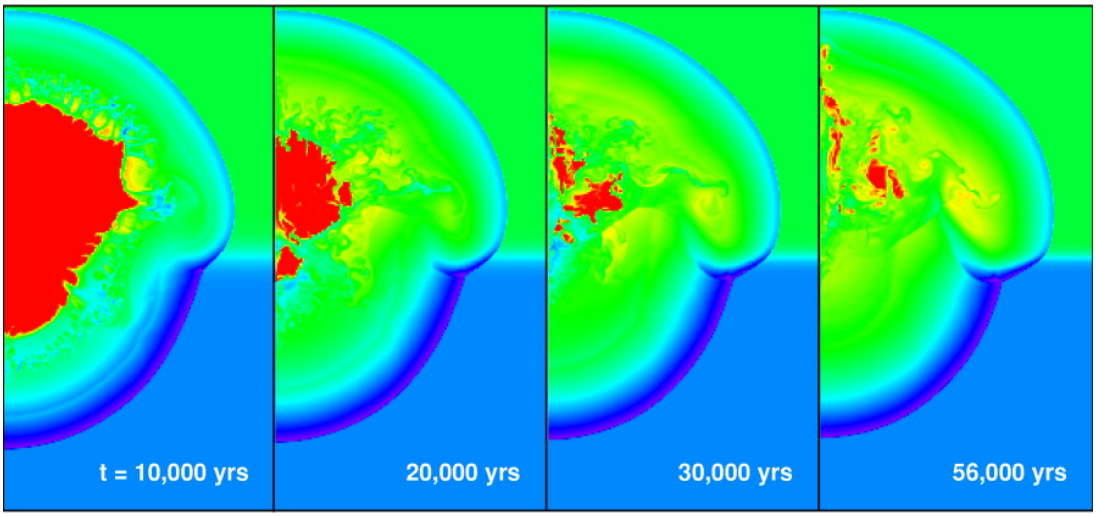

Figure 2.6.: Two-dimensional, two-fluid simulation of the crushing and re-expansion phase of a PWN in a non-uniform medium [BCF01]. The colour scale of the images represents of the fluid density, covering 2.5 orders of magnitude. In the simulation the PWN and the SNR ejecta / circumstellar gas have been modelled by fluids with adiabatic indices $\gamma = 4/3$ and $\gamma = 5/3$, respectively. Additionally, the non-uniform medium was approximated by a density gradient in z-direction, resulting in a density contrast of 5. It is clearly visible that the density gradient gives rise to a displacement of the PWN.

Moreover, pulsars have often gained a kick during their formation and therefore they move away from the centre of the PWN, see [vDK04]. When such a moving pulsar approaches the rim of the nebula an additional new nebula is formed, intersecting with the old, relic PWN, see Fig. 2.7. In radio such a deformed PWN can be observed, while in X-ray the emission of the new PWN may be rather weak. However, when the pulsar approaches the shell of the supernova remnant its velocity is likely to become supersonic and a bow shock is formed, see Fig. 2.7. This way the PWN becomes observable as a cometary appearance

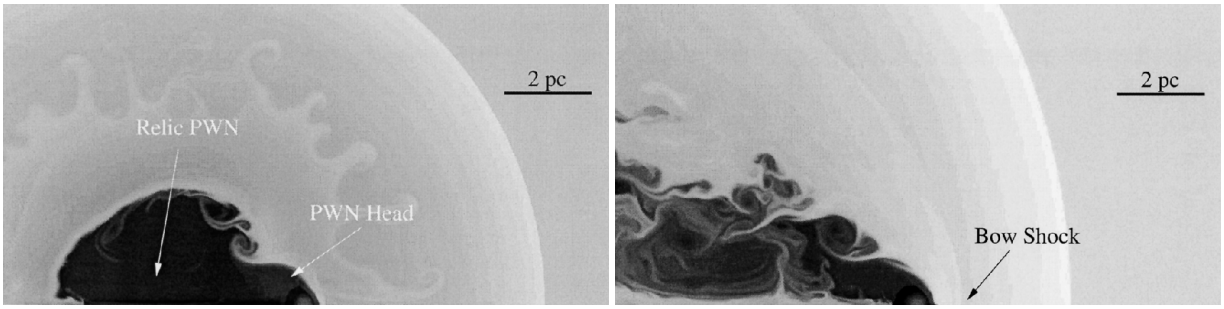

Figure 2.7.: Hydrodynamic simulation of the evolution of a PWN associated with a high-velocity pulsar. The logarithmic gray-scale plots were taken from [vDK04] and show the density distributions of the fluids. The left image illustrates the development of a deformed PWN, consisting of a relic and a newly formed PWN, when the PWN re-expands in the Sedov SNR. When the pulsar approaches the rim of the SNR the movement becomes supersonic and a bow shock is formed. This is illustrated in the image on the right-hand side.

in radio and X-rays. The last stage of the PWN evolution is reached when the pulsar crosses the shell of the supernova remnant after approximately 40 kyr. In the interstellar medium the pulsar eventually moves supersonically and thus a cometary appearance is furthermore expected. However, when the pulsar reaches regions of lower density or when the spin-down luminosity of the pulsar fades, the synchrotron emission gets so weak that it can no longer be detected.

2.3. H.E.S.S. Observations of PWNe

Having studied the structure and the evolution of PWNe within the last two sections, we will now have a closer look at the current state of PWNe observations with γ-ray telescopes, in particular with the H.E.S.S. telescope. As was shown in Fig. 1.4 PWNe comprise the largest group of VHE γ-ray sources, i.e. almost half of the detected Galactic sources. In fact, already the first detected VHE γ-ray source, the Crab nebula, was a pulsar wind nebula [W$^+$89]. Though the energy content of a PWN is smaller than the energy released in a supernova explosion – approx. 10^{49} erg vs. 10^{51} erg – the higher detection rates of PWNe are expected [HH09]. One of the main differences between these two classes of VHE γ-ray sources is the particle population considered responsible for the γ-ray emission. While these are electrons in case of PWNe, many models assume that the accelerated particles in supernova remnants predominantly are hadrons, which emit γ rays in hadronic processes. However, PWNe emit highly energetic electrons continuously over long periods, whereas supernova shocks decelerate and after approx. 10 kyr can no longer confine highly energetic nuclei. In addition, the emission processes of the VHE γ rays are unequally efficient. The hadronic γ-ray production requires the existence of suitable target material, e.g. molecular clouds, and the interaction time scales are in the order of 10^7 years. In contrast, target photons for γ-ray production via IC scattering are available everywhere, e.g. the CMB, and the radiative lifetimes are in the order of $10^3 - 10^4$ years. Indeed, statistical investigations suggest that the majority of all high spin-down pulsars has a counterpart in VHE γ rays [W$^+$08].

In this short overview we will concentrate on the most prominent H.E.S.S.-detected PWNe and use them to illustrate typical features. In general, the so far detected PWNe can roughly be sorted into two groups: young and evolved PWNe. The best studied representative of the first group is the Crab Nebula. Its important role is reflected in the denomination as "standard candle" of VHE γ-ray astronomy. Indeed, VHE fluxes are often quoted in units of the Crab flux. As was shown at the beginning of this chapter the non-thermal emission from the Crab Nebula has been detected over the entire electromagnetic spectrum from radio to γ rays and these observations have provided the base of our present understanding of PWNe, in particular the interpretation of the radiation as synchrotron and IC emission of electrons outflowing from by the pulsar, e.g. [AA96]. Due to historical records reporting the observation of the corresponding supernova explosion, the age of the Crab pulsar is precisely known to be 958 years. The pulsar is located at a distance of 2 kpc and exhibits a present rotation period of 33 ms and a spin-down luminosity of $5 \times 10^{38}\,\mathrm{erg\,s^{-1}}$. Due to the limited spatial resolution of the H.E.S.S. ex-

periment the Crab Nebula appears point-like in H.E.S.S. observations [A$^+$06d]. The TeV energy spectrum can be described by a power law with an exponential cut-off (photon index $\gamma = 2.39 \pm 0.03_{\mathrm{stat}}$, cut-off energy $E_{\mathrm{cut}} = (14.3 \pm 2.1_{\mathrm{stat}})$ TeV) and the integrated flux above 1 TeV accounts to $(2.36 \pm 0.08_{\mathrm{stat}}) \times 10^{-11}\,\mathrm{cm}^{-2}\,\mathrm{s}^{-1}$. Other young VHE PWNe are for instance SNR G 0.9+0.1, SNR G 21.5–0.9, Kes 75, HESS J1813–178, see [Nau11] and references therein. The corresponding pulsars have a young characteristic age and a high spin-down luminosity, the nebulae are compact and unresolved for TeV telescopes and the maximum of the VHE emission is located close to the pulsar position. Due to their similarity to the Crab Nebula, they are often referred to as "Crab-like".

A rather peculiar young PWN is SNR MSH 15–5*2*, which is associated with the pulsar PSR B1509–58 at a distance of approx. 5 kpc from Earth and an estimated age of about 2000 yr. In this special case the spatial resolution of the H.E.S.S. telescopes was for the first time sufficient to resolve the morphology of the VHE emission of a PWN [A$^+$05c]. While the centre of gravity of the VHE emission is only mildly offset from the pulsar position, the total emission region is elongated and slightly curved, see Fig. 2.8 (a, right side). On a smaller scale this feature had already been observed in X-rays, Fig. 2.8 (a, left side) and is generally understood to represent a jet-like structure. The resolved spatial TeV morphology is a feature that is far more common for PWNe belonging to the class of evolved PWNe, i.e. with characteristic ages higher than ∼10 kyr. These evolved PWNe are considerably more extended and exhibit source diameters up to 1.2°. Two representatives of this class are also shown in Fig. 2.8 (b) & (c): Vela X ($t_{\mathrm{c}} \approx 10$ kyr) [A$^+$06c] and HESS J1825–137 ($t_{\mathrm{c}} \approx 22.4$ kyr) [A$^+$05b]. In the case of Vela X the huge apparent size is at least partially owed to its proximity to Earth, as the corresponding pulsar is located at a distance of only 290 pc. But HESS J1825–137 is located at a distance of about 4 kpc and still exhibits a size larger than 1° in diameter. Besides the sizes, the asymmetry of the TeV emission region is striking. The pulsars are no longer located at the centre, but rather at the edge of the VHE emission region. As we have seen above, such a feature may be caused by proper motions of the pulsars or by asymmetric reverse shocks. Another feature of evolved PWNe becomes evident when additionally considering the corresponding X-ray PWNe. While the sizes and appearance forms of X-ray and γ-ray PWNe of young pulsars are comparable, they differ significantly for older pulsars, see Fig. 2.8. In the case of Vela X the sizes of the PWNe are still of the same order, at least when the different point spread functions of the X-ray and γ-ray telescopes are taken into account. But the centre of gravity of the emission region which in X-ray is located close to the pulsar is shifted to the south in the VHE image. Finally, in the case of HESS J1825–137 neither the sizes nor the emission centres are comparable. The different X-ray and γ-ray morphologies can be explained by lepton populations of different age which are responsible for the respective emission. While the X-ray emission is mainly caused by young and highly energetic electrons, the VHE emission can also be generated by cooled leptons that have been emitted earlier in the lifetime of the pulsar.

Such an energy-dependent morphology has not only been demonstrated for the X-ray and the γ-ray regime, but also for different energy slices in the VHE regime. Indeed, an energy-dependent morphology has been verified for HESS J1825–137 and HESS J1303–631, cf. [FHdJ08] and [Dal10]. The energy-dependent spatial distribution of the photons can be

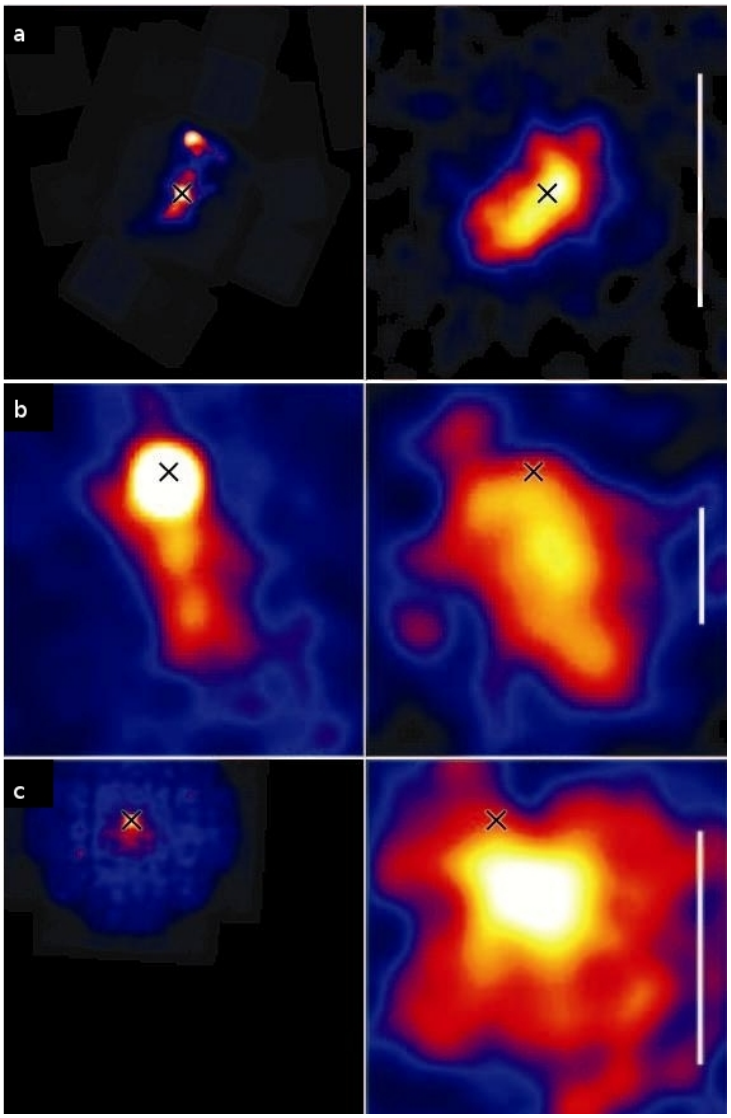

Figure 2.8.: Spatially resolved VHE PWNe (right side) and their X-ray counterparts (left side), illustrating the different sizes and morphologies in the two wavebands (images taken from [HH09]). From top to bottom the H.E.S.S. sources MSH 15–5*2*, Vela X and HESS J1825–137 are shown. The X-ray images have been generated by Hinton et al. using public X-ray data. The white lines indicate an extension of 0.5° and the black crosses mark the location of the corresponding radio pulsars.

studied well by means of RGB sky maps, i.e. sky maps that display the source fluxes in three different energy ranges. In Fig. 2.9 such RGB maps are shown for HESS J1825–137 and HESS J1303–631. Both sky maps clearly indicate that the more energetic photons are located closer to the pulsar. A corresponding effect, i.e. the steepening of photon spectra for regions further away from the pulsar, has been observed in X-ray observations, e.g. [S$^+$04, PDW03]. However, in X-rays it is not immediately clear that variations in the photon spectra correspond to variations in the spectrum of the emitting particles. Indeed, spatial variations of the magnetic field may also have a significant impact. This is different in the TeV range. As long as it is assumed that the target photon fields do not vary significantly over the emission region, spatial variations in the photon spectrum hint directly at variations in the particle spectrum. Assuming further that the electrons which are farther away from the pulsar have been emitted earlier in the lifetime of the pulsar, conclusions about the evolution of the pulsar, e.g. particle injection spectra, transport mechanisms and cooling mechanisms can be drawn. Within the scope of this work, a simplified model of an evolved PWN was developed, which allows to study the electron distribution and the corresponding X-ray and TeV photon distributions based on certain assumptions. The objective was to compare this model with observational data of HESS J1825–137 and to deduce information on the model parameters. To motivate the assumptions that have been made in the model of HESS J1825–137 we will have a closer look at typical assumptions in PWN models in the next section.

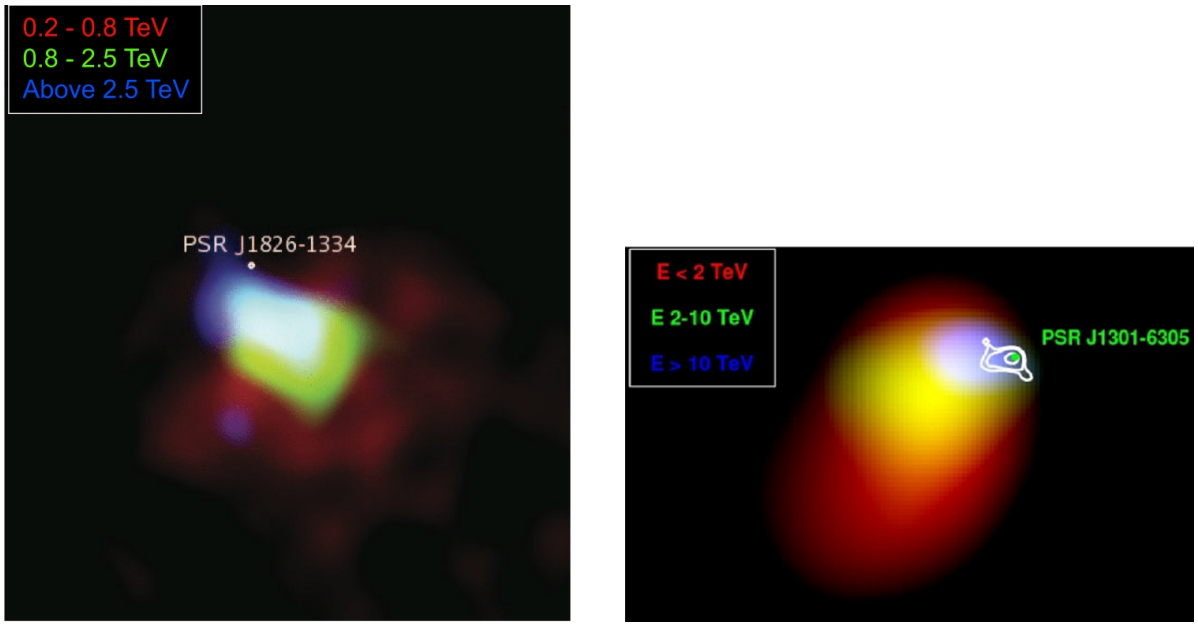

(a) HESS J1825–137 [FHdJ08] (b) HESS 1303–631 [Dal10]

Figure 2.9.: RGB sky maps illustrating the energy-dependent morphology of VHE γ-ray sources.

However, before we turn our attention to the modelling of HESS J1825–137, this chapter is rounded off by an outlook to another application of PWN modelling, namely the identification of so far unidentified VHE γ-ray sources. As a matter of fact, it is assumed that PWNe constitute a large portion of the unidentified TeV sources [Gal07]. However,

due to the diversity of appearance forms of VHE PWNe they are very difficult to identify. For instance, the first step in the identification process is the search for a pulsar in the close vicinity which can be considered as the energy source of the nebula. As we have seen in Sec. 2.1.1, such pulsars are predominantly discovered via their pulsed emission in the radio regime. However, as the pulsed emission is beamed, there is a high probability that the beam does not cross the observer's line of sight and is therefore not detectable. Moreover, due to the proper motion of the pulsars and due to asymmetric reverse shocks the pulsars are often located far away from the maximum of the VHE emission and thus there might be several pulsar candidates which could account for a newly detected VHE γ-ray source. Therefore, the (apparent) efficiency is often evaluated in order to establish an unambiguous association between a VHE source and a pulsar. This measure compares the integrated VHE γ-ray flux in a characteristic energy range with the current spin-down energy of the pulsar [Gal07]. The issue with this criterion is that it depends strongly on the age of the PWN [M$^+$08]. Especially for evolved PWNe the present spin-down energy can be fairly weak, while the cooled electrons, which have been emitted in earlier epochs, can still generate significant VHE emission. An example of a VHE γ-ray source that has been prematurely dismissed as PWN due to the low present spin-down energy of the associated pulsar is HESS J1303-631. The identification of this source did only succeed with the verification of the energy-dependent morphology in the VHE regime.

In many cases the detection of a PWN in X-rays provided a decisive key in the identification procedure. Though the X-ray PWNe may be considerably smaller than the VHE PWNe, similarities in the morphologies, e.g. elongation, orientation and alignment, can strongly favour an association. Furthermore, the fluxes in the X-ray and γ-ray regime can be compared and the viability of a leptonic scenario can be evaluated. Again, the expected fluxes depend on the age of the PWN. In particular in the evolved systems the X-ray fluxes may be weak and difficult to detect with current X-ray satellites. In order to facilitate the discovery of associated X-ray PWNe, Michael Mayer, a former colleague at the University of Erlangen I have been working with, has developed a one-zone model which allows to study the time-dependent evolution of the X-ray and γ-ray emission of PWNe, for details see [M$^+$12]. By fitting this model to the detected TeV emission of PWN candidates, it is possible to draw conclusions on the expected X-ray emission. We are confident that this model can soon be used to evaluate the possibility of detecting X-ray counterparts within deep X-ray observations.

2.4. Main Constituents of PWN Models

In the previous sections it was shown that PWNe are fascinating but very complex systems. Studying PWNe it is possible to learn a lot about the origin of cosmic rays, about acceleration mechanisms for charged particles, about emission processes of VHE γ rays, about the evolution of PWNe, in particular their interaction with the surrounding SNR and the interstellar medium, etc. In order to understand these physical processes in PWN systems various models have been developed that allow the reconstruction of observed properties of PWNe. In the following section an overview of typical assumptions

of PWN models will be presented. Later in this theses we will use these assumptions in the construction of our own model for HESS J1825–137.

One of the most renowned and probably the most cited PWN model is the model of Kennel & Coroniti, [KC84a] and [KC84b], which aimed to explain the synchrotron emission of the Crab Nebula. In the first step of this steady-state, spherically symmetric, magneto-hydrodynamic model the flow of the relativistic leptonic plasma and the magnetic field is predicted. Subsequently, the spatial distributions of the particles and the magnetic field is used to calculate the expected synchrotron emission. In the energy range from optical to γ rays this model predicts the observed emission very well. When TeV emission from the Crab Nebula was discovered the model from Kennel & Coroniti was soon extended to include also IC radiation. Thereby, de Jager & Harding [dH92] were the first to consider the up-scattering of synchrotron photons, while Atoyan et al. [AA96] accounted also for photons from the CMB and optical and infrared photons from starlight and dust. Another enhancement of the Kennel & Coroniti model consists in the inclusion of energy losses of the particles during their propagation. This was first proposed by de Jager & Harding [dH92] and was applied successfully to explain the variation of photon spectra for subregions of several X-ray PWNe, e.g. [Sch10] and [H$^+$12].

While these models have proven well suited to explain the observed emission from young PWN, they can not account for evolved PWNe since the time-dependent evolution is neglected. Especially for evolved PWNe it is important to consider that the luminosity of the pulsar decreases with time and that after a few thousand years the PWN interacts with the surrounding supernova remnant. Hydrodynamic simulations of the latter have been developed amongst others by Blondin et al. and van der Swaluw and an impression of their results was given in Sec. 2.2. Other authors have used one zone models, i.e. models that do not consider spatial variations, with time-dependent injection-spectra to study the time-dependent evolution of the photon spectra from PWNe, e.g. [VJ06, ZCF08, TT10]. One model that assigns great importance to the simultaneous modelling of the dynamical and radiative evolution of PWNe is the one by Gelfand et al. [GSZ09]. However, even this comprehensive model has the disadvantage of not considering spatial distribution and hence of not being able to account for asymmetries that arise from inhomogeneities in the interstellar media or from the reverse shock.

For the future, the development of a model that combines all features mentioned above would be desirable. Such a model should include magneto-hydrodynamic calculations, but not under the steady-state assumptions; it should consider the time evolution of the PWN and the three-dimensional geometry of the system, inhomogeneities in the surrounding media etc. As one can easily imagine such a model would soon become arbitrarily complex and it is certainly out of the scope of this thesis. Nevertheless, we wanted to make first steps in the development of a PWN model for HESS J1825–137, that considers the special features of this source. Instead of determining spectra for subregions of the emission regions and instead of fitting simple geometric shapes to the morphology of the source, we decided to choose a more holistic approach. Our goal was to develop a simplified model which is able to reproduce an energy-dependent morphology as observed for HESS J1825–137 and to fit this model to the observed data. In doing so we have used

certain assumptions that have been introduced in the above quoted publications. These assumptions will be presented in the following.

2.4.1. Evolution of Pulsar Spin-down

As has been stated before, the common perception is that the energy of the PWN is provided by the pulsar. The released energy is withdrawn from the pulsar's rotational energy. The amount of energy that is released at a specific time strongly depends on the age of the system. In the following it will be shown how the released energy can be assessed quantitatively.

In general it is assumed that the time dependence of the angular velocity Ω of the pulsar can be parametrised in the following way:

$$\dot{\Omega} = -k\Omega^n, \tag{2.5}$$

where k and n are constants, e.g. [GS06]. The so called braking index n is characteristic of the underlying energy loss process. In case of pure magnetic dipole radiation ($P_{\mathrm{rad,mag}} = \frac{2}{3c^3}|\vec{m}|\Omega^4 \sin^2\alpha$, with $|\vec{m}|$ being the magnetic dipole moment and α the angle between the magnetic axis and the rotation axis) a braking index of $n = 3$ is expected. Sometimes the braking index can be derived from long-term observations of a pulsar. While the current rotation period ($P = 2\pi/\Omega$) and its time derivative ($\dot{P}$) can be determined for most pulsars by means of radio measurements, the second derivative is less frequently accessible. This is a pity, as these measurands could be used to determine the braking index:

$$n = \frac{\Omega\ddot{\Omega}}{\dot{\Omega}^2} = 2 - \frac{P\ddot{P}}{\dot{P}^2}. \tag{2.6}$$

All in all, braking indices have been reliably measured for five pulsars, with values ranging from 1.4 ± 0.2 for the Vela pulsar to 2.91 ± 0.05 for the pulsar PSR J1119–6127, see [L$^+$96] and [C$^+$00]. However, recent studies with a larger subset of radio pulsars have also hinted to drastic deviations from a braking index of 3 [CBO10]. In this context it should be noted that Eq. 2.5 describes the slow-down of the pulsar over a very long period of time. In comparison, current measurements only cover short periods and may be influenced by short-time variations, e.g. glitches. In general the extremely strong magnetic fields in the magnetosphere will dominate the emission processes and therefore braking indices of about 3 are still considered a reliable estimate.

Based on Eq. 2.5 an expression for the rotation period in dependency on the age of the system can be derived [PS73]:

$$P(t) = P_0 \left(1 + \frac{t}{\tau_0}\right)^{\frac{1}{n-1}}, \tag{2.7}$$

where P_0 is the rotation period of the pulsar immediately after its birth and τ_0 stands for the initial spin-down time scale. The latter is defined as

$$\tau_0 \equiv \frac{P_0}{(n-1)\dot{P}_0}. \tag{2.8}$$

Furthermore, an estimate of the age of the system can be obtained following Manchester et al. [Man77]:

$$t_{\mathrm{age}} = \frac{P}{(n-1)\dot{P}} \left[1 - \left(\frac{P_0}{P} \right)^{n-1} \right]. \tag{2.9}$$

Assuming pure magnetic dipole radiation, i.e. a braking index of 3, and $P_0 \ll P$, this equation can be simplified and the following expression for the characteristic age is obtained:

$$\tau_c \equiv \frac{P}{2\dot{P}}. \tag{2.10}$$

By means of Eqs. 2.9 and 2.10 the expression for the initial spin-down time scale can be rewritten:

$$\tau_0 = \frac{2\tau_c}{n-1} - t_{\mathrm{age}}. \tag{2.11}$$

Based on these equations and definitions an estimate of the spin-down luminosity of the pulsar can be derived in the following way [PS73]:

$$\dot{E} = -\frac{\mathrm{d}E_{\mathrm{rot}}}{\mathrm{d}t} = 4\pi^2 I \frac{\dot{P}}{P^3}, \tag{2.12}$$

where $I \approx 10^{45}\,\mathrm{g\,cm^{-2}}$ is the momentum of inertia of the neutron star, assuming a mass of 1.4 solar masses and a radius of 10 km. Inserting the time-dependency of the period, specified by Eq. 2.7, the time-dependent spin-down luminosity reads:

$$\dot{E} = \dot{E}_0 \left(1 + \frac{t}{\tau_0} \right)^{-(n+1)/(n-1)}, \tag{2.13}$$

where E_0 is the initial spin-down luminosity of the pulsar. According to Eq. 2.13 the luminosity of the pulsar evolves in the following way: As long as the age of the pulsar is small in comparison to the initial spin-down time scale, the luminosity of the pulsar remains almost constant, while it decreases rapidly when the age is larger than τ_0.

2.4.2. Lepton Injection Spectrum

For modelling the emission of PWNe the injection spectrum of the leptons, i.e. the spectrum after the crossing of the termination shock, plays an important role. Traditionally, a power-law distribution has been assumed for the differential energy spectrum, e.g. [KC84a]. This assumption is in good agreement with the presumed diffusive shock acceleration, i.e. first-order Fermi acceleration, see Sec. 2.1.3. However, attempts to model the spectral energy distribution of the photons from young PWNe as the Crab Nebula, see Fig. 2.2, with a single electron population, whose energy spectrum was specified as a power law, were not successful. Therefore, today it is assumed that the energy distribution of leptons at the termination shock is better described by a broken power law [VJ06]:

$$Q(E) = \begin{cases} Q_0 \left(\frac{E}{E_{\mathrm{b}}} \right)^{-\alpha_1}, E < E_{\mathrm{b}} \\ Q_0 \left(\frac{E}{E_{\mathrm{b}}} \right)^{-\alpha_2}, E_{\mathrm{b}} \leq E < E_{\mathrm{max}} \end{cases}. \tag{2.14}$$

The lower component is needed to explain the observed photons in the radio to infrared energy range, while the more energetic component is responsible for the photons in the X-ray and γ-ray regime. Theoretically, the formation of the break in the energy distribution can be explained by different acceleration mechanisms that prevail in the two energy ranges, see Sec. 2.1.3. The best fitting values of α_1, α_2, E_b and E_max vary for different PWNe. Nevertheless, typical values are $\alpha_1 \approx 1.0$, $\alpha_2 \approx 2.2$ and $E_\mathrm{b} \in [1\,\mathrm{keV}, 5\,\mathrm{TeV}]$, cf. [VJ06].

The maximum energy that can be achieved in the acceleration processes is commonly assessed on the basis of two different limits, cf. [Sch10]: the synchrotron limit and the gyroradius limit. The former has been introduced by de Jager [Jag96] and is a result of the synchrotron losses which increase with the energy of the accelerated particle. In the case of the maximum energy E_max the synchrotron losses are equal to the energy gain by the diffusive acceleration mechanisms. For electrons and positrons de Jager et al. have shown that the maximum energy is given by:

$$E_\mathrm{max} = 6.1 \times 10^{14} \left(\frac{\alpha}{\langle \sin^2 \theta \rangle \; B_{-3}} \right)^{1/2} \mathrm{eV}. \tag{2.15}$$

In this equation α is a proportionality factor which relates the acceleration rate and the gyrofrequency ($t_\mathrm{acc}^{-1} = \alpha \nu_\mathrm{g}$, $\alpha \leq 1$), θ is the pitch angle, i.e. the angle between the particle's velocity vector and the direction of the magnetic field, and B_{-3} is the strength of the magnetic fields in units of $10^{-3}\,\mathrm{G}$. Under the assumptions that $\alpha = 1$ and that the particles move isotropically the synchrotron limit for electrons decreases from $E_\mathrm{max} = 750\,\mathrm{TeV}$ for a magnetic field strength of $10\,\mu\mathrm{G}$ to $E_\mathrm{max} = 240\,\mathrm{TeV}$ for $B = 100\,\mu\mathrm{G}$.

The gyroradius limit was put forward by Harding et al. [HG90] and was further developed by de Jager et al. [dJDA09]. The key assumption of this limit is that the gyroradius of the particles (r_L) with the highest energies must be smaller than the termination shock radius (R_S): $r_\mathrm{L} = \epsilon R_\mathrm{S} < R_\mathrm{S}$. By means of estimates of the magnetic field strength at the termination shock (see [dJDA09] for details), the maximum energy of the electrons in the gyroradius limit is given by

$$E_\mathrm{max} = e\epsilon\kappa \left(\frac{\sigma}{1+\sigma} \frac{\dot{E}}{c} \right)^{1/2} = 110\kappa \left(\frac{\epsilon}{0.2} \right) \left(\frac{\sigma}{0.1} \dot{E}_{36} \right)^{1/2}, \tag{2.16}$$

where κ is the magnetic compression ratio which depends on the σ-parameter at the termination shock. For weak shocks $\kappa \approx 1$ while it is equal to 3 for strong shocks with $\sigma \ll 1$. $\dot{E}_{36}$ is the spin-down luminosity of the pulsar in units of $10^{36}\,\mathrm{erg\,s^{-1}}$. The gyroradius limit results also in maximum energy values of $[10^{14}, 10^{15}]$ TeV, but in contrast to the synchrotron limit it decreases with decreasing magnetic field strengths and therefore becomes more important for older PWNe.

2.4.3. Photon Emission Processes

Highly energetic electrons emit photons by means of three processes: Bremsstrahlung when the electrons are decelerated in electromagnetic fields of atoms and ions, IC scat-

tering off photons of ambient radiation fields and synchrotron radiation in the interaction with magnetic fields. An extensive treatment of these three processes (e.g. scattering rates, energy-loss rates, photon spectra) for highly relativistic electrons (i.e. $\gamma \gg 1$) is presented in [BG70]. In the following those results which are of immediate relevance for the PWN modelling presented in this thesis will be quoted.

Bremsstrahlung

Whenever highly relativistic electrons transverse a medium with a high density of ions, atoms or electrons the electrons are decelerated in the Coulomb fields and Bremsstrahlung is emitted. For high density media Bremsstrahlung can contribute significantly to the total observed photon emission. Indeed there a several astrophysical sources for which Bremsstrahlung by electrons and protons has been detected, e.g. in shell-type supernova remnants or in galaxy clusters. However, in PWNe the mean matter densities are rather low due to the preceding supernova blast wave and therefore, if at all, only a small contribution by Bremsstrahlung is expected, cf. [AA96]. Consequently, a detailed discussion is omitted here.

Inverse-Compton Scattering

Target photons for the γ-ray production via IC scattering are supplied by a wide range of photon fields. There are photon fields which can be found everywhere in the Universe, e.g. the cosmic microwave background and photon fields emitted by stars and dust and there are photon fields which are specific for certain sources, e.g. synchrotron photons in young PWN with strong magnetic fields. Concerning PWNe the latter has only been needed to explain the observed γ-ray emission of the Crab Nebula [AA96]. In other nebulae the γ rays could be explained by the first-mentioned photon fields, whereat the main contribution is ascribed to the CMB, [Aha04], p. 284. For the calculation of the expected IC photon distribution the target photon gas is described by its differential density $n(\epsilon) = \mathrm{d}n/\mathrm{d}\epsilon$, where $\mathrm{d}n$ is the number of photons with energies within $\mathrm{d}\epsilon$. Usually two different limits are distinguished in IC calculations: the Thomson limit and the Klein-Nishina limit. This classification depends on the impact parameter $b = 4E_\mathrm{e}\epsilon/m^2c^4$, where E_e and m are the energy and the mass of the electron. When b is significantly smaller than 1 the scattering takes place in the Thomson regime, for $b \gg 1$ in the Klein-Nishina regime [HH09]. The reason for this distinction is, that in the Thomson regime only a small fraction of the energy of the electron is transferred to the scattered photon. Hence, several calculations can be simplified. In the Klein-Nishina regime, however, a significant fraction of the energy of the electron is transferred to the photon and thus the energy losses of the electron can no longer be described as continuously.

An exception of this differentiation is the calculation of the spectrum of the scattered photons for a single electron (characterised by γ) interacting with quasi monoenergetic

photons (initial energy ϵ). In this case a universal formula can be derived that is valid for the Thomson regime, the Klein-Nishina regime and the energies in between, see [BG70] and references therein. To improve the readability the expected spectrum is usually expressed as a function of the scattered photon energy (ϵ_1) in units of the initial electron energy (γmc^2), i.e. $E_1 = \frac{\epsilon_1}{\gamma mc^2}$, and two additional parameters $\Gamma_\epsilon = 4\epsilon\gamma/mc^2$ and $q = E_1/\Gamma_\epsilon\,(1 - E_1)$ are introduced. Thus, the final formula reads:

$$\frac{\mathrm{d}N_{\gamma,\epsilon}}{\mathrm{d}t\,\mathrm{d}E_1} = \frac{2\pi r_0^2\, mc^3}{\gamma}\frac{n(\epsilon)\,\mathrm{d}\epsilon}{\epsilon}\left[2q\,\ln q + (1+2q)(1-q) + \frac{1}{2}\frac{(\Gamma_\epsilon q)^2}{1+\Gamma_\epsilon q}(1-q)\right], \tag{2.17}$$

where r_0 is the classical electron radius. In the more general case that neither the electrons nor the target photons are monoenergetic the resulting IC photon spectrum is computed by summing up all contributions from Eq. 2.17. For instance, in the event that the spectra of the emitting electrons is given by a power law with index α_e and the target photons by a black body distribution, then the resulting IC TeV Spectrum in the Thomson regime is well described by a power law, which has an index of $\alpha_\mathrm{p} = (\alpha_\mathrm{e}+1)/2$. A transition to the Klein-Nishina regime would become visible by a steepening of the spectra, characterised by $\Delta\alpha_\mathrm{p} \approx (\alpha_\mathrm{e}+1)/2$ [HH09].

Synchrotron Radiation

Synchrotron emission is emitted whenever a charged particle traverses a magnetic field. Especially in areas with strong magnetic fields synchrotron emission dominates the photon production. This is certainly the case in the magnetosphere of pulsars, but the pulsar wind nebulae are also strong sources of synchrotron emission. As the emitted spectrum extends over a huge range of wavelengths, synchrotron photon emission is a process that has been well studied by various astrophysical experiments.

The synchrotron emission of a single electron with a pitch angle α between the magnetic field and the electron momentum vector can be described by

$$P(\nu) = \frac{\mathrm{d}E}{\mathrm{d}t\,\mathrm{d}\nu} = \frac{\sqrt{3}e^3\, B\sin\alpha}{4\pi\epsilon_0 mc}\, F\left(\frac{\nu}{\nu_\mathrm{c}}\right), \tag{2.18}$$

where ν_c is the critical frequency $\nu_\mathrm{c} = (3eB\sin\alpha\,\gamma^2)/(4\pi m)$, $F(x) = x\int_\mathrm{x}^\infty \mathrm{d}x\; K_{5/3}(x)$ and $K_{5/3}(x)$ is the modified Bessel function of 5/3 order [Poh11]. Assuming a randomized isotropic movement of the electrons with respect to the magnetic field, the spectral power that is emitted by a single electron can be approximated by

$$P(\nu) = \frac{\sqrt{3}e^3}{4\pi\epsilon_0 mc}\; 1.85\,\sqrt{\frac{2}{3}}\, B\left(\frac{\nu}{\nu_{\mathrm{c},\pi}}\right)^{1/3} \exp(-\nu/\nu_{\mathrm{c},\pi}), \tag{2.19}$$

where $\nu_{\mathrm{c},\pi}$ is the critical frequency for a pitch angle of $\pi/2$ [N$^+$12]. For a power-law distribution of the emitting electrons with index α_e $P(\nu)$ can be calculated analytically, e.g. [BG70], and the corresponding photon spectra, i.e. $\frac{\mathrm{d}N}{\mathrm{d}\epsilon}$, in the X-ray regime can be

described by a power law with an index α_p which is linked to the electron index in the following way $\alpha_\mathrm{p} = (\alpha_\mathrm{e} + 1)/2$.

Expected spectral energy distribution of photons in PWNe

To get a better feeling for the different photon emission processes for relativistic electrons and their contribution to the observable photon spectra, Fig. 2.10 shows the spectral energy distributions (SEDs) for mono-energetic electrons as well as for power-law electron spectra with exponential cut-offs at different energies. As described above the emission processes which are of interest for the course of this thesis are the synchrotron and the IC emission (depicted as solid lines). In the top panel the red line represents the SED for electrons with an energy of 1 TeV. Clearly visible is the double hump structure, i.e. synchrotron emission is emitted in the X-ray regime, while the VHE emission is ascribed to IC emission. In the case of the 1 TeV electron the contributions of the different photon fields to the IC emission can be distinguished (from left to right: CMB, far infra-red, FIR, and near infra-red, NIR). For the 100 TeV electron the SED (blue line) is shifted to higher energies and the IC emission is clearly dominated by the scattering on the CMB. The contribution of the other photon fields is suppressed as the scattering takes place in the Klein-Nishina regime.

For the modelling presented in the following chapter it is helpful to study the relationship between the peaks of the synchrotron and IC emission and the energy of the emitting electron [HH09]. In case of the synchrotron emission this relationship is given by

$$E_\mathrm{Sy,eV} \approx 0.087\ E^2_\mathrm{e,TeV}\ B_\mathrm{\mu G}. \tag{2.20}$$

For the IC emission the peak depends on the considered photon fields. In many cases this photon fields can be approximated by a black-body spectrum of temperature T and the mean energy of the photon gas is thus given by $2.80\,kT$. Under this assumption the relation between the peak of the IC emission and the energy of the electron in the Thomson regime reads:

$$E_\mathrm{IC,TeV} \approx 33\ E^2_\mathrm{e,TeV}\ kT_\mathrm{eV}. \tag{2.21}$$

Conversely, this relationship can be used to estimate the energy of the electrons that account for the observed photons. While typical X-ray observations detect photons in the order of 1 keV, a typical VHE photon detected by H.E.S.S. has an energy of 1 TeV. In a magnetic field of 3 µG and considering IC scattering on the CMB only, the corresponding electron energies are 60 TeV and 10 TeV, respectively. Hence, the X-ray photons are usually generated by electrons which have an higher energy than the electrons that account for the TeV photons.

In real astrophysical sources it is expected that the spectra of newly ejected electrons can be described by a power law with a cut-off at energies higher than 1 TeV. The lower panel in Fig. 2.10 shows the resulting SEDs for a cut-off at 1 TeV (red line) and a cut-off at 100 TeV (blue line). One sees immediately that the slope of the particle at energies higher

than 1 TeV strongly influences the course of the SED. Especially the energy ranges which we will consider later in the modelling of HESS J1825–137, i.e. 1 keV for X-ray observations and 1 TeV for TeV observations are dominated by the highly energetic electrons.

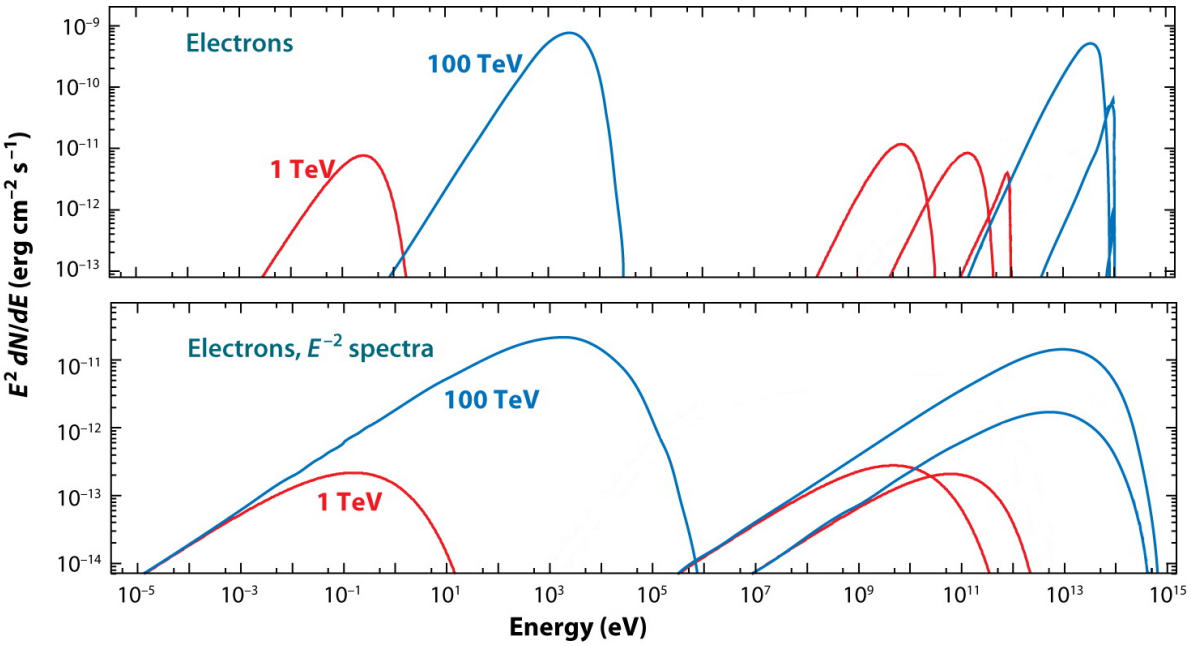

Figure 2.10.: Spectral energy distributions of photons emitted in different radiation processes. From left to right the contributions by synchrotron emission and IC Scattering on CMB, dust and starlight photons (solid lines) are shown. The SEDs are shown for mono-energetic electrons (1 TeV and 100 TeV, top panel) and power-law particle spectra with exponential cut-off (cut-off at 1 TeV and 100 TeV, bottom panel). The conditions which were used in the calculation of the SEDs are: a total particle energy of 10^{48} erg, a distance of 1 kpc, a magnetic field of 3 µG and photon fields which were approximated by black body radiation spectra CMB ($kT = 2.35 \times 10^{-4}$ eV, $\omega_{\mathrm{ph}} = 0.26\,\mathrm{eV\,cm^{-3}}$), FIR ($kT = 0.02$ eV, $\omega_{\mathrm{ph}} = 0.26\,\mathrm{eV\,cm^{-3}}$) and NIR ($kT = 1.5$ eV, $\omega_{\mathrm{ph}} = 1.0\,\mathrm{eV\,cm^{-3}}$). The image has been adapted from [HH09].

2.4.4. Magnetic Field

The magnetic fields of pulsars belong to the strongest magnetic fields in the Universe. An estimate of the strength at the surface of a pulsar can be obtained from the rotation period and its time derivative. The calculation is based on the assumption that the pulsar emits only magnetic dipole radiation and that this energy is withdrawn from the rotational energy of the pulsar. Thus the surface magnetic field is given by:

$$B_{\mathrm{S}} = \sqrt{\frac{3c^3 P\dot{P}}{8\pi^2 R^6 \sin^2\alpha}}, \tag{2.22}$$

where R is the radius of the pulsar and α the angle between rotation and dipole axis [LK04]. Estimates of the magnetic fields in PWNe can be obtained by means of the

three following techniques, see [RGB12] and references therein: By assuming equipartition of the energy between particles and magnetic field for synchrotron emission regions, by complementing synchrotron observations with the observation of IC emission and by evaluating physical models that predict the magnetic field at the termination shock in dependence on the (sometimes) observable radius. All in all, typical magnetic field intensities in PWNe are in the order of 1 µG to 100 µG [M$^+$08]. For comparison the typical intensity of the magnetic field in the interstellar medium is in the order of 3 µG.

Concerning the spatial distribution, radio polarimetry measurements have revealed a high degree of order of the magnetic fields close to the termination shock. There has been observational evidence for toroidal magnetic fields, cf. Sec. 2.1.4, for radial magnetic fields and even for more complex structures [RGB12]. Nevertheless, theoretically magnetohydrodynamic models favour the toroidal appearance for young PWNe. Indeed, Kothes et al. have shown that such a toroidal magnetic field can also account for the other appearances when the viewing angle is considered, see [KRU06] for details. Though progress in the understanding of the overall structure of the magnetic field has been made, the spatial distribution of the magnetic field intensities is still not well understood. Especially for evolved PWNe, where a relic PWN has been formed due to the interaction with the reverse shock, this field of research is still in its very early stages.

Just like the spatial distribution the temporal evolution of the magnetic field within the PWN is subjected to large uncertainties. For simplicity in most of the approaches to describe the temporal evolution the spatial distribution is neglected and the magnetic field is assumed to be uniform over the total emission region. Venter & de Jager [VJ06] assumed for instance that the time-dependence of the magnetic field can be described in the following way:

$$B(t) = \frac{B_0}{1 + (t/\tau_{0,\mathrm{M}})^k}. \tag{2.23}$$

In this equation, $\tau_{0,\mathrm{M}}$ is a characteristic time-scale for the evolution of the magnetic field and in the case of the PWN G0.9+0.1 Venter & de Jager assumed $\tau_{0,\mathrm{M}} = 500\,\mathrm{kyr}$ and $k = 0.5$, resulting in $B(t) \propto t^{-0.5}$ for $t > \tau_{0,\mathrm{M}}$. Another model was presented by Tanaka et al. [TT10] who assumed that a certain fraction of the rotational energy of the pulsar, characterised by the parameter η_{M}, is converted to the magnetic field energy and that this energy is conserved during the evolution of the PWN. Thus, their time- dependent magnetic field for a spatial spherically symmetric PWN reads

$$B(t) = \sqrt{\frac{3(n-1)\,\eta_{\mathrm{M}} \dot{E}_0 \tau_0}{(R_{\mathrm{PWN}}(t))^3} \left(1 - (1 + \frac{t}{\tau_0})^{-\frac{2}{n-1}}\right)}. \tag{2.24}$$

In case of $t > \tau_0$ this approximation predicts $B(t) \propto t^{-1.5}$. Though the approximation of Tanaka et al. may be considered a rough estimate, they could show that their result is in good agreement with the most prevalent approximations, see [TT10] and references therein.

2.4.5. Transport Mechanisms

In astrophysics the two propagation mechanisms of cosmic rays that are usually distinguished are convection and diffusion. An elaborate introduction in this topic can be found in [SMP07]. Concerning PWNe, the regions close to the pulsar or rather to the termination shock are certainly dominated by convection mechanisms. Indeed, there have been several successful modelling approaches based on bulk motions that were able to reproduce observational characteristics of rather young PWNe, e.g. [Sch10] and [H$^+$12]. However, for evolved PWNe, especially after the crushing by the reverse shock, diffusive processes may prevail, e.g. [H$^+$11]. We will therefore concentrate on diffusive propagation in the following.

Diffusion of charged particle in the ISM is governed by scattering off irregularities in the magnetic fields and by random magneto-hydrodynamic waves that are excited by the cosmic rays themselves. The characteristic quantity to describe the diffusion process is the diffusion coefficient D, by means of which the mean quadratic propagation can be specified: $\langle r^2 \rangle = 4Dt$. In general, the diffusion coefficient is proportional to the mean free path for scattering and the velocity of the considered particles, i.e. in the case of the CRs the velocity of light. In case that diffusion within magnetic fields is considered, cf. [HH09], it is common practice to express the mean free path length as a multiple of the gyration radius r_g:

$$D \approx \frac{1}{3}\,\eta\, r_\mathrm{g}\, c. \tag{2.25}$$

For relativistic particles the gyration radius for particles with unit charge may be approximated as $r_\mathrm{g,pc} \approx 0.0011\ \frac{E_\mathrm{TeV}}{B_{\perp,\mu\mathrm{G}}}$ [HH09]. The proportionality coefficient η is determined by the mean magnetic field strength and the degree of turbulence δB on length scales in the order of r_g: $\eta \approx (\delta B/B)^2$ [SMP07]. A widely-used approximation is the so-called Bohm diffusion, in which η is set equal to one. In this case the diffusion coefficient for a 1 TeV electron in a magnetic field of 3 µG is $D \approx 4 \times 10^{-5}\,\mathrm{pc^2\,yr^{-1}}$. Moreover, for diffusion perpendicular to magnetic field lines de Jager et al. argued that η should be significantly smaller than 1 [dJDA09]. In contrast, the values of the diffusion coefficients that have been obtained from fitting models to the CR data of the Milky Way are significantly larger [SMP07]. The most common assumption in this context is that $D \approx (3-5) \times 10^{28}\ \left(\frac{E}{1\,\mathrm{GeV}}\right)^\alpha\ \mathrm{cm^2\ s^{-1}}$, where α is in the order of 0.3. For a 1 TeV electron this corresponds to a diffusion coefficient of $D \approx 2.5 \times 10^{-1}\ \mathrm{pc^2\,yr^{-1}}$.

2.4.6. Energy Losses

While the particle move away from the termination shock, they continuously lose energy. In the following we will have a closer look at the prevailing energy loss processes for highly energetic electrons. Of great importance in this context are radiation losses, which initially enable us to observe PWNe. As has been motivated in Sec. 2.4.3 Bremsstrahlung losses will be suppressed in PWNe, but synchrotron and IC emission will contribute. Again, a detailed discussion of the radiation losses can be found in [BG70] and therefore we will only quote the main results.

Inverse-Compton losses

As long as the energy losses take place in the Thomson regime the mean energy loss of an electron characterised by γ is given by

$$-\left(\frac{\mathrm{d}E}{\mathrm{d}t}\right)_{\mathrm{IC}} = \frac{4}{3}\,\sigma_{\mathrm{T}}\,c\,\omega_{\mathrm{ph}}\,\gamma^2, \tag{2.26}$$

where $\sigma_{\mathrm{T}} = \frac{8\pi}{3}\,r_0^2 = 6.65 \times 10^{-25}\,\mathrm{cm}^2$ is the Thomson cross section and ω_{ph} is the total energy density of the photon field. In the Klein-Nishina regime in contrast the energy losses are suppressed due to the energy-dependence of the cross section. For a rough estimate, it is convenient to account for this suppression by an reduced photon density $\omega'_{\mathrm{ph}} = \eta \cdot \omega_{\mathrm{ph}}$. For the CMB and electrons in the TeV range η is in the order of $\approx \frac{2}{3}$ [A$^+$06b]. The corresponding IC cooling time is

$$\tau_{\mathrm{IC}} = \frac{\mathrm{E}}{-(\mathrm{d}E/\mathrm{d}t)_{\mathrm{IC}}} \approx 3.1 \times 10^5 \left(\frac{\omega'_{\mathrm{ph}}}{\mathrm{eV\,cm^{-3}}}\right)^{-1} E_{\mathrm{TeV}}^{-1}\ \mathrm{yr}, \tag{2.27}$$

which for a 100 TeV electron interacting with CMB photons ($\omega_{\mathrm{ph}} = 0.26\,\mathrm{eV\,cm^{-3}}$) accounts to $\tau_{\mathrm{IC}} \approx 18\,\mathrm{kyr}$.

Synchrotron losses

As synchrotron radiation can be understood as IC scattering on the virtual photons of the magnetic field, an expression similar to Eq. 2.26 can be derived for the mean synchrotron energy losses in a magnetic field B:

$$-\left(\frac{\mathrm{d}E}{\mathrm{d}t}\right)_{\mathrm{Sy}} = \frac{4}{3}\,\sigma_{\mathrm{T}}\,c\,\left(\frac{B^2}{2\,\mu_0}\right)\,\gamma^2. \tag{2.28}$$

In this case the corresponding cooling time is

$$\tau_{\mathrm{Sy}} \approx 3.1 \times 10^5\ \left(0.025\,B_{\mu\mathrm{G}}^2\right)^{-1} E_{\mathrm{TeV}}^{-1}\ \mathrm{yr}, \tag{2.29}$$

which for a 100 TeV electron in the interstellar magnetic field of $\approx 3\,\mu\mathrm{G}$ accounts to $\tau_{\mathrm{Sy}} \approx 14\,\mathrm{kyr}$.

Impact of the radiation losses on the electron spectrum

Since synchrotron and IC losses are proportional to γ^2 they strongly influence the energy spectrum of the electrons, cf. [BG70]. For the evaluation of these influences one usually starts with the differential equation that accounts for the temporal changes of the electron energy spectrum $N_e = \mathrm{d}N/\mathrm{d}E$:

$$\partial N_{\mathrm{e}}/\partial t = Q(E,t) - \partial/\partial E(\dot{E}N_{\mathrm{e}}). \tag{2.30}$$

In this equation $Q(E,t)$ represents a source term, while the second term accounts for the energy-dependent energy fluxes. In case of the synchrotron and IC losses which are proportional to E^2 (e.g. $\mathrm{d}E/\mathrm{d}t = aE^2$) and for a source term which is given by a power law ($KE^{-\Gamma}$) the solution of Eq. 2.30 in the stationary case reads:

$$N_\mathrm{e}(E) = (K/a(\Gamma-1))E^{-(\Gamma+1)}. \tag{2.31}$$

Thus, synchrotron losses as well as IC losses result in a steepening of the spectral index of the electron spectrum by one. The problem gets considerably more complex, when the energy losses are no longer continuously, e.g. for IC scattering in the Klein-Nishina regime. In this case the differential equation must be replaced by an integro-differential equation. For the respective solution the interested reader is referred to [BG70].

Adiabatic energy losses

While the PWN expands the particles suffer adiabatic losses. Following de Jager & Harding [dH92] the total adiabatic energy loss of an ultra-relativistic gas is given by:

$$-\left(\frac{\mathrm{d}E}{\mathrm{d}t}\right)_\mathrm{ad} = \frac{1}{3}E\ \vec{\bigtriangledown}\vec{v}, \tag{2.32}$$

where $\vec{v}$ is the velocity of propagation. Especially for young spherically symmetric PWN, where velocity profiles for the bulk motion can be derived on the basis of MHD simulations, this equation can be used to derive the energy losses for different populations of particles, cf. [Sch10]. Another application is in one-zone models where the total adiabatic energy loss may be derived from the evolution of the PWN radius, see [TT10]. In contrast to the radiation losses which influence the index of an injected power-law particle energy spectrum, see Eq. 2.31, the adiabatic energy losses have only impact on the normalisation of the energy spectrum. However, lately there have been studies which provided indications that in the case of evolved PWNe the adiabatic energy losses play only a subordinate part, as it is likely that a huge part of the lost energy is returned when the reverse shock crushes the PWN [H$^+$11].

3. Introducing HESS J1825–137

In this chapter a survey of the observations of HESS J1825–137 in various wavelength regimes is given. In doing so the results of several experiments will be addressed. In order to give the reader an overview of the quoted experiments a glossary is included at the end of this thesis, which provides for each experiment the key data. In the running text only the respective observation results are discussed. For HESS J1825–137 observations of the pulsar as well as of the pulsar wind nebula are presented. Concerning the latter, we will focus on observations in the X-ray and in the γ-ray regime, because these observations will later be compared with the predictions of the newly developed model. With regard to the γ-ray emission it is discussed which parts of the observed TeV γ-ray emission in the field of view can actually be ascribed to HESS J1825–137. Having studied the distinctive features of HESS J1825–137, an overview of previous modelling approaches for HESS J1825–137 is given.

3.1. PSR J1826–1334 and G18.0–0.7

PSR J1826–1334	
position	R.A. $= 18^{\mathrm{h}}26^{\mathrm{m}}13.175^{\mathrm{s}}$, Dec. $= -13°34'46.8''$
pulse period	$P = 101.5\,\mathrm{ms}$
time derivative of pulse period	$\dot{P} = 75.061 \times 10^{-15}$
spin down power	$\dot{E} = 2.8 \times 10^{36}\,\mathrm{erg\,s^{-1}}$
characteristic age	$\tau_{\mathrm{c}} = 21.4\,\mathrm{kyr}$
distance	$d = 4.12\,\mathrm{kpc}$
proper motion	$\mu_\alpha = 23.0\,\mathrm{mas\,yr^{-1}},\ \mu_\delta = -3.9\,\mathrm{mas\,yr^{-1}}$

Table 3.1.: Overview of the key data of PSR J1826–1334. References: see text.

The pulsar PSR J1826–1334 (previously known as PSR B1823–13) was detected in the radio regime within the Jodrell Bank observatory 1400 MHz survey [C$^+$92]. Regular monitoring of the pulsar by the Nanshan radio telescope of the Urumqi Observatory between 2002 and 2008 allowed a very accurate determination of its position R.A. $= 18^{\mathrm{h}}26^{\mathrm{m}}13.175^{\mathrm{s}}$ and Dec. $= -13°34'46.8''$, its period 101.5 ms and the period derivative $\dot{P} = 75.061 \times 10^{-15}$ [Y$^+$10]. By means of Eq. 2.10 and Eq. 2.12 these values allow the determination of the characteristic age $\tau_{\mathrm{c}} = 21.4\,\mathrm{kyr}$ and the current spin-down luminosity $\dot{E} = 2.8 \times 10^{36}\,\mathrm{erg\,s^{-1}}$. Among the 2008 pulsars currently listed in the ATNF pulsar

catalog, PSR J1826–1334 belongs to the the 55 with the lowest characteristic age and the 32 with the highest energy output[5]. The distance to the pulsar was estimated based on the dispersion of the radio pulses, see Sec. 2.1.1: $d = 4.12\,\mathrm{kpc}$ [CL03]. The proper motion of PSR J1826–1334 was determined by Pavlov et al. [PKB08] who re-analysed two archival VLA observations (Project AF118 & Project AC761). The two observations were taken under comparable observation conditions (20 cm band in A configuration, spectral line mode, one observation at about 1385 MHz the other at about 1665 MHz), but with a temporal distance of more than 18 years. The spatial resolution in these observations was in the order of $1.5'' \times 2.1''$ and Pavlov et al. could identify 5 suitable reference sources. With respect to these reference sources the proper motion of PSR J1826–1334 was determined by means of a linear fitting procedure which was introduced by McGary et al. for proper motion measurements with VLA [M$^+$01]. In the local standard of rest the proper motion is well described by: $\mu_\alpha = (23.0 \pm 2.5)\,\mathrm{mas\,yr^{-1}}$ and $\mu_\delta = (-3.9 \pm 3.1)\,\mathrm{mas\,yr^{-1}}$ [PKB08]. A first impression of how far the pulsar may have moved within its characteristic lifetime is given in Fig. 3.1.

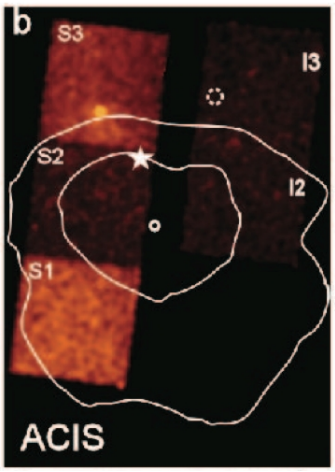

Figure 3.1.: Chandra ACIS images of the vicinity of PSR J1826–1334 [PKB08]. All point sources but PSR J1826–1334 have been removed and the image has been corrected for differences in the exposure and smoothed with a Gaussian accounting for the spatial resolution. The only remaining point source (on the chip labelled S3) indicates the present position of PSR J1826–1334. The dashed circle indicates the probable place of birth of the pulsar as derived from the measured proper motion. The significance contour lines and the small white ring illustrate the extended TeV emission as presented in the H.E.S.S. publication. The white star marks the position of a strong IR and radio source.

First radio searches for any supernova remnant, i.e. a shell or a pulsar wind nebula, in the vicinity of PSR J1826–1334 with VLA (covering a $40'$ square centred on the pulsar) were not successful [BGL89]. However, in 1996, X-ray observations with ROSAT revealed a point-like source embedded in a compact nebula (of diameter $40''$) and surrounded by a diffuse emission region of size $4'$–$5'$ [FSP96]. ASCA observations [S$^+$01] could only distinguish the pulsar and a surrounding diffuse emission region, but allowed a first estimate

[5] http://www.atnf.csiro.au/research/pulsar/psrcat

of the corresponding energy spectra which in the 2–10 keV energy range were well fitted by power laws with spectral indices of 1.9 ± 0.2 and 2.0 ± 0.1, respectively.

In 2001 the emerging image of a pulsar which is surrounded by a PWN was finally confirmed by XMM-Newton [G$^+$03], which surpassed the preceding observation in terms of sensitivity and spatial, spectral and temporal resolution. In the two XMM-Newton observations, with an effective exposure of ≈ 40 ks for the MOS detectors and ≈ 20 ks for the PN detector, as it was operated in $4' \times 4'$-small-window mode, a direct detection of the pulsar failed but a diffuse emission region and an elongated core could be resolved. Both components are shown in Fig. 3.2. The core can be observed when the full intensity range of the MOS images is mapped, see Fig. 3.2(b). Clearly visible is an elongated emission region which extends along the east-west direction and has a length of about $30''$. The diffuse emission region is fainter and only becomes visible when the intensity range of the MOS images is restricted to 0 % and 30 % of the peak intensity in the selected region, see Fig. 3.2(a). This diffuse emission region is no longer centred on the pulsar, but is shifted to the south and has an extension of at least $5'$. An even larger possible extension could not be excluded, as the XMM detectors got background dominated for larger extents of the diffuse emission component. For both regions spectra were extracted. The spectrum for the core region was extracted from a circle with $18''$-radius centred on the pulsar, depicted in Fig. 3.2(b). The spectrum for the diffuse region was determined from a circular region with $200''$-radius centred on (R.A. $= 18^{\mathrm{h}}26^{\mathrm{m}}14.4^{\mathrm{s}}$, Dec. $= -13°36'14.8''$), from which the regions around the core and two additional point-sources were excluded, c.f. Fig. 3.2(a). While the spectrum from the core region was well described by an absorbed power law with photon-index $1.6^{+0.1}_{-0.2}$ and $N_{\mathrm{H}} = (1.0 \pm 0.2) \times 10^{22}\,\mathrm{cm}^{-2}$, the power-law fit to the diffuse emission region revealed a spectral index of $2.3^{+0.1}_{-0.2}$ and $N_{\mathrm{H}} = (1.4^{+0.5}_{-0.2}) \times 10^{22}\,\mathrm{cm}^{-2}$. Assuming a distance of 4 kpc this corresponds to X-ray luminosities in the energy range between 0.5 and 10 keV of $L_{\mathrm{X}} \approx 9 \times 10^{32}\,\mathrm{erg\,s}^{-1}$ and $L_{\mathrm{X}} \approx 3 \times 10^{33}\,\mathrm{erg\,s}^{-1}$, respectively.

Gaensler et al. [G$^+$03] showed that these observations can be well explained in a PWN scenario, where the core region represents the wind termination shock and the diffuse emission is ascribed to the PWN: In PWN scenarios it is expected that the leptons only emit synchrotron emission when they have passed the wind termination shock. Therefore, the wind termination shock can be visible as a distinct feature in X-rays. From observations of other PWNe, i.e. the Crab Nebula, it was known that typical sizes of termination shocks are in the same order as the core region. In addition, the observed power-law index of the photon spectrum at the termination shock agreed well with the expected index of approx. 1.5 – assuming a particle spectrum with index 2.0 – and the steepening of the photon index for the diffuse emission region could be ascribed to synchrotron losses, c.f. Sec. 2.4.3. Finally, in this scenario the elongation of the core could be explained by an asymmetric outflow from the pulsar and the offset of the PWN in relation to the pulsar by an asymmetric reverse shock. Gaensler et al. named their newly detected PWN G18.0–0.7, according to its Galactic coordinates. The fact that neither the pulsar nor the surrounding shell is detected in X-rays was motivated by means of a comparison with Vela X, which is in a similar evolutionary stage as G18.0–0.7: when the measured data from either the Vela pulsar or its shell were converted as if they had been observed under the same circumstances as G18.0–0.7, i.e. same distance and same column

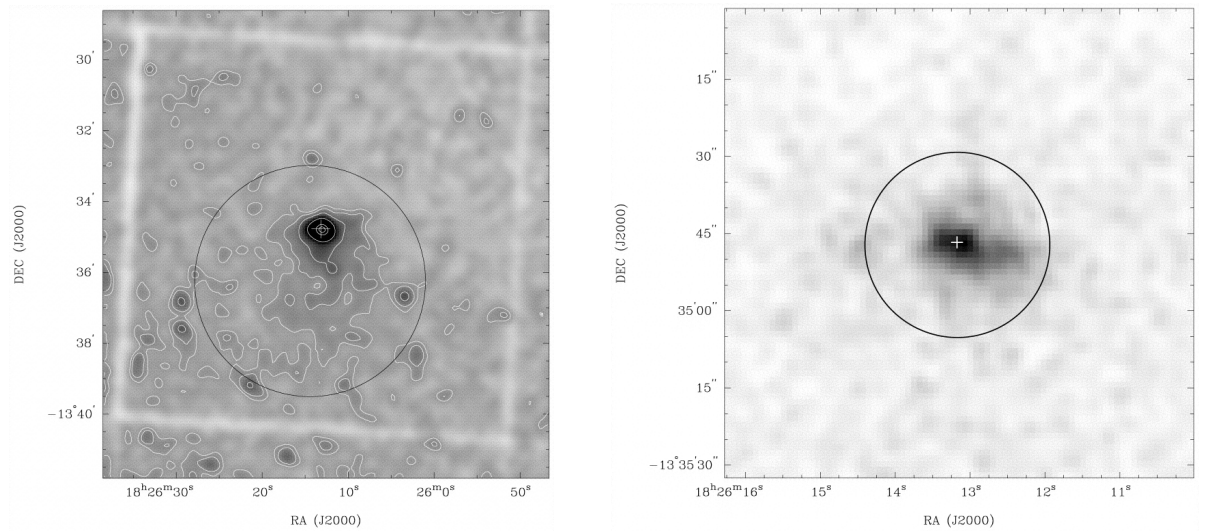

(a) Diffuse emission region

(b) Core region

Figure 3.2.: XMM-Newton Observation of PSR B1823–13, taken from [G+03]. Both images show combined count maps of the EPIC MOS detectors and are centred on PSR J1826–1334. (a) $10' \times 10'$ image section, smoothed with a Gaussian of FWHM $20''$. A linear transfer function is applied so that the intensity range between 0 % and 30 % of the peak intensity in the image can be studied in detail. Clearly visible is the faint diffuse emission component extending to the south of the pulsar. (b) Central $90'' \times 90''$ image section, smoothed with a Gaussian of FWHM $3''$. In this case the linear transfer function maps the full intensity range. The image shows the east-west elongation of the core region.

density, the expected flux values were well below the detection limit of XMM Newton. Moreover, Gaensler et al. presented a first estimate of the magnetic field within the PWN. Assuming pressure balance at the termination shock and equipartition between particles and magnetic fields upstream of the shock, the magnetic field in PWN is expected to be in the order of 10 µG.

3.2. VHE γ-ray Observations of HESS J1825–137

3.2.1. Detection by H.E.S.S.

In the initial phase of the H.E.S.S. Galactic plane survey in 2004 indications of a TeV source close to PSR B1826–1334 were found, [A+05a]. By means of follow-up observations, resulting in a total live time of 8.4 h, the new source could be established in 2005 and was denoted HESS J1825–137 [A+05b]. This new source is located in the south-west of the pulsar at a distance of $11.2'$ and exhibited a statistical significance of $13.4\,\sigma$ for a source extension with radius 0.4°. Due to difficulties in finding suitable background regions the first determination of the energy spectrum was based on 5.4 h live time only. Nevertheless, a spectrum could be extracted that was well-fitted by a power law with a

photon index of $2.40 \pm 0.09_{\mathrm{stat}} \pm 0.2_{\mathrm{sys}}$ and resulted in an integrated flux above 230 GeV of $(3.4 \pm 0.2_{\mathrm{stat}} \pm 1.0_{\mathrm{sys}}) \times 10^{-11}\ \mathrm{cm}^{-2}\,\mathrm{s}^{-1}$.

Although multiwavelength searches for other counterparts were conducted, PSR B1826–1334 remained the only plausible counterpart. An association with this pulsar was favoured by the similarities in morphology: Both the X-ray PWN and the γ-ray PWN extend to the south / south-west of the pulsar. A plausible explanation of this asymmetry by an asymmetric reverse shock from the supernova remnant had already been given by Gaensler et al. [G$^+$03]. Assuming a constant convection speed for the populations of X-ray and γ-ray emitting leptons, Aharonian et al. could show that due to the different cooling times for synchrotron emission and IC scattering differences in the radii of the corresponding PWNe by a factor of six are not unexpected [A$^+$05b]. Moreover, the interpretation of the steepening of the spectra between core and extended nebula in the XMM data as a result of synchrotron losses could be transferred to the TeV observation: While the cooled leptons which have been emitted in early epochs of the pulsar's lifetime can still contribute to the IC scattering of background photons to TeV energies, they do no emit synchrotron radiation in the X-ray regime any longer.

To confirm the association of HESS J1825–137 with PSR B1826–1334 several follow-up observations were carried out in 2005. As HESS J1825–137 is also located in the field of view of LS 5039, which is another prominent H.E.S.S. source, ≈ 67 h of observation were soon accumulated that resulted in 53.1 h of dead-time corrected live time. With the help of these new data the association between HESS J1825–137 and PSR B1826–1334 could be firmly established by means of a detection method that was applied for the first time in VHE γ rays [A$^+$06b]. In the following we will have a closer look at this approach. For the details of the H.E.S.S. data analysis the interested reader is referred to the adjacent chapter. For the time being we will concentrate on the published H.E.S.S. results on HESS J1825–137 and their implications, see [A$^+$06b].

The published excess map of HESS J1825–137, i.e. a background subtracted count map, is shown in Fig. 3.3. As the acceptance to γ rays differs within the field of view of the H.E.S.S. telescopes such influences were counterbalanced, i.e. the sky map is acceptance-corrected, so that the true morphology of the source can be studied. To account for the limited resolution of the telescopes the sky map was smoothed with a smoothing radius of $2.5'$. In addition the maximum of the color scale was fixed to the maximum of the emission of HESS J1825–137 to allow a detailed study of the morphology of the PWN[6]. Thus the special characteristics of HESS J1825–137 are directly visible: the huge size of the γ-ray source (with a diameter of about $1°$), the asymmetric shape with an elongation to the south-west, and the offset to the proposed counterpart, the pulsar PSR B1826–1334. To better quantify the morphology of the TeV source an asymmetric Gaussian, which was convolved with the point-spread function of the instrument, was fit to the data and revealed a best fit position of (R.A. $= 18^{\mathrm{h}}25^{\mathrm{m}}41^{\mathrm{s}} \pm 4^{\mathrm{s}}_{\mathrm{stat}}$, Dec. $= -13°50'20'' \pm 40''$), extensions of $\sigma_{\mathrm{source},1} = 0.23° \pm 0.02°_{\mathrm{stat}}$ and $\sigma_{\mathrm{source},2} = 0.26° \pm 0.02°_{\mathrm{stat}}$ and a position angle of $17° \pm 12°_{\mathrm{stat}}$. The results of this fit are indicated in Fig. 3.3 by the black ellipse. The main axis of the ellipse is consistent with the line connecting pulsar and best fit position.

[6]Note that the strength of the emission from the direction of LS 5039 exceeds that of HESS J1826–137

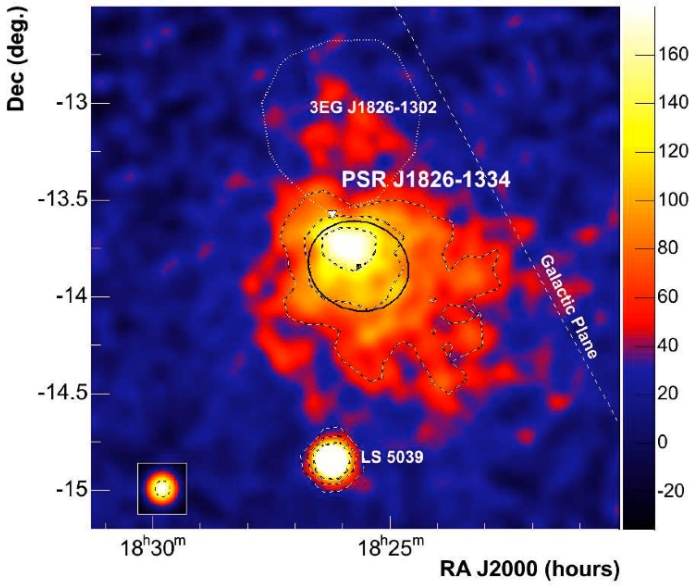

Figure 3.3.: H.E.S.S. excess map of the re-observation of HESS J1825–137, taken from [A+06b]. The map is corrected for different camera acceptances within the field of view and is smoothed with a smoothing radius of 2.5′. The convolved point spread function that corresponds to this observation and the applied analysis is shown in the inset in the bottom left corner. The maximum value of the color scale of the sky map has been fixed to the maximum emission detected for HESS J1825–137 which results in a truncated representation of the strong TeV source LS 5039, but allows to study the morphology of HESS J1825–137 in detail. The morphology of the TeV emission is clearly elongated and was fitted with an asymmetric Gaussian which is represented in the figure by a black ellipse. The best fit position, marked by the black dot, is shifted to the south-west with respect to the position of PSR J1826–1334 which is indicated by a white triangle.

In addition also the peak position of the TeV emission was further investigated. For this purpose a symmetric Gaussian was fit to a restricted region around the maximum of the TeV emission that yielded a peak position of $18^{\mathrm{h}}25^{\mathrm{m}}57^{\mathrm{s}}$, $-13^{\circ}43'36.8''$. All in all, the center of gravity of the TeV emission is located at a distance of $\sim 17'$ to the pulsar, while the peak emission is located a little bit closer with a distance of $\sim 10'$.

The increased data set allowed the study of the energy spectra in more detail. Since the acceptance-corrected sky map revealed an even larger extension of HESS J1825–137 than the one assumed in the previous publication, the radius of the spectrum extraction region was extended from $\theta = 0.4^{\circ}$ to $\theta = 0.8^{\circ}$. The re-evaluation of the significance of this region yielded $33.8\,\sigma$. The total spectrum was determined for energies between 270 GeV and ~ 35 TeV. Due to the increased source radius the source flux was significantly higher than the one reported before, i.e. a power-law fit hinted at a flux of $\approx 68\,\%$ of the flux of the Crab Nebula above 1 TeV. Aharonian et al. showed, however, that the spectrum was better described by a spectrum shape with a cut-off at higher energies, than by the default power law. The authors tested power laws with exponential cut-off or energy-dependent exponent, as well as broken power laws. All cited spectrum shapes improved the quality

of the fit, but none was significantly better than the other. Therefore, only the results of the fit of the power law with an exponential cut-off, i.e. $\frac{\mathrm{d}N}{\mathrm{d}E} = I_0\ E^{-\Gamma} \exp^{-E/E_\mathrm{c}}$, are quoted here. The best fit parameters were $I_0 = (21.0 \pm 0.5_{\,\mathrm{stat}}) \times 10^{-12}\,\mathrm{TeV}^{-1}\,\mathrm{cm}^{-2}\,\mathrm{s}^{-1}$, photon index $\Gamma = 2.26 \pm 0.03_{\,\mathrm{stat}}$ and cut-off energy $E_c = (24.8 \pm 7.2)$ TeV.

Due to the size and the strength of the TeV source it was possible to extract spectra for sub-areas of the total emission region. In order to investigate the connection to the pulsar the first analysis region, a circle with radius 0.1°, was centred on the pulsar. The other extraction regions, so called wedges, were chosen as ring segments with an opening angle of 90° and a radial thickness of 0.1°, see inset Fig. 3.4. The purpose of this choice was to have wedges with widths larger than the point spread function (PSF) of the telescopes and to include the main part of the emission region, while avoiding contamination by LS 5039. For all these wedges spectra were extracted and fitted with power laws. The results are shown in Fig. 3.4. In order to display all spectra in the same image, the data and the power-law fits for each wedge were scaled with a factor $10^{2 \cdot i},\ i \in \{0, ..., 11\}$, where i is the number of the wedge when the counting is started at the outermost wedge. To visualise how the spectra change with increasing distance to the pulsar, for each wedge the power-law fit to the spectrum of the innermost wedge, which has been scaled in the same way as the data of the respective wedge, is depicted as dashed line. In doing so it becomes evident that the spectra get softer, i.e. the power-law index increases, with increasing distance to the pulsar.

This behaviour is observable even better when the indices of the power-law fits are plotted as a function of the distance to the pulsar, see Fig. 3.5(a). While the innermost wedge corresponds to a photon index of ~ 1.9, the outer rings correspond to photon indices in the order of 2.5. The two series of measurement shown in the figure (indicated by the open and the filled black circles, respectively) are based on different background estimates. The filled circles represent an analysis procedure in which the background was assessed from the same observation runs as the source data, i.e. from regions in the field of view where a contamination by another γ-ray source was excluded. The open circles have been derived by means of background estimates from dedicated off-runs. While the individual points differ within the measurement errors, both series of measurement hint at a significant increase of the photon indices. In addition the surface brightness, i.e. the integrated flux between 0.25 TeV and 10 TeV divided by the corresponding wedge area, has been calculated for each wedge, see Fig. 3.5(b). Once again it becomes evident that the maximum of the TeV emission is not located at the position of the pulsar, but at a certain offset.

The verification of the different energy spectra for individual wedges, in particular the varying photon indices, was the very first proof of an energy-dependent morphology in the VHE γ-ray regime and attracted a lot of interest. Aharonian et al. discussed three plausible origins [A$^+$06b]: energy losses of the emitting particles, energy-dependent transport mechanisms and a time-dependent particle injection spectrum. As in the XMM-Newton publication Aharonian et al. studied at first the influence of the energy loss mechanisms. In particular they investigated the time scales of synchrotron and IC emission for TeV γ-ray emitting electrons and showed that both are well below the characteristic age of

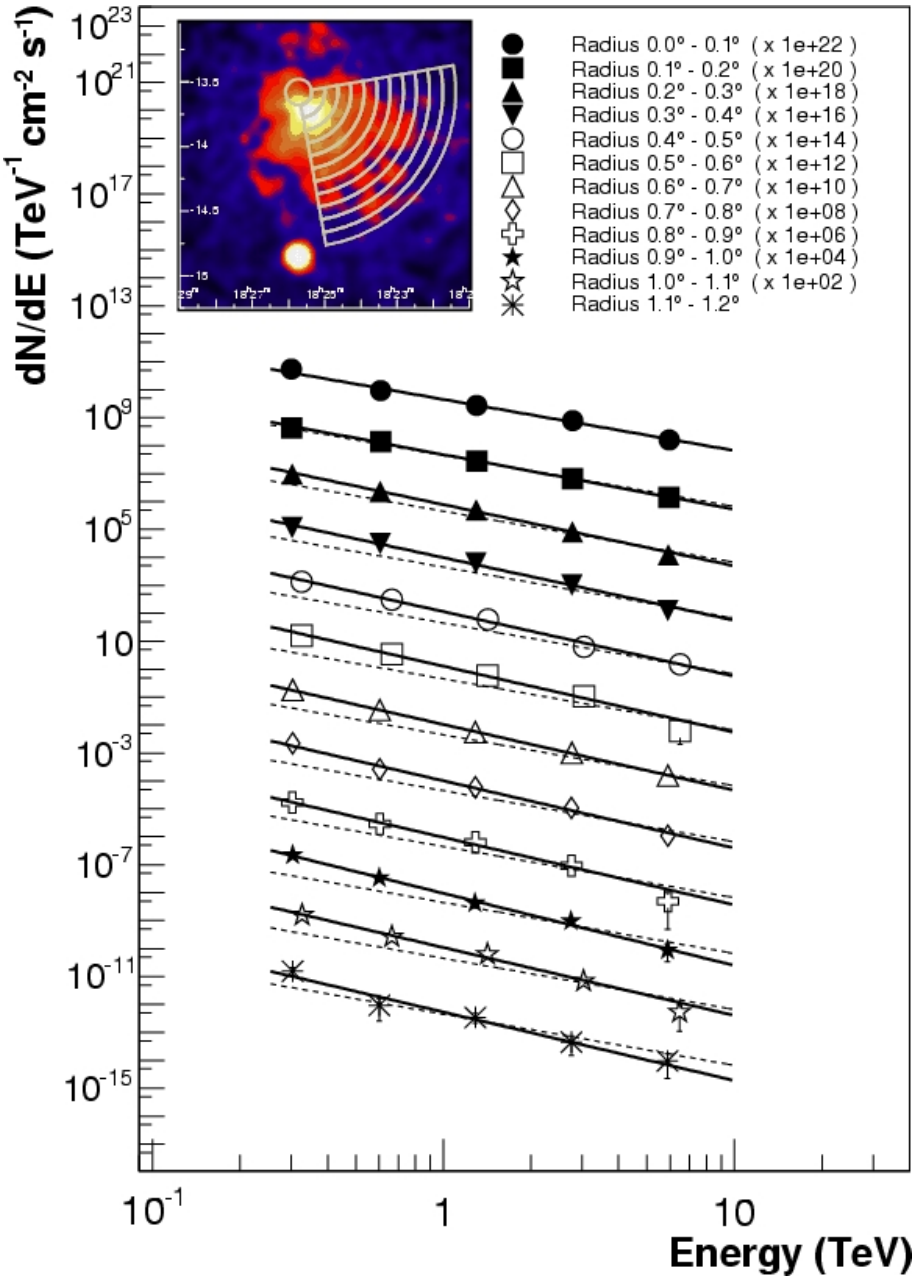

Figure 3.4.: HESS J1825–137: Spectra and the corresponding best fitting power law for radial bins [A$^+$06b]. In the inset in the upper left corner the arrangement of the extraction regions, so called wedges, is shown. The innermost wedge is a circular region with a radius of 0.1° centred on the pulsar, the other wedges are ring segments with an opening angle of 90° and a radial thickness of 0.1°. The energy range was restricted to energies between 0.25 TeV and 10 TeV. The spectrum of each wedge was fitted with a power law. For reasons of presentation the data as well as the the corresponding best fitting power laws have been scaled with powers of 10, so that adjacent wedges differ by a factor of 100. For all wedges the spectrum of the innermost wedge (dashed line) is shown for comparison.

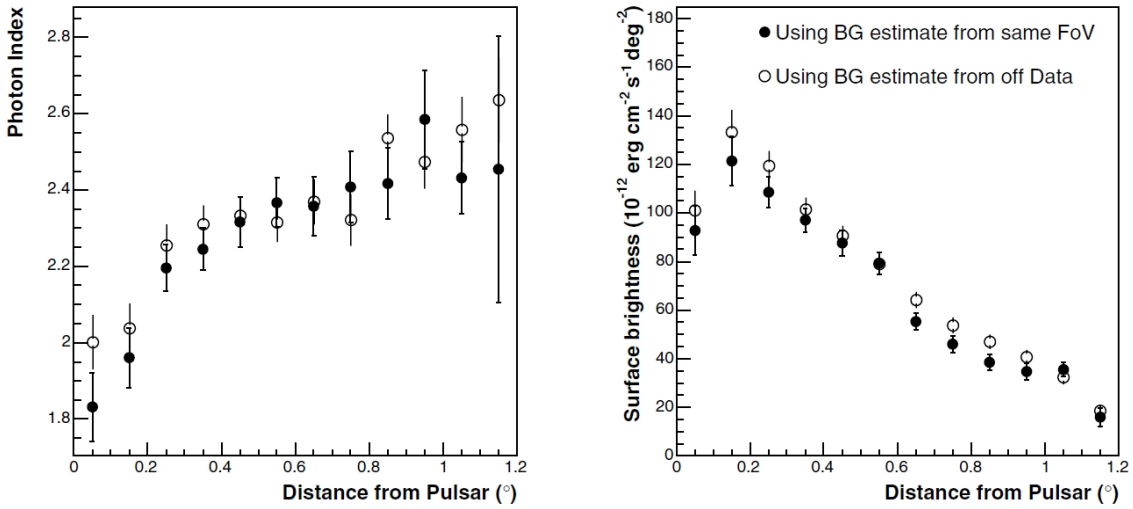

(a) Photon indices

(b) Surface brightnesses

Figure 3.5.: HESS J1825–137: Spectral photon indices (a) and surface brightnesses (b) as function of the distance to the pulsar [A$^+$06b]. Two series of measurements are shown that correspond to different background estimates. In the analysis represented by the filled black circles the background was assessed from a source-free region in the field of view of the respective observation, while the open circles have been calculated on the basis of background estimates from dedicated off-runs.

PSR J1826–1334. Moreover, Aharonian et al. used the different cooling times to derive an estimate for the expected γ-ray efficiency. In doing so they were able to show that the observed γ-ray efficiency can not be explained by the present spin-down luminosity of the pulsar, but that a higher luminosity in the past is needed. Additionally, Aharonian et al. pointed out that besides the radiation losses the transport mechanisms play a very important role. To illustrate this point they presented some examples, which were based on the assumption of spherical symmetry. In their first two example the propagation was governed by convection. As a start Aharonian et al. showed that assuming a constant radial velocity, it was easy to account for a particle volume density $\propto 1/r^2$ and a corresponding surface brightness $\propto 1/\theta$, c.f. Fig. 3.5. However, in this scenario the conservation of energy requires that the magnetic field decreases with increasing distance to the pulsar and therefore a full treatment of the calculation of the energy losses is rather complicated and was beyond the scope of the presented studies. Instead as an alternative scenario in the second example the velocity profile was approximated by $v(r) \propto 1/r$. In this case the surface density of the particles as well as the magnetic field in the PWN are assumed to be constant and Aharonian et al. showed that the steepening of the spectrum could exclusively be ascribed to the radiation losses. Subsequently, Aharonian et al. also examined particle propagation due to diffusion with a diffusion coefficient $D(E) = D_0(E/E_0)^\delta$. When the cooling times of the radiation processes are small in comparison to the age of the pulsar, the source radius is proportional to $E^{(\delta-1)/2}$. While for $\delta = 0$ the radius is proportional to $E^{-1/2}$, the radiation losses may even counterbalance the influence of the

energy-dependent diffusion in the case of $\delta = 1$. Finally, Aharonian et al. argued that one should also bear in mind that the injection spectrum of the particles may also vary with time. Considering the synchrotron limit (see Sec. 2.4.2), they suggested that especially at early times in the evolution of the PWN the magnetic fields may have been very high and therefore the maximum energy of the accelerated particles may have been lower than today.

3.2.2. Adjoining VHE γ-ray Sources

In the new analysis and modelling of HESS J1825–137 we will exclude two large sky regions as they are influenced by γ-ray sources in the close vicinity. In the following a short overview of these sources and their counterparts is given.

LS 5039

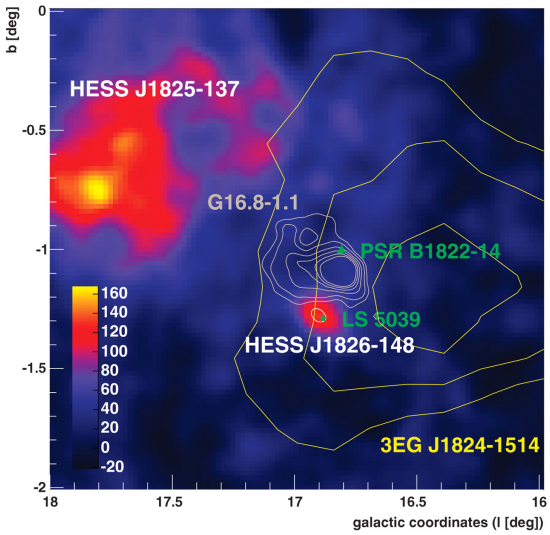

Figure 3.6.: Smoothed H.E.S.S. γ-ray excess map of the vicinity of LS 5039, taken from [A$^+$05e]. Note, that in the detection paper the VHE γ-ray source was initially called HESS J1826-148. The small white ellipse represents the 3σ confidence region of the H.E.S.S. source and the green star indicates the position of the radio source associated with LS 5039. While the association of the binary system and 3EG J1824–1514 is ambiguous, the spatial coincidence of the VHE γ-ray source and the radio source is compelling.

LS 5039 is a high-mass X-ray binary and was the very first binary system proven to emit photons at energies higher than $E \geq 0.1\,\mathrm{TeV}$ [A$^+$05e]. A short introduction into the processes responsible for the γ-ray emission in binary systems can be found in Sec. A.1. Before the detection by H.E.S.S. in 2004 LS 5039 had been detected in radio [MPR98] and X-ray [BR$^+$05] and its binary nature was already established. The system is located at a distance of $d \approx 2.5\,\mathrm{kpc}$ and consists of a compact object which orbits a O6.5V star with an orbital period of $\approx 3.9\,\mathrm{days}$ [C$^+$05]. 3EG J1824-1514 was suggested as possible counterpart

in the GeV range [P$^+$00]. H.E.S.S. observations of the vicinity of LS 5039 revealed a point-like source, denoted as HESS J1826-148, which is spatially coincident with LS 5039, see Fig. 3.6. The H.E.S.S. source is located at (R.A. = $18^h26^m15^s$, Dec. = $-14°49'30''$) and an upper limit on the extent is given as $50''$ [A$^+$05e]. The binary nature of HESS J1826-148 was proven beyond doubt by the detection of flux and spectra modulations in the VHE data, which are in agreement with the orbital period of 3.9 days [A$^+$06a].

HESS J1826–131

Right from the start a possible connection between the TeV emission of HESS J1825–137 and the EGRET source 3EG J1826–1302 (also called GeV J1825–1310[7]) was examined, e.g. Fig. 3.3. The EGRET source is located in the north of PSR J1826–1334 at (R.A. = 276.55°, Dec. = −13.04°) and the radius of the circle which encompasses the same solid angle as the 95 % EGRET contour is given by $\theta_{95} = 0.46°$ [H$^+$99]. According to the catalogue the spectrum of 3EG J1826–1302 is well described by a hard power law with a photon index of 2.0 ± 0.11 and shows no indication of a cut-off. A first search for pulsed emission had no positive outcome [N$^+$96]. However, using an enhanced analysis method evidence of variability emerged [N$^+$03]. Therefore, it was suggested that 3EG J1826–1302 belongs to the class of PWNe, as for these systems a variable signal from the pulsar was expected. Since PSR J1826–1334 is located close to GeV J1825–1310, see Fig. 3.7, the radio pulsar was suggested as plausible counterpart already at an early stage [Fie95]. The association was supported by the work of Zhang and Cheng, who modelled the fraction of the spin-down power of PSR J1826–1334 that should be observable in γ rays and who showed that their predictions agreed well with the measured EGRET data [ZC98].

However, in 2001 ASCA observations of GeV J1825–1310 revealed a so far unknown extended X-ray source, AX J1826.1–1300, at (R.A. = 276.5204°, Dec. = −12.9967°) [RRK01]. Figure 3.7 shows the 2–10 keV ASCA Gas Imaging Spectrometer image of these ASCA observations and the new source, which is denoted as “Nebula”and encompasses two subpeaks, is located almost in the centre of the image. In addition, also the contours of the 68 %, 95 %, 99 % confidence regions for GeV J1825–1310, as calculated by [RRK01], are depicted in the figure. Due to this representation it is visible that the new source is located much closer to the centre of GeV J1825-1310 than PSR J1826-1334, which is only located at the outer edge of the 99 % confidence region. Consequently, new scenario were developed which tried to establish a link between GeV J1825-1310 and AX J1826.1–1300. In doing so, hints for time variability of the ASCA source were again taken as evidence for a PWN scenario. By means of a Chandra observation with 15 ks exposure taken in 2003 the inner part of GeV J1825–1310 was resolved in more detail [R$^+$07]. Figure 3.8(a) displays the Chandra 2–6.5 keV image with the ASCA contours overlaid in blue. The ASCA nebula was split into a southern part ascribed to a stellar cluster and a northern part containing a point-like source embedded in a $4'$ trail of hard X-ray emission. Due to the difficulties in the detection as well as in the discrimination from the surroundings the

[7] In the following sometimes the source identifier GeV J1825–1310 will be used instead of 3EG J1826–1302. In principle both terms denote the same EGRET source, but GeV J1825–1310 was detected in EGRET data with a higher energy threshold of 1 GeV [LM97].

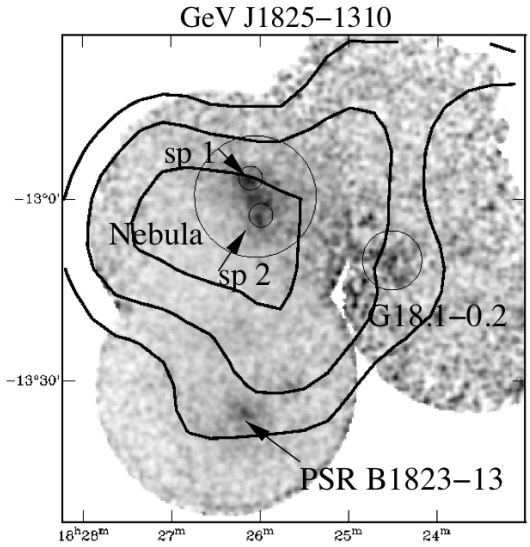

Figure 3.7.: ASCA sky map of GeV J1825–1310, taken from [RRK01]. Three ASCA sources are visible: the pulsar PSR J1826–1334, formerly known as PSR B1823-13, the supernova remnant G 18.1-0.2 and the newly discovered "Nebula", which encompasses two subpeaks ("sp 1" and "sp 2"). In addition, the contours represent the 68 %, 95 %, 99 % confidence regions for GeV J1825–1310, while the circles indicate spectrum extraction regions.

authors called this new nebula the Eel Nebula.

At the time of the publication of the Chandra results, the H.E.S.S. Collaboration had just firmly established the association of HESS J1825–137 and PSR J1826-1334 [A$^+$06b]. One of the prevailing explanations for the asymmetry of the TeV emission at that time was that the pulsar itself was moving in northern direction. However, under this assumption it is difficult to explain the northern part of the TeV emission, see Fig. 3.3. Therefore, the authors of the Chandra publication suggested for the first time that the emission in the northern part of HESS J1825-137 is indeed a separate source, denoted as HESS J1826–131, which is associated with the Eel Nebula instead of PSR J1826-1334. This scenario was further strengthened by the detection of 1FGL J1826.1–1256 at (R.A. = 276.5354°, Dec. = −12.9434°) by the Fermi satellite in 2009 [Rob09]. The key discovery was that in good agreement with the Fermi source a new γ-ray pulsar, PSR J1826–1256, could be established in a blind frequency search [A$^+$09a]. PSR J1826–1256 thus belongs to the still very limited class of radio-quiet γ-ray pulsars. For these pulsars it is assumed that their narrow radio beam does not cross the line of sight towards the Earth, whereas the γ-ray beam is wider and is therefore more likely to be detected [W$^+$09]. Applying a time-differencing technique a rotation frequency of 9.07 Hz (equivalent to a period of 0.11 s) and a frequency derivative of $-10.0 \times 10^{-12}\,\mathrm{Hz\,s^{-1}}$ were detected for PSR J1826–1256. These values correspond to a spin-down age of 14.4 kyr and $\dot{E} = 3.6 \times 10^{36}$ erg s^{-1}. In 2011 an improved timing analysis allowed to determine the position of PSR J1826–1256 with an accuracy of 1″ as R.A. = 276.5355° and Dec. = −12.9425° [R$^+$11]. This position is consistent with the Eel Nebula and in particular with the ASCA point-like source AX J1826.1–1257 (R.A. = 276.5341°, Dec. = −12.9461°), depicted as "sp 1" in Fig. 3.7.

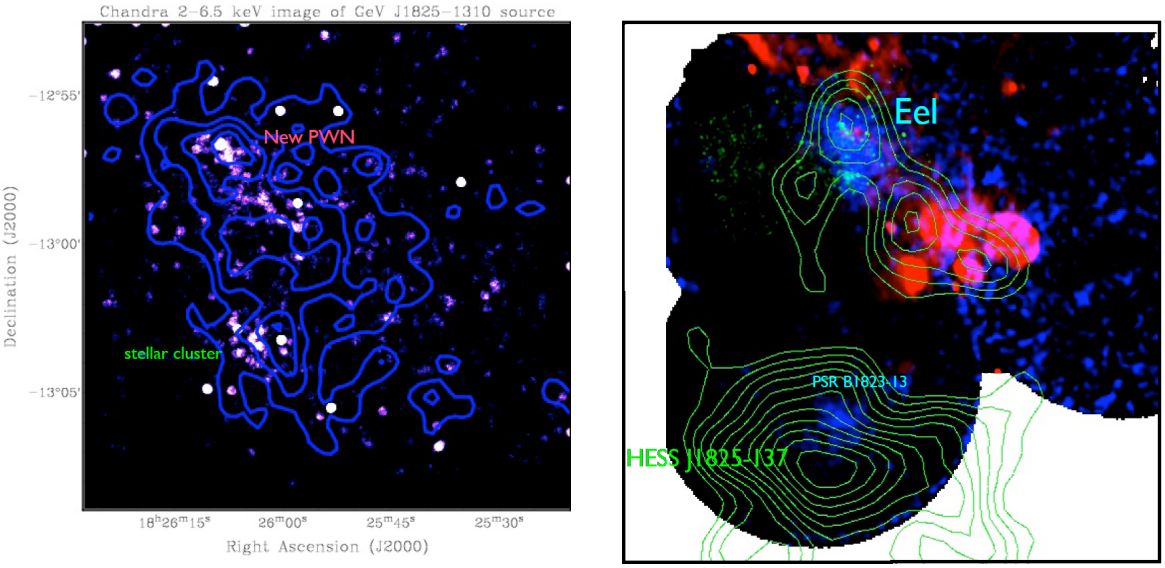

(a) Chandra sky map of GeV J1825–1310 (b) ASCA sky map of GeV J1825–1310

Figure 3.8.: Multi-wavelength images of GeV J1825–1310. (a) Chandra 2–6.5 keV image of the central area of GeV J1825–1310 [Rob09]. The blue lines indicate the contours of AX J1826.1–1300. The southern part is associated with a stellar cluster, the northern part with the Fermi source PSR J1826–1256. (b) ASCA observations of GeV J1825–1310 [Rob09]. In addition to the ASCA data in dark blue and the Chandra data in cyan 20 cm VLA data are shown in red. The green lines represent contour lines of HESS J1825–137.

3.3. Vicinity of HESS J1825–137 at Lower Energies

The observed TeV emission is expected to depend on the physical environment. For instance, photon fields can locally enhance the emission of IC photons and molecular clouds can influence the expansion of the PWN. In hadronic scenarios the latter may also serve as target material and thus enhance the observed γ-ray emission.

Infrared and Radio

Searching for potential photon fields, Pavlov et al. analysed archival optical-NIR, IR and radio data, which covered the total emission region of HESS J1825–137 [PKB08]. Among them were Spitzer IRAC 8 µm, MIPS 24 µm from the GLIMPSE survey and NRAO VLA Sky Survey data. All in all, Pavlov et al. discovered three radio sources, of which only one could also be detected in IR. This bright source (IRAS 18231–1340) is located right in the middle between the pulsar position and the maximum of the TeV emission. The source is extended (4′) and exhibits a two-sided shell morphology. Pavlov et al. concluded that the observed emission is most likely caused by thermal emission of dust ($T \approx 30 - 50\,\mathrm{K}$) as well as by molecular / atomic clouds which are heated by radiation from young stars.

Molecular Clouds

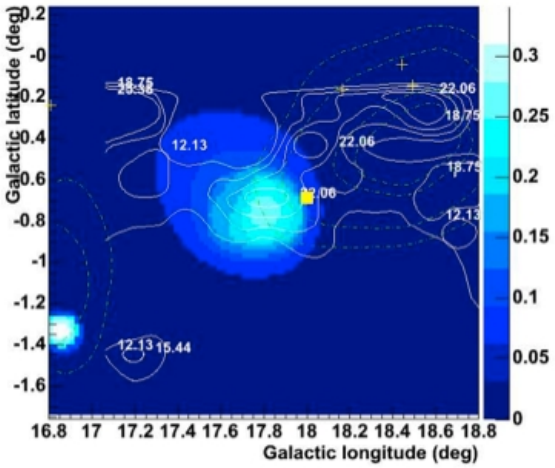

Figure 3.9.: Molecular clouds in the vicinity of HESS J1825-137, taken from [LTDA05]. The sky maps shows an excess map of HESS J1825-137, which was generated in 2005 by means of an alternative multi-scale analysis. While the TeV map became obsolete a long time ago, the white lines still indicate the location of molecular clouds, which may cause the asymmetric expansion of the PWN. The numbers represent the CO column intensity level in K km s^{-1} and the yellow square indicates the position of PSR J1826–1334.

Searching for counterparts of Galactic H.E.S.S. sources in CO and HI data, Lemiere et al. discovered a CO cloud in the northern part of HESS J1825–137 (in Ra / Dec coordinates) which could account for the asymmetric development of the PWN [LTDA05]. The analysed CO data were taken from the composite CO survey of the Milky Way conducted by Dame et al. [D$^+$01], which provides the carbon monoxide brightness temperature as a function of latitude, longitude and velocity. To identify possible CO counterparts of HESS J1825–137 Lemiere et al. first derived a velocity profile by summing up the CO cubes in longitude and latitude over the total extension of the H.E.S.S. source. In this velocity profile seven peaks fulfilled the predefined selection criterion that possible counterparts should exhibit an intensity higher than $1.5\,\mathrm{K\,deg^2}$. But only for one peak the distance estimate based on an empirical Galactic rotation curve model matched the estimated distance of 4 kpc to PSR J1826–1334. A Gaussian fit to this peak allowed to assess the velocity distribution of the molecular cloud: $\delta V = [45, 53]\,\mathrm{km/s}$, whereby δV is defined as the FWHM of the fitted Gaussian. Summing the CO cubes from the survey over δV Lemiere et al. also generated a map of the molecular cloud. The contour lines of this molecular cloud are overlaid on a now obsolete H.E.S.S. excess map of HESS J1825–137 in Fig. 3.9. Note, that the galactic longitude is plotted mirror-inverted in comparison with other plots in this thesis. The molecular cloud is located in the east of PSR J1826–1334 and Lemiere et al. suggested that it may cause the one-sided morphology of the PWN. Another point which supports the hypothesis that the detected molecular cloud is associated with HESS J1825-137 is the rather broad δV distribution which hints to an interaction of the cloud with the PWN.

3.4. Follow-up X-ray Observations

The promising discoveries in the X-ray and VHE γ-ray regime triggered several follow-up observations. Here we will briefly summarise the results of a Chandra observation of PSR J1826–1334 in 2002 which allowed to study the inner part of the X-ray nebula in detail and a Suzaku observation which enabled investigations of the X-ray PWN at even larger distances to the pulsar.

Chandra

Though ROSAT had revealed first signs of an X-ray signal from the neutron star itself, the XMM-Newton data did not confirm this observation. Instead, for the time being the XMM-Newton data did only allow to distinguish between a core component and a diffuse emission extended to the south-west of the pulsar. To better resolve the structures within the nebula, an X-ray telescope with a better angular resolution was required. This was provided by Chandra. In a 41 ks observation conducted in 2002, Pavlov et al. [PKB08] could resolve four different components within the nebula: the pulsar/neutron star, a compact nebula with distinct inner component and an extended asymmetric diffuse emission region. All four components are shown in Fig. 3.10. The highest brightness peak in the unprocessed ACIS-S3 image, see Fig. 3.10 top panels, agrees well with the position of PSR J1826–1334, considering the uncertainties on the measured position and the proper motion of the pulsar. The prominent peak is embedded in a compact nebula, the so called outer component, which becomes visible in the smoothed ACIS-S3 image, Fig. 3.10 top right. In agreement with the XMM-Newton observations this nebula is extended along the east-west direction, but the measured size, i.e. $25'' \times 10''$, is a little bit larger than the previously reported core region. Moreover, distinct structures can be distinguished within the compact nebula: there is the inner PWN component, which is centred on the pulsar and extends in northeast-southwest direction and there is an additional peak in the west of the pulsar, which might be connected with the inner component by a faint bridge. The diffuse emission region becomes visible when a larger field of view with increased pixel sizes and smoothing is considered, Fig. 3.10 bottom right. The diffuse component clearly extends to the south, but the true size can not be determined as the emission extends over the edge of the S3 chip.

Spectra have been extracted for the pulsar, the compact and the extended nebula. The respective extraction regions are shown in the bottom images of Fig. 3.10. The spectrum extraction region of the pulsar corresponds to a tiny circle with a radius of $\simeq 0.49''$, which is indicated in the figure by a black circle. Since the pulsar is located on an emission plateau formed by the compact nebula, the background spectrum was estimated from a directly adjoining annulus ($0.74'' < r < 1.5''$). The spectrum of the compact nebula was derived from the region indicated by the white ellipse and the corresponding background from an adjacent annulus in the diffuse emission region. Finally, the spectrum extraction region for the extended nebula was limited by the edge of the S3 chip and is therefore

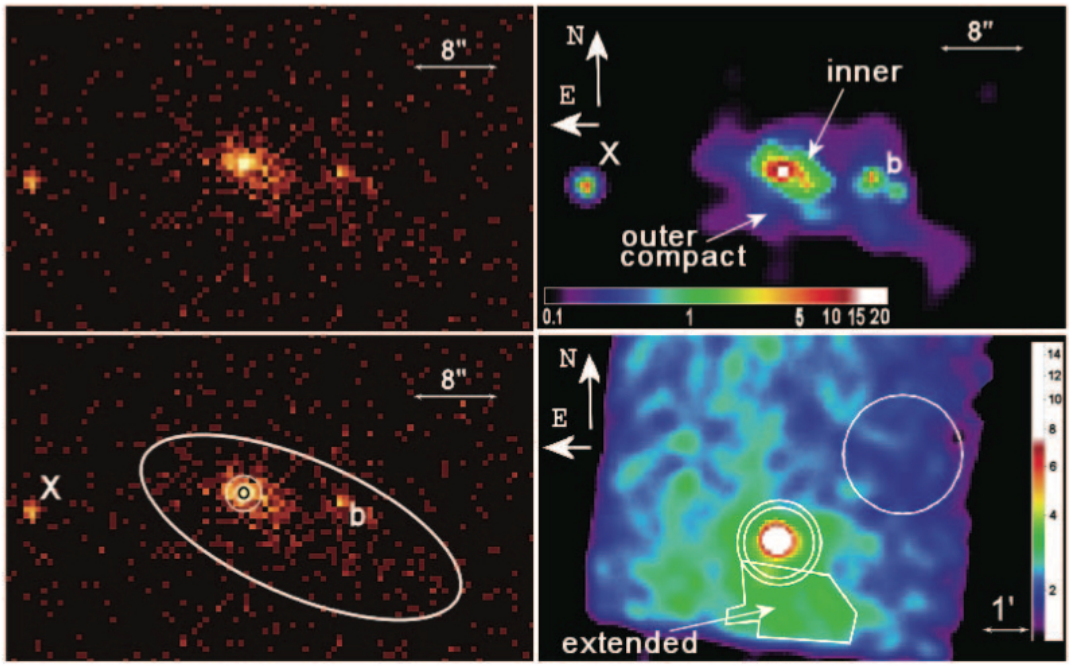

Figure 3.10.: Sky maps of the Chandra observation of PSR B1823–13, taken from [PKB08]. All subfigures show parts of the ACIS-S3 field of view, but are processed differently. Top left: Unprocessed $77'' \times 48''$ image with a pixel size of $0.49''$ containing events with energies between 0.7 and 7 keV. Top right: The same image as before, but adaptively smoothed and processed using a subpixel-resolution tool. Bottom left: Again the unprocessed image, but with overlaid contours indicating the spectrum extraction regions of the pulsar and the compact PWN. Bottom right: Enlarged image section with pixel size $3.94''$ containing events with energies between 0.5 and 8.0 keV. The colour scale and the smoothing of the image with a Gaussian kernel of $r = 27''$ were adapted such that the diffuse emission region in the south is emphasised. The white contours indicate the extraction regions for the diffuse emission, as well as the background region (i.e. the annulus) for the spectrum determination of the compact PWN.

determined from a polygon shape. The background was determined from the few source free regions on the S3 chip and is indicated by a white circle. By default, X-ray spectra are fitted by models which include the column density n_{H} as a free parameter to account for the absorption within the interstellar medium. However, it is not expected that the column density varies significantly for the spectra considered here. Therefore, Pavlov et al. first determined a reasonable value of the column density ($n_{\mathrm{H}} = 1.0 \cdot 10^{22}$ cm^{-2}, see [PKB08] for details) and fixed this parameter for all upcoming fits. In doing so the following values were obtained for the $0.5 - 8$ keV energy range and for a distance of 4 kpc: The spectrum of the pulsar is well fitted by a power law with index $\Gamma_{\mathrm{PSR}} = 2.4$ and corresponding luminosity $L_{\mathrm{PSR}} \approx 8 \cdot 10^{31}\,\mathrm{erg\,s^{-1}}$. In general, it is expected that the spectrum of the pulsar is composed of a thermal component from the surface of the neutron star and a non-thermal component from the magnetosphere of the pulsar. However, due to the low statistics and the high absorption within this observation, it was not possible to distinguish these two components. While the compact nebula was best described by a power law with

an index of $\Gamma_{\mathrm{comp}} = 1.3$ and a luminosity $L_{\mathrm{comp}} \approx 3 \cdot 10^{32}$ erg s^{-1}, the power-law fit to the spectrum of the extended nebula resulted in $\Gamma_{\mathrm{ext}} = 1.9$ and $L_{\mathrm{ext}} \approx 10^{33} - 10^{34}$ erg s^{-1}. This measurement confirms the relationship between the inner and outer nebulae, that had already been observed in the XMM-Newton data: $\Gamma_{\mathrm{ext}} - \Gamma_{\mathrm{comp}} \approx 0.5$.

Pavlov et al. [PKB08] interpreted the segmentation of the PWN into the extended and the compact emission region as a relic PWN and a newly formed nebula. In this context they explained the east-west elongation of the compact PWN as a result of the proper motion of the pulsar and the fuzziness of the outer compact region was ascribed to instabilities in the contact discontinuity surface. Moreover, the inner region of the compact PWN was attributed to the shocked pulsar wind immediately beyond the termination shock. Though this image seemed to be convincing, there were several aspects which it could not explain. For instance, there was no bow shock or tail which would have been expected along the direction of motion. Instead the inner component of the compact nebula extended almost perpendicular to the direction of motion of the pulsar. In addition, also the extended nebula was displaced to the south of the pulsar and not to the west, as expected. Pavlov et al. argued that the observed dislocation could be ascribed to the earlier mentioned asymmetry of the reverse shock, but optionally also to a strong north wind or to an anisotropic large-scale magnetic field. To be able to clarify these complex issues Pavlov et al. suggested deeper high-resolution X-ray observations as well as enhanced modelling of anisotropic magnetised PWNe of fast-moving pulsars.

Suzaku

While Chandra was well suited to study the details of the nebula, the true extent of the X-ray emission remained an unresolved question. In 2006 observations with the X-ray telescope Suzaku with a field of view of $18' \times 18'$ and an angular resolution of $\sim 2'$ finally contributed to the resolution of this question [U$^+$09]. In order to make use of the total field of view two observations (of about 50 ks) were scheduled: one centred on the maximum of the VHE emission and one targeted on a source-free field in the close vicinity that was used for background estimates.

In Fig. 3.11 the smoothed count maps of the source observation in the energy bands 1–3 keV and 3–9 keV are presented. By splitting the data with respect to the two energy bands, it is possible to study the spatial distribution of the lower and higher energetic photons separately. While the maximum emission is located at the position of the pulsar in both energy bands, it is clearly visible that the more energetic photons are located closer to the pulsar than the lower energetic photons which are more evenly spread over the field of view. To determine the extent of the X-ray emission a radial profile was derived from the full data set, see [U$^+$09]. Following the approach of the H.E.S.S. analysis the extraction region of the profile (indicated by the green lines in Fig. 3.11) was centred on the position of PSR J1826–1334 and covered the full field of view. Five additional X-ray point sources (2XMM J182557.9–134755, 2XMM J182620.9–134426, 2XMM J182617.1–134111, 2XMM J182629.5–133648 and a newly discovered source at (R.A. = $18^{\mathrm{h}}26^{\mathrm{m}}12^{\mathrm{s}}$, Dec. =

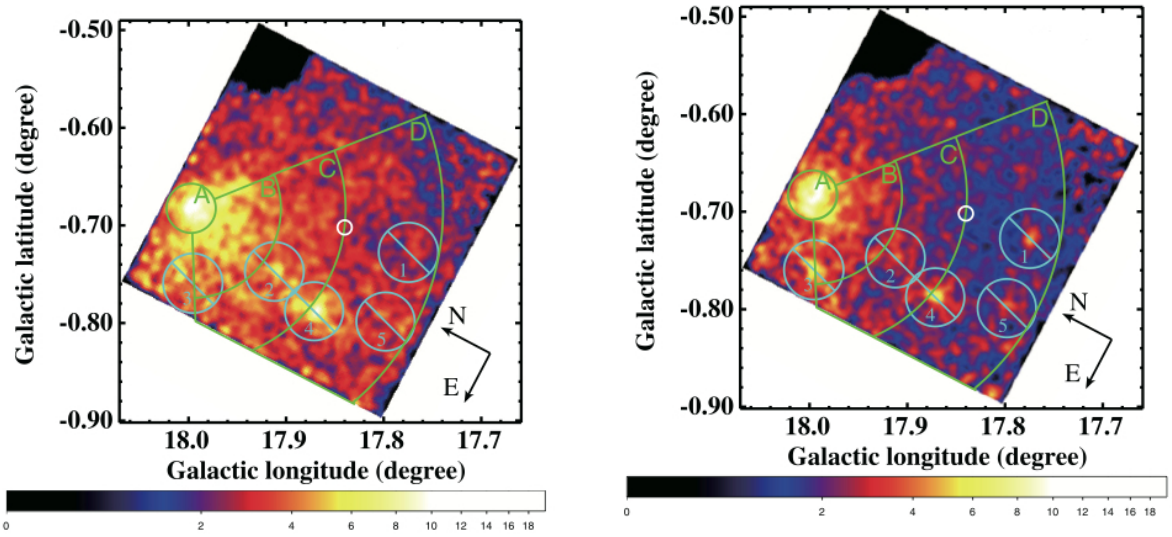

(a) Energy range 1–3 keV

(b) Energy range 3–9 keV

Figure 3.11.: Smoothed count maps ($\sigma = 0.2'$) of the Suzaku observation of HESS J1825–137 in the 1–3 keV and 3–9 keV range, respectively. The images are taken from [U+09]. The observation is centred on the peak of the VHE emission, indicated by the white circle. Spectra have been extracted for four regions (A–D), which are depicted by green lines. Five additional point sources were excluded from the analysis. The corresponding exclusion regions are represented in the image by the cyan circles.

$-13°48^m33^s$)) had to be excluded from this and all following investigations. The excluded regions are indicated in the figure by blue circles with radii of 1.8′. In comparison with the background observation the radial profile revealed an increased surface brightness up to the edge of the field of view, i.e. up to a distance of 15′ to the pulsar. Hence, G 18.0–0.7 belongs to the largest X-ray PWNe ever detected.

In the same way as in the H.E.S.S. analysis X-ray spectra have been determined for different radial bins in the Suzaku data (region A–D in Fig. 3.11). Again, the innermost region, a circle with radius 1.5′, was centred on the pulsar position. The region was chosen such that it corresponded to the core region observed in the XMM-Newton data. Likewise, the adjacent region B covered an area that is related to the diffuse emission region in the XMM-Newton data. Finally, the regions C and D sampled the remaining field of view and thus regions where spectra have never before been determined in the X-ray regime. All spectra were fitted with absorbed power laws and the best fit results are quoted in Tab. 3.2. The best fitting N_H was again in the order of $1.0 \times 10^{22}\,\mathrm{cm}^{-2}$. While the photon index of region A was $\Gamma \approx 1.7$, the spectrum steepened for region B, i.e. $\Gamma \approx 2.0$, and remained almost constant for regions C and D. At the same time the flux in the 0.8–10 keV range was in the order of $(1.3 \pm 0.1) \times 10^{-12}\,\mathrm{erg\,s}^{-1}\,\mathrm{cm}^{-2}$ for all considered regions.

The Suzaku spectra agreed well with the previous XMM-Newton observation: While the XMM-Newton data had unsheathed a steepening of the spectra with increasing distance

region	N_{H} ($\times 10^{22}\,\mathrm{cm}^{-2}$)	Γ	normalisation at 1 keV ($\times 10^{-4}\,\mathrm{keV}^{-1}\,\mathrm{s}^{-1}\,\mathrm{cm}^{-2}$)
A	$1.11^{+0.14}_{-0.15}$	$1.69^{+0.09}_{-0.07}$	$3.0^{+0.5}_{-0.5}$
B	$0.98^{+0.11}_{-0.12}$	$1.97^{+0.09}_{-0.09}$	$4.2^{+0.6}_{-0.6}$
C	$0.91^{+0.12}_{-0.11}$	$2.01^{+0.10}_{-0.10}$	$4.4^{+0.7}_{-0.7}$
D	$0.86^{+0.14}_{-0.15}$	$1.94^{+0.12}_{-0.08}$	$4.5^{+0.9}_{-0.8}$

Table 3.2.: Suzaku observations of HESS J1825–137: Results of absorbed power-law fits to the energy spectra of selected subregions (A–D, for definition see Fig. 3.11). Data taken from [U$^+$09].

to the pulsar from a spectral index of 1.6 to 2.3, Suzaku confirmed a steepening from 1.6 to 2.0. If one considers the errors on these measurements and the slightly different extraction regions, these differences are accommodated in the uncertainties. Region C and D are regions from which never before X-ray spectra had been extracted. In particular region C is a very special region as it covers the location of the peak γ-ray emission. Uchiyama et al. took advantage of this overlap and used the observation in X-rays and γ rays to derive an estimate of the magnetic field strength in this region: 7 µG. This value agreed well with the estimate by Gaensler et al. which had hinted at 10 µG. In the Suzaku publication Uchiyama et al. used the estimated magnetic field to draw conclusions on the strength of potential diffusion processes. Based on an X-ray source radius of 17 pc and a synchrotron live time of 1.9 kyr they concluded that the diffusion coefficient should be at least $D = 5 \times 10^{28}\,\mathrm{cm}^2\,\mathrm{s}^{-1}$. From this result they inferred that the η parameter in Eq. 2.25 should be approximately 80. Following the argumentation from de Jager et al. [dJDA09], this is only possible if the electrons diffuse parallel to magnetic field lines and not perpendicular.

The presented Suzaku observation was recently extended by four additional observations with the purpose of covering a larger area of the emission region of HESS J1825–137 [ER11]. Following the analysis procedure of Uchiyama et al. [U$^+$09] van Etten et al. [ER11] used the enlarged data set to extract X-ray spectra for sky regions similar to the wedge regions of the presented H.E.S.S. analysis. The definition of the new wedges was influenced by the fact that van Etten et al. used these wedges in a simultaneous simulation of the X-ray and VHE γ-ray emission of HESS J1825–137, see Sec. 3.6. Since van Etten et al. assumed a kind of rotational symmetry in their model and since they wanted to cover a larger part of the γ-ray emission region of HESS J1825–137, especially the region in the south-east of the pulsar, they enlarged the opening angle of the original wedges by 45°. The analysed X-ray wedges correspond to the three innermost newly defined wedge regions. However, the Suzaku field of view did not completely cover the outer two modified wedge regions and there were also additional regions which had to be excluded from the analysis due to contamination by point sources. Consequently, van Etten et al. determined the X-ray spectra from the available data, fitted them with absorbed power-laws, and scaled the results such that the missing detection area was compensated. The results of this procedure are quoted in Tab. 3.3.

region	N_{H} ($\times 10^{22}\,\mathrm{cm}^{-2}$)	Γ	unabs. 1–8 keV fluxes $10^{-12}\,\mathrm{erg\,cm^{-2}\,s^{-1}}$
wedge* 0	$1.26^{+0.06}_{-0.06}$	$1.93^{+0.05}_{-0.05}$	$4.90^{+0.34}_{-0.32}$
wedge* 1	1.3 (fixed)	$2.17^{+0.05}_{-0.05}$	$3.18^{+0.15}_{-0.15}$
wedge* 2	1.3 (fixed)	$1.78^{+0.18}_{-0.18}$	$1.04^{+0.22}_{-0.19}$

Table 3.3.: Enlarged Suzaku observations of HESS J1825–137: Results of absorbed power-law fits to the energy spectra of modified wedge subregions. Data taken from [ER11]. See text for definition of regions.

3.5. Follow-up Observation with Fermi-LAT

With the launch of the Fermi observatory in 2008 the energy range between X-rays and VHE γ rays, i.e. energies between 1 and 100 GeV, could finally be probed with an adequate sensitivity. Since HESS J1825–137 is located close to the Galactic Plane, a region that in the studied energy range is strongly dominated by the diffuse galactic emission, and as it is a very extended source, the data of the Fermi-Large Area Telescope (Fermi-LAT) required a careful analysis. But finally, after 20 months of data taking, Grondin et al. could announce the detection of HESS J1825–137 [G$^+$11]. In their analysis Grondin et al. performed a detailed search for a pulsed signal from the pulsar itself. For this purpose they determined the ephemeris from the radio data and subsequently phase-folded the Fermi data, which had been extracted in accordance to the energy-dependent Fermi point spread function from regions centred on the radio pulsar position. The folded data were evaluated by means of the H-test, but did not reveal a significant pulsation.

A very first impression of the morphology of HESS J1825–137 is given in Fig. 3.12(a). This image shows the smoothed count map above 10 GeV. The field of view is rather crowded, comprising several Fermi sources and the galactic diffuse emission along the Galactic Plane. To get a better idea of the true morphology of HESS J1825–137 in GeV all additional γ-ray sources were included in a background model and the corresponding test statistic (TS) map was calculated, see Fig. 3.12(b). For each pixel in the TS map it was evaluated how well the data are described by a point source assumption in contrast to the background model. By means of the TS map a familiar picture emerged: The GeV emission region is extended with a predominant direction along the south-west axis and the maximum emission is located offset from PSR J1826–1334. In comparison to the observed TeV emission the size of the emission region is smaller. In this context, however, one should note that the angular resolution of Fermi Lat is only in the order of $\approx 0.6^\circ$ and thus worse than the H.E.S.S. resolution. To better quantify the GeV morphology Grondin et al. fitted different source morphologies to the data. The authors considered a point source model, a Gaussian and a uniform disk model and a model template that was derived from the observed TeV morphology. In the fitting process two different algorithms were compared, which yielded consistent results: All extended source models described the data much better than the point source model. The best fitting Gaussian model

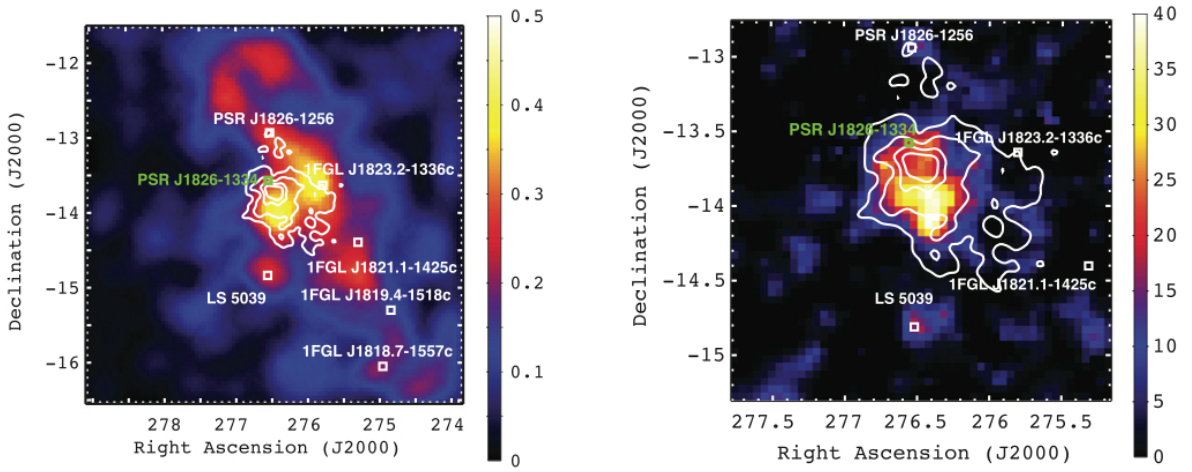

(a) Fermi Lat count map

(b) Fermi Lat TS map

Figure 3.12.: Fermi-LAT observation of HESS J1825–137, taken from [G$^+$11]. (a) Count map above 10 GeV, which has been smoothed with a Gaussian of $\sigma = 0.35°$. The positions of 1FGL sources are marked with white squares. Moreover, the contours of HESS J1825–137 are depicted by white solid lines and the position of PSR J1826–1334 is indicated by a green square. (b) Zoomed section of the corresponding Fermi-LAT TS map. Combining the known Fermi sources and a model for the diffuse emission in the overall background model, the test statistic (TS) values have been determined assuming point sources at the centre of each pixel.

(centre at $l = 17.57°$, $b = -0.43°$, $\sigma = 0.56° \pm 0.07°$) for instance had a significance of $8.6\,\sigma$. The template derived from the H.E.S.S. data matched the Fermi data better than the point source model, but fell back behind the Gaussian and uniform disk models. As Grondin et al. concluded this is not unexpected as the TeV observations had revealed a morphology that strongly depends on the considered energy.

The spectrum of HESS J1825–137 in the 1–100 GeV range was determined under the assumption that the true spatial shape was given by the best fitting Gaussian model. Using a maximum-likelihood approach the spectral data were reproduced best by a power law with a spectral index of $1.38 \pm 0.12_{\mathrm{stat}} \pm 0.16_{\mathrm{sys}}$ and an integrated flux of $(6.50 \pm 0.21_{\mathrm{stat}} \pm 3.90_{\mathrm{sys}}) \times 10^{-9}\,\mathrm{cm}^{-2}\mathrm{s}^{-1}$ above 1 GeV. Grondin et al. demonstrated that the quoted systematic uncertainties account for the uncertainties in the assessments of the diffuse emission, the true morphology and the effective area and energy dispersion.

In the discussion of their results Grondin et al. investigated how well the Fermi data can be described by a time-dependent one-zone SED model. The applied model was based on a model first presented by Abdo et al. [A$^+$10]. In this one-zone model spatial dependencies, e.g. transportation mechanisms, were generally neglected. Instead, the final SED was calculated from a multitude of electron populations that had been injected in the PWN at different lifetimes of the pulsar. For the spectral shape of the particle injection spectrum two different assumptions were studied: a power law with an exponential cut-off and a relativistic Maxwellian plus power-law tail. The normalisation of the electron spectrum was assumed to evolve analogously to the spin-down of the pulsar. For the

radius of the source default assumptions for PWNe ($R \propto t$ in the free expansion phase and $R \propto t^{0.3}$ in the Sedov phase) were applied. Moreover, it was assumed that the time-dependence of the magnetic field is given by Eq. 2.22. The energy losses per time-step comprised radiation losses and adiabatic losses. Finally, the observable SED was modelled by synchrotron and IC emission, considering IC scattering off CMB, dust and starlight photons. Due to large covariances between some of the parameters of the model Grondin et al. had to fix several parameters, e.g. the initial spin period (10 ms) and the braking index (2.5). In doing so they ended up with three free parameters for the exponential power-law assumption and four for the relativistic Maxwellian. The comparison of the prediction of the model with the SEDs from H.E.S.S. and Fermi, as well as with an estimation of the one-zone Suzaku SED, revealed the following best fitting parameters: A present-day magnetic field of 4 µG, a power-law index of 1.9 and a cut-off at 57 TeV in the case of the power-law particle spectrum and a magnetic field of 3 µG, $kT = 0.14$ TeV, power-law index of 2.3 and a cut-off at 150 TeV for the Maxwellian electron spectrum.

3.6. Review of the Modelling Status

The models which have been presented previously were one zone models, i.e. they did not consider spatial dependencies. However, such spatial dependencies clearly exist for HESS J1825–137 and they actually are the reason why HESS J1825–137 is such an interesting source. Therefore, we will later present a model which tries to reproduce the peculiar spectral and spatial features of HESS J1825–137 at the same time. However, since HESS J1825–137 is a prime target for this kind of studies it has attracted the interest of other groups, as well. Indeed, Adam van Etten and Roger W. Romani have recently published an elaborate simulation for HESS J1825–137, see [ER11]. In view of the many degrees of freedom, it is not surprising that van Etten et al. have chosen a different approach than the one we will present later. For comparison, an overview of their simulation is given in this section.

The central assumption of the van Etten model was that the PWN was perceived as a series of expanding shell-like bubbles, moving away from the pulsar. In doing so, it was assumed that the pulsar is stationary. All in all, twelve 3-dimensional shells were considered, whose present-day shape was chosen to mimic the wedges of the H.E.S.S. publication, e.g. the thickness of the shells was equal to 0.1°. However, since van Etten et al. argued that the H.E.S.S. wedges did not cover the total VHE emission region they enlarged the original wedges by 45° to the south-west. The corresponding 3-dimensional shells were generated by rotating the modified wedges around their bisector, i.e. the assumed symmetry axis of the VHE emission. Note that, in order to calculate spectra for the modified wedges, van Etten et al. had to calculate projections of the shells, i.e. several shells contributed to the detected emission of an individual wedge.

In the model of van Etten et al. it was assumed that all electrons emitted by the pulsar within a specific time interval were predominantly contained in one of the expanding shells. Since the final shape of the shell was predefined, the respective time intervals depended

on the propagation velocity of the shells. To obtain a constant velocity expansion of the PWN as a whole, van Etten et al. suggested the following velocity profile:

$$v(r,t) = v_{\mathrm{outer}} \left(\frac{r}{R_{\mathrm{outer}}} \right)^{\alpha} \left(\frac{t}{T} \right)^{-\alpha}, \tag{3.1}$$

where R_{outer} is the present radius of the PWN, T its age and $v_{\mathrm{outer}} = R_{\mathrm{outer}}/T$. α is a free parameter of the model. The number of electrons expected to be injected into the PWN within a specific time interval was determined by the energy released by the pulsar, see Sec. 2.4.1, and the energy spectrum of the injected particles was presumed to be best described by a power law with an exponential cut-off. During the expansion of the shells a certain exchange of particles between adjacent shells was allowed. This exchange was ascribed to particle diffusion and the flux was approximated by

$$J_{\mathrm{i}}(E,t) = -D \, \frac{\partial n_{\mathrm{i}}(E,t)}{\partial R} \, \mathrm{cm}^{-2}\,\mathrm{s}^{-1} \tag{3.2}$$

For the cooling of the particles inverse Compton losses, synchrotron radiation and adiabatic energy losses were considered. The latter was approximated on the basis of the time-dependent total volume of the PWN. To assess the magnetic field strength within the PWN van Etten et al. first approximated the magnetic field strength at the termination shock ($B_{ts} = 400\,\mu\mathrm{G}$, the termination shock was assumed to be stationary: $r_{\mathrm{ts}} = 0.03\,\mathrm{pc}$) and derived an equation which relates the magnetic field strength to the distance to the pulsar and to the respective energy output of the pulsar:

$$B(r,t) = 400\,\mu\mathrm{G} \left(\frac{r}{0.03\,\mathrm{pc}} \right)^{\beta} \left(\frac{\dot{E}(t)}{2.8 \times 10^{36}\,\mathrm{erg\,s^{-1}}} \right). \tag{3.3}$$

Again, β is a free parameter of the model.

To obtain today's spatial and spectral distribution of the leptons in the PWN its evolution was considered as a series of time steps. At each time step the sizes and the mean magnetic field strengths of all already existing shells were determined. While for the innermost shell the amount of newly injected electrons was computed, for all other shells the contributions of diffusing leptons were considered. Subsequently, it was calculated how the energy losses within the respective time interval alter the obtained energy spectra and finally also the losses due to diffusion were taken into account. By repeating these steps until the pulsar reached its present age the final distributions of the electrons in each shell and thus also in each wedge were determined. The photon spectra for each modified wedge were computed considering inverse Compton emission as well as Synchrotron emission.

By means of their model van Etten et al. were able to simultaneously predict the VHE γ-ray spectra of all twelve modified wedges and the X-ray spectra for the three innermost wedges. The results of their simulation were compared to the published H.E.S.S. data presented in Sec. 3.2.1 and to previously unpublished Suzaku data, cf. end of Sec. 3.4. However, in both cases the available data did not cover the total area of the newly defined wedges: either data had only been published for subareas, or subregions had to be excluded

to avoid contributions from additional sources in the field of view. To circumvent this problem van Etten et al. used the following approximation: since their model was based on the assumption that the energy spectrum of the photons and also the fluxes do not change within an individual wedge, they extracted the spectra for the accessible regions and scaled them such that the missing areas were counterbalanced.

Searching for the parameters that described the observed data best, van Etten et al. proceeded step by step. Initially, they made rather simple approximations, e.g. an uniform expansion and a constant magnetic field, etc., and enhanced these approximations by additional features until the measured data were well reproduced. Finally, the best fitting parameter set was determined by means of a simplex minimisation (cf. Sec. 5.3 for details). This parameter set featured an initial rotation period of the pulsar of 13 ms, a braking index of 1.9 and an age of the pulsar of 40 kyr. Moreover, α took the value -0.5, and β the value -0.7. All in all, their studies showed that a rather high diffusion of high-energy particles was needed, which contradicted common assumptions of a toroidal magnetic field.

4. The H.E.S.S. View of HESS J1825–137

Having reviewed the published observations and modelling approaches for HESS J1825–137 in X-rays and γ rays in the previous chapter, we present now a new analysis of the increased H.E.S.S. data set. Since the modelling of the TeV data requires a profound understanding of the detection technique, this chapter is structured in the following way: At first a brief introduction into the detection of γ rays with imaging atmospheric Cherenkov telescopes is given. Subsequently the technical implementation as well as the data analysis chain of the H.E.S.S. experiment are presented in detail. Particular attention is given to the computation of sky maps and energy spectra for extended sources and the limitations, e.g. spatial and spectral resolution, that have to be considered. Finally, at the end of this chapter the new analysis of the H.E.S.S. data is presented which comprises twice the amount of data used in former publications.

4.1. Detection of VHE γ rays

Since γ rays are blocked by the Earth's atmosphere γ-ray astronomer, who directly detect γ rays, need balloons, rockets or satellites to lift the detectors above the atmosphere. These types of experiments are however limited with respect to their size and weight and hence their sensitivity, as γ-ray fluxes in the VHE range are rather small and therefore require a large collection area. To circumvent these limitations Blackett suggested in 1948 to detect γ rays indirectly through the Cherenkov light emitted in the Earth's atmosphere [Bla48]. In doing so the entire atmosphere could be used as a detector. With the advancement of technology the idea was taken up again in the 1980s and led to the first IACT, the Whipple telescope. Today there are four follow-up experiments: CANGAROO III, H.E.S.S., MAGIC and VERITAS. They are distributed evenly over the globe to allow a uniform exposure of the sky. The underlying technique will be explained in the following sections, which are revised excerpts from my diploma thesis, see [Bru07].

4.1.1. Particle Cascades and Cherenkov Radiation

Whenever a high-energy cosmic-ray nucleus or photon enters the atmosphere of the Earth, it starts a cascade of secondary particles, called air shower. With a photon or an electron as initial particle, a shower of electromagnetic nature is created. For atomic nuclei, which constitute the predominant cosmic radiation, interactions via the strong and the weak

force occur beside the electromagnetic ones and hadronic as well as electromagnetic subshowers evolve. In the case of photons the cascade starts when a photon with an energy higher than $2m_e c^2$ interacts with the electromagnetic field of a charged particle and an electron-positron pair is created via pair production. On their turn the two particles generate high energy photons via Bremsstrahlung and thus start sub-cascades of their own. This way the initial energy is dissipated until the mean energy of the particles drops below the critical energy ($E_c \approx 80\,\mathrm{MeV}$), at which the energy losses of electrons by ionisation of air molecules become dominant over those by Bremsstrahlung. From that moment on, no further particles are created. Accordingly, the point where the electrons reach the critical energy is referred to as the shower maximum.

The shower development can be described by a simple model [Hei54], see Fig. 4.1. It is assumed that after one radiation length (X_0) the incident photon produces an electron-positron pair whereat the energy is distributed equally between both particles. Moreover, it is expected that after passing a further radiation length each particle produces one Bremsstrahlung photon with exactly 50 % of its energy. Therefore, with each passage of X_0 the particle energy is halved and the number of particles doubles. As a result basic formulas for the number of particles (N) and the average particle energy (E) as functions of the atmospheric depth (X) can be derived: $N(X) = 2^{X/X_0}$ and $E(X) = E_0 \cdot 2^{-X/X_0}$, where E_0 is the energy of the primary photon. When the energy per particle reaches the critical energy the number of particles in the shower is $N_{\max} = E_0/E_c$ and the corresponding shower depth is given by $X_{\max} = X_0 \ln(E_0/E_c)/\ln 2$. Though being a rough estimate the model describes the real characteristics of electromagnetic air showers very well [Ber06]: the particle number is described by a power-law scenario, the maximum number of particles is proportional to the initial energy of the photon and the shower depth depends logarithmically on E_0. Realistically rendered is also the fact that the shower moves mainly straight ahead and shows only slight lateral spreading due to multiple scattering. For current research needing a more elaborate treatment of extensive air showers, Monte Carlo simulations are used [VB09, Ber08]. These simulations account for the multitude of involved physical processes, e.g. atmospheric interactions and emission processes, and provide a realistic and complete description of the air showers. In order to give a feeling for the magnitudes involved in electromagnetic air showers a few typical numbers shall be quoted here: The time scale on which an electromagnetic shower evolves is in the order of a few nanoseconds. The first reaction usually occurs ≈ 15–20 km above sea level and the shower maximum is reached at ≈ 8–12 km.

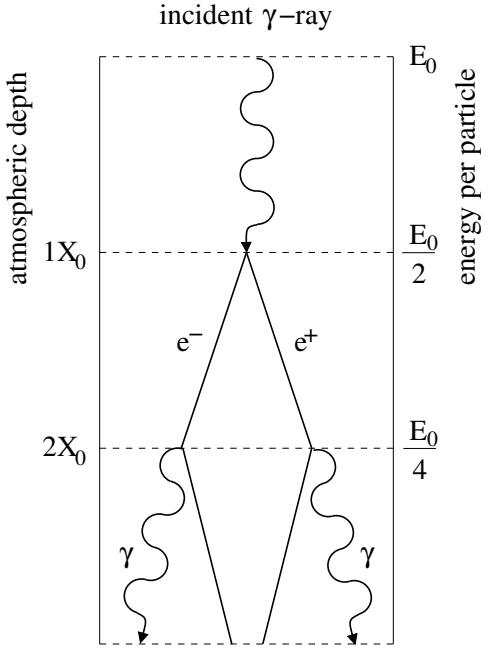

Figure 4.1.: Heitler model of an electromagnetic shower.

The essential point for the detection of VHE photons is that the highly energetic electrons and positrons of the air showers emit Cherenkov light. This ultraviolet / blue radiation is emitted whenever charged particles move through a medium with a velocity (v) higher than the local speed of light ($\frac{c}{n}$): $v \geq \frac{c}{n}$, where n denotes the refraction index of the medium. When charged particles pass through a medium they polarise nearby atoms and molecules which on their part emit photons in order to regain their equilibrium state. For particles moving with a velocity lower than the speed of light the generated photons interfere destructively and no radiation is detected. However, in the case that the particles move faster than the speed of light, the emitted light interferes non-destructively, forming a wave front that moves at a fixed angle with respect to the velocity vector, see Fig. 4.2.

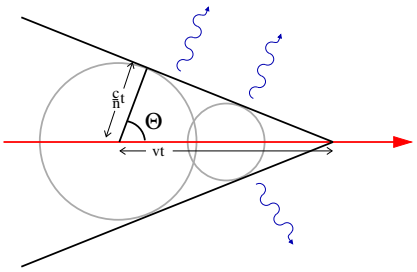

Figure 4.2.: Cherenkov radiation emitted by a particle moving faster than the local speed of light.

Based on Huygens' construction the opening angle satisfies the following condition $\cos(\theta) = c/(nv)$. A typical value for the cone angle in air is $\approx 1°$. As a result an electromagnetic shower illuminates on the ground an area with a diameter of $\approx 250\,\mathrm{m}$. The intensity of the Cherenkov light depends strongly on the number of shower particles and therefore on the energy of the primary photon. For a 1 TeV photon approximately 100 Cherenkov photons per m^2 reach the ground. This low intensity can only be detected by special instruments during dark, moonless nights. And even then it is difficult to distinguish it from the ambient night sky. The IACTs solve this problem by taking advantage of the fact, that the Cherenkov light flashes are only visible for a few nanoseconds.

One of the main challenges for the IACTs is that not only the electromagnetic showers induced by γ rays emit Cherenkov light, but also all other showers induced by constituents of the cosmic radiation (e.g. protons, nuclei or muons). As these showers are about 10 000 times more numerous than those generated by VHE photons, they provide a very strong background for the γ-ray detection. Serendipitously, the structure of the showers depends on the type of the initial particle and the respective interaction mechanism. The nuclei, for instance, undergo hadronic interactions which result in cascades of rather massive secondary particles (smashed atoms, pions, muons, etc.). As the secondary particles receive significantly more transverse momentum than the particles in electromagnetic showers, hadronic showers are considerably broader than electromagnetic ones. Fig. 4.3 contrasts an electromagnetic and a hadronic shower. Due to the different shapes the biggest part of the hadronic showers is rejected at a very early stage of the analysis. Nevertheless the indirect measurement of γ rays is a technique which stays background dominated and requires sophisticated methods to estimate the respective background level. These procedures will be presented in detail later in this chapter.

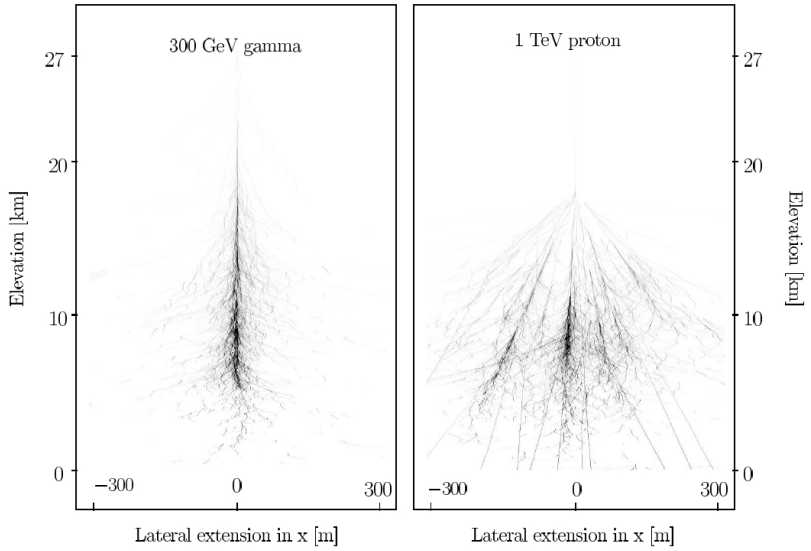

Figure 4.3.: Comparison of an electromagnetic and a hadronic shower as generated by Monte Carlo simulation [Ber06].

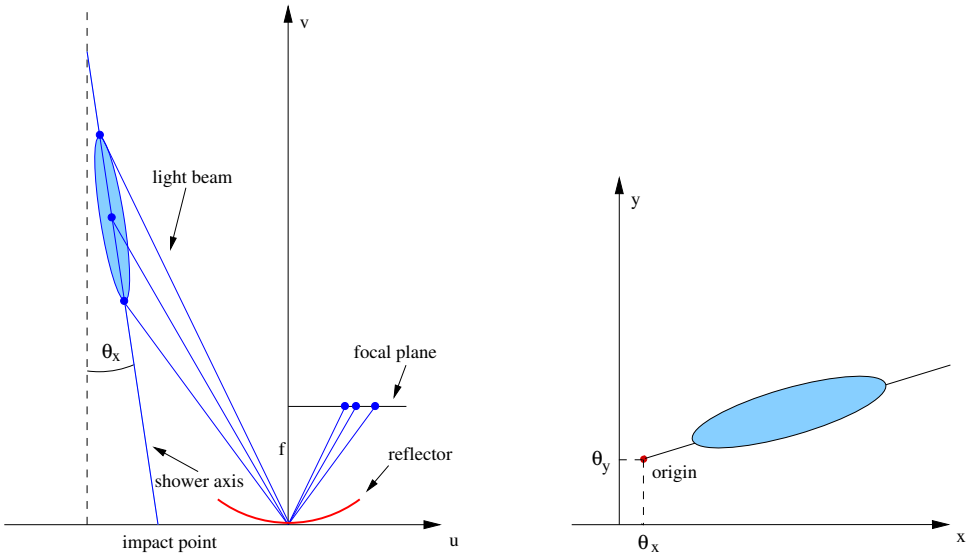

Figure 4.4.: Detection of air showers via their Cherenkov light. The schematic representation illustrates how the shower is mapped by the IACT and how the the corresponding camera image looks like.

4.1.2. The Imaging Atmospheric Cherenkov Technique

The imaging atmospheric Cherenkov technique (a current overview is given in [VB09]) takes advantage of the fact that the light emitted by the electromagnetic particle cascade illuminates an area with a diameter of about 250 m on the ground. A detector situated within the light pool can collect the incident photons and thus observe the air shower. As the air shower is detectable from any location within the light pool, the effective collection area of the Cherenkov telescope is given by the area of the light pool. This area is about $50.000\,\mathrm{m}^2$ and thus significantly larger than any detection area available in satellite experiments. Due to the low intensity of the Cherenkov light IACTs must have a light collecting area as large as possible. This is realised by large spherical or parabolic mirrors which reflect the Cherenkov light onto a camera in the focal plane. The main principle is illustrated in Fig. 4.4. On the left side a sketch of the shower and the imaging telescope is shown and on the right side the corresponding camera image is presented. It is interesting to note that the images of the air showers have a roughly ellipsoidal form. Indeed, in the early days of IACT γ-ray astronomy it was common practice to approximate the true shapes of the images by ellipsoids in the analysis procedures. This was justified as the information about the shower geometry can be attained very well from the elliptical approximated images: As the shower axis is mapped on the major axis of the ellipsoid, the image of the source (θ_x, θ_y) can be found along this line. The coordinates in the focal plane of the camera are thereby a measure for the inclination of the shower axis with respect to the system's pointing direction. Moreover, also the impact point of the shower on the ground can be assessed from the major axis of the ellipsoid. However, with the rapid progresses in computer technology it becames more and more common to keep the whole camera image for the shower reconstruction, omitting any approximation. Both approaches will be presented in detail in the next-but-one section.

Today's IACTs normally use the stereoscopic observation technique, whereby a shower is detected by at least two telescopes. This has several advantages. The most obvious is that stereoscopic reconstruction can be used for the determination of the shower geometry, as the shower is detected from different viewing directions. This improves the determination of the shower parameters, as the values from single telescope data are often imprecise and ambiguous (e.g. the source position). Another advantage is that the number of detected background events can be significantly reduced. While for a single telescope Cherenkov light emitted by local muons constitutes a large part of the background, these events are rejected in stereoscopic mode, as their Cherenkov light beam is rather small and hits only one telescope. Furthermore, the different viewing angles enhance the probability to identify background events, thus increasing the sensitivity and reducing the energy threshold.

4.2. The High Energy Stereoscopic System

The H.E.S.S. experiment is situated in the Khomas Highland in Namibia, a region almost perfect for star monitoring. From Namibia the Galactic Plane with its plenitude of γ-ray

candidates is very well observable and the good observation conditions, i.e. the absence of light pollution, the aridity and the many cloudless nights, are essential for the imaging atmospheric Cherenkov technique. The original design of the H.E.S.S. telescope system consisted of four imaging atmospheric Cherenkov telescopes mounted at the corners of a square with a side length of 120 m (Fig. 4.5). This design was developed to achieve best sensitivity in an energy range above 100 GeV, as several telescopes are located within a Cherenkov light pool, while the distances between the single telescopes is chosen as large as possible to obtain best stereoscopic viewing conditions as well as a large collection area. In this configuration the system has been in operation since December 2003. In order to extend the observable energy range to lower energies a fifth telescope with larger dimension was constructed at the centre of the original array (Fig. 4.5). The new telescope was inaugurated in September 2012, thus transforming H.E.S.S. phase 1 into H.E.S.S. phase 2. While the underlying technical principle is the same for all H.E.S.S. telescopes, in the following only the specifications of the small telescopes will be presented as this work was conducted in the framework of H.E.S.S. phase 1. In doing so, the following explanations are based on the corresponding section within my diploma thesis, cf. [Bru07].

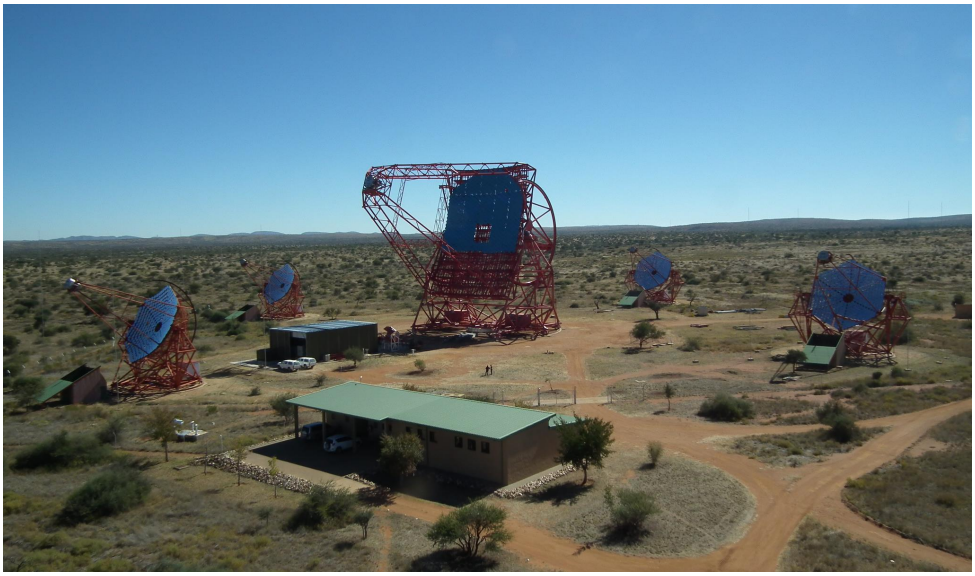

Figure 4.5.: Bird's eye view of the H.E.S.S. telescopes, state June 2012 (credit Frederick van Greunen, © H.E.S.S. Collaboration)

All telescopes consist of a large reflector which focuses the Cherenkov light onto a camera mounted in the focal plane (Fig. 4.6, left side). The reflector is composed of 382 round mirrors with a diameter of 60 cm and an initial reflectivity of 80–90 % (Fig. 4.6, middle). Each mirror can be aligned by a motorised mirror support structure. Altogether, the mirrors are arranged in a Davies-Cotton design, enabling good imaging even of off-axis events. The dish formed in this way has a diameter of 13 m and a focal length of 15 m. All in all it provides an effective mirror area of 107 m^2. As all the telescope use an alt-azimuth mount, it is possible to track any source from 0.0° to 89.9° elevation. The pointing precision achieved depends strongly on misalignments of the mirrors caused by wind or

gravity induced deformation in the telescope structure. For this reason the exact pointing of the telescopes is regularly verified by so called pointing runs, whereby the image of a bright star with well-known position is recorded by two CCD cameras mounted on the dish. While one of them directly observes the star, the other records the mapped image on the closed camera lid. By comparison of the two images the pointing errors can be detected. All in all the pointing error of the H.E.S.S. system is known to be smaller than $\approx 30''$. The description of the optical system at full length can be found in [B$^+$03, C$^+$03].

Figure 4.6.: Detailed view of one of the H.E.S.S. 1 telescopes [H.E12]. From left to right the images show the parked out telescope, a close-up view of the mirrors and the camera.

The reflected light is detected by a camera composed of 960 pixel which are arranged in a hexagonal shape (Fig. 4.6, right side). The light sensitive component of each pixel is a photomultiplier tube (PMT), which is equipped with a Winston cone light collector, that focuses the incident light on the active area of the PMT. Each pixel corresponds to a circular area with a diameter of 0.16° on the sky, leading to a total field of view of 5°. For the signal processing the PMTs are grouped in 60 drawers with associated acquisition and local trigger electronic cards. In the acquisition process the PMT signal is amplified in two channels: the high-gain channel and the low-gain channel. The high-gain channel with a linear response up to 150 photoelectrons (p.e.) is especially sensitive to single photoelectrons, while the low-gain channel covers the range up to 1600 p.e. Both signals are sampled at a rate of 1 GHz in Analogue Ring Samplers (ARSs), consisting of a ring buffer with 128 capacitor cells. Only when the trigger electronic of the camera indicates that a γ-like event has occurred are the data from the ARS further processed. Such a trigger is sent when at least 4 pixels within predefined camera sectors exceed within a time interval of 1.5 ns a threshold of 4 p.e. Having received a camera trigger, the sampling of the PMTs signals is stopped and all data that have been sampled in a time window of 16 ns around the time of the trigger generation are transmitted to an Analogue to Digital Converter, where the signals are transformed into charge equivalent ADC counts. Afterwards, the digitised signals are sent to a central station where a second trigger criteria is evaluated, which guarantees observations of events in stereo mode. This second criteria requests at least two telescopes to send a signal within a time interval of 80 ns. More information on the H.E.S.S. camera and the trigger system is presented in [A$^+$04a] and [F$^+$04].

The parameter which will be used in the data analysis to describe the signal amplitude of each pixel is the charge in p.e. that was induced by the light on the PMT. It is

estimated from the measured ADC counts in the high-gain and low-gain channel. The high-gain value is used up to ≈ 150 p.e., the low-gain value beyond ≈ 200 p.e. and for the intermediate values a weighted average is determined. For these calculations it is essential to know several time-dependant characteristics of each PMTs and its associated electronic: The pedestal position, which is the ADC value recorded in the absence of Cherenkov radiation, the gain of the PMT and a correction factor that accounts for diverging photo cathode and light collector efficiencies within the camera. While the pedestal value and its distribution can be monitored during data taking, the gain of the PMT, as well as the flat-field coefficient are evaluated on regular basis by specific calibration checks. The details of the camera calibration are summarised in [A$^+$04a] or more elaborate in [Jun03].

Usually a data taking unit of the H.E.S.S. system, a so called run, comprises 28 minutes. To be used in the analysis each run has to pass strict data quality checks to reject runs with hardware failure, e.g. broken camera pixel, or with poor observation conditions, e.g. presence of clouds. Consequently the hardware as well as the atmosphere are continuously monitored. For the monitoring of the atmosphere there are infrared radiometers, which measure the effective sky temperature, as well as a lidar, which detects light backscattered by clouds and aerosols. By monitoring the DC PMT currents conclusions about the night sky brightness can be drawn. An overview of the atmospheric sensors is given in [A$^+$04b].

In a nutshell, the H.E.S.S. experiment is able to detect γ rays with energies from 100 GeV to several tens of TeV. Since the field of view has a diameter of 5°, H.E.S.S. is well suited for scans of large sky areas, e.g. the Galactic Plane, as well as for the study of extended sources. For a single event the direction of the shower axis can be reconstructed with a typical accuracy of $\leq 0.1°$. The energy resolution is about 15 %. For a point-source the H.E.S.S. sensitivity reaches 1 % Crab, which means that a source with an integrated flux of 1 % of the Crab Nebula (for energies $E > 1$ TeV) can be detected with $5\,\sigma$ within 25 hours of observation time.

4.3. Data Analysis with H.E.S.S.

The analysis chain of H.E.S.S. consists of several steps: At the beginning the algorithm decides for each event whether it is considered γ- or hadron-like. Subsequently, the energy and the direction of the event are reconstructed. For a set of observation runs the events within a possible source region are compared with suitable background regions. Having detected a signal, the energy and spatial distributions of the photons are studied. All these investigations require a profound understanding of the detector, e.g. its effective area, its energy resolution and its point spread function. The determination of these quantities from the data set and additional Monte Carlo simulation is therefore also an important part of the analysis chain. In this chapter a brief summary of the main analysis procedures will be given. It should be noted, that within the H.E.S.S. collaboration at least two independent approaches exist for the Monte Carlo simulations, the camera calibration, the geometrical reconstruction and the background rejection, respectively. Even more methods exist for the signal extraction and the studies of the spectral energy and

spatial distribution. This has the advantage that analysis results can be cross-checked. Presenting all these analysis approaches, however, is out of the scope of this thesis. Instead, we concentrate on the analysis chain used for the new analysis of HESS J1825–137, viz. the French analysis. However, since the former publications on HESS J1825–137 were based on the complementary chain, viz. the German analysis, elements of this chain will be complementarily discussed. The German analysis is described whenever the two methods differ significantly, or when its description facilitates the understanding of the main principles of the analysis.

4.3.1. Shower Reconstruction and Event Selection

A crucial step in the analysis is the evaluation of the camera image which shows for each pixel the corresponding photoelectrons. Fig. 4.7 juxtaposes the camera images of an electromagnetic and a hadronic shower. In this subsection the standard analysis technique for the event selection and the shower reconstruction, which is part of the German analysis chain, will be presented first. Subsequently, it will be shown how these approaches were enhanced in the French analysis.

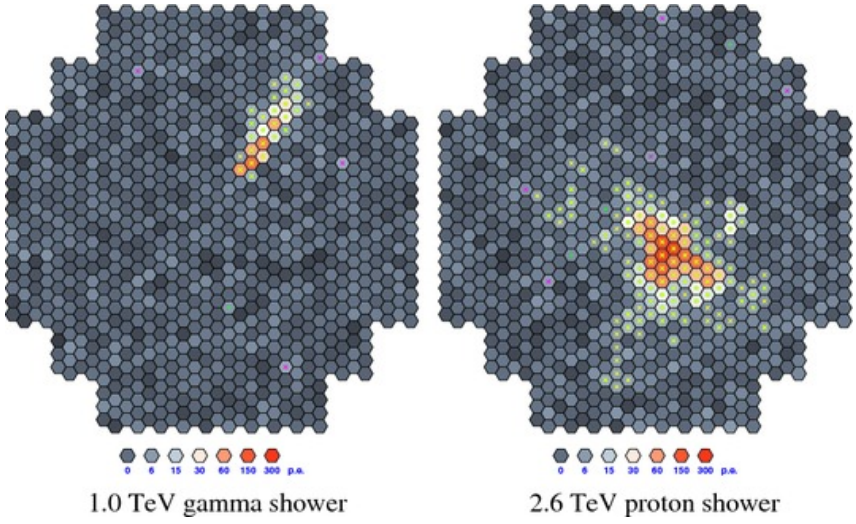

Figure 4.7.: Camera images of an electromagnetic and a hadronic shower [VB09].

Hillas analysis

The standard analysis technique – a compact summary is given in [Ben05] and one at greater length in [A$^+$06d] – is a variant of the Hillas-type analysis [Hil85] and processes the second moments of the shower images which are approximated by an ellipse. To access the Hillas parameters, first of all the images have to be cleaned. The cleaning algorithm takes advantage of the fact that the pixels which belong to a shower image form a cluster and exhibit larger p.e. values than the noisy pixels which give account of the PMT noise or the night sky background. Consequently, only pixels that have a intensities greater than

10 p.e. and at least one adjacent pixel with more than 5 p.e., or vice versa, are further processed. The remaining light distribution is then described by the Hillas parameters which refer to the shape, the position, the orientation and the brightness of the image. A sketch of a shower image and the corresponding Hillas Parameter is shown in Fig. 4.8(a). The parameters *length* and *width* describe the spread of the light along the major and minor axis of the ellipse. The distance of the centre of gravity to the camera centre is addressed by the *distance* parameter. The line connecting these two points and the major axis of the shower image form the angle *alpha* which describes the *orientation* of the image. Finally, the brightness of the image is given by the *size* parameter, i.e. the total number of photoelectrons in the image. Though being an approximation, the Hillas parameters already contain large parts of the information about the shower geometry and thus the incident particle. The shower morphology for instance is contained in the width and length parameters, while the size parameter is a measure for the energy of the incident γ ray. Moreover, the position and the orientation of the image can be used to reconstruct the arrival direction of the shower and the impact point on the ground.

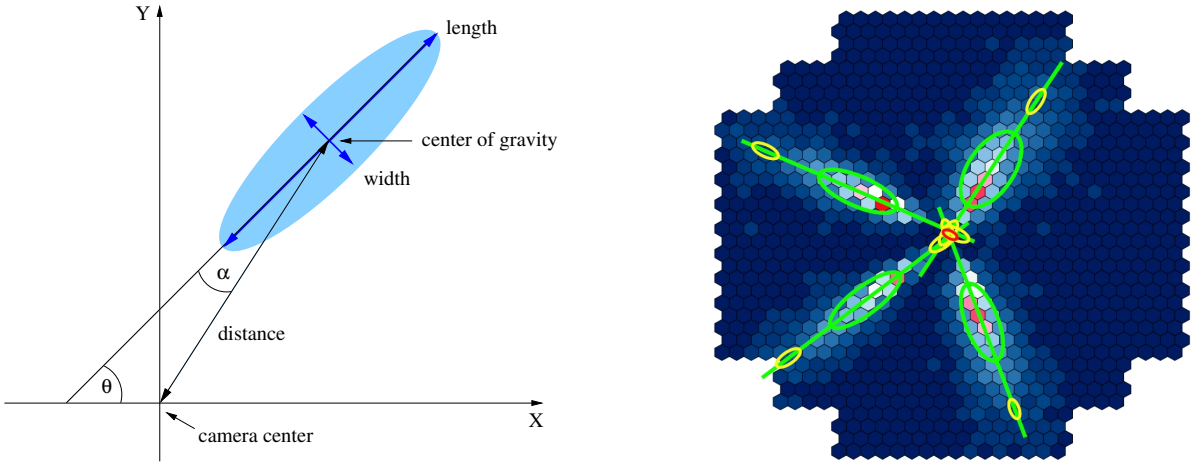

(a) Schematic representation of Hillas parameters

(b) Superimposed camera images [Ber06]

Figure 4.8.: Definition and application of the Hillas parameters. (a) Schematic representation of a shower image and the corresponding Hillas parameters. (b) Illustration how the Hillas parameters can be used to reconstruct the shower origin by means of superimposed shower images.

Since the showers are always detected by at least two telescopes, the stereoscopic technique can be used to reconstruct the shower geometry. In this way, for example, the origin of the γ ray is determined. For this purpose the camera images of different telescopes are superimposed as for each telescope the origin of the shower is mapped somewhere on the major axis of the corresponding ellipse, cf. Sec. 4.1.2. Consequently, the resulting intersection point of the main axes provides a good estimate of the origin of the primary particle, see Fig. 4.8(b). By means of the main axes the impact point of the shower on the ground can be reconstructed as well. In this case the position is determined by intersecting the image axes in the plane perpendicular to the telescopes' pointing direction. The knowledge of the exact position of the impact point is essential for the reconstruction

of the shower energy as its distance to the telescopes is an important parameter for the estimate of the total light emitted by the shower. In fact the shower energy is derived from look-up tables which provide the shower energy for different image sizes and impact points. These look-up tables are generated for different zenith angles, as well as muon efficiencies. The latter are a measure for the current reflectivity of the telescopes, which decreases with time and results in smaller image sizes. The determination of the muon efficiency is described in [A$^+$04a]

To exclude events of hadronic origin or of bad quality, selection cuts based on the Hillas parameter were developed. The permitted values of the selection cuts were derived from Monte Carlo simulations in combination with real data. The cuts were chosen such that the characteristics of the simulated source were identifiable in the best possible way. It turned out that the appropriate cuts depend mainly on the intensity and the energy spectrum of the source under study. Consequently, different selection cuts have been developed for the H.E.S.S. analysis, e.g. "hard cuts" for weak hard spectrum sources, "standard cuts" for sources with a flux of 10 % of the Crab Nebula, etc. An overview of the most common cuts is given in Table 2 in [A$^+$06d].

An essential part of the selection cuts is of technical nature, e.g. the cut on the minimum intensity of the recorded image or the cut on the maximum distance to the camera centre. Both cuts prevent a bad reconstruction, one time due to the lack of data, the other time due to the influences of the camera edge. Additional cuts deal with the problem of the high hadronic background. Therefore they are targeted on the shape of the images, as the hadronic showers develop in a more irregular manner and give rise to images which are on average broader and longer than those of electromagnetic showers. In the definition of the shape cuts it has to be considered that the shower development depends on the energy of the incident γ ray as well as on the observation conditions, i.e. the zenith angle and the impact point. Hence the measured values (p) of each telescope are firstly compared with tabulated expectation values ($\langle p \rangle$) under the same observation conditions and the difference is expressed in units of the expected scatter (σ_p, RMS spread):

$$p_\mathrm{sc} = \frac{p - \langle p \rangle}{\sigma_\mathrm{p}}. \tag{4.1}$$

In this way the reduced scaled width (RSW) and the reduced scaled length (RSL) are defined, where p stands for the width or the length of the ellipse, respectively. Furthermore, to take into account the stereo observation mode the reduced scaled values are averaged over the participating telescopes:

$$MRSL = \frac{1}{N_\mathrm{tel}} \sum_{i=1}^{N_\mathrm{tel}} p_\mathrm{sc,L,i} \quad \text{and} \quad MRSW = \frac{1}{N_\mathrm{tel}} \sum_{i=1}^{N_\mathrm{tel}} p_\mathrm{sc,M,i}. \tag{4.2}$$

The effect of the image cuts on the background is impressive: While the percentage of γ ray induced events is about 0.1 % of the total number of detected events without cuts, it is significantly improved with the image cuts, for a strong point source even resulting in a signal to noise ratio of 1:1 [A$^+$06d].

Model++

Though the Hillas analysis was proven to be efficient and robust, there exist several approaches to extract even more information from the camera images. An especially successful approach is the high performance likelihood reconstruction developed by Mathieu de Naurois and Loïc Rolland [NR09], which is referred to as Model++. This reconstruction is an essential component of the French analysis and was also applied in the new analysis of HESS J1825–137, which will be presented at the end of this chapter. In comparison to the Hillas analysis Model++ can achieve a factor of ≈ 2 better sensitivity [NR09].

The underlying concept of Model++ is a comparison of the total detected camera image of an electromagnetic shower with shower models, i.e. predicted camera images for γ-ray induced electromagnetic shower in dependence on the properties of the γ ray and the circumstances of the detection. This technique was introduced by the Cat experiment [B$^+$98] and was adapted in the French analysis to the challenges of the H.E.S.S. experiment. In order to predict the camera image of a γ ray induced electromagnetic shower first of all the shower development in the atmosphere has to be described. For this purpose Monte Carlo simulations based on an enhanced version of KASKADE [KS94, Guy03] are applied. The longitudinal, lateral and angular distribution of the charged particles in the shower is modelled as a function of the energy of the γ ray and the first interaction depth, which is introduced as a new parameter. This analytical description of the γ-ray induced air shower is an advancement of a model proposed by Hillas [Hil82].

In order to predict the corresponding camera images, several additional effects have to be considered. Among these are the zenith angle of the observation, as well as the position and the predominant direction of the shower in relation to the location and the pointing direction of the telescope. The latter results in the introduction of the impact point as additional parameter in the modelling. For the time being all shower models are generated on-axis because, under the assumption that the H.E.S.S. telescope behaves like a perfect telescope, a change of the source position only results in a translation in the camera. Furthermore, atmospheric absorption as well as technical characteristics of the telescopes, e.g. the light collection efficiency, the electronic response, the integration duration, etc., are included in the modelling. All in all, shower models are generated for 65 different energies, 6 first interaction depths, 40 different zenith angles and 40 impact distances, resulting in 624 000 templates. Figure 4.9 gives an impression of the shower images generated for a 1 TeV photon with different impact points and different first interaction depths. For the generation of shower images with arbitrary energy, first interact depth, impact distance and zenith angle an interpolation procedure in the four-dimensional space is applied.

The decision for a parameter set which reproduces the recorded image best is taken on the basis of a log-likelihood approach. To this end the recorded intensities in all pixels of the cameras are compared with the prediction from the model. In doing so it has to be considered that the recorded signal is composed of the actual signal, plus the electronic noise and plus a signal from the night sky background and that the PMTs are subjected to a limited resolution. Hence, the probability of observing a signal s in a pixel, when the expected value of the shower model is given by μ, is calculated by the sum over the

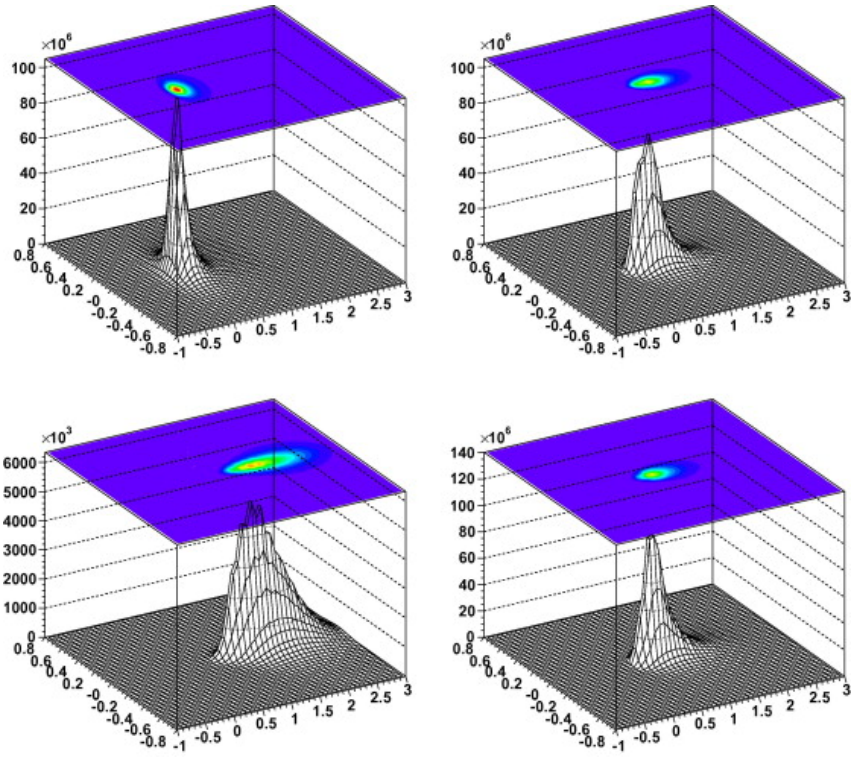

Figure 4.9.: Modelled shower images for a 1 TeV photon with a first interaction depth at $1X_0$ and an impact point in 20 m (top-left), 100 m (top-right) and 250 m (bottom-left) distance to the telescope. The bottom-right image shows the alteration of the top-right image when the first interaction takes place at 3 X_0 instead of 1 X_0. Image taken from [NR09].

probabilities that originally n photoelectrons ($n \in \mathbb{N}$) yielded a signal s due to the PMT resolution and the additional noise:

$$P(s|\mu, \sigma_\mathrm{p}, \sigma_\gamma) = \sum_n \frac{\mu^n e^{-\mu}}{n!} \cdot \frac{e^{-(s-n)^2/(2(\sigma_\mathrm{p}^2+n\sigma_\gamma^2))}}{\sqrt{2\pi(\sigma_\mathrm{p}^2 + n\sigma_\gamma^2)}}. \tag{4.3}$$

For each summand the Poisson distributed probability of detecting n photoelectrons is convolved with a Gaussian of width $\sqrt{\sigma_\mathrm{p}^2 + n\sigma_\gamma^2}$, where σ_p is the width of the pedestal and σ_γ is the width of the single photoelectron peak. As described in Sec. 4.2 both are monitored continuously during data taking. The corresponding pixel log-likelihood is defined as $L_\mathrm{pixel} = -2 \cdot \ln P(s|\mu, \sigma_\mathrm{p}, \sigma_\gamma)$ and the final log-likelihood value is obtained from the sum over all pixel log-likelihoods:

$$L = \sum_{i=1}^{N_\mathrm{pixels}} \ln L_\mathrm{i}. \tag{4.4}$$

The best fitting parameter set is found by minimising the log-likelihood by means of the Levenberg-Marquardt fit algorithm (LMA, [Lev44, Mar63]). The LMA combines properties of the Gauss-Newton algorithm and the method of gradient descent. The parameter sets for which the log-likelihood is evaluated depend on the first and second derivatives in the parameter space as well as on the fact whether the log-likelihood can locally be described by a quadratic form. Using starting values derived from the analysis of the camera image by the Hillas analysis the LMA converges fast and reliably, even though it can not be excluded that only a local minima is found. Furthermore, the errors on the best fit parameters can be estimated from the correlation matrix.

To evaluate whether a fit is compatible with the assumption that a photon and not a hadron was observed the goodness-of-fit variable is introduced. For each pixel the obtained log-likelihood value is compared with the expected log-likelihood value for the current shower model assumption. The differences are summed up over all pixels and normalised. Under the assumption that the pixels are uncorrelated the goodness-of-fit variable should behave like a standard normal distribution. For the details on the normalisation, the calculation of the expectation values and for the validation of the assumption that the goodness-of-fit behaves like a standard normal variable see [NR09]. In order to finally classify the recorded event two further variables are derived from the goodness-of-fit. They are defined in the same way as the goodness-of-fit, but refer to subclasses of the pixels. The so called *ShowerGoodness* (SG) takes account of all pixels (plus those in the close vicinity) for which the shower model predicts an amplitude above 0.01 p.e., while the *BackgroundGoodness* (BG) is calculated for the remaining pixels. The histogram in Fig. 4.10(a) shows the distribution of the ShowerGoodness parameter for real source data as well as for background data. The distributions differ significantly: while the ShowerGoodness of the source data accumulates around zero, the ShowerGoodness of the background data extends to much higher values.

In the same way as in the Hillas analysis only events that are observed by at least two telescopes, have an image amplitude larger than 60 p.e. per telescope and are located

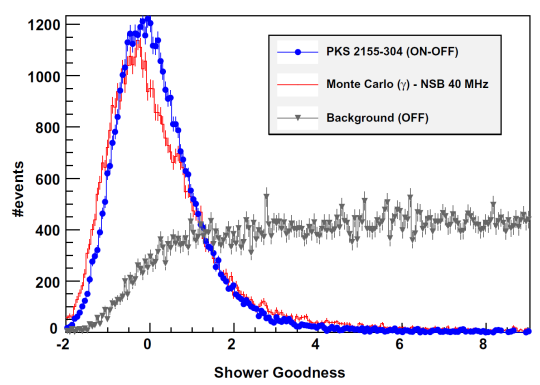

(a) Shower Goodness parameter

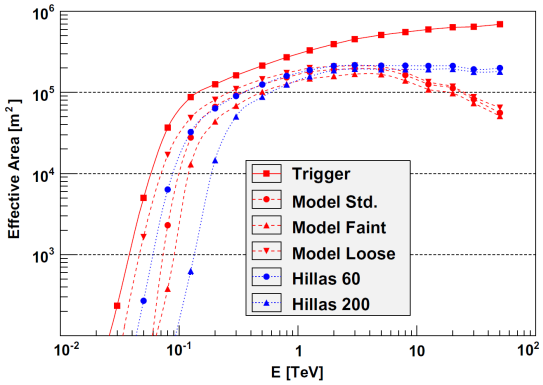

(b) Effective area

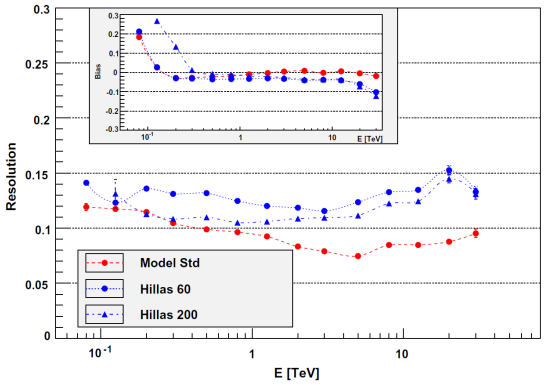

(c) Energy resolution and bias

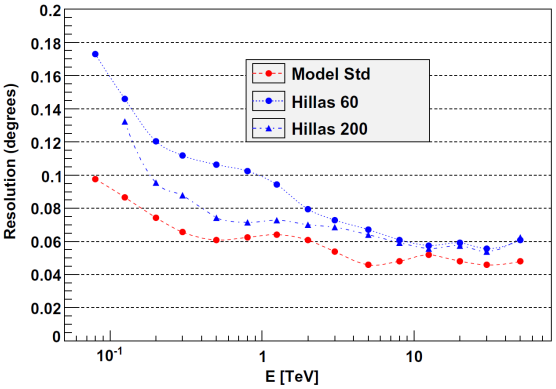

(d) Angular resolution

Figure 4.10.: Performance of Model++: (a) Distribution of the ShowerGoodness parameter for real data, the corresponding simulation and for pure background. Effective area (b), energy resolution & bias (c) and angular resolution (d) of H.E.S.S. at zenith as a function of the energy for different selection cuts. All histograms are taken from [NR09].

at a distance smaller than 2.0° to the camera centre are accepted for further processing in Model++. The cuts on $MRSL$ and $MRSW$ are replaced by cuts on the goodness variables. The highest reduction potential has the cut on the ShowerGoodness. In the standard configuration $SG \leq 0.6$ is used. Moreover, there is a cut on the Background-Goodness $BG \leq 2$ and a cut on the goodness-of-fit for the assumption that $\mu = 0$ in each pixel. Newly introduced is a cut on the first interaction depth $-X_0 \leq t_0 \leq 4\ X_0$ which takes advantage of the earlier interactions of the photons in comparison to the hadrons. An overview of the default reconstruction configurations is given in Table 1 in [NR09]. Besides the events which are classified as γ-like two other classes exist: the hadron-like events and the ambiguous events. While the γ-like and hadron-like classes contain events which fall in co-domains of the discriminant variables with high discriminating power, the third class accumulates those events with inconclusive values of the discriminant variable. The hadron-like events will later become important for the determination of the camera acceptance and can be used for background estimates (see *Template Background Method*).

As mentioned before the Model++ analysis yields a sensitivity which is increased by a

factor 2 in comparison with the Hillas analysis. This better sensitivity is due to the improved direction and energy reconstruction and the higher γ-ray efficiency as well as background rejection. The Figures 4.10(b), (c) and (d) give an overview of the performance of the Model++ analysis, i.e. the corresponding effective area, the energy resolution and the angular resolution. The results obtained for the default Model++ selection cuts are compared with those for the most common Hillas cuts. All distributions are shown for observations taken at zenith. For observations under different observation conditions, e.g. at different zenith angle, the distributions will vary, but the overall trend should be the same. The effective area in the mean energy range is rather independent from the particular selection cut. At lower energies, however, the Model++ analysis reveals larger effective areas, as can be seen by a comparison of the Loose Model cuts and the Hillas 60 cuts, which are both optimised for the detection of low-energy γ rays. Consequently the Model++ analysis is well suited for observations with lower energy threshold. The deviations at higher energies are of technical nature, as for the time of the quoted publication, the shower model had only been generated up to energies of 20 TeV. Due to the incorporation of additional parameters in the energy reconstruction the energy resolution which is defined as the RMS of the $\Delta E/E$ distribution is improved over the complete energy range and takes on values significantly smaller than 15 %. Moreover, the corresponding bias reveals a narrower distribution around zero. Finally, the angular resolution which is defined as the 68 % containment radius of a point source is significantly increased, especially at low energies. Due to the enhanced direction reconstruction in average values of about 0.06° are obtained.

4.3.2. Verification of γ-ray Signals

The event selection described in the previous section is an efficient mean to reduce the cosmic-ray background. However, even for strong sources the ratio of signal to background is still about 1:1 after event selection. In addition there are diffuse γ rays in all observations. These γ rays are produced by cosmic rays interacting with interstellar gas and photon fields and in contrast to the γ rays emitted by a single source they are distributed rather uniformly over the field of view. The high background rate has consequences for the detection of γ rays: in addition to any data taken in a selected region on the sky ("on region") an estimate of the background under comparable observation conditions (e.g. source position in the camera, zenith angle of the observation, level of night sky background) is needed. From the observational point of view there are two different approaches for this estimate [BFH07]. In On-Off observations the telescopes initially point directly on the target and take "on data". Afterwards the telescopes are directed to an area in the close vicinity where no sources are known and the telescopes take "off data". Generally, this approach is rather time-consuming and the consistency of the observation conditions is difficult to control when the off data are not taken immediately after the target observation. Nevertheless, for very extended sources this is certainly the method of choice. For smaller sources and in particular for telescopes with a wide field of view it is more convenient to observe in wobble mode. Thereby the field of view is not centred on target, but the source is detected with a certain offset. Thus, space for the background es-

timate is gained on the opposite side of the camera, ensuring almost identical observation conditions.

Signal Quantification

In order to quantify a potential signal in addition to the number of events in the target region (on events, N_{on}) the expected number of background events in the same region (N^{*}_{off}) has to be determined. This quantity can be derived from the number of events measured in a selected background region (off events, N_{off}). In doing so differences in the size and the shape of the on and the off region, i.e. the target and the background region, as well as in the telescope response have to be considered. Therefore, a normalisation parameter is introduced, which converts the off events as if they were measured under the same circumstances as the on events:

$$N^{*}_{\mathrm{off}} = \alpha \, N_{\mathrm{off}}. \tag{4.5}$$

The details on the calculation of α will be presented in the following section. Here, the quantification of a potential signal shall be described first. With the on events and the expected off events the γ-ray excess (N_{excess}) can be defined:

$$N_{\mathrm{excess}} = N_{\mathrm{on}} - \alpha N_{\mathrm{off}}. \tag{4.6}$$

The next step is to decide whether an excess originates from a source or is just due to background fluctuations. A straightforward approach to estimate the probability of observing a γ-ray source and not a background fluctuation, i.e. the significance of an observation, is to study the standard deviation. Li and Ma [LM83] showed that based on Poisson law and under the assumption that N_{on} and N_{off} are both due to background the significance can be written as

$$S = \frac{N_{\mathrm{excess}}}{\sigma(N_{\mathrm{excess}})} = \frac{N_{\mathrm{on}} - \alpha N_{\mathrm{off}}}{\sqrt{\alpha(N_{\mathrm{on}} + N_{\mathrm{off}})}}. \tag{4.7}$$

For a sufficiently large number of on and off counts ($N_{\mathrm{on}} \geq 10$ and $N_{\mathrm{off}} \geq 10$) and still under the assumption that no source is located in the observed region, the significance will approach a standard normal distribution with zero mean and unit variance with increasing number of events. As a consequence the Gaussian probability of S can be used as the confidence level of the observation. In addition, Li and Ma studied as a second approach a maximum likelihood ratio method, which is based on a hypotheses test with the null hypothesis that all detected photons are due to background [LM83]. In this approach the significance can be expressed as

$$S = \sqrt{2}\left\{ N_{\mathrm{on}} \ln\left[\frac{1+\alpha}{\alpha}\left(\frac{N_{\mathrm{on}}}{N_{\mathrm{on}} + N_{\mathrm{off}}}\right)\right] + N_{\mathrm{off}} \ln\left[(1+\alpha)\left(\frac{N_{\mathrm{off}}}{N_{\mathrm{on}} + N_{\mathrm{off}}}\right)\right]\right\}^{1/2}. \tag{4.8}$$

This definition has the same statistical properties as the definition in Eq. 4.7, but as Monte Carlo simulations revealed, it is more stable in the case of small numbers of observed events, especially when $\alpha \neq 1$. Therefore it is predominantly used in γ-ray astronomy.

Accounting for Differences in the Determination of On and Off Events

As addressed before, estimating the proportion of background events contained in the on events requires a careful comparison of the on and off region, as well as the respective observation conditions. For the H.E.S.S. Collaboration this topic was investigated in detail by Berge et al. [BFH07]. Here, only a short summary shall be given. Thinking about differences between on and off observations, the parameters that come to mind first are the observation times and the sizes of the observation regions. More elusive but equally important is the system acceptance, which describes the probability that an event is detected by the telescopes and that the event passes the selection procedure. This probability is influenced by several parameters. For instance, it depends on the date of the observation, as the technical condition of the experiment, e.g. the reflectivity of the mirrors, changes with time. Moreover, it depends on the respective night-sky background, as the presence of bright stars in the field of view hampers the identification of γ-like events. In addition, the zenith angle of the selected region plays a crucial role, since the shower development is affected by the magnetic field of the Earth. With increasing zenith angle the shower maxima are also further away from the telescopes, which is why the detectable amount of light on the ground as well as the appearance of the showers changes. Comparing regions which have been observed simultaneously, the detection probability of an events still depends on the shower position within the field of view. In general, the system acceptance exhibits a strong radial dependency: The larger the distance to the pointing position, the lower the detection probability. The reason for this tendency is that events which are recorded close to the camera edge are often truncated and worse reconstructed and are thus more likely to be rejected. Last but not least, the system acceptance depends on the energy of the detected event. With increasing energy of the incident γ ray, the Cherenkov photon intensity on ground becomes higher and hence simplifies the detection. However, when the energy becomes too high the showers are too extended to allow a reliable reconstruction and thus the system acceptance decreases again.

As a result of the multitude of influences, the system acceptance to γ-like events for different sky positions has to be modelled for each source's data set before the events from on and off regions can be compared. To this end, for each sky position the corresponding expected number of background events is determined from the data set. Under the assumption that the spectrum of the background events does not change over the field of view a comparison of the expected number of background events at different sky positions can be used to rate the system acceptance. In general, the system acceptance maps are normalised so that the value domain is restricted to $[0, 1]$, whereby 1 represents the maximum acceptance. The expected number of background events for each sky position is derived from those events which are not reconstructed within the target region or any other potential source region within the field of view. Indeed, all sky regions for which a contribution by a γ-ray source to the detected events is expected have to be excluded from the calculation of the system acceptance. These regions are therefore called exclusion regions. Usually the first steps of the system acceptance calculation are performed in the Nominal System (i.e. the coordinate system within the camera). This has the advantage

that due to the changing pointing positions the exclusion regions on the sky are located at different camera positions for different observation runs. As a consequence over the course of several runs an estimate of the acceptance can be gained for each position in the camera. In order to obtain the system acceptance in sky coordinates, the acceptance in the camera system is transferred to the sky for each single run taking into account the respective pointing positions and the run "weight", i.e. the percentage of background events observed in this run.

In the past the modelling of the system acceptance was performed run-wise and was based on the simplified assumption that the system acceptance is radially symmetric within the camera system [BFH07]. For each run the background events were plotted as a function of the squared angular distance to the camera centre. This representation had the advantage that when displayed as a histogram each bin covered an equally sized area in the camera system. When excluded regions were located in the field of view, for some bins the available area for the determination of the corresponding background events was reduced. To obtain the camera acceptance nevertheless, the bin contents in the affected bins were scaled with a weighting factor which compensated for the smaller extraction region. The disadvantage of the calculation of a radial acceptance is that it is only possible if the number of exclusion regions within the field of view is limited and if the target region does not contain the centre of the camera. Moreover, the approach neglects inhomogeneities within the camera, e.g. different responses of single drawers or camera edges, as well as the zenith angle dependency.

Therefore, in the meantime it is more convenient to work with a two-dimensional acceptance map [N$^+$12, Nau12]. The basic principles of the calculation of this map are presented in Fig. 4.11. Again the calculations are performed in the Nominal System. The first step in the calculation of the acceptance map is the generation of an event map that contains the γ-like events of all runs, which are not ascribed to an exclusion region. In addition, an exposition map is derived from the hadron-like events, which is a measure of the exposure for the different positions in the camera system. To calculate the exposition map the hadron-like events are filled into two maps: one map contains all events, the other only those outside the exclusion regions. The exposition map is the ratio of the second and the first map. As illustrated in Fig. 4.11 the system acceptance to γ-like events is finally obtained by dividing the events map by the exposition map. Subsequently, the acceptance in the camera system is transferred to the sky as described above.

Defining Suitable Background Regions

In order to keep the uncertainties in the background estimate for the signal detection and the spectrum determination as small as possible it is helpful to choose the off regions in such a way that the acceptance of the off regions differs as little as possible from that of the on region. This can be achieved in two ways [N$^+$12, Nau12]: The first method presented here is called *Ring Background*, the second *Multiple Off Regions Background*. In both approaches the off regions in each run are chosen on a ring around the camera centre in the Nominal System. The mean ring radius is equal to the offset of the target

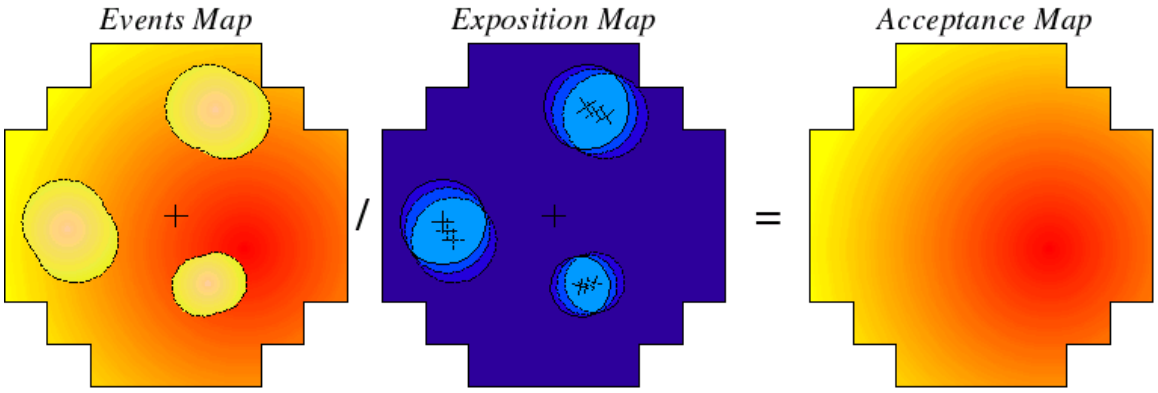

Figure 4.11.: Illustration of the calculation of the two-dimensional acceptance map [N+12]

region from the camera centre and its width matches the target width, see Fig. 4.12. This choice guarantees that the radial dependency of the system acceptance does not lead to disparities between the regions. Of course, the target region has to be excluded from the ring. In case of the *Ring Background* the total remaining area of the ring is considered for the background estimate, Fig. 4.12 left, whereas off regions with the same size and shape as the on region are investigated for the *Multiple Off Background*, Fig. 4.12 right. In both methods areas which may contain sources are excluded from the background estimate. In particular an additional exclusion region is constructed around the target in order to avoid contamination by the source itself. By default the *Multiple Off Background* is used for the spectrum extraction as it can easily be generalised for arbitrary region shapes.

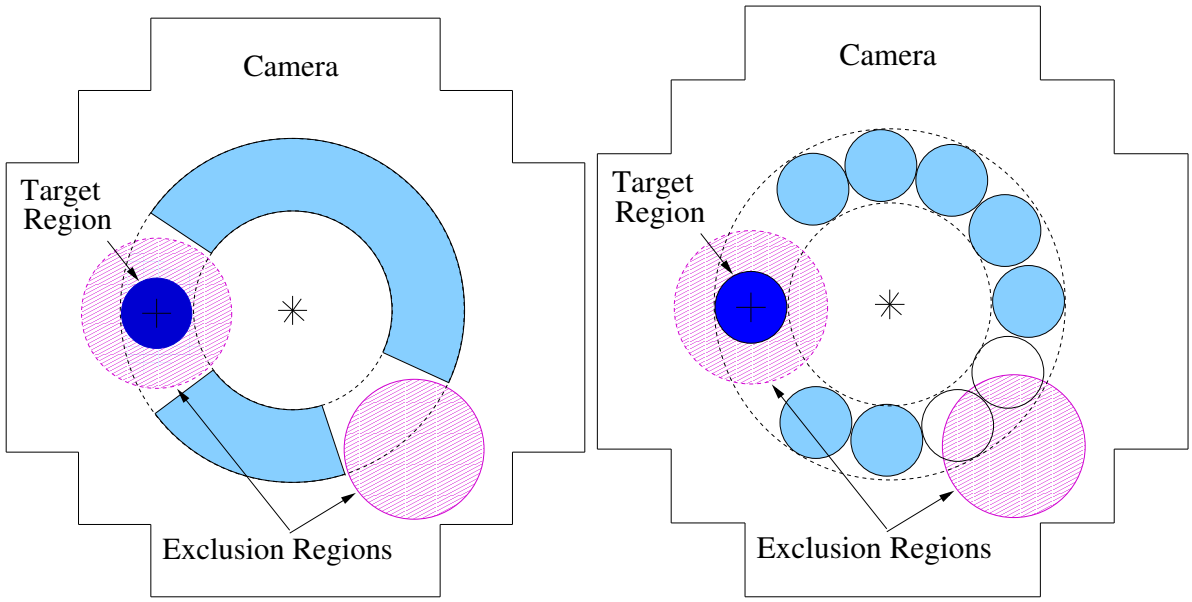

Figure 4.12.: Various methods for background estimates in the signal determination: *Ring Background* (*left side*) and *Multiple Off Regions Background* (*right side*).

Under the assumption that the acceptance is radial symmetric the normalization parameter from Eq. 4.5 for a single run (α_r) only has to account for the different geometrical shapes. In case of the *Multiple Off Region Background* it even simplifies to 1/(# off regions). When a more elaborate treatment is needed, e.g. when the camera acceptance is not radial symmetric, α_r is determined as the ratio of the camera acceptances $A_\mathrm{C}(\vec{r})$ in the on region and the off region:

$$\alpha_r = \left(\int_\mathrm{on} \mathrm{d}S\ A_\mathrm{C}(\vec{r})\right) \Big/ \left(\int_\mathrm{off} \mathrm{d}S\ A_\mathrm{C}(\vec{r})\right) . \tag{4.9}$$

For a set of observation runs the total normalisation parameter α is obtained as the weighted sum over the normalisation parameter of the single runs:

$$\alpha = \left(\sum_r \alpha_r N_\mathrm{off,r}\right) \Big/ \left(\sum_r N_\mathrm{off,r}\right) . \tag{4.10}$$

4.3.3. Generation of Sky Maps

For the calculation of the sky maps the skyregion around the target is split into several bins and for each of them the γ-ray signal is evaluated separately. In the following those types of sky maps, which are essential for the analysis as well as the simulation presented in this thesis, are introduced. The starting point for all sky maps is the γ-candidates map, which shows the distribution of the γ-like events over the sky. Moreover a sky acceptance map for γ-like events is obtained by transferring the camera acceptance map to the sky, see Sec. 4.3.2. All further sky maps, e.g. excess and significance map, depend on the model which is chosen for the background estimate. Again two different approaches are applied [N$^+$12, Nau12]. The first method is similar to the ring background estimate presented in the previous section, as for each bin a ring region surrounding the respective bin is used for the background estimate, see Fig. 4.13 left. Exclusion regions are once again not considered in the background estimate. In contrast to the *Ring Background* estimate presented in the last section the on and off region are now defined on the sky map and are subjected to significantly different sky acceptances. Consequently, the normalisation factor α has to be calculated for each bin following Eq. 4.9, in which the camera acceptance must be replaced by the sky acceptance.

For extended sources and for a field of view with several excluded regions the *Ring Background* method is difficult to apply. In this case the background can be assessed by the *Template Background* method, Fig. 4.13 middle & right. In this approach the background is no longer estimated from γ-like events, but from events which have been classified as hadrons in the event selection process. For this purpose a sky map containing only hadron events as well as a sky acceptance map for hadron events are generated. The sky acceptance map for hadrons is obtained following the same procedure as for the sky acceptance map for γ-like events presented in Sec. 4.3.2. The normalisation parameter α can be determined for each bin in a similar way as presented in Eq. 4.9. However, the equation has to be adapted slightly. The on and off events are now extracted from the same sky

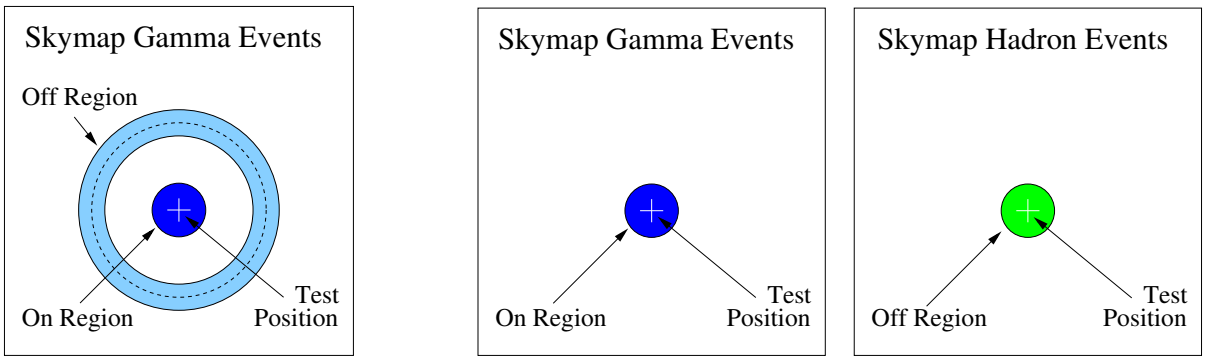

(a) *Ring Background* (b) *Template Background*

Figure 4.13.: Two examples of how to obtain background estimates within H.E.S.S. sky maps.

region and the camera acceptance has to be replaced by the sky acceptances to γ-like and hadron-like events ($A_{\mathrm{S}}(\vec{r})$ and $B_{\mathrm{S}}(\vec{r})$), respectively. Moreover, a proportionality factor r has to be introduced which accounts for the different normalisation factors that have been applied to the hadron- and γ-like acceptance maps:

$$\alpha = r \cdot \left(\int_{\mathrm{on}} \mathrm{d}S \; A_{\mathrm{S}}(\vec{r}) \right) \Big/ \left(\int_{\mathrm{on}} \mathrm{d}S \; B_{\mathrm{S}}(\vec{r}) \right) . \tag{4.11}$$

As we assume that the proportionality factor r is constant for all bins in the sky maps it can be determined as the expectation value of $(n_\gamma/a_\gamma)/(n_{\mathrm{h}}/a_{\mathrm{h}})$ for all bins in the sky map, omitting exclusion regions. n_γ and n_{h} are the bin contents in the γ- and hadron-like event maps, a_γ and a_{h} the entries in the sky acceptance maps. Having determined α for each bin the excess and the significance map can be calculated immediately. To study the morphology of a source, sky maps which have been corrected for the different sky acceptances within the field of view are very helpful. The most common example is the normalized excess map. For this map the bin contents of the excess map are divided by the corresponding bin contents of the sky acceptance map for γ-like events.

4.3.4. Morphology

To further quantify the morphology of the observed source different morphology shapes can be fit to the H.E.S.S. sky maps [N$^+$12, Nau12]: The most simple model is a point-like source:

$$M(x, y) = M_0 \cdot \delta(x - x_{\mathrm{i}}) \cdot \delta(y - y_{\mathrm{i}}). \tag{4.12}$$

In the case of an extended source it is very common to fit a symmetric Gaussian model

$$M(x, y) = \frac{M_0}{2\pi\sigma^2} \cdot e^{-\frac{(x-x_0)^2 \cos^2\beta + (y-y_0)^2}{2\sigma^2}}, \tag{4.13}$$

or when a predominant direction is visible an asymmetric Gaussian model

$$M(x, y) = \frac{L_0}{2\pi\sigma_1\sigma_2} \cdot e^{-\frac{((x-x_0)\cos\beta\cos\varphi + (y-y_0)\sin\varphi)^2}{2\sigma_1^2}} \cdot e^{-\frac{(-(x-x_0)\cos\beta\sin\varphi + (y-y_0)\cos\varphi)^2}{2\sigma_2^2}} . \tag{4.14}$$

Since the sky maps are usually plotted in spherical sky coordinates (e.g. in the equatorial or in the Galactic coordinates), the coefficient $\cos\beta$ is introduced to account for the different angular ranges which are covered on the X and Y axis. In doing so β in equatorial coordinates (α, δ) is defined as $\beta = 90° - \delta$.

In the detected sky maps the presented morphology shapes are not directly observable. Instead, the sky acceptance as well as the angular resolution of the telescope have to be considered. The latter is quantified by the point-spread function and is assumed to be radially symmetric. The histogram in Fig. 4.10(d) shows how the 68 % containment radius of the point-spread function behaves as a function of the energy for an observation at zenith, which is analysed with standard cuts. Besides the dependency on the selection cuts and the energy of the photon the point-spread function is influenced by the zenith and the off-axis angle of the observation. In order to determine the PSF which is suitable to describe the angular resolution of the respective data set, the energy spectrum of the investigated source is first fitted with a power law (see next subsection for details). For the different power-law indices there exist look-up tables generated by means of Monte Carlo simulations which predict the angular distribution for different zenith and off-axis angles. By weighting the point-spread functions of the single observation runs in accordance to their respective live time the point-spread function of the whole observation is generated.

By means of the PSF an improved prediction of the observable morphology shape can be made. For this purpose the expected density distribution of the excess events is calculated by convolving the morphology model with the PSF:

$$\frac{\mathrm{d}N}{\mathrm{d}x'\mathrm{d}y'} = \int\int \mathrm{d}x\mathrm{d}y\; M(x,y)\; PSF(\sqrt{(x-x')^2+(y-y')^2}). \tag{4.15}$$

In the sky maps the data are filled into bins, e.g. $[x'_1, x'_2] \times [y'_1, y'_2]$. Therefore, the expected number of source events n_s in a bin is obtained by integrating Eq. 4.15 over the bin area. If the sky acceptance of the H.E.S.S. telescope was the same for all sky positions, this would be the final solution. However, since this is not the case, the expected bin content has to be weighted with the corresponding sky acceptance $a_{\gamma,\mathrm{bin}}$:

$$n_\mathrm{s} = \mathrm{a}_{\gamma,\mathrm{i}} \cdot \int_{x'_1}^{x'_2} \int_{y'_1}^{y'_2} \mathrm{d}x'\mathrm{d}y'\; \frac{\mathrm{d}N}{\mathrm{d}x'\mathrm{d}y'}. \tag{4.16}$$

To quantify how good the number of measured photon events is predicted by a model a log-likelihood value is introduced again. The log-likelihood value of a single sky map bin is calculated based on the assumption of a Poisson distribution. Hence, the probability to detect N_on and N_off events when the expected numbers of source and background events are n_s and n_b, respectively, is given by

$$P(N_\mathrm{on}, N_\mathrm{off} \mid n_\mathrm{s}, n_\mathrm{b}) = \frac{(n_\mathrm{s}+\alpha n_\mathrm{b})^{N_\mathrm{on}}}{N_\mathrm{on}!} e^{-(n_\mathrm{s}+\alpha n_\mathrm{b})} \cdot \frac{n_\mathrm{b}^{N_{off}}}{N_\mathrm{off}!} e^{-n_\mathrm{b}} \tag{4.17}$$

and the corresponding log-likelihood value is defined as $L_\mathrm{bin} = -\log(P)$. To simplify matters the constant terms in the definition of the log-likelihood, e.g. $\log(N_\mathrm{on}!)$ are omitted.

While the normalisation parameter α can be derived as described above, n_b is unknown. Therefore the best estimate for n_b is used which is obtained by minimising L_bin:

$$n_\mathrm{b} = \frac{(\alpha(N_\mathrm{on}+N_\mathrm{off}) - (1+\alpha)n_\mathrm{s}) + \sqrt{(\alpha(N_\mathrm{on}+N_\mathrm{off}) - (1+\alpha)n_\mathrm{s})^2 + 4\alpha(\alpha+1)N_\mathrm{off}n_\mathrm{s}}}{2\alpha(\alpha+1)}. \tag{4.18}$$

In the same way as described in Sec. 4.3.1 the best fitting model and the corresponding parameter set is determined by adding all bin log-likelihood values and minimising the sum with the Levenberg-Marquardt fit algorithm.

4.3.5. Energy Spectrum

The energy spectrum of a source refers to the number of photons which are emitted per energy, area and time interval:

$$\phi(E) = \frac{\mathrm{d}^3N(E)}{\mathrm{d}E\,\mathrm{d}S\,\mathrm{d}t}. \tag{4.19}$$

Here, E denotes the true energy of the photons. The study of the energy distribution of the photons offers valuable clues to the emission processes taking place in the observed source. Unfortunately the true energy E is a quantity which is not directly accessible. Instead we have to work with the reconstructed energy E' which is ascribed to the photon by the reconstruction process. Nevertheless statements over the underlying source spectrum can be made. How this works will be shown in the following.

For the determination of the energy spectrum two quantities play an important role: the effective area and the energy resolution. The behaviour of these two quantities as a function of the energy for an observation at zenith is shown in Fig. 4.10(b) and (c). In case of real observations the runs are usually taken with different zenith angles, off-axis angles and muon efficiencies. Thus, the dependency of the effective area and the energy resolution on these quantities has to be considered. The effective area is therefore defined as $EA(E,\delta,\theta,\mu)$, where δ is the zenith angle, θ the off-axis angle and μ the muon efficiency. Moreover the energy resolution is described by a probability distribution $ER(E,E',\delta,\theta,\mu)$ which gives account of the probability that an event with the true energy E is reconstructed with an energy E' for the different zenith and off-axis angles. The particular values are obtained from look-up tables generated by means of Monte Carlo simulations.

Different approaches were used to determine the energy spectrum in the early analysis software versions and in the one used now. In the past (see [Ben05]) the spectrum was reconstructed in logarithmic bins in reconstructed energy. Only bins were the energy bias was less than 10 % were accepted for further processing. For each bin the corresponding exposure and the effective area were determined. It should be noted that the effective areas were determined as a function of the reconstructed energy. The disadvantage of this approach is that the effective areas as a function of the reconstructed energies depend on the assumed source spectrum because of the finite energy resolution. Consequently, the spectrum was determined iteratively. First, the spectrum was calculated under the

assumption that a power-law spectrum with an index of 2 was observed. When deviations to the assumed spectrum occurred the effective areas were recalculated under the new spectrum hypothesis and the determination of the spectrum was repeated, etc.

Today's practice omits the effective areas in reconstructed energy [N+12, Nau12]. Instead a certain spectral shape is assumed and by means of $EA(E, \delta, \theta)$ and $ER(E, E', \delta, \theta)$ it is predicted how the spectrum would look like when it had been detected by the H.E.S.S. telescopes under the particular observation conditions. Afterwards the forward folded spectrum is compared with the measured data. Again the set of parameter which reproduces the measured spectra with the highest probability is determined by means of a log-likelihood fit. The most common assumption on the spectral shape is that it can be described by a power law

$$\phi(E) = \phi_0 \left(\frac{E}{E_0} \right)^{\alpha_1} , \tag{4.20}$$

where ϕ_0 is the energy flux at the reference energy E_0 and α_1 is called the power-law index. Later in this thesis we will also perform a fit with a broken power law

$$\phi(E) = \phi_0 \cdot \begin{cases} \left(\frac{E}{E_0} \right)^{\alpha_2} & \text{for } E \leq E_{\text{cut}} \\ \left(\frac{E_{\text{cut}}}{E_0} \right)^{\alpha_2 - \alpha_3} \left(\frac{E}{E_0} \right)^{\alpha_3} & \text{for } E > E_{\text{cut}} \end{cases} , \tag{4.21}$$

which is composed of two power laws with the indices α_2 and α_3, respectively, and exhibits a break at energy E_{cut}.

For the comparison the measured data are filled in a four-dimensional table. The four dimensions are the energy, the zenith angle, the off axis angle and the muon efficiency. The number of bins in the table depends on the measured data, but is in the order of 2×10^5. It is self-explanatory that only bins containing data are considered in the fit, in particular it is requested that the exposure of a bin ($t_{\text{exp}}(\delta, \theta, \mu)$) is at least one minute. Let's first consider the energy distribution for fixed values of the zenith angle, the off-axis angle and the muon efficiency. In this case the expected number of source events n_s in a reconstructed energy bin $[E'_1, E'_2]$ is given by

$$n_{\text{s}} = t_{\text{exp}}(\delta, \theta, \mu) \cdot \int_{E'_1}^{E'_2} \mathrm{d}E' \int_0^{\infty} \mathrm{d}E \; \phi(E) \cdot EA(E, \delta, \theta, \mu) \cdot ER(E, E', \delta, \theta, \mu), \tag{4.22}$$

taking into account the energy distribution of the source flux as well as the effective area and the energy resolution. The lower energy threshold for the reconstructed energy bins is chosen such that the effective area in the first bin accounts for at least 10 % of the maximal effective area for the particular zenith angle, off-axis angle and muon efficiency. The upper energy threshold in turn is given by the highest measured photon energy.

The log-likelihood value for the single energy bin is calculated according to Eq. 4.17. In the same way as described in Sec. 4.3.1 the best parameter set is determined by adding all bin log-likelihood values and minimising the sum with the Levenberg-Marquardt fit algorithm. Moreover the flux uncertainties are derived from the covariance matrix (C):

$$\mathrm{d}\phi = \sqrt{\sum_{\text{i,j}} C_{\text{i,j}} \frac{\partial \phi}{\partial \alpha_{\text{i}}} \frac{\partial \phi}{\partial \alpha_{\text{j}}}} \, . \tag{4.23}$$

For most spectrum shapes the best fit values of the parameters depend on the reference energy E_0. In order to reduce the uncertainties on the spectrum parameters the reference energy is usually set to the decorrelation energy, i.e. the energy with the smallest flux uncertainty $\mathrm{d}\phi/\phi$ and the fit is performed a second time. The reason for this procedure is that the spectrum parameters at the decorrelation energy are almost uncorrelated.

The final spectrum is shown as a function of the true energy. By default the spectrum points are chosen such that the significance of each point is approximately $3\,\sigma$. For the calculation of the spectrum points it is necessary to determine the average true energy which corresponds to a bin $[E'_1, E'_2]$ in reconstructed energy. Based on the assumption of the underlying spectrum this can be achieved in the following way

$$\langle E \rangle = \frac{\int_{E'_1}^{E'_2} \mathrm{d}E' \int_0^\infty \mathrm{d}E \; E \; \phi(E) \; EA(E,\delta,\theta,\mu) \; ER(E',E,\delta,\theta,\mu)}{\int_{E'_1}^{E'_2} \mathrm{d}E' \int_0^\infty \mathrm{d}E \; \phi(E) \; EA(E,\delta,\theta,\mu) \; ER(E',E,\delta,\theta,\mu)} \; . \tag{4.24}$$

Finally, the corresponding flux is obtained by scaling the expected flux in accordance with the quotient of measured excess events and expected source events

$$\phi'(\langle E \rangle) = \frac{N_\mathrm{on} - \alpha N_\mathrm{off}}{n_\mathrm{s}} \cdot \phi(\langle E \rangle) \; . \tag{4.25}$$

4.4. New Analysis Results on HESS J1825–137

The analysis presented in the following was conducted with the Model++ software (version tag erlangen-paris-11-08-d) using lookup tables and dsts valid in August 2011. In the analysis all runs with an observation position within 2° to the earlier published best fit position of the symmetric Gaussian (see Sec. 3.2.1) were used. In doing so data taken between May 2004 and the 5th of July 2011 were considered. As additional selection criteria it was requested that all four telescopes participated in the observation runs and that a region which had been preselected for the comparison with the prediction of the newly developed model – a more precise definition follows in the next but one paragraph – was completely contained in the field of view during data taking. This way 255 runs were analysed, resulting in a dead-time corrected live time of 105.58 hours, which is approximately twice the amount of data as used in the earlier publication. Due to the proximity of the Galactic Plane several TeV sources and source candidates are located in close vicinity to HESS J1825–137. As described before, these regions have to be excluded from the analysis to prevent that background regions accidentally overlap with potential source regions. Thus 32 regions were excluded from the analysis presented in this chapter.

The results presented here were obtained using the Model++ analysis with standard selection cuts, see Sec. 4.3.1. A nice impression of the present appearance of HESS J1825–137 is given in Fig. 4.14. All sky maps in this new analysis were generated by means of the template background estimate. The sky maps displayed in Fig. 4.14(a) were smoothed with a smoothing radius of $\theta = 0.1°$ to account for the resolving capacity of the H.E.S.S. telescopes. Moreover, the maxima of the z-axes were fixed to the maximum values of the

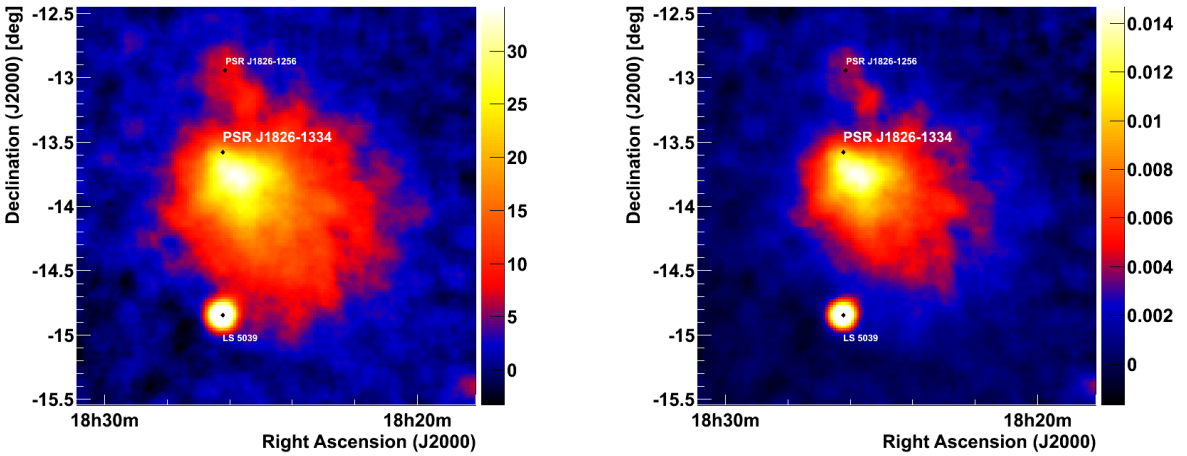

(a) Significance map

(b) Normalised excess map

Figure 4.14.: New significance map and normalised excess map of HESS J1825–137. In the significance map the colour threshold for the transition from blue to red is set to $5\,\sigma$. For better comparability the colour scale of the normalised excess map is adapted to the one used in Fig. 3.3.

emission region associated with HESS J1825–137. This approach resulted in truncated representations of the adjoining VHE γ-ray source LS 5039, but allowes detailed studies of the morphology of HESS J1825–137. In Fig. 4.14(a) the significance map of HESS J1825–137 is shown. In the colour scale the threshold for the transition from blue to red was fixed to $5\,\sigma$ so that the vast extension of HESS J1825–137 is clearly visible. Due to the huge size there are at least two subregions where probably more than one source contributed to the detected TeV emission: in the south the binary system LS 5039 and in the north the Eel nebulae associated with the radio-quiet pulsar PSR J1826–1256, cf. Sec. 3.2.2. In addition to the significance map in Fig. 4.14(b) the new normalized excess map is shown. Here, the colour scale was adapted to the one used in Fig. 3.3 to allow better comparison between the new and the old analysis. Anyhow the units on the z-axes differ as the acceptance maps in the Hillas and in the Model++ analysis are differently normalized. Nevertheless, the overall morphologies of the sky maps shown in Fig. 3.3 and Fig. 4.14(b) agree very well. Clearly visible are the vast extension, the asymmetry of the emission region and the significant offset of the emission maximum from the associated pulsar.

In the next chapter we will investigate in detail how the observed morphology agrees with a newly developed model. The sky region considered in this comparison, which in the following will be referred to as simulation region, comprises the whole emission region of HESS J1825–137 and is composed of two circular regions (region A and region B). To avoid any contamination by other sources two regions around LS 5039 and PSR J1826–1256 (region C) are excluded from the comparison. The sky map in Fig. 4.15(a) illustrates the resulting sky region and its composition. Additionally, the specifications of each region are listed in Tab. 4.1.

For the determination of the energy spectra in the new analysis the *Multiple Off Back-*

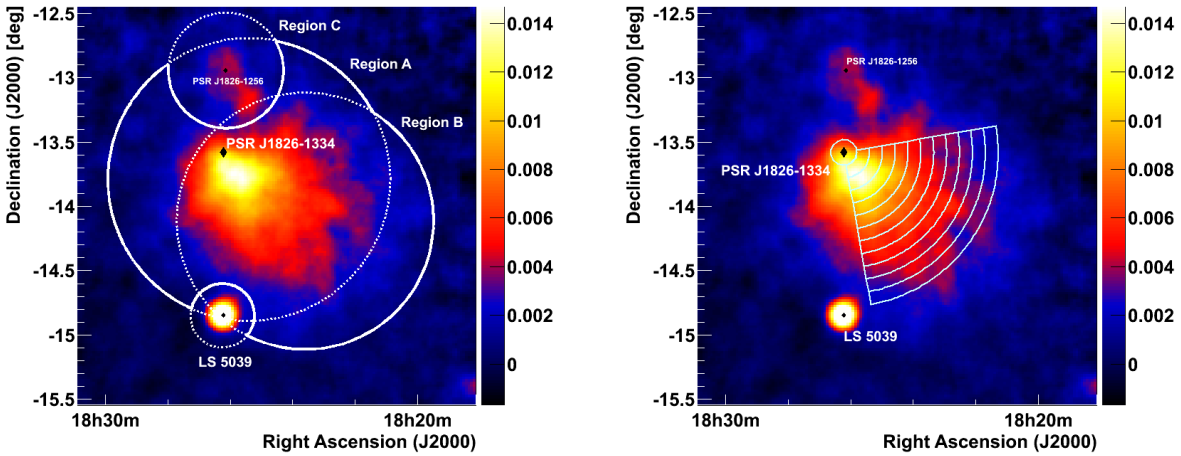

(a) Simulation region

(b) Wedge regions

Figure 4.15.: Illustration of regions of interest in the new analysis of HESS J1825–137. (a) The sky map region that will later be compared with the simulated data is composed of Region A & B. However, due to the contribution from other TeV sources the region around LS 5039 and Region C have to be excluded from this comparison. (b) The wedges that have been selected for spectrum extraction.

ground estimate was used. Unfortunately it was not possible to extract the total spectrum of the simulation region, since the region is very large and no off regions could be determined in the same field of view. Alternatively off regions from suitable off runs could be taken. However, the selection of suitable off runs is rather challenging and while such a procedure is included in the Hillas analysis, it is still under development in the Model++ analysis. Therefore, the determination of a total energy spectrum of HESS J1825–137 was postponed to future work. In the analysis presented here we were predominantly interested in deviations between energy spectra extracted from different locations within the emission region. Consequently, we re-analysed the wedge regions defined in the preceding H.E.S.S. publication, see Sec. 3.2.1. The location of the wedges is shown in Fig. 4.15(b) and their details are given in Tab. 4.1. Even for the smaller wedges it was not possible

name	center (Ra,Dec)	inner radius	outer radius	sector
region A	$(276.3510\,^\circ, -13.7906\,^\circ)$	-	$1.1\,^\circ$	-
region B	$(275.8990\,^\circ, -14.1142\,^\circ)$	-	$1.0\,^\circ$	-
region C	$(276.5354\,^\circ, -12.9434\,^\circ)$	-	$0.45\,^\circ$	-
LS 5039	$(276.5626\,^\circ, -14.8482\,^\circ)$	-	$0.25\,^\circ$	-
wedge 0	$(276.5549\,^\circ, -13.5797\,^\circ)$	-	$0.25\,^\circ$	-
wedge i	$(276.5549\,^\circ, -13.5797\,^\circ)$	$i \cdot 0.1^\circ$	$(i+1) \cdot 0.1^\circ$	[170°–260°]

Table 4.1.: Regions of interest in the new analysis of HESS J1825–137

to find suitable off regions in each run. In case of the inner wedges the observation position lay often within the wedges or close-by preventing any mirroring. For the outer wedges the extension of the regions hampered the positioning of the off regions between the exclusion regions. Consequently, the live times available for the spectrum extraction differed from wedge to wedge. The black line in the histogram in Fig. 4.16 shows how many hours of the total available 105.58 hours were used respectively. Furthermore, the detection significance of each wedge is indicated in blue.

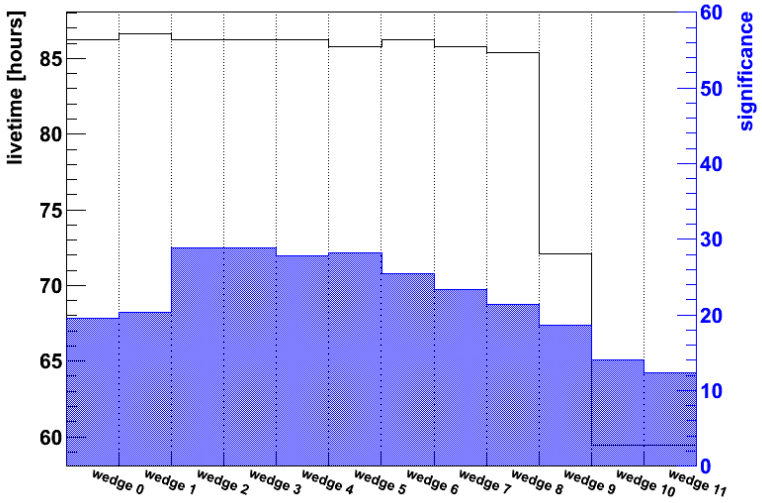

Figure 4.16.: Live time and significance per wedge in the new analysis of HESS J1825–137. With increasing size of the wedge regions it is more and more difficult to find suitable background regions in the same field of view. Therefore, the live time that can be used for the signal extraction is considerably reduced for wedge 9, 10 and 11. Nevertheless, the significances of the signals are well above 10 σ.

As in the preceding H.E.S.S. analysis of HESS J1825–137 the energy spectra of the wedges were fitted with power laws. For greater clarity detailed information on the fit results are summarised in the Appendix B.1. There, the Figures B.1, B.2 and B.3 show for each wedge the best fitting power law as a functions of the true energy and the fit values of all parameters are quoted. In addition, estimates of the spectrum points in true energy as well as the residuals for the reconstructed energy bins are presented. Neither the spectrum points nor the residuals indicate that the spectra would be better described by different spectrum shapes, e.g. broken power laws. Therefore, in Fig. 4.17 an overview of the best fitting power laws is given. To keep the single spectra visible, each spectrum was multiplied by a factor $10^{-(i-11)\times 3}$, where $i \in 0, ..., 11$ denotes the number of the respective wedge. Since an average significance of $3\,\sigma$ was requested for each spectrum point, the number of spectrum points varies per wedge. The red dashed lines indicate the course of the best fitting power law for wedge 0, when the same scaling as for the other energy spectra is applied. As in the preceding publication a steepening of the power-law index for wedges with greater distance to the pulsar is visible.

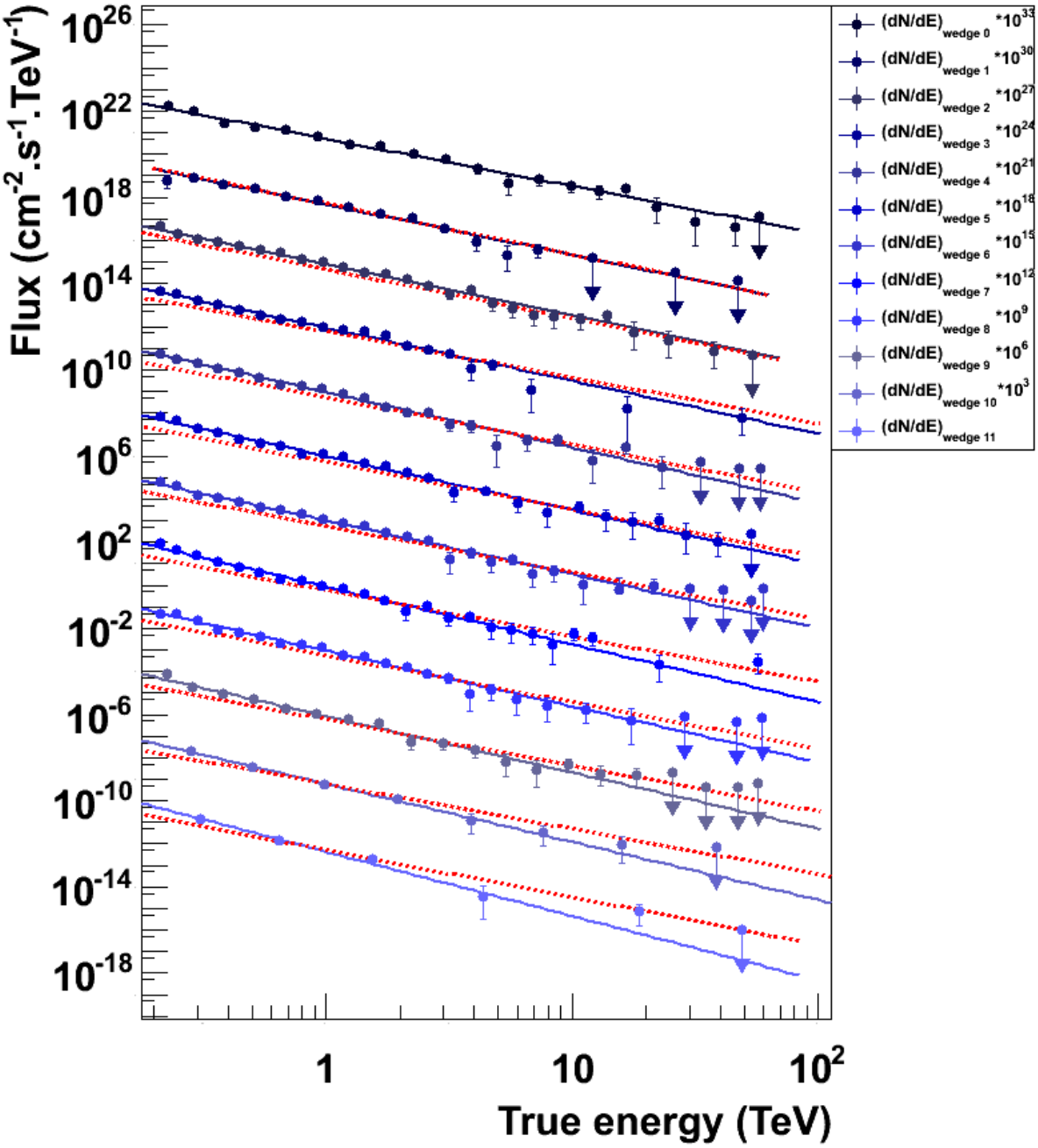

Figure 4.17.: The differential energy spectra for the different wedges are plotted in the style of Fig. 3.4 (top: wedge 0, bottom: wedge 11). The single spectra have been multiplied with powers of 10^3, so that all spectra can be shown in the same image. The solid bluish lines represent the best-fitting power law for each wedge, the bluish markers the forward folded spectrum points. Additionally, the dashed red lines indicate the course of the spectrum of wedge 0, when scaled with the same factor as the respective spectrum.

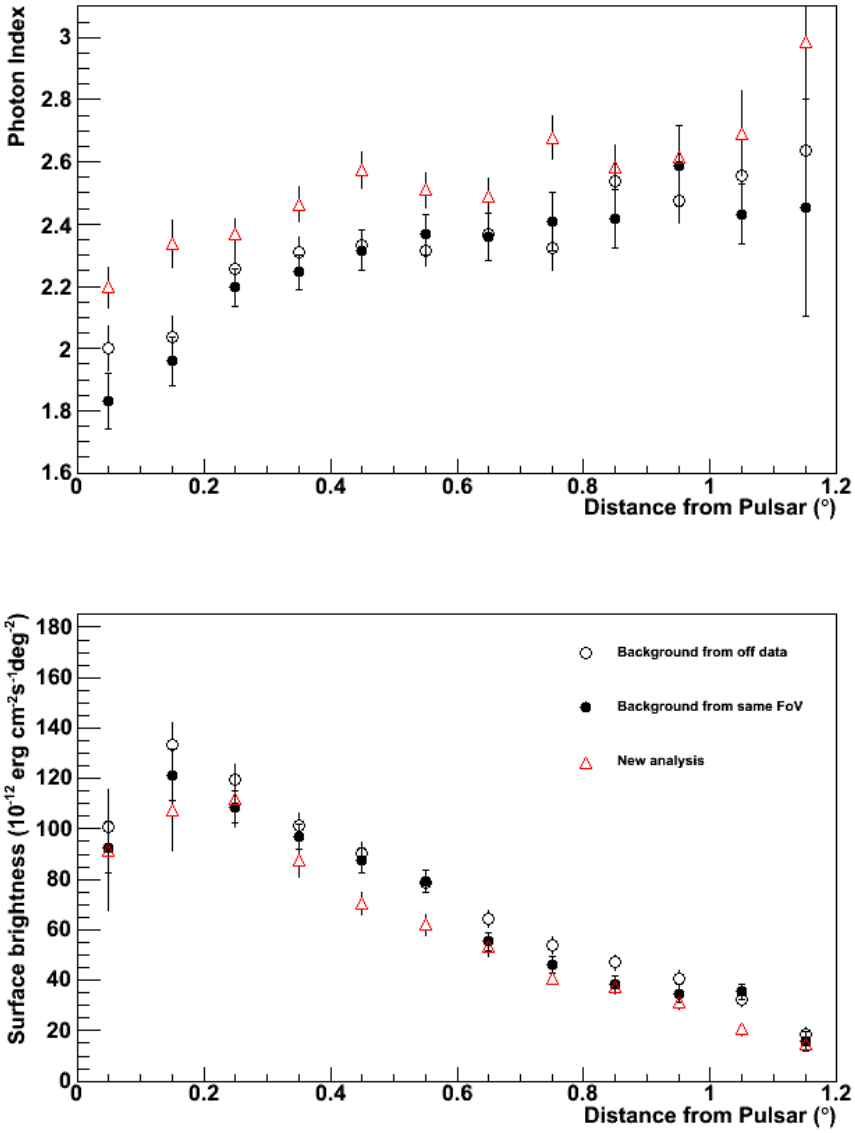

Figure 4.18.: Power-law index (top panel) and surface brightness (bottom panel) for the different wedges as a function of the distance to the pulsar. The black and white marker represent the data from the published analysis of HESS J1825–137, which have been obtained by means of different background estimates. The red triangles belong to new analysis of the increased data set, presented in this section. Note, that the energy range of the spectrum fit had been fixed to [0.25, 10] TeV in the old analysis, but was extended to the total available energy range in the new analysis. In the case of the surface brightness all graphs correspond to the restricted energy range.

Again, this tendency becomes even more evident when the power-law indices are plotted as a function of the distance to the pulsar, see upper part of Fig. 4.18. For comparison the results of the old Hillas analysis are also shown in this figure. The black circular data points correspond to the *Multiple Off Background* estimate, the white ones to a background estimate from pure off data. While the overall tendency is the same, the new data points (red outlined triangles) are shifted to higher values. To a certain extent this might be explained by the enlarged data sample and the differences between the new and the old analysis, i.e. the newly introduced forward-folding method in the spectrum determination. Careful analysis revealed, however, that this effect was mainly caused by the extension of the considered energy range. While the fit in the old analysis was restricted to energies between 0.25 TeV and 10 TeV, the new fit considered energies up to several tens of TeV. It seems that especially the observations at higher energies favoured steeper power laws. For completeness also the course of the surface brightness (restricted to an energy range between 0.25 TeV and 10 TeV) as a function of the distance to the pulsar is shown in the lower part of Fig. 4.18. In this case the steeper power laws result in a systematic shift to lower values.

In the following chapter a model will be presented which allows to study the energy-dependent morphology of evolved PWNe such as HESS J1825–137. In particular, the model can be used to calculate for arbitrary sky regions the expected energy spectra of the VHE γ rays. We will use this feature to compute the energy spectra of the wedges of the HESS J1825–137 analysis and compare these results with measurements. However, the choice of wedges is often rather arbitrary and by restricting ourselves to sub regions of the emission region, we neglect information. Hence, a long-term objective would be to not consider the energy spectra of arbitrarily chosen sky regions, but the distribution of all photons in a 3-dimensional histogram with two dimensions for the position in space and one dimension for the energy. Such a 3-dimensional distribution would be well suited for a comparison with the predictions of the model. However, the development of an algorithm which handles such 3-dimensional histograms requires fundamental changes to the software at hand which are out of the scope of this thesis. Instead, it was decided to work with the available routines.

Another feature of the measured data which can be compared with the predictions of the model by means of the available software is the overall morphology. In Sec. 4.3.4 it was reported that within the H.E.S.S. software framework there is the possibility to fit different morphology shapes to the H.E.S.S. sky maps. Considering these rather simple shapes the model that will be presented in the next chapter provides in principle too much information, viz. the source morphology in dependence on the energy (e.g. Fig. 5.3). However, it is of course possible to computationally eliminate this additional information, e.g. by adding up the spatial distributions of all energy slices. In doing so an energy-integrated morphology is obtained which can be compared with the measurements by means of the available routines. As was shown in Sec. 4.3.4 in the default morphology fit the predicted source events (n_{s}) are compared bin-wise with the detected on and off events (N_{on} and N_{off}). The sky maps which depict the information about N_{on} and N_{off} for the new analysis are presented in Figures 4.19(a) and (b). To be able to calculate the bin-wise log-likelihood, cf. Eq. 4.17, we also have to know the normalisation parameter α for each

bin. Following Eq. 4.11 the latter can be determined from the sky acceptance maps for γ- and hadron-like events. Both sky maps are shown in the lower panel of Fig. 4.19.

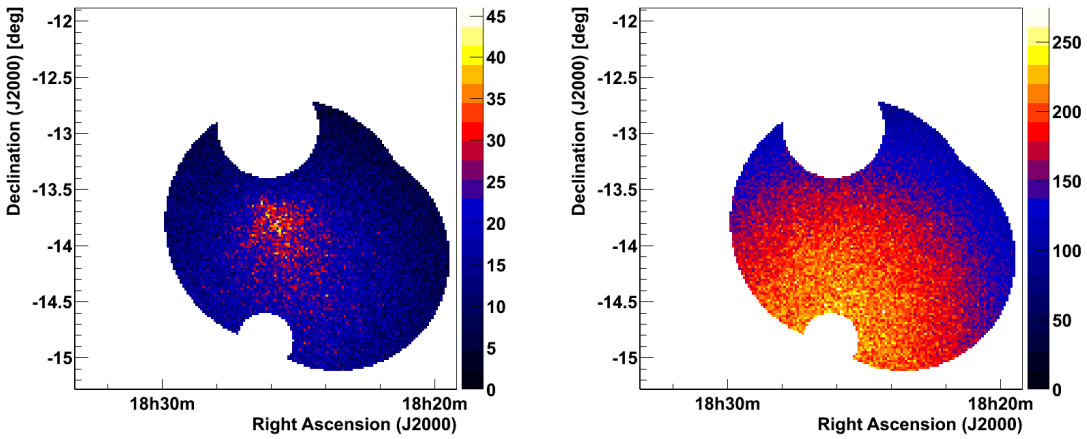

(a) Count map of γ-like events

(b) Count map of hadron-like events

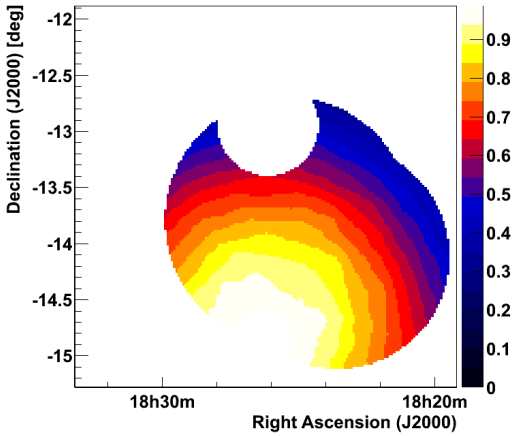

(c) Acceptance map for γ-like events

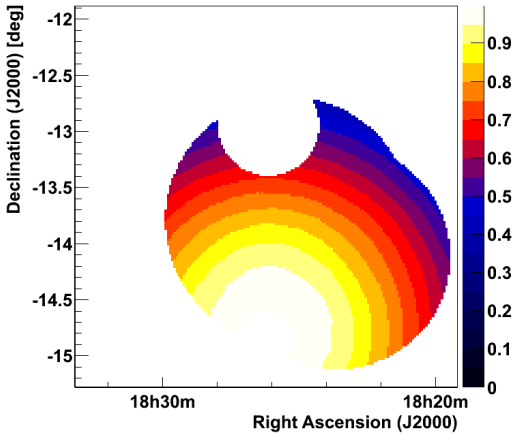

(d) Acceptance map for hadron-like events

Figure 4.19.: Various sky maps from the new analysis of HESS J1825–137, which are used in morphology fits. The default sky map binning size of $0.02° \times 0.02°$ was used. In the upper panel the count maps for γ- and hadron-like events (N_{on} and N_{off}) and in the lower panel the corresponding relative acceptance maps are presented. Note that, data is only shown for the sky region which will be used in the simulation.

Concerning the calculation of the expected source events per sky map bin it should be noted that in the default morphology fit procedure this number is obtained by convolving the specified energy-independent morphology shape with the point spread function of the telescopes and by weighting the result with the respective γ-ray acceptance, see Eq. 4.16. In the analysis presented here this procedure had to be slightly modified: Since the new model predicts the energy spectra per sky map bin, the expected number of source events

is obtained by convolving the spectra with the respective effective area and live time and by smoothing the spatial distribution with the PSF. Using the energy-dependent effective areas has the advantage that the non-uniform detection probabilities for photon events with deviating energies are taken into account. In this work the effective areas were made accessible by a 3-dimensional histogram which contained in each bin the effective area corresponding to the respective energy and sky position. In the calculation of the effective area per bin it was considered that the particular sky positions had been observed under different observation conditions, i.e. zenith and offset angles and muon efficiencies. To account for these differences the 3-dimensional effective area histograms were at first calculated for each observation run, taking into account the appropriate muon efficiency, the mean zenith angle of the observation as well as the offsets of the respective sky map bins. Afterwards, the total effective area histogram was obtained by summing up the effective area histograms of the individual runs, which had been weighted with the respective live time.

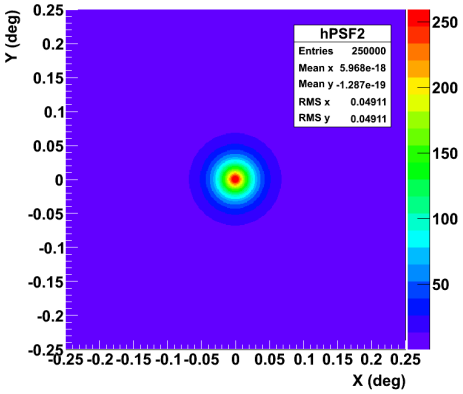

Figure 4.20.: Averaged 2-dimensional PSF of the new analysis of HESS J1825–137.

As final step in the calculation of the expected number of source events per sky map bin the distribution obtained by convolving the energy spectra with the effective areas and the live time had to be convolved once more, this time with the point spread function. As has been stated before, the PSF depends on the following ascendancies: the spectral index (it is assumed that the energy spectrum of the observed source can be described by a power law), the zenith angle and the offset of the observation position to the centre of the camera. The H.E.S.S. software provides look-up tables – which have been generate by means of Monte Carlo Simulations – for the different combinations of these three parameters. In the default calculation procedure at first the energy spectrum and thus the spectral index of the investigated source is determined. Unfortunately, this wasn't possible in the analysis presented here, since due to the sheer extent of the source no suitable background regions could be defined within the FoV. Instead, a spectral index of 2.5 was chosen, which corresponds to an intermediate index obtained for the various wedges. As the zenith and the offset angle of the target positions change from observation run to observation run, PSFs were determined for each run separately. The final PSF ascribed to the observation as a whole, was again determined by summing up the individual PSFs, which were weighted with the respective live time. The corresponding PSF is presented in Fig. 4.20. Its 68 % containment radius is 0.07°. For the future it would be desirable to access the probability density function for the direction reconstruction for photon events with specific energy, zenith and offset angle, but for the moment this is beyond the scope of this thesis.

5. A New Model for the Non-thermal Emission of HESS J1825–137

Based on the general PWN models presented in Sec. 2.4 and those specifically adapted to HESS J1825–137, see Sec. 3.5 and 3.6, we developed a new model with the aim to investigate the spatial and spectral features of the TeV γ-ray emission of HESS J1825–137 in more detail. In contrast to former models we wanted to refrain from steady-state assumptions, as well as from the restriction to one-zone or radially symmetric models, as these are in conflict with the observed features of HESS J1825–137. Instead, our aim was to include the time-dependence of the spin-down luminosity, the proper motion of the pulsar and the spatial evolution with its preferred direction. The main purpose of the newly developed model was to reproduce the features in the enlarged TeV data set presented in the previous chapter. In this chapter we will proceed in the following way: In the first subsection the basics of the model will be presented. Step-by-step it will be demonstrated which assumptions were made for the injected lepton population, for the particle propagation, the cooling processes and finally the photon emission processes. All in all, the model enabled us to calculate photon spectra for subareas of the emission region as well as sky maps covering the total emission region. The subsequent chapters will be dedicated to the search for the parameter sets that reproduced the measured data best. For this purpose the model parameter space was scanned and by means of a minimisation procedure parameter sets were identified which predicted the energy spectra of the wedge analysis particularly well. For the selected parameter sets the model predictions for the energy spectra in GeV γ rays and X-rays, as well as for the morphology of the H.E.S.S. sky maps will be compared to the observations presented in Chapter 2. Finally, alternative optimising methods will be discussed.

5.1. The New Model

Since, among the PWNe detected in TeV γ rays, HESS J1825–137 currently is the one with the largest angular extent and also one of only two PWNe for which an energy-dependent morphology has been verified, we wanted to develop a model that surpasses the widespread one-zone models. In this context the mechanisms that are assumed for the particle propagation are of particular importance. For young PWNe and for regions close to the termination shock the prevailing mechanism is convection. In contrast, for evolved

PWNe the influence of diffusion processes will be of increasing importance. Indeed, van Etten et al. have presented a model for HESS J1825–137 which is primarily based on convection, see Sec. 3.6. However, to be able to describe the observed data they had to modify their model by including some kind of diffusion processes as well. In this thesis we decided to choose a complementary approach and investigated whether the observed TeV emission could be explained by diffusive processes only. In doing so and in contrast to the model presented by van Etten et al., we do not need to assume particle emission in a rather arbitrarily defined spherical sector, do not rely on symmetry assumptions and can account for the proper motion of the pulsar. The details of our modelling will be presented in the following.

Distribution of Leptons

The first step in the modelling process is the calculation of the spatial distribution of the electrons. For this purpose, in cooperation with Prof. Klaus Mecke (Professor of Theoretical Physics at the University of Erlangen-Nuremberg) we developed a model that allowed us to combine a diffusion assumption with the proper motion of the pulsar and an additional drift velocity of the particles.

The starting point of our considerations is the density distribution of the leptons $\rho(\vec{r}, t)$ in space $\vec{r} \in \mathbb{R}^3$ and time $t \in \mathbb{R}$. In our diffusion approach the diffusion equation in its simplest form

$$\partial_t \rho(\vec{r}, t) - D \cdot \Delta\rho(\vec{r}, t) = 0 \tag{5.1}$$

is based on the assumption that the number of particles is conserved, i.e. that the continuity equation

$$\partial_t \rho(\vec{r}, t) + \vec{\nabla}\vec{j}(\vec{r}, t) = 0, \tag{5.2}$$

is satisfied and that the particle current $\vec{j}(\vec{r}, t)$ is proportional to the gradient of the density distribution:

$$\vec{j}(\vec{r}, t) = -D \cdot \vec{\nabla}\rho(\vec{r}, t)\ . \tag{5.3}$$

To be able to use this equation in the modelling of HESS J1825–137 two assumptions have to be made. The first is that we neglect any energy-dependence in the diffusion equation. This means that initially it is not taken into account that the particle density in the considered energy range also changes due to energy losses. Instead, in this first instance it is assumed that the propagation of the particles is only influenced by the the total particle density and the energy losses are incorporated later in a separate calculation step. However, this assumption requires that the diffusion process and in particular the diffusion coefficient do not depend on the energy of the respective particle. This is indeed a rather rough approximation. As was shown in Sec. 2.4.5 the CR diffusion in the interstellar medium is usually described by a diffusion coefficient that is proportional to $\left(\frac{E}{1\,\mathrm{GeV}}\right)^{0.3}$. Taking into account this dependency, however, would complicate the calculations significantly. Therefore, we decided to start with the simplified assumption and postpone a full treatment to future work. A helpful starting-point for the computation

of energy-dependent diffusion is the diploma thesis of J. Hahn [Hah10]. The second simplification is that we vassume that the diffusion coefficient does neither depend on the position in space nor on the specific time. In the interstellar medium this may be a well justified assumption. However, close to the pulsar and in particular under the influence of the strong magnetic field deviations are even expected. Nevertheless, the present knowledge about these processes is still very limited, see Sec. 2.4.4, and thus we decided to give the simplified assumption of a constant uniform diffusion coefficient a try. Again, improvements are postponed to future work.

In order to model the TeV observation of HESS J1825–137 by means of Eq. 5.1 some modifications have to be made. At first a source term has to be added, as particles are continuously injected into the PWN by the pulsar. In this context, it has to be considered that the spin-down of the pulsar is time-dependent. Thus, the total particle current is given by $\tau^{-1}(t)$. Since structures like the pulsar wind or the termination shock are far below the resolution power of current TeV experiments, it is further assumed that the particles are injected into the PWN at the position of the pulsar. In the case of HESS J1825–137 one also has to account for the fact that the pulsar moves with a constant velocity $\vec{v}_\mathrm{p}$ and that its time-dependent position is given by $\vec{R}(t) = \vec{R}_0 + \vec{v}_\mathrm{p} t$. Therefore, the diffusion equation takes on the following form

$$\partial_t \rho(\vec{r}, t) + \vec{\nabla}\vec{j}(\vec{r}, t) = \frac{1}{\tau(t)}\, \delta(\vec{r} - \vec{R}(t)) \,. \tag{5.4}$$

Due to the proper motion of the pulsar the emitted leptons have at least initially an additional momentum $m_\mathrm{e}\vec{v}_p$. Hence, the emitted leptons are dragged by the pulsar, i.e. the whole medium around the star is also moving with a velocity $\vec{v}_\mathrm{p}$. We model this effect by including an additional current $\vec{j}_\mathrm{p} = \rho \cdot \vec{v}_\mathrm{p}$ in Eq. 5.3:

$$\vec{j}(\vec{r}, t) = \vec{v}_\mathrm{p} \cdot \rho(\vec{r}, t) - D \cdot \vec{\nabla}\rho(\vec{r}, t) \,. \tag{5.5}$$

Moreover, due to the inhomogeneities in the surrounding medium, e.g. the molecular clouds, it is very likely that the evolution of the pulsar wind nebula does not proceed symmetrically but asymmetrically. In particular it is assumed that the reverse shock from the supernova returns earlier from the direction of the denser surrounding medium. In the same way as for the drag velocity we included an approximation of this effect by inserting an additional drift velocity $\vec{v}_\mathrm{D}$ of the leptons into Eq. 5.3:

$$\vec{j}(\vec{r}, t) = (\vec{v}_\mathrm{D} + \vec{v}_\mathrm{p}) \cdot \rho(\vec{r}, t) - D \cdot \vec{\nabla}\rho(\vec{r}, t) \,. \tag{5.6}$$

Including these assumptions in the original diffusion equation, we finally end up with the following modified diffusion equation:

$$(\partial_\mathrm{t} + (\vec{v}_\mathrm{D} + \vec{v}_\mathrm{p}) \cdot \vec{\nabla} - D \cdot \Delta)\, \rho(\vec{r}, t) = \frac{1}{\tau(t)}\, \delta(\vec{r} - \vec{R}(t)) \,. \tag{5.7}$$

This inhomogeneous differential equation can be solved by means of a Green's function $G(\vec{r}, t)$, so that

$$\rho(\vec{r}, t) = G(\vec{r}, t) \otimes \frac{1}{\tau(t)}\, \delta(\vec{r} - \vec{R}(t)) = \int\limits_{\mathbb{R}} \mathrm{d}t' \int\limits_{\mathbb{R}^3} \mathrm{d}\vec{r}'\, G(\vec{r} - \vec{r}', t - t') \cdot \frac{1}{\tau(t')}\, \delta(\vec{r}' - \vec{R}(t')) \,. \tag{5.8}$$

A rather simple way to determine the Green's function is a transformation into Fourier space, e.g. $\tilde{f}(\vec{k},t) = \int_{\mathbb{R}^3} \mathrm{d}^3\vec{r}\; f(\vec{r},t)\, e^{-i\vec{k}\cdot\vec{r}}$. Due to the constant coefficients in Eq. 5.7 the Fourier-transformed Green's function $\tilde{G}(\vec{k},\omega)$ obeys the relation

$$\tilde{G}(\vec{k},\omega) = \frac{1}{i\omega + i\,(\vec{v}_\mathrm{D} + \vec{v}_\mathrm{p})\,\vec{k} + D\vec{k}^2}. \tag{5.9}$$

Inverse transformation yields

$$\begin{aligned} G(\vec{r}-\vec{r}\,';t-t') &= \int\limits_{\mathbb{R}} \frac{\mathrm{d}\omega}{2\pi} \int\limits_{\mathbb{R}^3} \frac{\mathrm{d}^3\vec{k}}{(2\pi)^3}\; \tilde{G}(\vec{k},\omega)\, e^{i\vec{k}\cdot(\vec{r}-\vec{r}\,')+i\omega(t-t')} \\ &= \int\limits_{\mathbb{R}} \frac{\mathrm{d}\omega}{2\pi} \int\limits_{\mathbb{R}^3} \frac{\mathrm{d}^3\vec{k}}{(2\pi)^3}\; \frac{e^{i\vec{k}\cdot(\vec{r}-\vec{r}\,')+i\omega(t-t')}}{i\omega + i(\vec{v}_\mathrm{D}+\vec{v}_\mathrm{p})\vec{k} + D\vec{k}^2}. \end{aligned} \tag{5.10}$$

The integration over ω can be performed by means of the residue theorem, so that

$$G(\vec{r}-\vec{r}\,';t-t') = \begin{cases} \int\limits_{\mathbb{R}^3} \frac{\mathrm{d}^3\vec{k}}{(2\pi)^3} e^{i\vec{k}\cdot(\vec{r}-\vec{r}\,'-(\vec{v}_\mathrm{D}+\vec{v}_\mathrm{p})(t-t'))-D\vec{k}^2(t-t')}, & \text{if } t \geq t', \\ 0, & \text{if } t < t' \end{cases}. \tag{5.11}$$

Moreover, for $t \geq t'$ the integral can be evaluated with the help of the Gaussian integrals and thus the Green's function of the diffusion operator of Eq. 5.7 with open boundaries reads

$$G(\vec{r}-\vec{r}\,';t-t') = \frac{1}{(4\pi D(t-t'))^{\frac{3}{2}}} e^{-\frac{(\vec{r}-\vec{r}\,'-(\vec{v}_\mathrm{D}+\vec{v}_\mathrm{p})(t-t'))^2}{4D(t-t')}}\;, \tag{5.12}$$

and fulfils

$$\int\limits_{\mathbb{R}^3} \mathrm{d}^3\vec{r}\, G(\vec{r}-\vec{r}\,';t-t') = 1\;. \tag{5.13}$$

The lepton density $\rho(\vec{r},t)$ is finally obtained by inserting Eq. 5.12 into Eq. 5.8. To check the plausibility of our results, we first consider the case that the leptons are only injected at $t' = 0$. Then the right-hand side of Eq. 5.7 reads $\frac{1}{\tau_0}\delta(\vec{r}-\vec{R}_0)\delta(t-0)$ and the lepton density is given by

$$\begin{aligned} \rho(\vec{r},t) &= \int\limits_{\mathbb{R}^3} \mathrm{d}^3\vec{r}\,'\; G(\vec{r}-\vec{r}\,';t-0)\; \frac{1}{\tau_0}\; \delta(\vec{r}-\vec{R}_0) \\ &= \frac{1}{\tau_0\,(4\pi D t)^{\frac{3}{2}}} e^{-\frac{(\vec{r}-\vec{R}_0-(\vec{v}_\mathrm{p}+\vec{v}_\mathrm{D})t)^2}{4Dt}}\;. \end{aligned} \tag{5.14}$$

As expected the typical broadening of diffusing particles yielding a Gaussian density profile with maximum at $\vec{r}_\mathrm{max} = \vec{R}_0 + (\vec{v}_\mathrm{p}+\vec{v}_\mathrm{D})t$ is found. In the more general case that leptons are also emitted for $t > 0$ the lepton density is given by

$$\rho(\vec{r},t) = \int_0^t \frac{\mathrm{d}t'}{\tau(t')} \int_{\mathbb{R}^3} \mathrm{d}^3\vec{r}\,'\; G(\vec{r}-\vec{r}\,';t-t')\,\delta(\vec{r}\,' - \vec{R}_0 - \vec{v}_\mathrm{p}t')$$

$$= \int_0^t \frac{\mathrm{d}t'}{\tau(t')} \frac{\exp\left\{-\frac{(\vec{r}-\vec{R}_0-\vec{v}_\mathrm{p}t'-(\vec{v}_\mathrm{p}+\vec{v}_\mathrm{D})(t-t'))^2}{4D(t-t')}\right\}}{(4\pi D(t-t'))^{\frac{3}{2}}}. \tag{5.15}$$

Substituting the age of the lepton population $t^* = t - t'$, Eq. 5.15 can be simplified even further to

$$\rho(\vec{r},t) = \int_0^t \frac{\mathrm{d}t^*}{\tau(t-t^*)} \frac{\exp\left\{-\frac{(\vec{r}-\vec{R}_0-\vec{v}_\mathrm{p}t-\vec{v}_\mathrm{D}t^*)^2}{4Dt^*}\right\}}{(4\pi Dt^*)^{\frac{3}{2}}} \,. \tag{5.16}$$

For the assessment of the lepton distribution of HESS J1825–137 by means of the presented model, the total particle current can be estimated from the spin-down of the pulsar. In doing so it is assumed that the time-dependent energy output of the pulsar is described by Eq. 2.13. Moreover, our model is based on the presumption that the energy spectrum of the injected electrons can be described by Eq. 2.14. Since we are only interested in the electrons responsible for the X-ray and γ-ray photons, only the case $E_\mathrm{b} \leq E < E_\mathrm{max}$ is considered:

$$\frac{\mathrm{d}N}{\mathrm{d}E\,\mathrm{d}t}(t) = N_0(t) \left(\frac{E}{1\ \mathrm{TeV}}\right)^{-\alpha}, \tag{5.17}$$

with time-dependent normalisation N_0, but constant index α. From the assumption that the acceleration process at the termination shock stays the same at all times it is concluded that the fraction η of the spin-down energy of the pulsar that is converted into leptons in the considered energy range stays the same, as well:

$$\int_{E_\mathrm{b}}^{E_\mathrm{max}} \frac{\mathrm{d}N}{\mathrm{d}E\mathrm{d}t}(t)\, E\, \mathrm{d}E = \eta\, \dot{E}(t). \tag{5.18}$$

η is a free parameter of the model. For a pulsar such as PSR J1826–1334, for which the present rotation period and its time derivative have been measured, $\dot{E}(t)$ can be calculated by means of Eq. 2.13. However, in doing so an additional dependency of the model on the assumed original rotation period of the pulsar P_0 and the braking index n is introduced. Inserting Eq. 5.17 into Eq. 5.18:

$$\int_{E_\mathrm{b}}^{E_\mathrm{max}} N_0(t) \left(\frac{E}{1\ \mathrm{TeV}}\right)^{-\alpha} E\, \mathrm{d}E = \eta\, \dot{E}(t)\,, \tag{5.19}$$

it is possible to determine $N_0(t)$:

$$N_0(t) = \begin{cases} \frac{1}{(1\ \mathrm{TeV})^2 \ln(E_\mathrm{max}/E_\mathrm{b})}\, \eta\, \dot{E}(t)\,, & \text{if } \alpha = 2 \\ \frac{-\alpha+2}{\left(E_\mathrm{max}^{-\alpha+2} - E_\mathrm{b}^{-\alpha+2}\right)(1\ \mathrm{TeV})^\alpha}\, \eta\, \dot{E}(t)\,, & \text{if } \alpha \neq 2 \end{cases}. \tag{5.20}$$

Hence, the total particle current is given by

$$\tau^{-1}(t) = \int_{E_\mathrm{b}}^{E_\mathrm{max}} N_0(t) \left(\frac{E}{1\ \mathrm{TeV}}\right)^{-\alpha} \mathrm{d}E = \begin{cases} \frac{N_0(t)}{(1\ \mathrm{TeV})^{-1}}\, \ln\left(\frac{E_\mathrm{max}}{E_\mathrm{b}}\right), & \text{if } \alpha = 1 \\ \frac{N_0(t)}{(-\alpha+1)(1\ \mathrm{TeV})^{-\alpha}} \left(E_\mathrm{max}^{-\alpha+1} - E_\mathrm{b}^{-\alpha+1}\right) & \text{if } \alpha \neq 1 \end{cases}. \tag{5.21}$$

At the end of this section the predicted distribution of the leptons shall be visualised. For this purpose as many parameters of the model as possible have been fixed to values known for PSR J1826–1334 (cf. Tab 3.1), viz. the position, the distance, the proper motion, the present period and its time derivative as well as the present spin-down luminosity of the pulsar. It should be noted that, while the model predicts the lepton density in the 3-dimensional space, the velocities of the pulsar and of the drift are assumed to be effectively 2-dimensional, i.e. the vectors have only non-zero components in the plane perpendicular to the line-of-sight to the pulsar. This assumption is vindicated since later we will consider projections of the particle distributions onto sky maps so that the third component of the vector will not have any influence.

For a first impression of the predicted lepton distribution the remaining free parameters of the model have been set to reasonable values for PWNe and in particular for HESS J1825–137: $P_0 = 20\,\mathrm{ms}$, $\alpha = 2.0$, $n = 3.0$, $\eta = 0.4$, $E_\mathrm{b} = 0.1$ TeV, $E_\mathrm{max} = 500$ TeV, $v_{\mathrm{D,x}} = -74.9$ mas yr^{-1}, $v_{\mathrm{D,y}} = -77.9$ mas yr^{-1}, $D = 5 \cdot 10^{-2}$ pc^2 yr^{-1}, $B = 10\,\mu\mathrm{G}$. Since the main purpose of the model is to predict the γ-ray photon distribution as observed in the H.E.S.S. sky maps, see Fig. 4.19, an analogue representation was chosen for the lepton distribution. This means, that while the model predicts the lepton density, cf. Eq. 5.16, in Fig. 5.1 the integrated quantity is shown. The limits of the integration are given by the physical dimensions of the sky map bins, i.e. $0.02^\circ \times 0.02^\circ$, and by $[-\infty, +\infty]$ in the direction perpendicular to the sky map. The integration of Eq. 5.16 has been performed numerically.

The quoted parameters can be used to calculate today's age of the modelled PWN, cf. Eq. 2.9: $t_\mathrm{age} = 20.607\,\mathrm{kyr}$. Subsequently the present distribution of the leptons can be determined by identifying t with t_age in Eq. 5.16 and by evaluating the integration in time and space. The corresponding sky map is presented in the upper left panel in Fig. 5.1. Having a close look at Eq. 5.16, this means that all contributions from lepton populations that have been emitted at different times throughout the evolution of the pulsar are summed up. This interpretation of Eq. 5.16 can further be used to study not only the spatial distribution of all leptons that have ever been emitted, but also the distribution of leptons that have been emitted within specific epochs. For this purpose the integration over $\mathrm{d}t^*$ must only be restricted to the time range one is interested in. An example is shown in Fig. 5.1. For this purpose the present age of the pulsar has been divided in 100 equidistant time bins ($\Delta t = 206.07\,\mathrm{yr}$). The sky maps in Fig. 5.1 show the spatial distribution of the leptons that have been emitted in the time bin immediately after the formation of the pulsar Fig. 5.1(b), in the time bin in the middle of the past lifetime, Fig. 5.1(c), and in the very last time bin before today, Fig. 5.1(d). This representation illustrates that the oldest lepton population is widely spread, while the youngest population is confined in the region close to the pulsar at the centre of the sky map. However, since the spin-down luminosity of the pulsar has decreased during the evolution of the PWN, the contribution of the youngest population to the total number of leptons is less significant than that of the oldest population. Of course, the exact distribution depends strongly on the choice of the free parameters. Nevertheless, already these arbitrarily chosen parameters nicely reproduce the peculiar morphological features of HESS J1825–137, i.e. the asymmetry of the emission region and the offset of the peak emission to the present

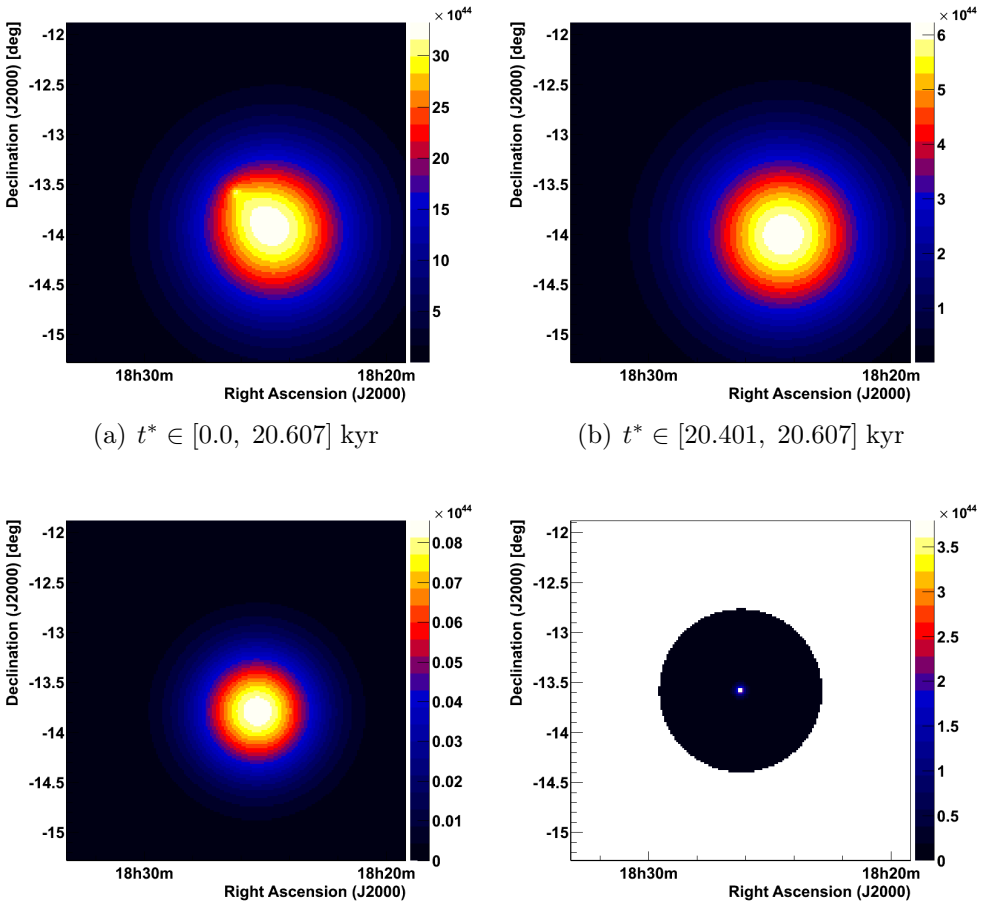

(a) $t^* \in [0.0,\ 20.607]$ kyr

(b) $t^* \in [20.401,\ 20.607]$ kyr

(c) $t^* \in [10.047,\ 10.303]$ kyr

(d) $t^* \in [0.0,\ 0.206]$ kyr

Figure 5.1.: New model: Simulation of lepton distributions. The free parameters of the model have been fixed to typical values for PWNe, see text for details. The presented sky maps map the number of leptons expected within a sky map bin, obtained by integrating Eq. 5.16 along the line of sight and over the bin area (i.e. $0.02° \times 0.02°$). The sky map on the top left (a) illustrates the current distribution of all leptons that have been injected during the previous evolution of the PWN. The centre of the sky map is equivalent to the present position of the pulsar. The other three sky maps show the present-day distributions of lepton populations that have been injected at different times in the lifetime of the pulsar: right after the birth of the pulsar $t' \in [0.0,\ 0.206]$ kyr (b), within $t' \in [10.304,\ 10.560]$ kyr (c) and very recently before today $t' \in [20.401,\ 20.607]$ kyr (d). Note, that t' denotes the period which at the time of the lepton emission has passed since the birth of the pulsar, while t^* denotes the complementary age of the lepton population.

pulsar position. For more precise statements about the suitability of the model to reproduce the observed γ-ray emission energy losses and photon emission processes have to be included as well. The implementation will be presented in the next subsections.

Cooling of Leptons

Synchrotron losses dominate the radiative energy losses of electrons in PWNe in magnetic fields with $B > 3\,\mu\mathrm{G}$, see Sec. 2.4.6. Therefore, in our model we concentrated as a start on this kind of energy losses. Due to the huge uncertainties in the dependency of the magnetic field on time and location, see Sec. 2.4.4, we further decided to examine in our first modelling attempt the most simple assumption of a constant magnetic field. In future studies this assumption may be replaced by approximations like those shown in Sec. 2.4.4. Preliminary work towards this objective has already been presented by our working group [M$^+$12]. Moreover, in future studies it will be desirable to include IC losses as well. Due to the analogy of Eqs. 2.27 and 2.29 only small modifications to the chosen approach will be necessary, at least as long as the losses take place in the Thomson regime. When the Klein-Nishina regime shall be considered as well the calculation gets more involved, but successful approaches have for instance been presented in [Hah10] or [H$^+$11]. Another challenge for the future is the incorporation of adiabatic energy losses in asymmetric evolved PWN models, see Sec. 2.4.6. For the moment we follow the argumentation that a large part of these losses may be compensated during the crushing by the reverse shock and that they may therefore be neglected.

Returning to the computation of the energy losses in our model, a relation describing the evolution of the energy E of an electron with original energy E_0 as a function of the age of the lepton t_a can be derived on the basis of Eq. 2.28, assuming a constant magnetic field:

$$E_\mathrm{TeV}(t_\mathrm{a}) = \frac{1}{1/E_{0,\mathrm{TeV}} + \beta t_\mathrm{a}}, \tag{5.22}$$

where $\beta = (B_\mathrm{\mu G})^2/(1.3 \times 10^7\ \mathrm{yr})$. For a given electron injection spectrum this equation allows the calculation of the energy distribution of the leptons after arbitrary time periods. Let us see how this can be used in our model. For simplicity we will first consider the case that the total energy spectrum of a PWN shall be determined. For this purpose the present age of the pulsar is divided into equidistant time bins and for each bin the spectral distribution of the corresponding electron population as of today is calculated. In this calculation it is assumed that the initial total energy spectrum of the electrons is given by $\frac{\mathrm{d}N}{\mathrm{d}E} = k\left(\frac{E}{1\ \mathrm{TeV}}\right)^{-\alpha}$. Thus, k can be computed by integrating Eq. 5.21 over the corresponding time interval. For the calculation of the cooled energy spectrum of the respective electron population we further adopt the approximation that all electrons in the time bin have been emitted at once at the same instant of time, which is chosen as the centre of the corresponding time bin. Based on this assumption the cooled energy spectrum of the electron population can be derived by means of Eq. 5.22. The total energy spectra of the leptons in the PWN can easily be obtained by adding up the contributions

from all populations.

For the computation of the expected energy spectrum in an arbitrary sky region, e.g. a wedge or a sky map bin, it has to be considered that only a certain percentage of the respective electron population is located within the boundaries of the considered region. By following the approach described in the previous section, i.e. by integrating Eq. 5.16 within the appropriate integration limits, this percentage can be determined for each population. Subsequently, the cooled energy spectra are scaled accordingly, before they are finally added up again.

For the studies presented here 100 equidistant time bins, sampling $[0,\ t_{\mathrm{age}}]$, and 10 000 equidistant logarithmic energy bins, covering the energy range $[E_{\mathrm{b}},\ E_{\mathrm{max}}]$, were used. While the choice of the number of time and energy bins may seem arbitrary, in fact they were chosen such that a further refinement did no longer noticeably change the resulting photon spectra for the investigated spectrum wedges. This was tested by means of parameter sets that well reproduced the observed γ-ray emission.

Photon Spectra

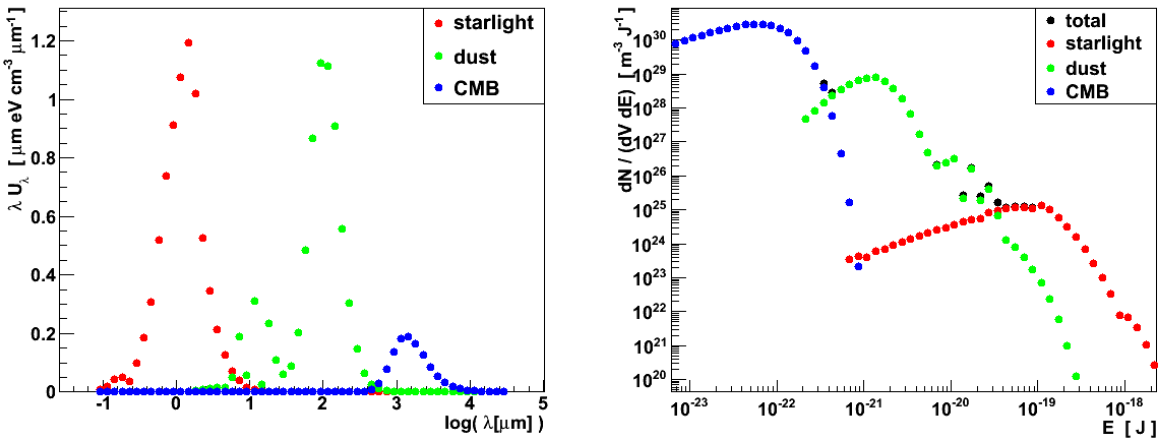

Figure 5.2.: Spectral energy and number density of the local photon fields in the vicinity of HESS J1825–137.

Once the total electron energy spectrum of the investigated region has been calculated the corresponding synchrotron emission in the X-ray regime can be determined by means of Eq. 2.19. In the case of the IC emission in the γ-ray regime the calculation is a little bit more complicated, as an estimate of the contributing photon fields has to be obtained first. The target photon fields considered in the presented model are the cosmic microwave background, starlight and photons from dust emission. While the CMB exhibits a very high degree of spatial uniformity, a good estimate of the other two photon fields at the location of PSR J1826–1334 can be obtained from the GALPROP code[8]. GALPROP is

[8] http://galprop.stanford.edu/

a public numerical code which is used by the scientific community to model the propagation of relativistic charged particles and the corresponding diffuse emission within the Galaxy. For this purpose an up-to-date modelling of the interstellar radiation field (ISRF) is included in the code [MPS06, Por05], which for various positions in the Galaxy (characterised in cylindrical coordinates by the height over the Galactic Plane z and the distance to the Galactic Center R) provides the spectral energy density λU_λ of the three photon fields (CMB, dust and starlight photons) as a function of wavelength. The spectral energy densities for the GALPROP photon fields at the position of PSR J1826–1334 ($z = -50\,\mathrm{pc}$ and $R = 4.3\,\mathrm{kpc}$) are shown on the left-hand side of Fig. 5.2. For the calculation of the observable IC emission by means of Eq. 2.17, however, it is more convenient to work with the $\frac{\mathrm{d}N}{\mathrm{d}V\,\mathrm{d}E}$ representation of the photon fields. This representation is shown on the right-hand side of Fig. 5.2.

Sky Map

To obtain energy-dependent sky maps of the simulated γ-ray source photon spectra have to be calculated for each sky map bin. Subsequently, the predicted photon fluxes in various energy ranges can be studied almost immediately. The only thing left to do is to integrate the photon spectra over the selected energy range. For the parameter set used for the illustrations of the age-dependent spatial distributions of the lepton populations (cf. Fig. 5.1) the predicted γ-ray photon fluxes in four different energy ranges are shown in Fig. 5.3. These photon flux sky maps reveal similarities to the sky maps of HESS J1825–137. In particular, the energy slices, which have been adapted to the ones used in the RGB map of HESS J1825–137 (see Fig. 2.9(a)) reproduce nicely the special characteristic of HESS J1825–137, i.e. the most energetic photons are located in the vicinity of HESS J1825–137, while the less energetic photons are spread over a larger area.

Comparing the simulated and the measured H.E.S.S. sky maps requires processing the simulated results according to technical aspects of the H.E.S.S. observations and characteristics of the telescopes which influence the detection probability and reconstruction accuracy. These include the observation conditions for the different observation runs, e.g. the zenith and offset angles, the muon efficiencies, the live times, etc., as well as the corresponding effective areas and the PSF. Consequently, the simulation was extended to consider these influences as well. For this purpose the photon spectra for the individual sky map bins have been processed as described in detail at the end of Sec. 4.4. Briefly summarised, the spectra have been convolved with the effective areas corresponding to the respective observation conditions, have been weighted by the observation live times, are integrated over the specified energy ranges and have been smoothed with the corresponding PSF. The resulting photon count maps for the same energy ranges as in Fig. 5.3 are presented in Fig. 5.4. In comparison to the photon flux sky maps the observable structures have slightly altered: as a consequence of the weighting with the effective areas the contributions of the individual energy slices to the the total photon distribution have shifted and by smoothing with the PSF the structures have coarsened. Nevertheless, the

overall tendency stayed the same. Very nice is the fact, that the predicted number of γ-ray photons in each sky map bin is already in the order of a couple of photons and thus in the order of the measured data. Note, that further details on the comparison of the model predictions and the measured data will be presented in Sec. 5.5.2 and in Fig. 5.14. However, for the time being it is sufficient to know that the model presented in this thesis seems capable of reproducing the most prominent characteristics of HESS J1825–137.

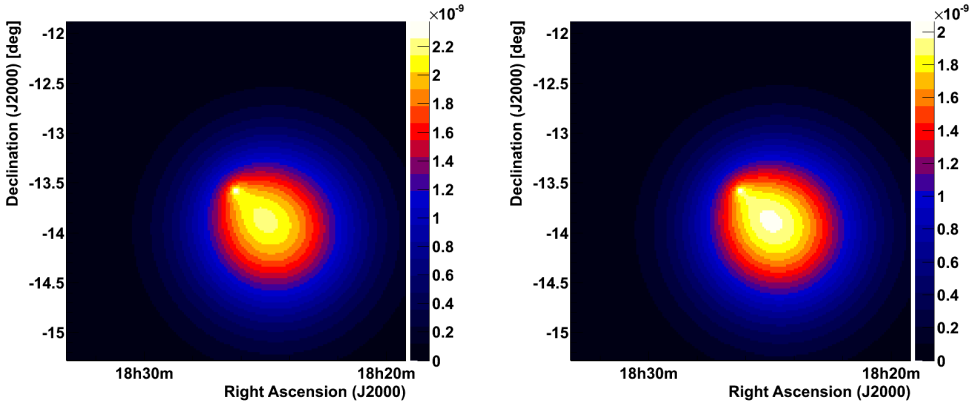

(a) $E_{\mathrm{p}} \in [0.1, 100]$ TeV

(b) $E_{\mathrm{p}} \in [0.1, 0.8]$ TeV

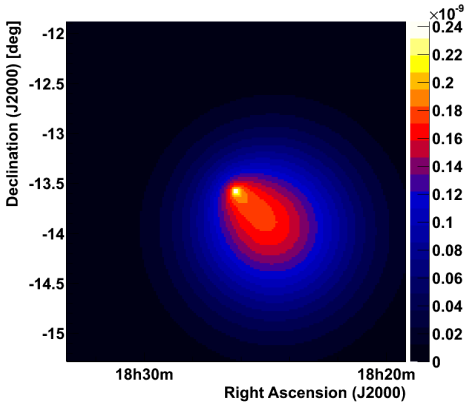

(c) $E_{\mathrm{p}} \in [0.8, 2.5]$ TeV

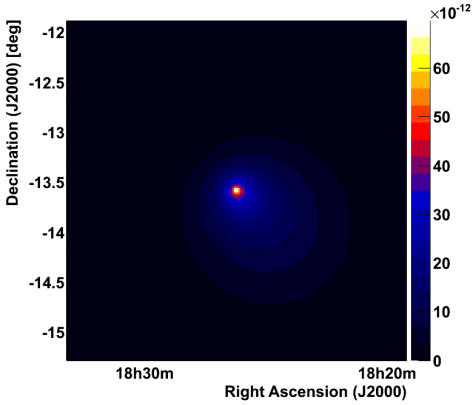

(d) $E_{\mathrm{p}} \in [2.5, 100]$ TeV

Figure 5.3.: Simulation of γ-ray fluxes $\left[\frac{\text{photons}}{\text{m}^2\ \text{s}}\right]$ within various energy slices. The sky map in (a) shows the total photon flux expected in the energy range [0.1, 100] TeV, while the sky maps in (b), (c) and (d) present the subfluxes in the energy ranges [0.1, 0.8] TeV, [0.8, 2.5] TeV and [2.5, 100] TeV, respectively.

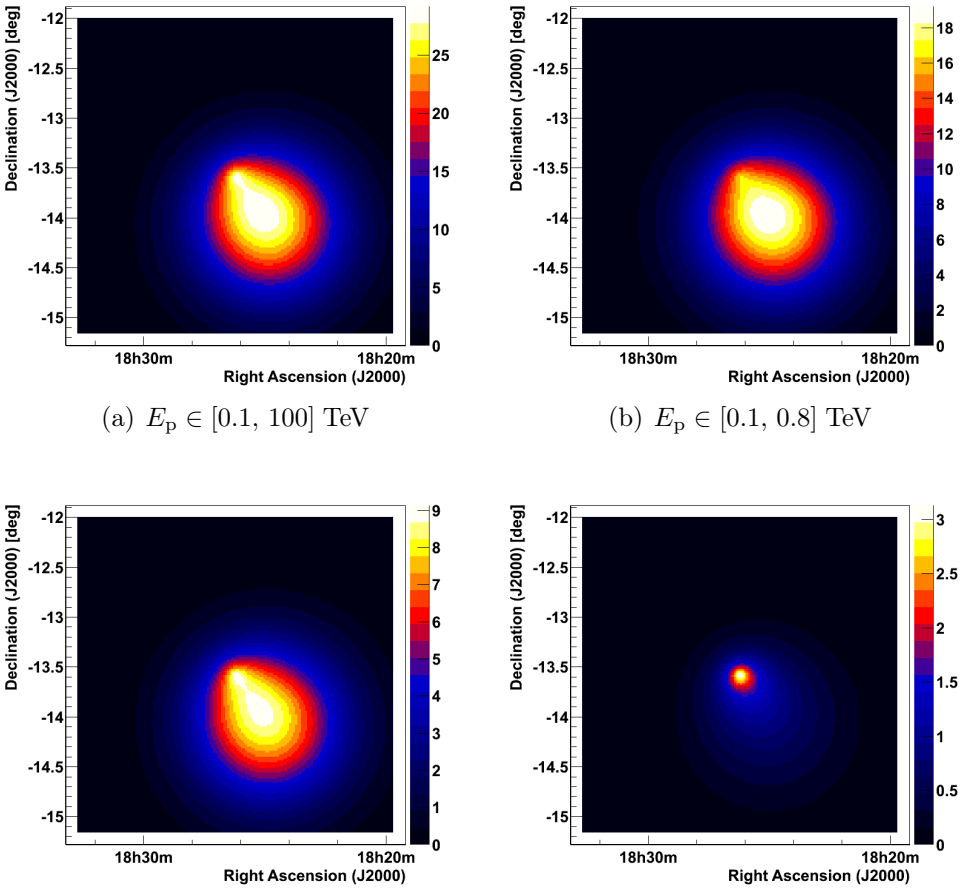

(a) $E_{\mathrm{p}} \in [0.1, 100]$ TeV

(b) $E_{\mathrm{p}} \in [0.1, 0.8]$ TeV

(c) $E_{\mathrm{p}} \in [0.8, 2.5]$ TeV

(d) $E_{\mathrm{p}} \in [2.5, 100]$ TeV

Figure 5.4.: Simulation of γ-ray photons as detected with the H.E.S.S. experiment within various energy slices. The sky map in (a) shows the total number of photons expected in the energy range [0.1, 100] TeV, while the sky maps in (b), (c) and (d) present the photons in the energy ranges [0.1, 0.8] TeV, [0.8, 2.5] TeV and [2.5, 100] TeV, respectively.

5.2. Discussion of Model Parameters

Having presented the details of the newly developed model for HESS J1825–137 in the previous section, it is now of particular interest to determine the parameter set that reproduces the observed γ-ray emission best. For this purpose, the model parameters and their assumed co-domains are discussed in this section. In addition, for each parameter a subset of values is selected that will be used in a scan of the parameter space presented in the next section. Since the simulation of all possible combinations is highly time-consuming, only four values per parameter are investigated. A brief summary of the considerations of this section is given in Tab. 5.1.

symbol	description [unit]	co-domain	grid points			
n	braking index	$[1.4, 3.]$	1.5	2.0	2.5	3.0
P_0	initial rotation period of pulsar [ms]	[10, 101.5]	10.	20.	40.	60.
η	conversion efficiency of spin-down power	[0, 1]	0.1	0.2	0.4	0.6
α	power-law index of injection spectrum	[1.5, 2.5]	1.6	1.8	2.0	2.2
E_{max}	maximum energy of injection spectrum [$\times 10^2$ TeV]	[1, 10]	1.5	3.0	5.0	8.0
$\tilde{v}_{\mathrm{D,x}}$, $\tilde{v}_{\mathrm{D,y}}$	characteristics of drift velocity in x and y direction	[0.75,1.5]	0.75	1.0	1.25	1.5
$\tilde{D}$	characteristic of diffusion coefficient	[1.0,4.0]	1.0	1.78	2.78	4.0
B	magnetic field strength [µG]	[3, 100]	3.	6.	9.	12.

Table 5.1.: Parameters of the new model of HESS J1825–137 and their assumed co-domain, as well as the values considered in the scan presented in Sec. 5.3. See text for parameter definitions and further explanations.

The first subgroup of parameters, i.e. the braking index n and the initial rotation period P_0, has been introduced to describe the evolution of the spin-down luminosity of the pulsar. Assuming pure magnetic dipole radiation the braking index takes the value 3. Reliable measurements of the braking index have only been obtained for five pulsars. These results cover a range from 1.4 to 2.9, see Sec. 2.4.1. Although it can not be excluded that these measurements are biased (as it is easier to measure the braking indices of rapidly rotating pulsars) an initial co-domain of $[1.4, 3.0]$ will be used in this study. The values of the braking index considered in the scan were chosen such that they are evenly spread over this range. The initial rotation period of the pulsar is even more difficult to access. The most intuitive approach is to determine the initial periods of pulsars for which reliable measurements of the braking indices as well as hints at the true age exist. The most prominent example is the Crab Pulsar, whose initial period has been determined as $P_0 = 19$ ms, [LPG93]. Unfortunately, such good evidence is more the exception than the rule. Alternative estimates may be obtained from population studies, e.g. from the distribution of pulsars in the $P\dot{P}$-space, e.g. [Lor05] and references therein.

However, pulsars that power PWNe in X-rays or even in VHE γ rays form only a small subgroup of all detected radio pulsars and therefore such a population study suffers from poor statistics. Consequently, it is more common to consider estimates that empirically derive the initial period from observed quantities of the PWNe. For instance, van der Swaluw and Wu [vdSW01] showed that the ratio of the PWN radius and the supernova remnant forward-shock radius can be used to obtain an estimate of the initial rotation period. In their study the majority of PWNe was ascribed an initial period in the order of $P_0 = 40$ ms. Unfortunately, this approach can not be applied directly to PSR J1826–1334, as the SNR radius has not yet been determined. Nevertheless, a rough estimate of the viable P_0 values for HESS J1825–137 is given by $[10\text{ ms}, 101.5\text{ ms}]$. The upper limit is given by the present rotation period of PSR J1826–1334. The lower limit has been chosen according to the range of measured rotation periods of rotation-powered pulsars and is influenced by a recent H.E.S.S. publication which showed that the γ-ray emission of the PWN N157B is best explained by an initial rotation period of 10 ms or even smaller [A$^+$12a]. For the scan of the parameter space, we decided to concentrate on the lower part of this co-domain, as a lower initial rotation period corresponds to a higher age of the pulsar and therefore more intuitively explains the large extent of HESS J1825–137.

The transfer of the released energy from the pulsar to the electron population, which causes the γ-ray emission, is characterised by the η parameter. This parameter quantifies the conversion efficiency of the spin-down power of the pulsar to the energy of the electrons that are injected into the PWN. In case that all the energy is transferred to the electrons η takes the value 1, whereas in case that all energy is transferred to the magnetic field η is equal to zero. Thus the co-domain is given by $[0, 1]$. Many models consider equipartition between the energy of the particles and the energy residing in the magnetic field. Since we consider only the high-energy component of the electrons this assumption would hint at a value of η smaller than 0.5. Therefore in the parameter scan emphasis is placed on the investigation of the smaller values.

The next subgroup of parameters α, E_b and E_max are used to describe the energy spectrum of the electrons that are injected into the PWN. The α parameter denotes the index of the electron spectrum at the termination shock. Assuming particle acceleration due to first-order Fermi acceleration, see Sec. 2.1.3, α is expected to take a value of approx. 2. So far no feature which could have been identified as termination shock has been observed for G18.0–0.7. Instead, the smallest extraction regions in the XMM / Suzaku and Chandra observation revealed X-ray spectra with photon indices of 1.6 and 1.3, respectively. As synchrotron emission is the underlying emission process in the X-ray regime this hints at an injection electron spectrum with an index of 2.2 and 1.6, respectively, see Sec. 2.4.3. Therefore, these two values are tested explicitly in the parameter scan. The energy range of the considered electrons is limited by E_b and E_max. In our modelling E_b is fixed to 0.1 TeV. This value is a rough estimate of the lowest energy of electrons still contributing to the emission of 0.1 TeV photons, which represent the lowest energetic photons that can be observed with the H.E.S.S. experiment. In general, E_b may be raised[9], but since the contribution of the low-energy electrons to the observed γ-ray emission is of very

[9] 1 TeV is also a common approximation

little account and another limit would require a more sophisticated justification, we opted for the most simple approximation. The maximum energy of the electron spectrum is restricted by the synchrotron limit and the gyroradius limit, as discussed in Sec. 2.4.2. Both limits predict restrictions that are in the order of 100 TeV to 1,000 TeV for typical PWNe, c.f. [Sch10]. Therefore, in the parameter scan the following values will be tested: 150 TeV, 300 TeV, 500 TeV and 800 TeV. While other studies needed more sophisticated energy cut-offs, e.g. exponential or even time-dependent cut-offs, to explain observed data, our studies showed that variations of the maximum energy by ±100 TeV have only minor impact on the predicted γ-ray spectra in the observed energy range. Instead, they have much more influence on the X-ray photons which are generated via synchrotron emission. Since our modelling is targeted at the observed TeV emission we decided to work with the hard cut-offs and leave an adapting of the maximum energy parameter to future modelling that incorporates the fitting of the X-ray emission.

The modelled spatial distribution of the electrons in the PWN depends on the drift velocity and the diffusion coefficient. For the definition of the corresponding parameters ($\tilde{v}_{\mathrm{D,x}},\ \tilde{v}_{\mathrm{D,y}},\ \tilde{D}$) in the parameter scan and in the minimisation procedure an approach was chosen which considers that an estimate of the present extent of the PWN can be obtained from the measured TeV data. Taking another look at Eq. 5.16 and especially at Fig. 5.1 it becomes clear that this information can be used to draw conclusions on the spatial distribution of the oldest electron population and in addition on the drift velocity and the diffusion coefficient. Indeed, the maximum extent of today's lepton population is determined by that of the oldest electron population, c.f. the upper panel in Fig. 5.1. Moreover, if one approximates the total emission region by a circle its centre is in good agreement with the centre of gravity of the oldest electron population. These two quantities, the maximum extension and the displacement of the oldest electron population with respect to the present position of the pulsar, however, reflect the strength of the drift and the diffusion processes. Consequently, in order to determine a well-suited parametrisation of the drift velocity and the diffusion coefficient we started by fitting a circle to the displayed data in the normalised excess map, see Fig. 4.14. The circle which was found best suited to encompass the total emission region of HESS J1825–137 is centred at (R.A. = 276.110°, Dec. = −14.0076°) and has a radius of $r_C = 0.9°$. Following the explanation above the distance vector from the present position of the pulsar to the centre of the fitted circle ($\vec{d}_{\mathrm{P,C}}$) divided by the age of the pulsar (t_{age}, see Eq. 2.9) is taken as an approximation of the drift velocity: $\vec{v}_{\mathrm{D,1}} = \frac{\vec{d}_{\mathrm{P,C}}}{t_{\mathrm{age}}}$. To obtain an approximation of the diffusion coefficient the procedure is a little more complicated. In this case the $3\,\sigma$-radius $r_{3\sigma}$, i.e. the radius of the circle that encompasses approx. 99 % of the oldest electron population, can be taken as a starting point. For the Gaussian distribution considered in our model, see Eq. 5.16, $\sigma = \sqrt{2\ D\ t_{\mathrm{age}}}$ and thus $r_{3\sigma} = 3\ \sqrt{2\ D\ t_{\mathrm{age}}}$. If one assumes that $r_{3\sigma}$ is equal to r_C, then the diffusion coefficient can be approximated by $D_1 = \frac{r_{\mathrm{C}}^2}{18 t_{\mathrm{age}}}$. However, it should be noted that the estimates obtained from the measured data are rather coarse. For instance, it can not be excluded that the electrons may have spread further than the observed γ-ray emission, but are no longer observable in VHE γ rays due to cooling effects or due to a photon flux which is below the detection limit of the

H.E.S.S. experiment. Moreover, although an acceptance correction has been applied to the normalised excess map in Fig. 4.14, the fact that the majority of the observation runs of HESS J1825–137 were targeted to the south of the emission region may result in a slightly truncated representation of the northern emission regions. Consequently, the calculated values $\vec{v}_{\mathrm{D},1}$ and D_1 are used as an initial assessment, but deviating values are also tested in the scan and in the minimisation procedure. The quoted parameter values for the drift velocity and the diffusion coefficient, c.f. Tab. 5.1, can be understood in the following way:

$$\begin{aligned} v_{\mathrm{D,x}} &= \tilde{v}_{\mathrm{D,x}} \cdot \vec{v}_{\mathrm{D},1} \cdot \vec{e}_{\mathrm{x}} = \tilde{v}_{\mathrm{D,x}} \cdot \vec{d}_{\mathrm{P,C}} \cdot \vec{e}_{\mathrm{x}} \;/\; t_{\mathrm{age}} \\ v_{\mathrm{D,y}} &= \tilde{v}_{\mathrm{D,y}} \cdot \vec{v}_{\mathrm{D},1} \cdot \vec{e}_{\mathrm{y}} = \tilde{v}_{\mathrm{D,y}} \cdot \vec{d}_{\mathrm{P,C}} \cdot \vec{e}_{\mathrm{y}} \;/\; t_{\mathrm{age}} \end{aligned} \tag{5.23}$$

and

$$D = \tilde{D} \cdot D_1 = \tilde{D} \cdot \frac{r_{\mathrm{C}}^2}{18\, t_{\mathrm{age}}}. \tag{5.24}$$

Due to the uncertainties in the derived estimates it is difficult to define co-domains for $\tilde{v}_{\mathrm{D,x}}$, $\tilde{v}_{\mathrm{D,y}}$ and $\tilde{D}$. To be on the safe side the co-domains are therefore chosen rather large. In particular we allowed the drift velocity to be 1.5 times as large as the value derived from the γ-ray emission and the diffusion coefficient to cause a spatial distribution with $r'_{3\sigma} = 2r_C$. The scan values of the parameters are chosen to cover the full co-domain, i.e. the scan values of $\tilde{v}_{\mathrm{D,x}}$, $\tilde{v}_{\mathrm{D,y}}$ are 0.75, 1.0, 1.25 and 1.5, while those of $\tilde{D}$ correspond to values of $r_{3\sigma}$ which are equal to 0.9°, 1.2°, 1.5° and 1.8°, respectively.

The last parameter of our model, B, describes the strength of the magnetic field in the PWN. This value is of particular importance for the energy losses of the electrons as well as for the observed synchrotron emission. In general the magnetic field is assumed to be time-dependent with higher strength in the past. However, the modelling of the evolution of the magnetic field is subject to large uncertainties and therefore in this first modelling of the spatial features of HESS J1825–137 we started to work with an initial hypothesis of a constant and uniform magnetic field. Hints at the present strength of the magnetic field of HESS J1825–137 were presented in previous publications. For instance, Gaensler et al., suggested a magnetic field strength of 10 µG to explain the XMM Newton observation of G18.0–0.7 assuming equipartition, c.f. [G$^+$03] and Sec. 3.1. In contrast to Gaensler et al. Grondin et al. considered the evolution of the PWN in more detail, see Sec. 3.5, and their modelling hinted at a present magnetic field in the order of 3 µG. This value agrees well with typical estimates of the magnetic field strength in the interstellar medium. A suitable range for the co-domain of the constant magnetic field of this new model is difficult to obtain. While the lower limit for the magnetic field strength in PWNe can be approximated by the magnetic field strength in the ISM, upper limits may be as high as a few 100 µG. However, since we consider an evolved PWN and the magnetic field strength is supposed to decrease rapidly after a characteristic time of about 100 years and to reach a plateau value afterwards, see Sec. 2.4.4, we concentrate on the lower end of the possible magnetic field strengths in the parameter scan.

5.3. Optimising the Model Parameters by Fitting the Energy Spectra

Having studied the parameters of the presented model in the previous section, this section is devoted to the search for the parameter set that reproduces the observed TeV data best. Initially, we will concentrate on the simulation of the spectra determined for the twelve wedges which have already been studied in the original analysis of HESS J1825–137, see Fig. 4.17. The reason for this restriction is that a full simulation of the sky map is very time consuming. Instead, the results of the simulation of the wedge spectra will be used to preselect promising parameter sets. Later, the corresponding sky maps and their suitability to reproduce the measured data will also be investigated.

Minimising X^2

In order to be able to evaluate which set of parameters reproduces the measured data best, the X^2 parameter[10] is defined as:

$$X^2 = \sum_{\mathrm{i}=1}^{n_\mathrm{w}} \sum_{\mathrm{j}=1}^{n_{\mathrm{sp,i}}} \frac{(y_{\mathrm{d,i,j}} - y_{\mathrm{s,i,j}})^2}{\sigma^2_{\mathrm{d,i,j}}}, \tag{5.25}$$

where $y_{\mathrm{d,i,j}}$ is the y value of the j-th measured spectrum point of the i-th wedge and $y_{\mathrm{s,i,j}}$ is the corresponding simulated spectrum point. $\sigma_{\mathrm{d,i,j}}$ is the measurement uncertainty on the respective spectrum point. Note that, as the measurement uncertainties are asymmetric, see Fig. 5.25, for each spectrum point the appropriate uncertainty is chosen, which depends on the location of the simulated data point with respect to the measured value. All wedges (n_w) and all spectrum points per wedge ($n_{\mathrm{sp,w}}$) are considered in the summation of Eq. 5.25.

Scanning the Parameter Space

In a first "brute force" approach the wedge spectra were simulated for as many parameter sets as possible. The limiting factors in this approach are the computing power and the time budget. In our study four test values per parameter proved to be reasonable, which resulted in a sample of 262 144 parameter combinations in total. For each of these parameter sets the spectra of all twelve wedge regions were calculated and subsequently compared to the measured data by means of the X^2 parameter. All in all, the co-domain of the X^2 values was given by $[4.65 \times 10^2,\ 2.45 \times 10^8]$. The histograms in Fig. 5.5 give an impression of the distribution of the X^2 values, e.g. the histogram in Fig. 5.5(a)

[10] Note, that the definition of X^2 is derived from the definition of $\chi^2 \equiv \sum_{\mathrm{i}=1}^{\mathrm{n}} \frac{[y_\mathrm{i} - f(x_\mathrm{i};\vec{a})]^2}{\sigma_\mathrm{i}^2}$, which is introduced in the method of least squares. The aim of this method is to determine the parameters ($\vec{a}$) of a theoretical function $f(x_\mathrm{i};\vec{a})$ – with linear dependency on the parameters – which reproduce the measured data ($y_\mathrm{i}, \sigma_\mathrm{i}$) best. Moreover, there is also a connection to the χ^2 distribution, which is the probability distribution of a sum of squares of independent standard normal random variables.

shows the abundances of the X^2 values smaller than 10 000. In addition Fig. 5.5(b) presents an enlarged view on the distribution around the X^2 minimum, because we are especially interested in the parameter sets that reproduce the measured data best, i.e. in the parameter sets which have the smallest X^2 value.

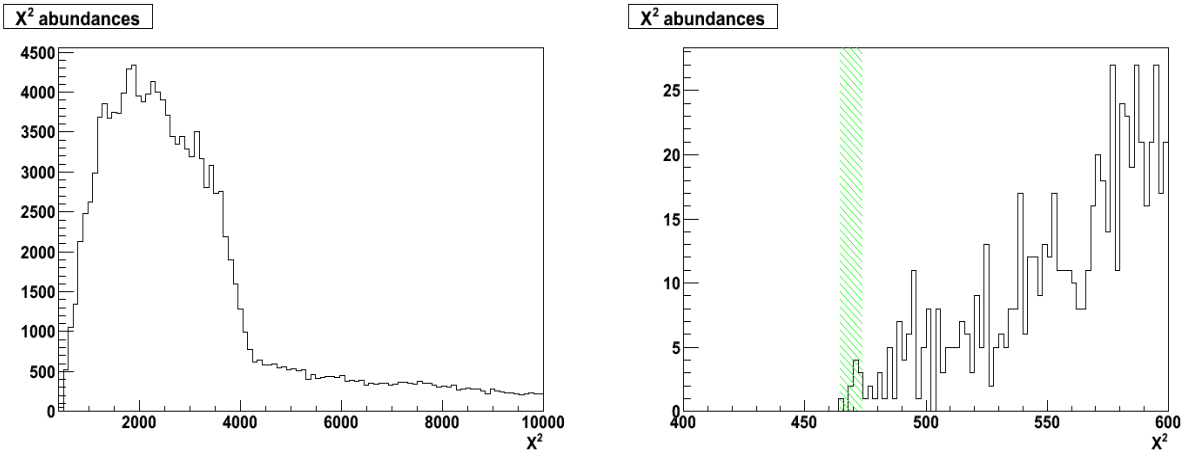

(a) $400 \leq X^2 \leq 10\,000$ (b) $400 \leq X^2 \leq 600$

Figure 5.5.: Parameter scan: Abundances of X^2. While the histogram on the left-hand side (a) gives an impression of the abundances of X^2 values smaller than 10 000, the histogram on the right-hand side (b) focuses on X^2 values in the vicinity to the minimum. The hatched green area marks the ten smallest X^2 values.

The parameter set which exhibited the smallest X^2 value within the parameter scan ($X^2_\mathrm{S} = 464.695$) was identified as $n = 2.5$, $P_0 = 20.0\,\mathrm{ms}$, $\eta = 0.1$, $\alpha = 2.2$, $E_\mathrm{max} = 800\,\mathrm{TeV}$, $\tilde{v}_\mathrm{D,x} = 0.75$, $\tilde{v}_\mathrm{D,y} = 1.0$, $\tilde{D} = 1.78$, $B = 9.0\,\mu\mathrm{G}$. To assess whether this parameter set might minimise the X^2 distribution, it was investigated how the X^2 value changes when one of the parameters is relocated within its co-domain, while the others are kept fixed. The result of this investigation is shown in Fig. 5.6. For several parameters (i.e. n, P_0, $\tilde{v}_\mathrm{D,y}$, $\tilde{D}$, B) the distributions are suggestive of X^2_S being at least in the vicinity of a minimum. However, in case of the other parameters X^2_S is located on the verge of the sampled value range. For these parameters the sampled range had to be expanded to allow statements whether a true minimum was found.

However, before we investigated how it might be possible to find the true minimum of the X^2 distribution in the vicinity of X^2_S, we had another look at the distribution of the X^2 values presented in Fig. 5.5(b). In this figure it is shown that the smallest X^2 values lie close together. For instance, the ten smallest values lie within $[464.695, 473.899]$, cf. the hatched green area in Fig. 5.5(b). Since the grid points in the parameter scan have been chosen rather coarse, the smallest X^2 values only indicate that a minimum might be in the vicinity. Which of the true minima reproduces the observed data best had to be examined separately. To get a feel for the parameter sets within the parameter scan which exhibit small X^2 values, the ten smallest X^2 values (sorted in ascending order) and the corresponding parameter values were summarised in Tab. 5.2. Note that the restriction to

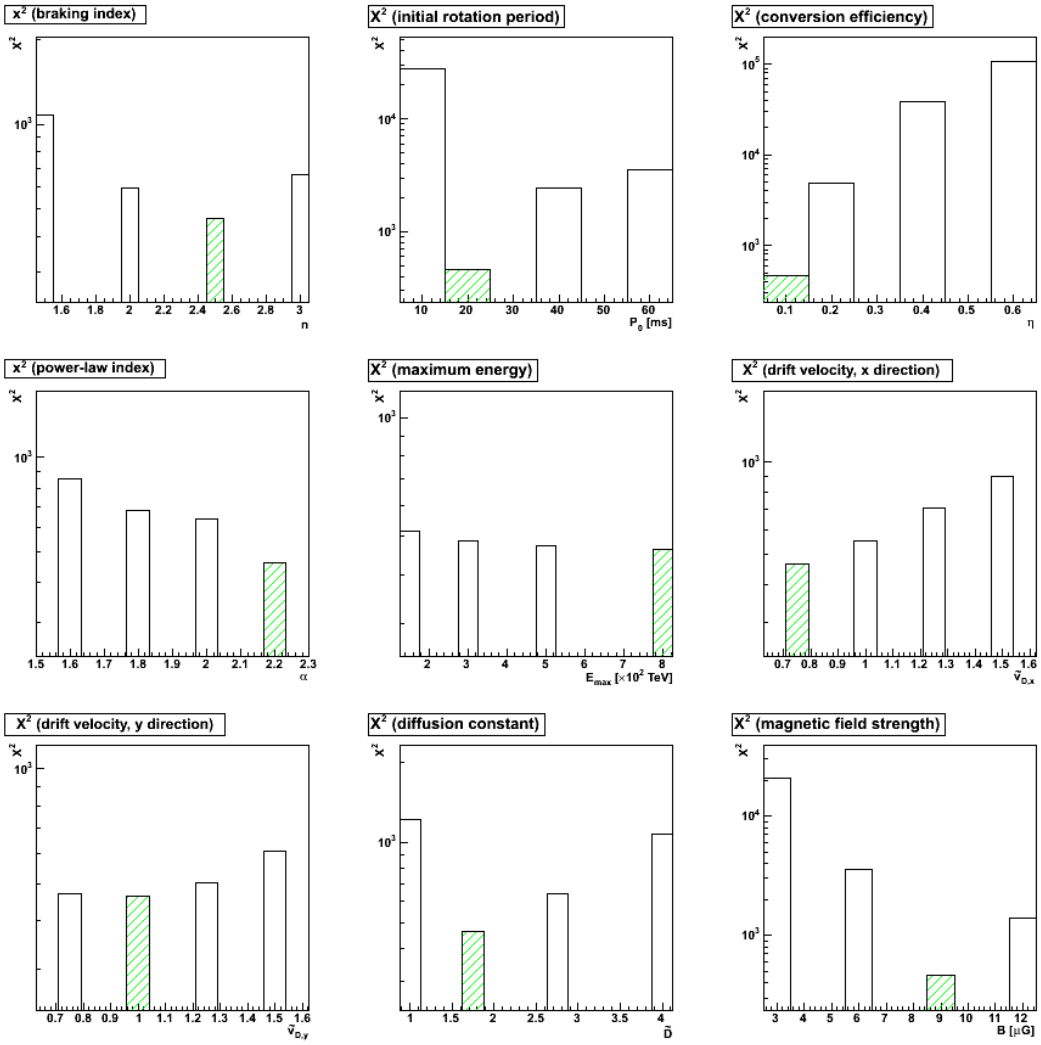

Figure 5.6.: Distribution of the X^2 values in the vicinity of the smallest X^2 value of the parameter scan, viz. $X^2_\mathrm{S} = 464.695$. The parameters that correspond to X^2_S are: $n = 2.5$, $P_0 = 20.0\,\mathrm{ms}$, $\eta = 0.1$, $\alpha = 2.2$, $E_\mathrm{max} = 800\,\mathrm{TeV}$, $\tilde{v}_\mathrm{D,x} = 0.75$, $\tilde{v}_\mathrm{D,y} = 1.0$, $\tilde{D} = 1.78$, $B = 9.0\,\mu\mathrm{G}$. The individual histograms show how the X^2 value changed when one of the parameters was allowed to take deviating values within its co-domain. Note that the parameters were restricted to only take values of the predefined grid-points, thus merely four values per parameter were tested. The green hatching marks the bin which corresponds to X^2_S.

ten values was rather arbitrary and might be expanded in the future. For each X^2 entry in Tab. 5.2 an additional parameter array is presented, which gives account of the location of each parameter within its co-domain. The array is defined in the following way: Each entry in the array represents one of the parameters, i.e. [n, P_0, η, α, $E_{\max}$, $v_{\mathrm{D,x}}$, $v_{\mathrm{D,y}}$, D, B], and can take the values 1, 2, 3 or 4. The numerical value indicates whether the respective parameter value corresponds to the first (1), second (2), third (3) or forth (4) sampled grid point within the co-domain, see definition in Tab. 5.1. Accordingly a value of 1 or 4 means that the parameter is on the verge of the sampled co-domain.

no.	X^2	n	P_0 [ms]	η	α	$E_{\max}$ [TeV]	$\tilde{v}_{\mathrm{D,x}}$	$\tilde{v}_{\mathrm{D,y}}$	$\tilde{D}$	B [µG]	parameter array
1.1	464.695	2.5	20.0	0.1	2.2	8.0	0.75	1.00	1.78	9.0	[3 2 1 4 4 1 2 2 3]
1.2	468.670	3.0	40.0	0.4	2.2	8.0	1.50	1.00	1.78	12.0	[4 3 3 4 4 4 2 2 4]
1.3	469.866	3.0	40.0	0.4	2.2	5.0	1.25	1.25	1.78	12.0	[4 3 3 4 3 3 3 2 4]
1.4	470.806	3.0	40.0	0.4	2.2	8.0	1.25	1.25	1.78	12.0	[4 3 3 4 4 3 3 2 4]
1.5	471.162	3.0	40.0	0.4	2.2	5.0	1.50	1.00	1.78	12.0	[4 3 3 4 3 4 2 2 4]
1.6	471.515	3.0	40.0	0.4	2.2	5.0	1.50	0.75	1.78	12.0	[4 3 3 4 3 4 1 2 4]
1.7	471.913	3.0	40.0	0.4	2.2	8.0	1.50	0.75	1.78	12.0	[4 3 3 4 4 4 1 2 4]
1.8	472.740	2.5	20.0	0.1	2.2	8.0	0.75	0.75	1.78	9.0	[3 2 1 4 4 1 1 2 3]
1.9	473.273	3.0	40.0	0.4	2.2	3.0	1.25	1.25	1.78	12.0	[4 3 3 4 2 3 3 2 4]
1.10	473.899	2.5	20.0	0.1	2.2	5.0	0.75	1.00	1.78	9.0	[3 2 1 4 3 1 2 2 3]

Table 5.2.: Parameter scan: Overview of the ten smallest X^2 values, sorted in ascending order. For each X^2 value the corresponding parameter values are quoted. In addition, also a parameter array is presented, which gives account of the location of each parameter within its co-domain. See text for the definition of the array.

The use of the parameter matrices made it is easier to compare the individual parameter sets. Indeed a comparison of the parameter matrices in Tab. 5.2 showed that there were several parameter sets which hardly differed from each other: Both, the X^2 values with the numbers[11] 1.1, 1.8 and 1.10 and those with the numbers 1.2, 1.3, 1.4, 1.5, 1.6, 1.7 and 1.9 form subgroups, for which the parameter matrices only differ at one, two or at most at three positions. In both subgroups the differing parameters were $E_{\max}$ and the two components of the drift velocity. As has been stated above this clustering was not really surprising as the true minima of the X^2 distribution were expected to be located somewhere between the sampled grid points in the parameter space. Nevertheless, this observation emphasised the need for some more effort to find the true minima of the X^2 distribution. Moreover, studying the parameter arrays we also noticed that each array contained entries which took the values 1 or 4. Accordingly, the corresponding parameters were on the verge of their sampled co-domains. This observation, too, indicated that further improvements were still required.

[11] See Tab. 5.2 for the assignment of the numbers

Application of Minimisation Algorithm

Since the parameter scan had given us a rough idea of the regions in the parameter space where minima might be found, we decided to refine our search strategy by using a minimisation algorithm. Our method of choice was the Simplex minimiser as proposed by Nelder and Mead [NM65], which is a multidimensional minimisation routine. We used the Simplex minimiser provided within the TMinuit class[12], that is the C++ version of the Fortran minimisation package (MINUIT, [JR75])[13] established at CERN. In principle, an n-simplex is the smallest n-dimensional geometrical figure with n + 1 corners, e.g. a 2-simplex is a triangle. Accordingly, in the Simplex minimisation procedure the n-parameter function to minimise is evaluated repeatedly at the n+1 corners of a simplex, which is stepwise adapted to the local landscape. The initial simplex is determined by the parameter starting values and by minimising the function value along the coordinate axes. Subsequently, the function is evaluated at each corner and the corner with the highest function value is identified (P_h). By reflecting the latter at the centroid of the remaining corners a new test point ($\bar{P}$) is computed. Depending on the function value at the test point and its location with respect to the function values of the previously evaluated corners, the algorithm decides whether and how the simplex is expanded or contracted along the line connecting P_h and $\bar{P}$. The details of this approach can be looked up in [NM65]. This procedure is repeated until the simplex converges in the vicinity of a minimum. A widely-used convergence criterion is that the interval spanned by the function values of the current simplex has to be smaller than a predefined value.

[12] `http://root.cern.ch/root/html/TMinuit.html`
[13] `http://wwwasdoc.web.cern.ch/wwwasdoc/minuit/minmain.html`

new no.	X^2	n	P_0 [ms]	η	α	E_max [TeV]	$\tilde{v}_\mathrm{D,x}$	$\tilde{v}_\mathrm{D,y}$	$\tilde{D}$	B [μG]	old no.
2.1	361.340	3.45	39.00	0.60	2.56	15.23	0.94	0.98	2.17	9.66	1.2
2.2	369.713	4.14	29.75	0.44	2.54	8.41	0.91	0.04	2.86	9.68	1.7
2.3	371.087	4.73	35.25	0.56	2.50	15.85	0.82	0.37	2.77	10.95	1.4
2.4	371.369	3.90	40.27	0.58	2.47	7.44	0.93	0.92	2.19	10.88	1.5
2.5	371.593	3.98	38.98	0.54	2.45	24.21	1.10	0.62	2.22	11.04	1.3
2.6	385.717	4.14	37.76	0.50	2.35	25.57	1.03	0.49	2.52	11.83	1.6
2.7	391.809	5.74	41.86	0.62	2.33	2.65	0.76	0.73	2.67	13.83	1.9
2.8	404.587	2.81	20.95	0.16	2.27	9.33	0.25	1.04	2.78	8.84	1.8
2.9	418.701	2.54	21.10	0.16	2.20	10.49	0.35	1.08	2.73	9.08	1.1
2.10	431.696	2.44	21.50	0.11	2.19	5.88	0.75	0.98	2.05	8.87	1.10

Table 5.3.: Results of Simplex minimisation, using the smallest X^2 values of the parameter scan (as listed in Tab. 5.2) as starting values. The new X^2 values are again sorted in ascending order. The allocation to the respective starting values of the parameters is given by the "old number", which represents the position of the initial parameter set within Tab. 5.2.

In a first minimising attempt we decided to use the parameter sets presented in Tab. 5.2 as starting values for the Simplex minimisation procedure. In order to interfere as little as possible with the minimisation no limits were placed on the individual parameters. The results of these minimisation procedures are presented in Tab. 5.3, where the new X^2 values are again sorted in ascending order. By means of the quoted "old number" it is indicated from which parameter set the minimisation procedure started: the "old number" corresponds to the position of the initial parameter set in Tab. 5.2. Not surprisingly, the sequential arrangement was shuffled, e.g. the minimisation procedure that started from the parameter set which exhibited the smallest X^2 value within the parameter scan did not result in the smallest X^2 value after the minimisation procedure. However, it is interesting to note, that the parameter sets which were previously assigned to different subgroups due to their location in parameter space are now also separated with regard to their X^2 values: the parameter sets which belong to the first group now have X^2 values smaller than 400, whereas those of the second subgroup have larger values.

Since no limits have been imposed in the minimising procedure, several parameters left the previously defined co-domains, cf. Tab. 5.1. One of these parameters is the braking index. Especially in the first subgroup of parameter sets there seems to be a tendency towards slightly higher values than the theoretically predicted value of 3. However, it has been stated before that reliable measurements of the braking index exist only for five pulsars and while values higher than 3 might not be the first values that come to one's mind, they are not physically impossible. Rather peculiar are also the values taken by $E_{\max}$. They are significantly larger than the presumed co-domain and they vary strongly and no pattern can be recognised. Indeed, there was soon growing evidence that $E_{\max}$ is a parameter which can not be determined within the framework of the presented model. For instance, our next step to examine the reported minima was to evaluate how the X^2 values of the individual minima in Tab. 5.3 changed when one of the parameters was varied. In doing so the test ranges of the parameters were chosen such that they comprised the previously defined co-domains as well as the values taken in the minimisation procedure.

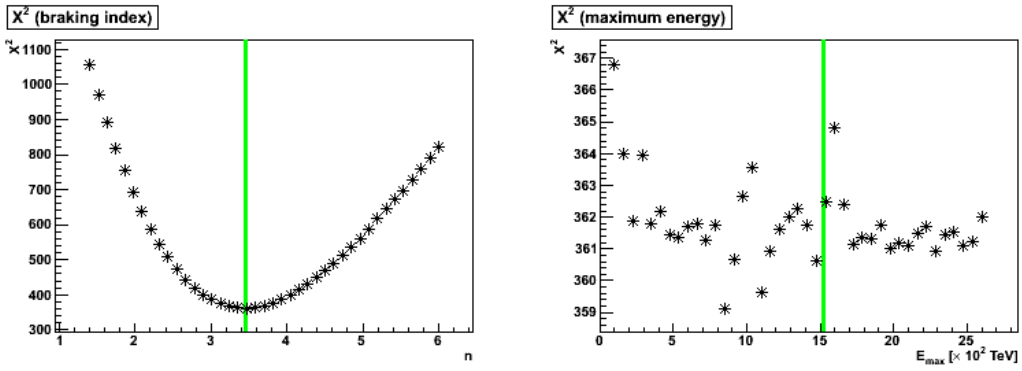

Figure 5.7.: X^2 as function of the braking index (histogram on the left-hand side) and of $E_{\max}$ (histogram on the right-hand side). Both histograms have been obtained by initially setting the model parameters to the values quoted for minimum 2.1 in Tab. 5.3 and by varying the respective parameter. The green lines indicate the position of the minimum.

For all but the $E_{\max}$ parameter smooth curves were obtained which covered a large X^2 value range and which exhibited prominent minima, cf. the left-hand histogram in Fig. 5.7 which shows the evolution of the X^2 value with varying braking index for the minimum labelled 2.1. The equivalent curves for $E_{\max}$ exhibited a different behaviour, compare for instance the histogram on the right-hand side of Fig. 5.7: the X^2 value range was very small and the sampled X^2 values fluctuated strongly. Additionally, no trend was observable for the X^2 values over the total value range of $E_{\max}$. Close investigation of this phenomenon have revealed the following: since leptons with energies higher than approx. 300 TeV play only a minor role in the generation of γ rays with energies within [0.1, 100] TeV the extension of the energy range to higher energies had hardly any impact. Instead, the observed discontinuities were a result of the numerical computation, in which the respective energy binning of the spectra played an important role. As a consequence of this observation, we had to conclude that the new model can not be used to draw conclusions on $E_{\max}$. Instead, we decided to fix $E_{\max}$ in our modelling ($E_{\max} = 500\,\text{TeV}$) and to leave its determination to other simulations which consider for instance X-ray observations, as the highly energetic leptons play a more important role in this energy range.

Having fixed $E_{\max}$ to 500 TeV, which is approximately the mean value of the initial co-domain, the Simplex minimisation was repeated to find minima in the shrunken parameter space. As new starting values the parameters presented in Tab. 5.3 were used, with the only difference that $E_{\max}$ had been fixed to its new value. The results of this second minimisation are presented in Tab. 5.4. Using the minimum with the smallest X^2 value, i.e. the minimum labelled 3.1, as an example, Fig. 5.8 shows how the X^2 value changed when the individual model parameters are varied within their co-domains. The same representations for the other minima listed in Tab. 5.4 have been moved to Appendix B.2. For all minima and for all parameters smooth curves with prominent extrema were obtained. The latter seem to be well located by the minimiser, as the green lines in the histograms indicate the position found in the Simplex minimisation process. Moreover, the shapes of the curves give a first – but very rough – impression of how well the individual parameters may be determined in the modelling process.

It has to be stressed, that it is not self-evident that so far minima have been found in each minimisation cycle and for each starting parameter set. This is certainly an advantage of the Simplex minimiser, as it is very robust and usually converges after a multitude of minimisation steps. However, the Simplex approach suffers from the fact that the minimisation depends strongly on the starting values as well as on the details of the minimisation steps and that it is difficult for the algorithm to distinguish between a local and the sought-after global minimum. Therefore the quoted minima in Tab. 5.4 can only be understood as indications of the parameter set that minimise the X^2 distribution. In particular, it is rather unlikely that the minimum with the smallest X^2 value represents the global minimum of the distribution. Since some of the corresponding model parameters are also far outside the initial co-domain, it seems appropriate not to ascribe a particular relevance to the smallest minimum, but to treat all minima in Tab. 5.4 equally. Even though these minima might only represent indications, we will use them in the following to get a better impression of the predictions of the model.

new no.	X^2	n	P_0 [ms]	η	α	E_{max} [TeV]	$\tilde{v}_{\mathrm{D,x}}$	$\tilde{v}_{\mathrm{D,y}}$	$\tilde{D}$	B [µG]	old no.
3.1	349.836	4.09	36.37	0.73	2.70	500	0.87	0.45	2.63	8.23	1.3
3.2	356.304	3.30	39.09	0.70	2.60	500	1.15	0.65	2.49	9.37	1.2
3.3	363.233	3.95	41.17	0.68	2.52	500	0.81	1.02	2.35	10.36	1.5
3.4	368.583	4.78	35.89	0.65	2.55	500	0.73	0.48	2.85	10.93	1.4
3.5	370.342	4.17	29.85	0.47	2.57	500	0.94	0.06	2.79	9.60	1.7
3.6	371.008	5.29	37.60	0.66	2.55	500	0.76	0.55	2.55	11.50	1.6
3.7	380.381	6.68	39.29	0.68	2.48	500	0.61	0.62	2.60	13.48	1.9
3.8	385.450	3.62	25.15	0.29	2.41	500	0.29	0.81	3.10	9.75	1.1
3.9	389.106	3.43	21.56	0.22	2.40	500	0.01	1.08	2.83	9.28	1.8
3.10	399.612	2.63	22.10	0.20	2.36	500	0.32	1.14	2.55	8.97	1.10

Table 5.4.: Results of the second Simplex minimisation, using the previous minimisation results as starting values. Note that the parameter E_{max} has been fixed to 500 TeV before conducting the minimisation. Again, the new X^2 values are sorted in ascending order and the "old number" identifies the position of the initial parameter set in Tab. 5.2.

For this purpose for each of the parameter sets presented in Tab. 5.4 the corresponding γ-ray energy spectra of all wedges of HESS J1825–137 were computed. The results of these simulations are presented as green graphs in Fig. 5.9. In addition, the H.E.S.S. spectrum points are indicated by black markers. Overall, the simulated curves are in good agreement with the H.E.S.S. data. However, there seems to be a trend that the presented model underpredicts the energy spectra at high energies, especially at greater distances to the pulsar.

There are various possibilities to understand this phenomenon: On the one hand it might be due to simplified assumptions in the modelling process. A rather obvious explanation is for instance that the diffusion coefficient was assumed to be energy-independent. In reality particles with higher energy will move away from the pulsar faster than those with less energy. Consequently, the concentration of highly energetic leptons and thus also the flux of highly energetic γ rays at larger distances to the pulsar should be increased in comparison with the predictions of the model. Considering convection processes should have a similar effect. Since they cause a higher propagation velocity the particles might reach the verges of the PWN having suffered less energy losses. Further possible reasons are also the shape of the assumed injection spectrum, or the way the energy losses were modelled. All in all, it should be noted that the presented version of the new model is a preliminary one. The listed simplifications have been made to get a first impression of the potential of the modelling and further adaptions are foreseen for future work. And so far the obtained results indicate that we might be on the right track.

Another possible cause for the deviations between the simulated and the observed data might be that the H.E.S.S. data points were calculated by means of a forward folding procedure. In this approach a certain spectral shape is assumed, fitted to data and

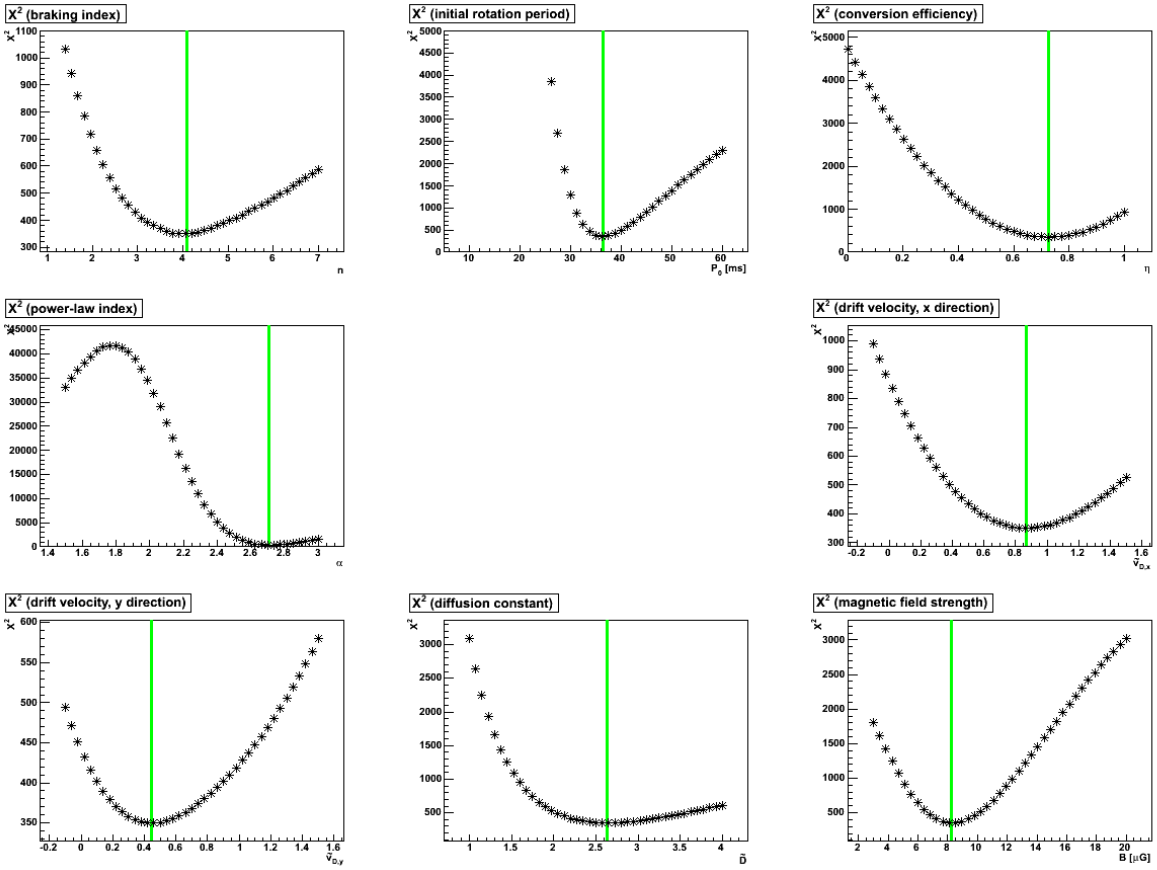

Figure 5.8.: Distribution of the X^2 values in the vicinity of minimum 3.1, see Tab. 5.4. One after the other the dependencies in the individual model parameters are shown. The green lines indicate the position of the minimum.

subsequently used to calculate the spectrum points, see Sec. 4.3.5. In the case of the spectrum points presented in Fig. 5.9 a power-law shape was assumed. If this assumption is wrong, which is not very unlikely for cooled energy spectra, then the calculation of the spectrum points is biased. Therefore, in the next but one section, i.e. Sec. 5.5, it will be investigated whether an alternative fitting method will change the X^2 distribution.

5.4. Predictions for the X-ray and GeV γ-ray regime

Having identified several parameter sets for which the predictions of the new model agree well with the observed TeV data, our next step was to study the predictions for other energy ranges, too. For such investigations the X-ray and the GeV γ-ray regimes were well suited. On the one hand, spatially resolved spectroscopic data were available for these energy ranges (see Sec. 3.4 and 3.5) and on the other hand it was rather straightforward to expand the model such that these energy ranges could be studied as well. In particular, the photon emission observable in these energy ranges is generated by the

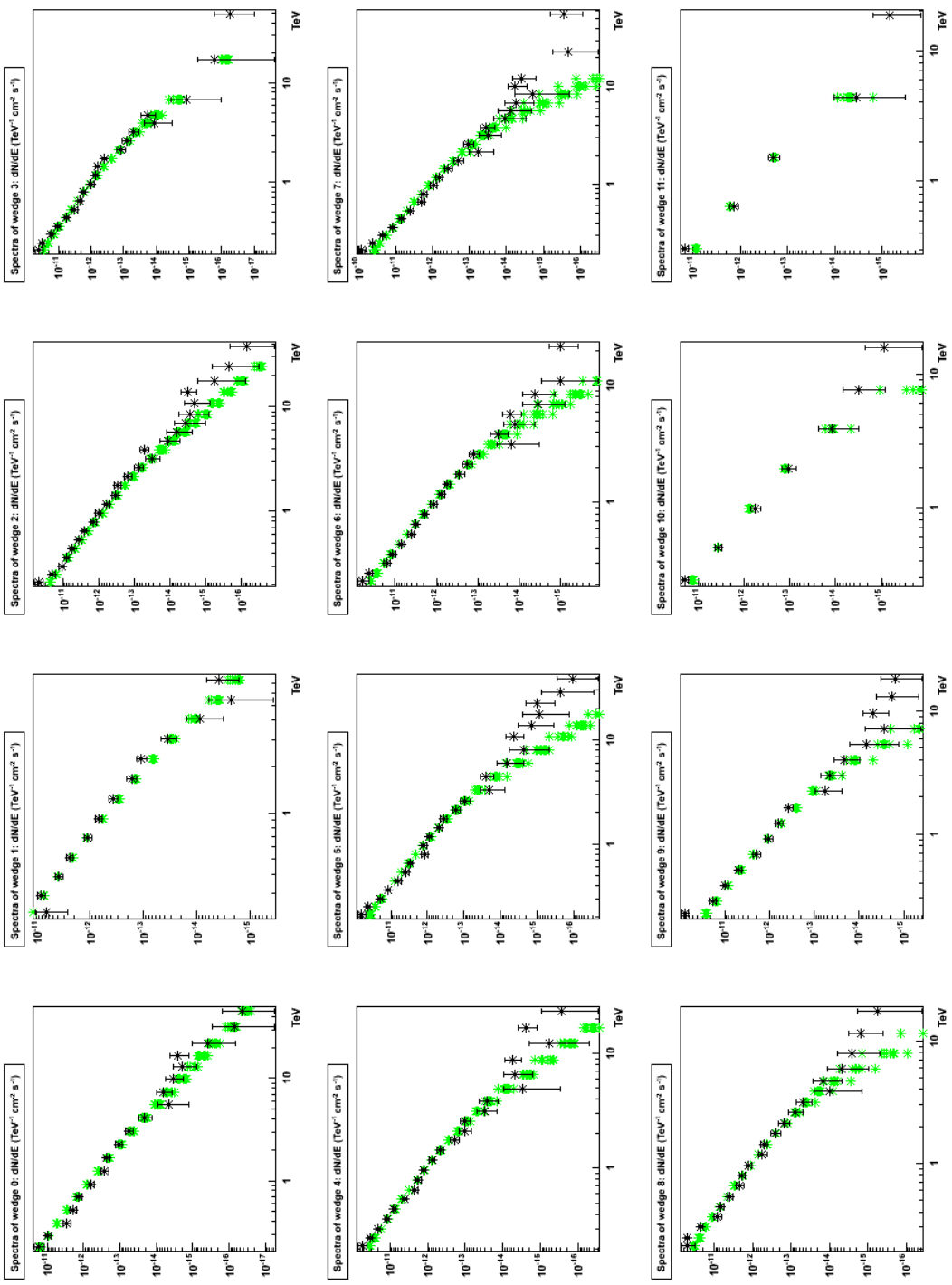

Figure 5.9.: Comparison of the observed wedge spectra of HESS J1825–137 (black markers) and the simulated ones (green markers). Simulations have been performed for all model parameter sets listed in Tab. 5.4.

same lepton population as the TeV γ rays, cf. Sec. 2.4.3. Thus, only that part of the simulation dealing with the photon emission processes had to be adapted. For the X-ray emission only synchrotron emission processes were considered, while inverse Compton and synchrotron emission were included for the GeV γ-ray regime.

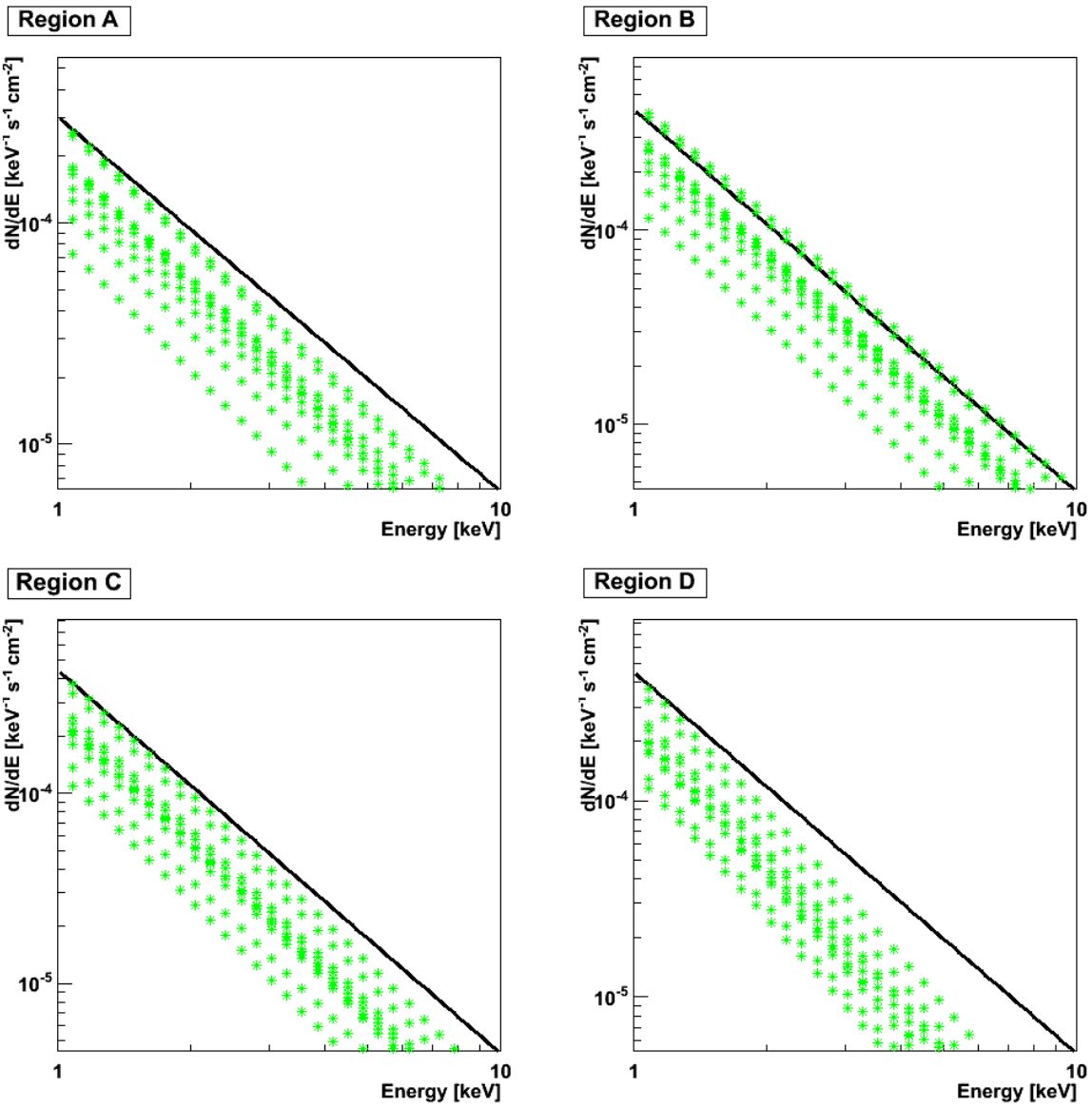

Figure 5.10.: Comparison of observed X-ray energy spectra for HESS J1825–137 and the predictions of the new model. The measured data were recorded with the Suzaku telescope. Energy spectra have been determined for four subregions (A–D, see Fig. 3.11). For each of these regions the power-law which describes the observed data best is shown as a black line. In addition the green graphs depict the predictions of the model. Each graph corresponds to one of the parameter sets listed in Tab. 5.4.

In the X-ray regime the best coverage of the emission region of HESS J1825–137 was obtained by Suzaku. We concentrated on the analysis results by Uchiyama et al. [U$^+$09],

which have been presented in Sec. 3.4. Our decision against the analysis results by van Etten et al. [ER11] was due to the fact that some scaling assumptions were made in their analysis, which might not be justified. Uchiyama et al. determined the energy spectra of four subregions (region A–D). Tab. 3.2 gives an overview of the results of power-law fits to the individual energy spectra. Moreover, the respective power laws are plotted in Fig. 5.10. For comparison, the predictions of the adapted model for the energy range accessible for Suzaku were calculated for the parameter sets listed in Tab. 5.4. These predictions are represented in Fig. 5.10 by green graphs. Considering that the parameter sets used in the modelling have been determined by fitting only the TeV data, the predictions for the X-ray regime agree rather well with the observed data. However, the simulation shows a clear tendency of underpredicting the measured data. Furthermore, the steepening of the spectra for larger distances to the pulsar is more pronounced for the simulated spectra as for the observed ones. The possible causes are most likely the same simplifying assumptions that have already been suggested to explain the differences between the simulated and measured TeV energy spectra (cf. previous section). However, it should be stressed that for the X-ray data the shape of the particle injection spectrum, especially at higher energies, is of particular importance. While a hard cut-off might be an appropriate assumption for the modelling of TeV data, more elaborate shapes should be considered in the modelling of X-ray data.

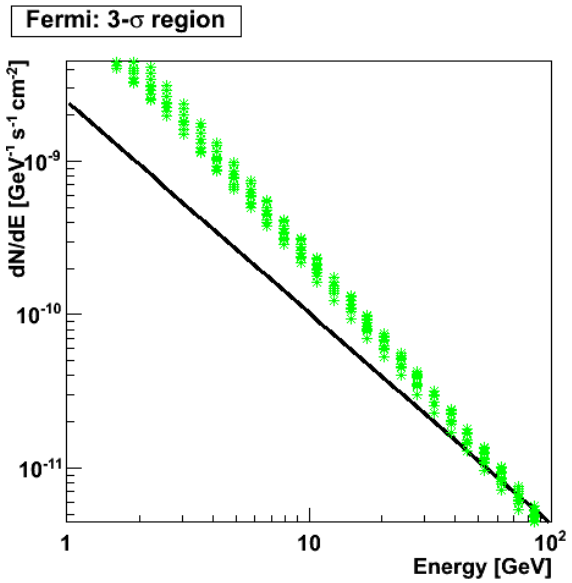

Figure 5.11.: Comparison of the observed Fermi-LAT spectrum of HESS J1825–137 and the predictions of the simulation. The black line represents the power law that fitted the total Fermi-LAT energy spectrum best. The predictions of the simulation for a circular region with radius $r = 3\sigma$ are depicted by the green graphs.

In the Suzaku analysis the spectrum extraction regions were specified precisely. On the contrary, for the analysis of the Fermi-LAT data it was only reported that the true GeV-morphology was assumed to be well described by a Gaussian model (centre at $l = 17.57°$, $b = -0.43°$, $\sigma = 0.56° \pm 0.07°$). No specific source radius was quoted for the computation of the total energy spectrum. For want of any precise information, in

the simulation a circular spectrum extraction region centred on the position of the Gaussian with a radius of $r = 3\sigma$ was investigated. The predicted total energy spectra for this region in the Fermi-LAT energy range for all ten parameter sets of Tab. 5.4 are shown in Fig. 5.11. Again, the simulated and the measured data (indicated by the black line) are of the same order and exhibit similar trends. However, the simulated curves are again steeper than the measured one. Even though this time the total energy spectrum of the source was considered, the explanations that have been offered for the deviations of the simulated and measured data in the X-ray and TeV γ-ray regime should still be valid. By allowing the leptons to propagate faster away from the pulsar, the PWN could be ascribed a younger age and the leptons would have suffered less energy losses. Moreover, the injection spectrum and the modelling of the cooling processes (in particular the modelling of the time and space dependent magnetic field) should play an important role.

The studies in this section have shown the following: Although the new model was targeted at investigating the TeV data and though the parameters were fixed such that the H.E.S.S. data were reproduced in the best possible way, the predictions for the X-ray and the GeV γ-ray regime did not deviate strongly from real measurements. Considering the size of the covered energy range and the fact that completely different spatial regions were investigated this observation should be taken as a good sign. Of course, further fine-tuning of the model assumptions is necessary, but the newly developed model seems to provide a good starting point for future studies.

5.5. Alternative Optimising Methods

Optimising the model parameters by minimising X^2 had the advantage that it was a very fast approach, as the computing time required for the computation of the energy spectra of the wedges and of the corresponding X^2 value was relatively small. However, the method had some weak points, which will be discussed in this section. As a consequence two alternative approaches are presented and their applicability is investigated.

5.5.1. Log-likelihood Comparison of the Simulated and Observed Energy Spectra

As has been stated before, the calculation of energy spectra by means of forward folding, which is the default procedure in the H.E.S.S. software, requires the pre-selection of a specific spectrum shape. As a consequence the computed spectrum points depend on the selected shape. For instance, the energy spectra presented in Sec. 4.4 have been calculated assuming a power-law distribution. However, we have already seen that the model predictions for the individual wedges can deviate from this assumption, see Fig. 5.9. Therefore, it might be an alternative to omit the detour over the power-law fit and to fit the model predictions directly to the observed data. In the default spectrum fitting procedure the determination of the best fitting spectrum parameter sets is based on a log-likelihood comparison, see Sec. 4.3.5. To this end, for a specific spectrum shape and

a specific parameter set the expected numbers of source events per reconstructed energy bin are computed. Subsequently, the negative log-likelihood is calculated for each bin, cf. Eq. 4.17, and by adding up the contributions from all bins an indicator (viz. $-LL_{\mathrm{sp,i}}$) is defined which can be used to quantify how well the current model prediction agrees with the measured data. By making a few changes to the software at hand this approach can be modified such that the energy spectra which are calculated on the basis of a certain spectrum shape can be replaced by the spectrum predictions of the model presented in this thesis. Thus, the $-LL_{\mathrm{sp,i}}$ variable can also be used to evaluate how well the spectrum predictions of the new model agree with the measured data.

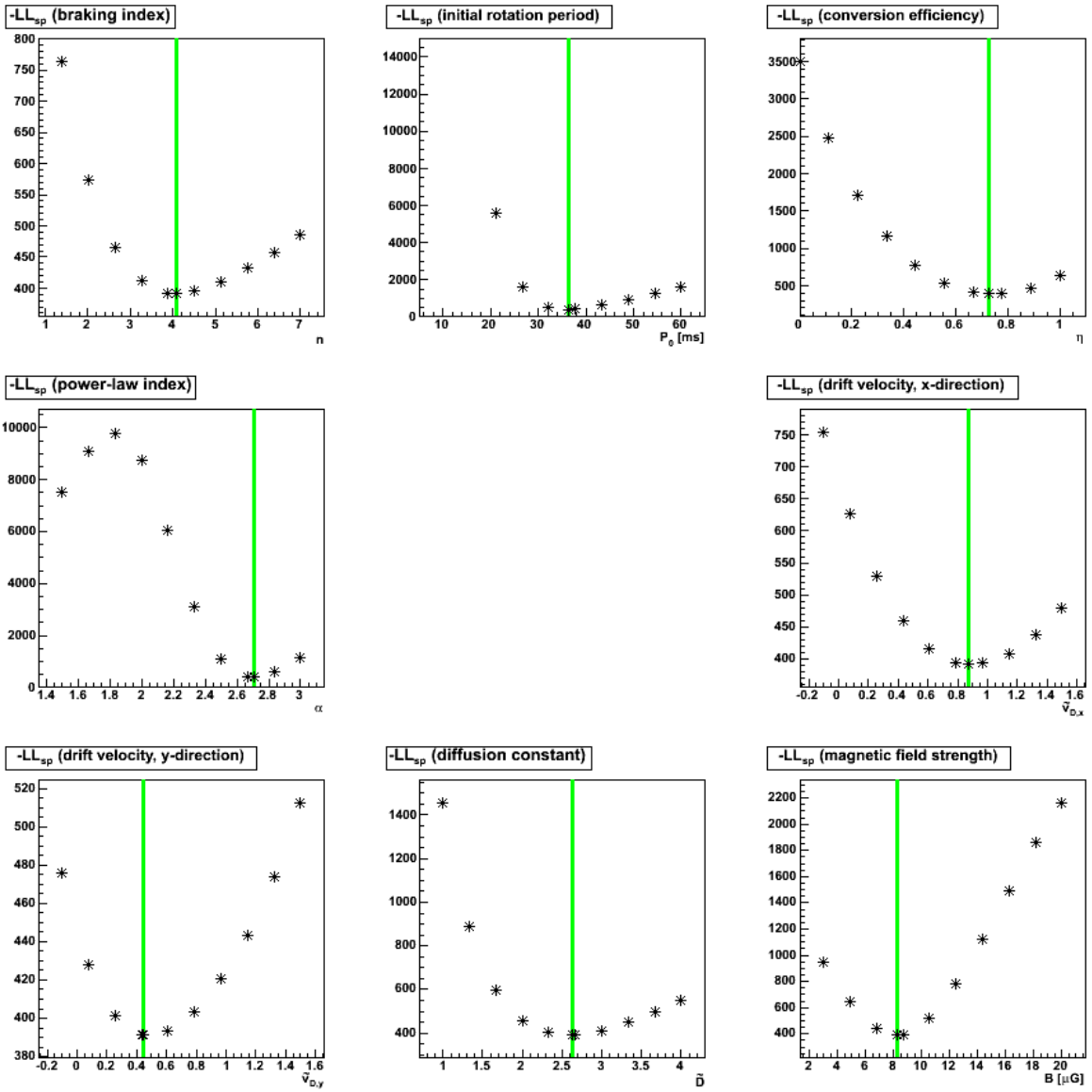

Figure 5.12.: Distribution of the $-LL_{\mathrm{sp}}$ values in the vicinity of minimum 3.1. $-LL_{\mathrm{sp}}$ is an alternative indicator to evaluate how well the forward-folded model spectrum agrees with the measured data. See text for definition. The green lines indicate the location of the minimum, which was found by minimising X^2.

By default the best fitting spectrum parameter set is determined by minimising $-LL_{\mathrm{sp,i}}$ using the method of steepest descent. Due to the complexity of the presented model (at least in comparison with a simple power-law shape) it is not possible to adopt this method or to use it in a slightly modified form. Instead, we decided to get a first impression of the modifications that might be introduced by the new comparison method, by studying how the $-LL_{\mathrm{sp,i}}$ variable behaves in the vicinity of the minima listed in Tab. 5.4. However, prior to this another small modification had to be made: So far, $-LL_{\mathrm{sp,i}}$ was defined as the sum over the negative log-likelihood values ascribed to the reconstructed energy

bins of a single spectrum. However, in this chapter we are not looking for the parameter set that reproduces a single spectrum, but for the parameter set which reproduces all 12 energy spectra of the wedges at the same time. Therefore, a new definition of the $-LL_{\mathrm{sp}}$ variable was introduced: in the following $-LL_{\mathrm{sp}}$ is understood as the sum over the negative log-likelihood values ascribed to the reconstructed energy bins of all twelve wedges.

In the style of Fig. 5.8, Fig. 5.12 shows the distribution of the $-LL_{\mathrm{sp}}$ values in the vicinity of minimum 3.1. The respective plots for the other minima of Tab. 5.4 have been moved to Appendix B.3. Due to the increased computing time only 11 sampling points are shown per parameter co-domain. Nevertheless, the obtained curves show the same trends as the histograms in Fig. 5.8. In fact, the minima of the curves remained at the location, that had been determined in the Simplex minimisation and which are indicated by the green lines in the plots.

We interpret this observation such, that the exchange of the minimising variable ($-LL_{\mathrm{sp}}$ instead of X^2) does not alter the location of the minima in parameter space. However, it has to be noted that while the positions of the ten minima of Tab. 5.4 in the parameter space does not change, their ranking does. In other words: regarding these ten minima the minimum with the smallest X^2 value does not have the smallest $-LL_{\mathrm{sp}}$ value and in the same way also the ranking of the other minima changes. This behaviour is a consequence of the weighting of the individual wedges: In the calculation of X^2 a sum over all spectrum points of all wedges is evaluated. Since the individual spectrum points have been chosen such that each point is ascribed a significance of $3\,\sigma$, the wedges with a high significance (see Fig. 4.16) have a stronger impact on X^2 than those with a smaller significance. In contrast, in the definition of $-LL_{\mathrm{sp}}$ all wedges have the same weight. Of course, it would be possible to adapt the weighting in the $-LL_{\mathrm{sp}}$ computation and in doing so one would only change the ranking of the minima and not their location in parameter space. However, since the weighting in the X^2 computation seems very natural and since the calculation of X^2 is many times faster than that of $-LL_{\mathrm{sp}}$ and finally since the X^2 method is despite certain approximations capable of identifying the well suited parameter sets, we consider the observations in this section as an affirmation, that it well justified to adapt the model spectra to the observed ones by means of X^2.

5.5.2. Log-likelihood Comparison of the Simulated and Observed Sky Maps

At the end of Sec. 5.3 the energy spectra resulting from the parameter sets obtained in the X^2 minimisation were presented. Beyond that, the model presented in this thesis also provides the possibility to study the corresponding sky maps as observed by the H.E.S.S. telescopes. A detailed description of the necessary computation steps was given in Sec. 5.1 and the sky maps that correspond to the minima presented in Tab. 5.4 are shown in Fig. 5.13. The order of the sky maps corresponds to the order of the parameter sets in the tabular. Having a close look at these sky maps it is very interesting to note that the morphology shapes vary significantly.

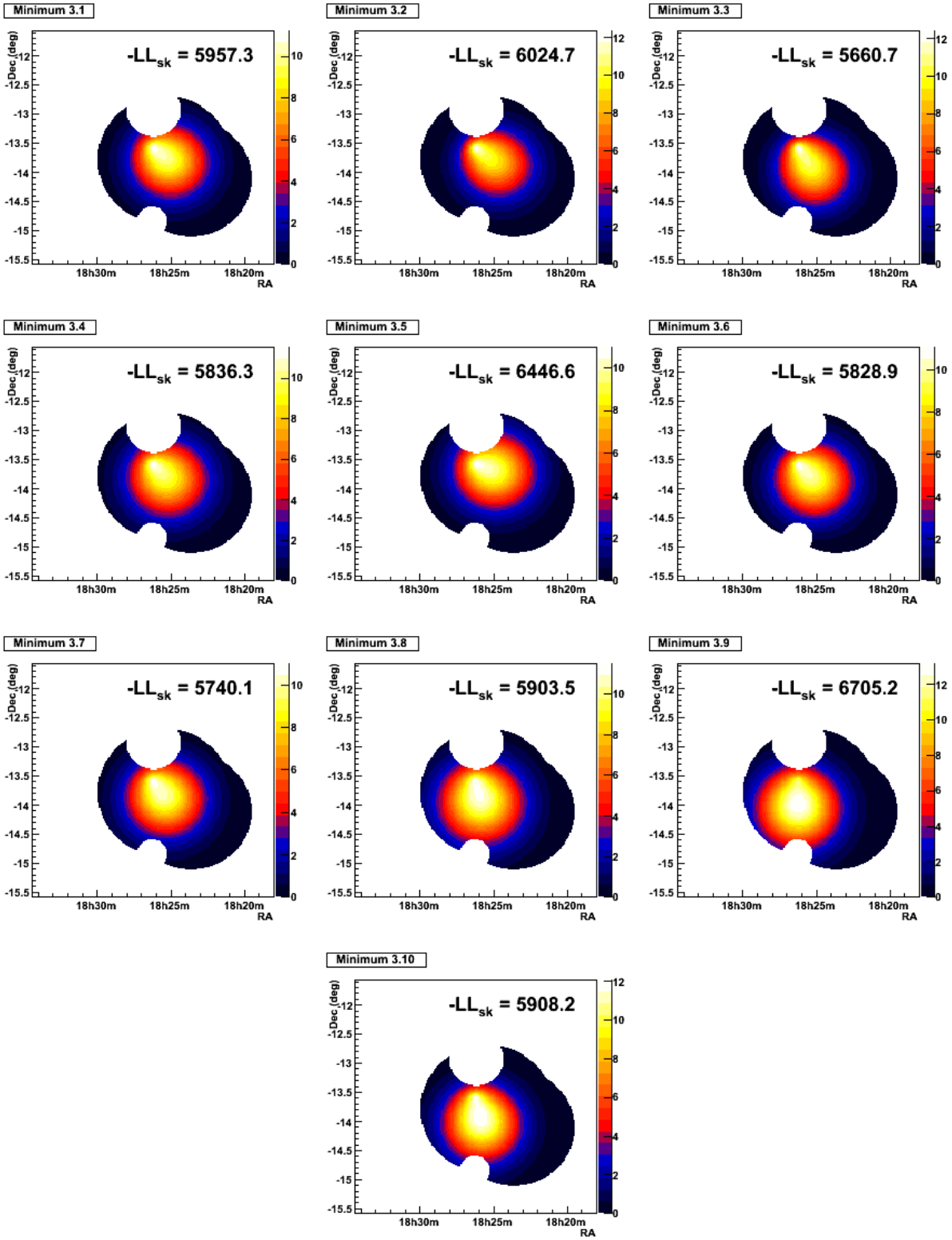

Figure 5.13.: Simulated H.E.S.S. sky maps for the parameter sets listed in Tab. 5.4.

Only by eye it is very difficult to judge how well the modelled sky maps match those of the new analysis of HESS J1825–137. There are several obstacles. For instance, the modelled sky maps only represent expectation values, while the measured γ-ray count maps should fluctuate around these values. This is illustrated in Fig. 5.14: While sky map (a) shows the predicted distribution for minimum 3.3, sky map (b) shows an example of what a corresponding event map may look like. The latter was generated in a random process assuming in each bin a Poisson distribution with an expected value equal to the prediction of the model. Out of all sky maps provided by the H.E.S.S. analysis procedure the simulated γ-ray count map is best compared to the excess map, cf. Sec. 4.3.3, because this map has been corrected for background events. The respective sky map for HESS J1825–137 is shown in panel (c) of Fig. 5.14. Note that the γ-ray counts in both sky maps are roughly of the same order. However, in the excess map the fluctuations are significantly stronger as not only the source events fluctuate, but also the subtracted background events.

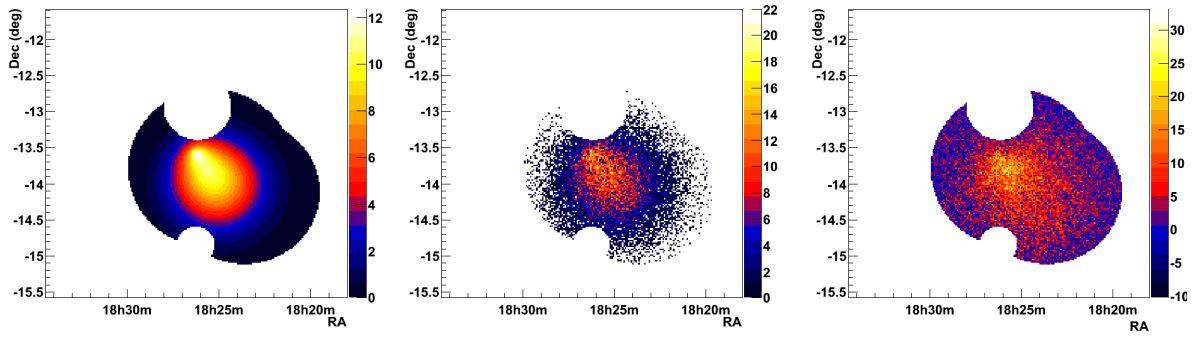

(a) Model (b) Simulated γ-ray events (c) Excess Map

Figure 5.14.: Comparison of the model prediction for parameter set 3.3, an example of what a corresponding event map may look like and finally the measured excess map of HESS J1825–137.

Therefore, in order to evaluate objectively which of the presented sky map simulations agrees best with the observed data, we fell back on the underlying principle of the default morphology fit in the H.E.S.S. software, cf. Sec. 4.3.4 and the end of Sec. 4.4. Knowing the number of γ- and hadron-like events as well as the corresponding acceptance values per bin, see Fig. 4.19, and having calculated the number of expected source events by means of the simulation, Eq. 4.17 was used to assign a negative log-likelihood value to each bin: $-LL_{\mathrm{sk,i}}$. Subsequently, a total measure of how well the simulation describes the measurement was obtained by adding up the negative log-likelihood values of all bins encompassed in the simulation region: $-LL_{\mathrm{sk}} = \sum_{\mathrm{i}} -LL_{\mathrm{sk,i}}$. The $-LL_{\mathrm{sk}}$ which corresponded to the simulated sky maps are quoted in Fig. 5.13. By sorting the sky maps in ascending order with respect to the $-LL_{\mathrm{sp}}$ values a sequence is obtained which is shuffled in comparison to the one of Tab. 5.4. This new order indicates that the minimum labelled 3.3 reproduces the measurements best.

However, at once the question arises, whether the term “minimum” is still appropriate.

To investigate whether this claim can be maintained the distributions of $-LL_{\mathrm{sk}}$ in the vicinities of the quoted values were studied. Note that, in order to save computation time, a coarser binning has been applied to the sky maps, i.e. in comparison to the sky maps shown in Fig. 5.13 2×2 bins were merged to a new bin. In the style of Fig. 5.8, Fig. 5.15 shows how the corresponding $-LL_{\mathrm{sk}}$ value changes when the individual model parameters are varied using the parameter set of minimum 3.1 as an example. The distributions for the other parameter sets of Tab. 5.4 have been moved to the appendix. The figures show that the $-LL_{\mathrm{sk}}$ distributions have been shifted significantly, i.e. the minima of the new distributions no longer coincide with the minima of the X^2 distribution.

Studying the $-LL_{\mathrm{sk}}$ more elaborately, i.e. identifying the minima of this distribution by means of a parameter scan or a minimisation procedure is currently too expensive, as the calculation of the photon spectra for the finely binned sky maps is very time-consuming. Moreover, it is also questionable, how goal oriented such an approach would be, since for the future it would be desirable to fit spatial and spectral features at the same time, and not to consider individual aspects separately. Therefore, the question rises, how the presented methods could be combined to obtain improved results.

5.5.3. Future approaches

Fitting the model to the energy spectra of the wedges of the formerly published analysis of HESS J1825–137 has the advantage that this approach is rather fast and robust. However, a weak point is that the choice of the wedges was rather arbitrary. Of course, it made sense in the original analysis to choose wedges which were centred on the pulsar, but there are several arguments why their extent, i.e. their opening angle and their thickness, could have been chosen differently. Moreover, by concentrating on the predefined wedges a large area of the emission region, see Fig. 4.15, and thus additionally available information is neglected.

On the other hand, by fitting the morphology all information considering the energy distribution is ignored. This might be circumvented by considering a 3-dimensional histogram instead of the 2-dimensional sky maps, in which the additional dimension provides information on the energy distribution. Currently such an approach is prevented by technical difficulties. For instance, as already mentioned the computation of the simulated sky maps is rather time-consuming. However, in the future it should be possible to significantly speed up this procedure, e.g. by using look-up tables. Moreover, the bins in a 3-dimensional histogram must be enlarged to increase the statistics in each bin. Fortunately, this would have the helpful side-effect of decreasing the computation time. In addition, it has to be considered that the measured data must be provided in an appropriate way. However, there has been a lot of activity in the field of computing energy-dependent H.E.S.S. sky maps so that this should be achievable with minor changes to the current software. An elaborate treatment of the technical details of the imaging process of the H.E.S.S. telescopes is even more complex. In the approach described above the PSF and the effective areas were calculated under the simplifying assumptions of mean zenith or offset angles. Moreover, the energy dependence of the PSF was treated rather roughly.

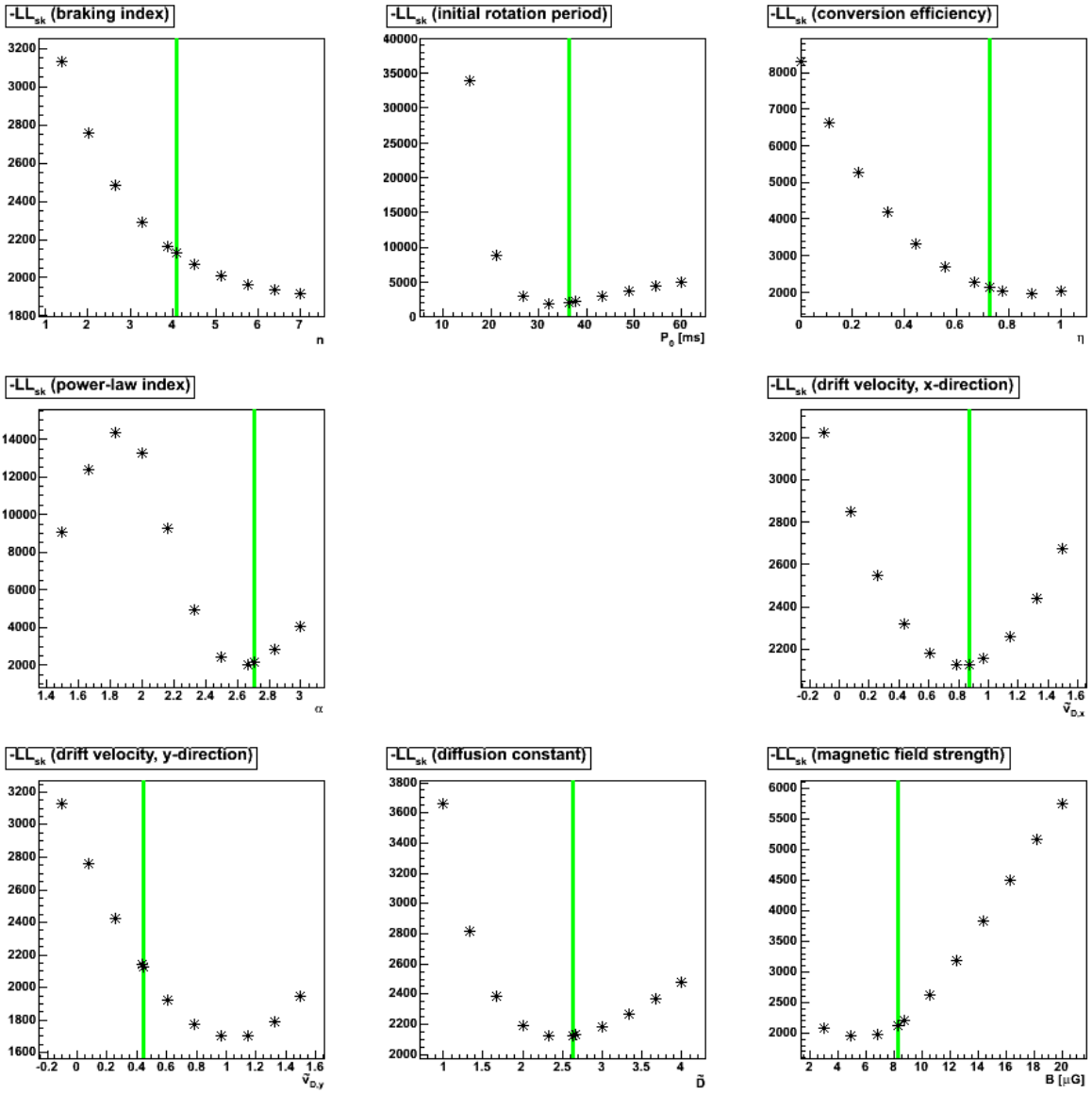

Figure 5.15.: Distribution of the $-LL_{\mathrm{sk}}$ values in the vicinity of minimum 3.1, in the style of Fig. 5.8. The green lines indicate the position of the minimum of the X^2 distribution.

For the future it would be desirable to consider these influences in greater depth, but this requires time-consuming Monte Carlo studies.

For all these reasons an alternative approach, which might be easier to realise, is to modify the fitting procedure of the wedge energy spectra. Instead of fitting the energy spectra of the wedges as defined in the published analysis of HESS J1825–137, new quadratic ("bin-like") wedges might be chosen which are evenly distributed and which cover the emission region as a whole. In doing so, one effectively obtains a 3-dimensional sky map, but at the same time the advantages of the wedge fitting procedure are preserved. In particular, the technical details of the imaging process of the H.E.S.S. telescopes are extensively treated in the default spectrum fitting procedure. By taking their computation out of the

comparison procedure, the latter becomes less challenging and easier to handle.

6. Summary & Outlook

In this work the TeV γ-ray source HESS J1825–137 was studied in depth. The point which made HESS J1825–137 particularly interesting was that this source can be considered an archetype of the class of evolved pulsar wind nebulae. In particular, it exhibits all the specifics ascribed to this source class: The emission region is vastly extended and strongly asymmetric and the pulsar, which is considered the engine of the nebula, is not located in its centre. Beyond that, HESS J1825–137 is one of only two pulsar wind nebulae for which an energy-dependent morphology could be established in TeV γ rays. Since these exceptional spatial and spectral features sort of map the integrated history of the pulsar wind nebula, HESS J1825–137 is a prime target for simulations aiming to reconstruct the evolution of PWNe.

In order to obtain an overall picture of HESS J1825–137 a detailed review of observations in various energy ranges was presented. The focus within this work was on the non-thermal emission component. In fact, a new analysis of the H.E.S.S. data of HESS J1825–137, which comprised twice the amount of live time and was performed with a more sensitive analysis software than in previous publications, was carried out. This new analysis confirmed earlier important results, e.g. the steepening of the energy spectra for larger distances to the pulsar, even though the considered energy range had been extended significantly. Moreover, hints at an enlarged emission region emerged. On the contrary, a large part of the northern emission region, which was originally ascribed to HESS J1825–137, is now considered to represent a separate TeV γ-ray source, viz. HESS J1826–131, and was excluded from the analysis as well as from the modelling performed in this thesis.

The purpose of the newly developed model was to comprehend the formation of the specific morphological and spectral features of HESS J1825–137. The new model took its cue from well-established pulsar wind nebula models. Taking into account time dependencies, the particle emission by the pulsar, the propagation of the particles into space, their energy losses and finally the γ-ray emission were simulated. The key features of the presented model is that the particle propagation is ascribed to diffusion processes, that particle emission by a moving object is considered and that an additional drift term can be included. Furthermore, the model can be used to simulate energy spectra for arbitrary sub-regions of the emission region as well as sky maps as observed by the H.E.S.S. telescopes. The latter requires a careful consideration of the imaging properties of the H.E.S.S. experiment.

In this work the primary focus of the modelling was placed on reproducing the TeV γ-ray data of HESS J1825–137 in the best possible way. More precisely, this thesis is concentrated on reproducing the energy spectra of twelve regions of particular interest, which already played an important role in the previous H.E.S.S. publication dedicated

to HESS J1825–137. By means of a scan of the model parameters and by consulting an additional minimisation procedure ten parameter sets were identified, which reproduced the TeV energy spectra particularly well. For the selected parameter sets a comparison of the model predictions for the X-ray and GeV energy range with measurements also showed a relatively good agreement.

However, not unexpected for such a complex simulation, some deviations between the model predictions and the measurements were found. For instance, for all energy ranges the simulated spectra were steeper than the measured ones. These deviations were most likely caused by simplifying assumptions made in the modelling process, which included the neglect of convection, an energy-independent diffusion, the disregard of adiabatic energy losses and the assumption of a constant magnetic field. All assumptions require further investigations and leave room for future improvements. Moreover, for the future an adaption of the parameter optimising procedure is desirable. As an alternative to fitting the energy spectra of the selected sub regions one might consider fitting a 3-dimensional histogram, which allows to study the distribution of the γ rays not only in space but also in energy. In addition, a larger part of the emission region should be covered and data from observations in other wavelengths should be considered in the fitting process. First steps in this directions have been presented in this thesis.

A. HESS J0632+057: A New γ-ray Binary?

A.1. γ-ray Binaries

X-ray emitting binaries are a very common source class in the Milky Way. In the γ-ray regime in contrast, only six binary systems have been identified until today. These sources are PSR B1259–63 [A$^+$05d], LS 5039 [A$^+$05e], LSI +61°303 [A$^+$08a], Cygnus X–3 [T$^+$09], 1FGL J1018.6–5856 [A$^+$12b] and HESS J0632+057. During my work as a PhD student, I was part of a working group who contributed to the identification of HESS J0632+057 as a binary system. In the following it is presented which perceptions of γ-ray emitting binary system exist and why these objects are especially interesting. Taking HESS J0632+057 as an example it is explained how this source, which was first detected in TeV by H.E.S.S., was finally identified as binary system.

A short up-to-date overview of the binary compositions in which γ rays may be generated is given in [Mir12]: All γ-ray emitting binaries have in common that a compact star, i.e. a neutron star or a black hole is orbiting a massive star. In some configurations it is even possible that the compact star accretes mass from its companion, thus forming a microquasar, see Fig. A.1 centre. The physical environment, in which the γ-ray emission in binary systems takes place, differs significantly from those of other Galactic TeV emitters, e.g. PWNe and SNRs, [HH09]. In binary systems the density of high-frequency photons is increased, the magnetic field is stronger than in the ISM and interactions with target material from stellar winds / discs are expected. These differences in the environment are propagated to the observable γ-ray spectra. Moreover, the emission processes take place on shorter time scales. In general, γ-ray emission is not expected for the total orbit, but only for certain phases and thus periodic or flaring signals are predicted.

The two main γ-ray emission processes in binary systems are electron / proton interactions with protons and electron-photon interactions [Mir12]. The latter occur predominantly when the electrons from a pulsar wind – which is caused by a fast rotating neutron star – or from a microquasar hit the UV photons emitted by a massive star, see sub-figure B & C in Fig. A.1. Thereby the UV photons are up-scattered via IC interaction. During the orbit the γ-ray signal is expected to be strongest when the compact star is located along the line of sight to the massive star on the side facing away from the observer. In the second scenario the γ-ray emission is due to interactions of charged particles with protons. These may occur for instance when the particle winds of a pulsar intersect with stellar disks, as they are known from Be stars, see sub-figure A in Fig. A.1. In this case γ-ray

emission is expected only for the short transition phase. Charged particle interactions with protons may also occur when the relativistic jets of microquasars hit cold proton clumps which can develop in stellar winds of massive stars, see sub-figure B in Fig. A.1.

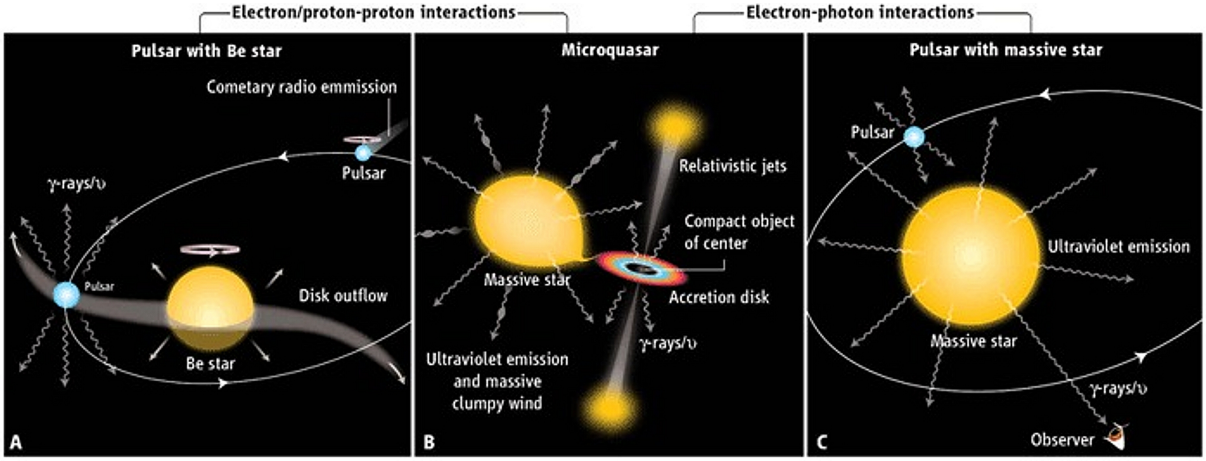

Figure A.1.: VHE emission scenarios in binary systems. From [Mir12]. Reprinted with permission from AAAS.

The orbital modulations are very characteristic for binary systems. Therefore, the identification of a γ-ray emitting binary system is usually based on the detection of a periodic signal in the γ-ray data or in corresponding multiwavelength data. However, even when a periodic signal is detected, it is still very challenging to identify the scenario in which the γ rays are generated. For this purpose in-depth multi-wavelength coverage is needed. Crucial evidence is for instance the detection of radio pulses by a pulsar or of certain radio characteristics of the jets in the microquasar scenario. So far the identification of the compact companion in a γ-ray emitting binary system was only successful for PSR B1259–63, where the compact object is known to be a pulsar. Cygnus X–3 is usually ascribed to the microquasar scenario, while for LS 5039, LSI +61°303 and 1FGL J1018.6–5856 there are hints at the microquasar scenario as well as at the pulsar scenario. To further improve our understanding of the nature of the γ-ray emission in binary systems it is desirable to increase the number of known systems. In the following it is briefly summarised how the identification of HESS J0632+057 as fourth TeV γ-ray emitting binary system succeeded.

A.2. HESS J0632+057

Detection by the H.E.S.S. Experiment

Searching for a TeV signal from a suspected interaction region of the Monoceros Loop supernova remnant (SNR) and a young stellar cluster / molecular cloud complex known as Rosette Nebula (see Fig. A.2(a)), HESS J0632+057 was detected by chance. In the SNR / molecular cloud scenario a TeV signal was expected that should have been correlated with data from the NANTEN telescope, tracing molecular clouds. The 13.5 hours of

H.E.S.S. data taken in 2004 - 2006, however, revealed a single point-like source [A$^+$07]. The new source was located at the outer rim of the SNR, but exhibited a significant offset to the clusters of ^{12}CO emission, as shown in Fig. A.2(b). Searches for better suited counterparts revealed an EGRET source (3EG J0634+0521), a ROSAT source (1RXS J063258.3+054857) and finally a Be star (MWC 148), compare Fig. A.2(b) and (c). As for 3EG J0634+0521, HESS J0632+057 is located close to the 99% contour line. Due to the position uncertainty of EGRET, however, this was considered likely to be by chance. Especially, as the binary system SAX J0635+0533 is also a possible counterpart of 3EG J0634+0521 [K$^+$99]. Nevertheless, a comparison of the H.E.S.S. spectrum, which was well fitted by a power-law spectrum (photon index $\Gamma = 2.53 \pm 0.26_{\mathrm{stat}} \pm 0.20_{\mathrm{sys}}$, flux normalisation $k = (9.1 \pm 1.7_{\mathrm{stat}} \pm 3.0_{\mathrm{sys}}) \times 10^{13}\,\mathrm{cm}^{-2}\,\mathrm{s}^{-1}\,\mathrm{TeV}^{-1}$) and the EGRET flux above 100 MeV ($(25.5 \pm 5.1) \times 10^{-8}\,\mathrm{photons\,cm}^{-2}\,\mathrm{s}^{-1}$, index 2.03 ± 0.26) showed good agreement. Searching for a counterpart, the positional coincidence of the new TeV source and the ROSAT source was even more promising, see Fig. A.2(c). But the rather weak X-ray flux of about $10^{-13}\,\mathrm{erg\,cm}^{-2}\,\mathrm{s}^{-1}$ did not allow spectral comparison with the TeV source and challenged standard models in which the X-ray and TeV emission are explained by synchrotron and IC emission of a single primary electron population. Instead the X-ray emission was related to secondary electrons generated in a π^0-decay scenario. The most striking observation, however, was the positional coincidence of the TeV emission and the Be star. Such an coincidence was considered extremely rare. The suggested possible emission scenarios encompassed shocks in stellar winds and binary systems, where the Be star should be orbited by a so far undetected compact companion.

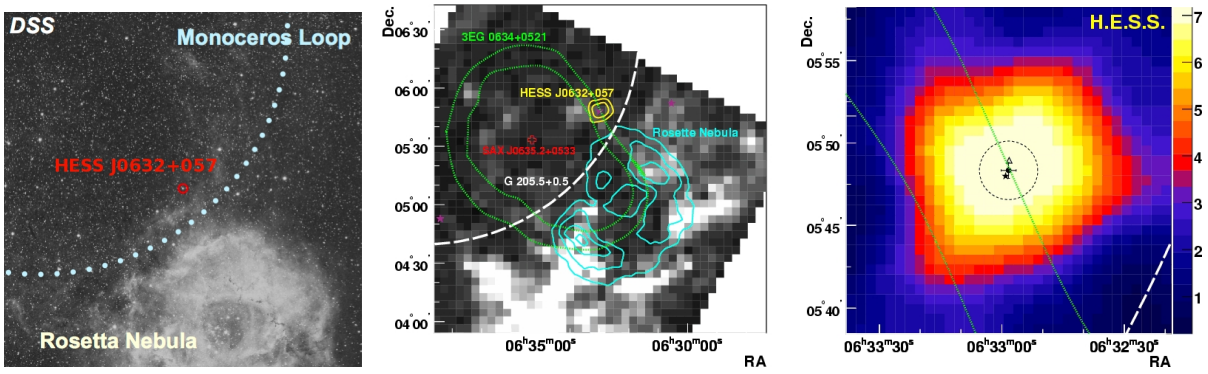

(a) Digitized Sky Survey image (b) NANTEN image (c) H.E.S.S. significance map

Figure A.2.: Multi-wavelength images of the sky region around HESS J0632+057. (a) Digitized Sky Survey image showing the position of HESS J0632+057 with respect to the Monoceros Loop SNR (position from the Green Catalogue) and the Rosette Nebula [MS11a]. (b) Velocity integrated (0-30 km s^{-1}) ^{12}CO (J = 1 → 0) NANTEN image [A$^+$07]. The white areas with the highest flux are offset to HESS J0632+057, for which the 4- and 6-σ-contour-lines are indicated in yellow. In addition the 95 % and the 99 % confidence regions of 3EG J0634+0521 are shown in blue. (c) H.E.S.S. significance map [A$^+$07]. 1RXS J063258.3+054857 (triangle) and MWC 148 (black star) are located within the rms size limit of the TeV source.

Follow-up Observation with XMM-Newton

To reveal the nature of the TeV emission mechanism in HESS J0632+057 follow-up observation in other wavelengths were required. For this purpose HESS J0632+057 was observed for 46 ks with the X-ray satellite XMM-Newton in September 2007 (observation ID 0505200101). Together with Jim Hinton, Jo Skilton and Stefan Funk, I analysed these data and our results were published in [H$^+$09]. For our analysis we used the XMM-Newton Science Analysis Software (SAS, version 7.1.0). Due to a strong proton flare at the end of the observation only 26 ks of the available data set could be used for further investigations. Despite the reduced exposure our analysis revealed a new point-source: XMMU J063259.3+054801. As shown in Fig. A.3(a), the best fit position of the XMM-Newton source ($6^{\mathrm{h}}32^{\mathrm{m}}59.29^{\mathrm{s}} \pm 0.01^{\mathrm{s}}, 5°48'1.5'' \pm 0.1''$) agreed very well with the position of MWC 148. Indeed the two positions were only separated by 0.6″. The likelihood of a chance association of a massive star and a XMM-Newton point-source was estimated smaller than 10^{-6}.

The spectrum of XMMU J063259.3+054801 was determined for all XMM-Newton cameras (MOS-1, MOS-2, PN) from a circular region with a radius of 25″ centred on the best-fit position. In the case of the MOS cameras the background was estimated from a 50–100″ annulus around the source position and for the PN camera from a 75″ circle, located at a distance of 150″ to the source. The choice of the background regions was motivated by the intention to avoid further point-sources and CCD chip edges in the vicinity of XMMU J063259.3+054801. Two different spectrum models agreed well with the observed data. A simultaneous fit to the data of all XMM cameras of an absorbed power law ($\Gamma = 1.26 \pm 0.04$, $N_{\mathrm{H}} = (3.1 \pm 0.3) \times 10^{21}$ cm^{-2}, normalisation at 1 keV: $(5.4 \pm 0.4) \cdot 10^{-5}$ keV^{-1} cm^{-2} s^{-1}) and of a two temperature black body model ($kT_1 \approx 0.4$ keV and $kT_2 \approx 2$ keV) exhibited a χ^2/dof = 27.6/27.0 and 15.8/25, respectively. A single temperature black body model on the contrary was rejected. The fit of the two temperature model was motivated by the fact that such spectra had been observed for isolated magnetic Bp stars and had been linked to shock heating in magnetically confined winds, e.g. [TOUD07]. However, under default assumptions such thermal models are not able to explain the observed TeV emission. Therefore, we decided to concentrate on a non-thermal origin in binary systems.

This decision was backed up by the discovery of first evidence for time variability. To study the time variability we split the total time of observation into six subsets and calculated for each interval the background subtracted count rate summing up the shares of all XMM-Newton cameras. The resulting light curve is shown in Fig. A.3(b). Over the total observation time the flux was decreasing. While a fit with a constant was rated very unlikely, a linear fit revealed a decrease of about 39 %. For comparison the estimated background light curve for the different time intervals is also shown in Fig. A.3(b), indicating that the changes in the source light curve are not due to background fluctuations. Splitting the data set into two subsets and applying the power-law fit to the individual subsets, whereby N_{H} was fixed to the obtained value for the fit to the total data set, did not reveal any changes in the spectrum shape.

An estimate of the distance to MWC 148 was derived by comparison of the apparent visual magnitude $m_V = 9.16$ and an assumed absolute magnitude $M_V = -4.0$. The resulting value of about 15 kpc is in good agreement with a position within the Rosette Nebulae. The intrinsic size of XMMU J063259.3+054801 and its angular distance to MWC 148 were then used to estimate the radiation density at the origin of the X-ray emission to be higher than $10^6\,\mathrm{eV\,cm^{-3}}$. Under these circumstances the γ-ray emission via IC scattering of TeV electrons takes place in the Klein-Nishina regime and the cooling of the electrons is dominated by IC cooling rather than synchrotron emission. Such a scenario would account for the hard X-ray and soft γ-ray spectrum, the time scale of the variability of the X-ray emission and even for the non-detection of spectral variability. Based on this scenario, a simple one-zone model was constructed and presented in our publication. Using standard assumptions for the free parameters the model could well describe the observed emission in X-ray and TeV and was used to illustrated the close resemblance of the spectral energy distribution (SED) to that of the known binary system LSI +61°303. The only difference between the two SEDs was that the luminosity of HESS J0632+057 seems to be significantly lower than that of LSI +61°303.

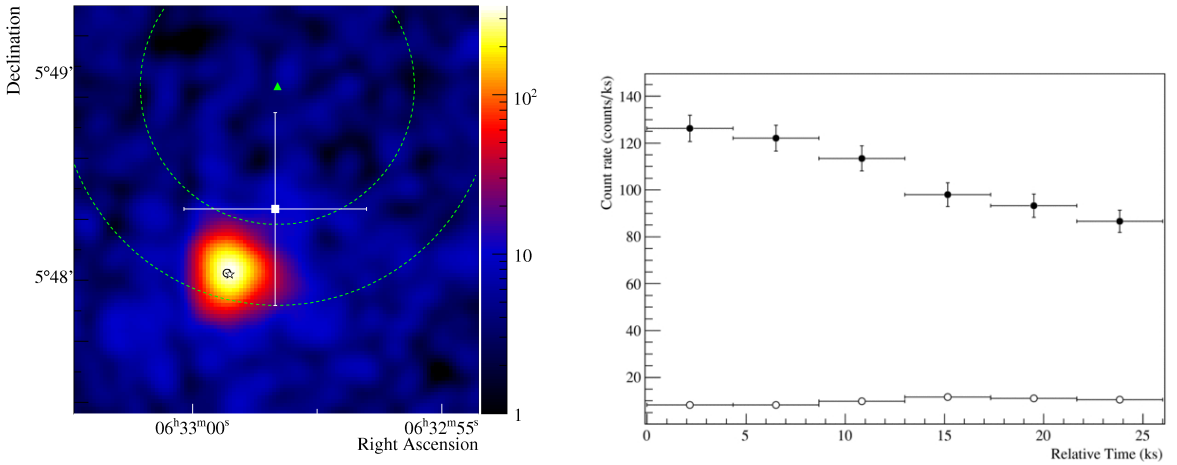

(a) XMM-Newton smoothed count map

(b) XMM-Newton lightcurve

Figure A.3.: XMM-Newton observation of HESS J0632+057. (a) Combined count map of two of the XMM-Newton cameras (MOS-1 & MOS-2) smoothed with a Gaussian with $\sigma = 3''$. The best fit position for XMMU J063259.3+054801 (open circle) agrees very well with the position of MWC 148 (star), and the position of HESS J0632+057 (square marker with error marker). In addition also the position and the estimated 90 % and 99 % CL position errors for 1RXS J063258.3+054857 are depicted (triangle and dashed circles). (b) Background subtracted lightcurve (closed circles) of the three EPIC cameras of XMM-Newton. The open circles indicate the level of the estimated background.

Identification as Binary System

All the presented features of HESSJ0632+057 / XMMU J063259.3+054801, i.e. the counterparts in various wavelengths, the observed SED and the time variability resemble the

features of identified binary systems and thus hint to a binary nature of the TeV emission. Due to the rareness of such systems, the results presented in the last two sections triggered a multitude of follow-up observations by other experiments. To round up this chapter about HESS J0632+057 the present status of these investigations shall be shortly summarised.

While initial searches for periodicity in the increased H.E.S.S. data set (HESS J0632+057 was revisited every year after its detection) were not successful, first hints at variability of the TeV emission were presented by the VERITAS collaboration in 2009 [A$^+$09b]. Though VERITAS had observed HESS J0632+057 for 31 hours in 2006, 2008 and 2009 they could not detect a significant signal in one of these observation periods. By combining their results with the above presented results of the H.E.S.S. Collaboration HESS J0632+057 was rejected as a constant γ-ray emitter with a probability of 99.993 %. Moreover, radio observations with GMRT (at 1280 MHz) and with VLA (at 5 GHz) revealed a point-like radio source coincident with MWC 148 [S$^+$09]. In this case, the radio fluxes extracted from the 6 hours of VLA data taken over the course of 3 months were subjected to variability on month scale. The binary nature of HESS J0632+057 was finally established by the detection of the orbital period with the SWIFT X-ray telescope [B$^+$11]. In this long term campaign XMMU J063259.3+054801 was observed for 463 ks in the time between 2009 January 26 and 2011 March 27. Each observation lasted approximately 5 ks and whenever possible the observations were taken with a temporal distance of 1 week. A first analysis of early Swift-XRT data (January to May 2009) had confirmed variability on day to month scale but did not allow the determination of a period [F$^+$10]. The light curve generated from the full data set [B$^+$11], however, exhibited characteristic peaks and dips which occurred on regular basis, see Fig. A.4. By fitting the peaks and dips with a model consisting of a constant and 10 Gaussians, the most prominent outlier were identified and from their distances a period of 321 ± 5 days was derived.

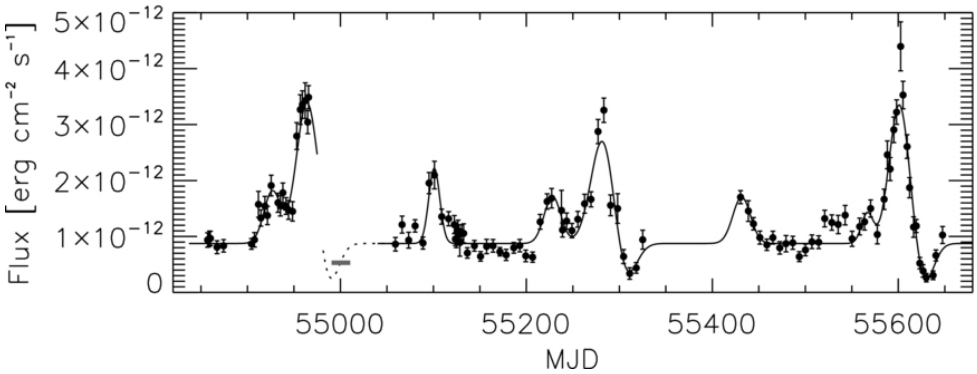

Figure A.4.: Background subtracted X-ray light curve (0.3 – 10 keV) of XMMU J063259.3+054801 as observed by Swift-XRT [B$^+$11]. The result of fitting a model consisting of a constant and 10 Gaussians is overlaid on the data as solid black line.

In Fig. A.5 X-ray fluxes detected by Swift-XRT are presented as function of the orbital phase. Clearly visible is the prominent peak at an orbital phase of about 0.32, followed by a dip and later by a less distinct elevation. In the lower part of the figure the hardness

ratio (2.0–10.0 keV)(0.3–2.0 keV) for the corresponding phase are shown for intervals of 25 days. Especially between the high and the low flux state, the hardness ratio changes significantly. This observation was confirmed by Rea et al., who analysed additional Chandra data and also reported spectral changes between their observation taken at the time of high flux level and the XMM-Newton observation presented above, which was taken at a significant lower flux level [RT11].

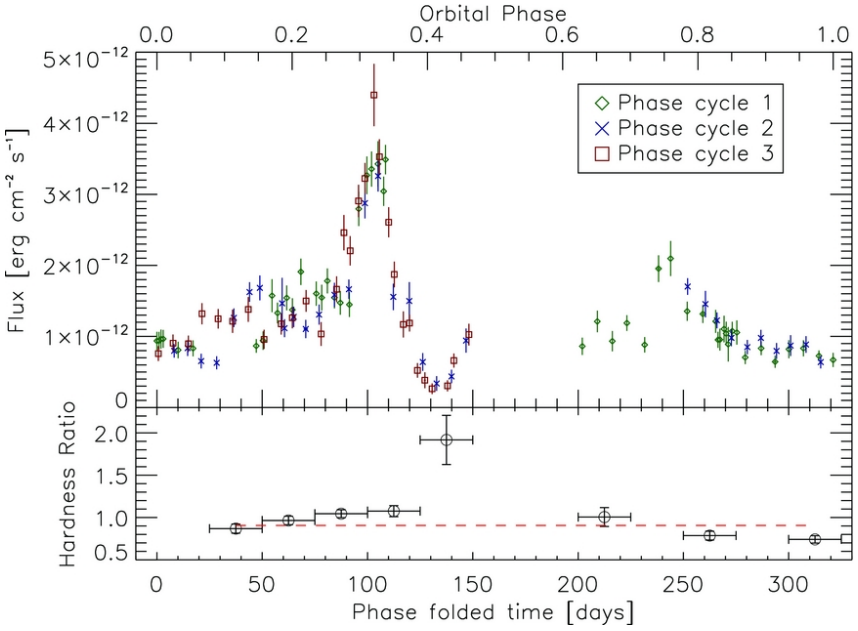

Figure A.5.: Swift-XRT light curve as function of the phase of the 321 days orbit [B+11]. The different cycles are indicated by different symbols (diamond, x and square). In the lower part of the figure the hardness ratio $(2.0 - 10.0\text{keV})/(0.3 - 2.0keV)$ corresponding to the respective phase are also shown.

The knowledge about the orbital period from the Swift data simplified the search for this period within the TeV data. In Fig. A.6 the folded TeV light curve in accordance to the phase provided by Swift is shown, taken from [MS11b]. In this figure data points from H.E.S.S. are shown side by side with data points from VERITAS. The data from both telescopes were taken over the course of seven years. Again a peak is clearly visible at a phase of about 0.3. In contrast to the X-ray data, however, the peak seems shifted to earlier times in the orbital phase. A paper discussing the implications of this observations is expected to be published in the near future.

The identification of HESS J0632+057 as a binary system has increased the number of known TeV γ-ray binaries to four. Today, it is still unclear which type of compact star is hidden in the system and how exactly the γ-ray emission is generated. However, as the system has attracted a great deal of attention over the last years, the results of further observations will soon help to improve the understanding of this truly special source class.

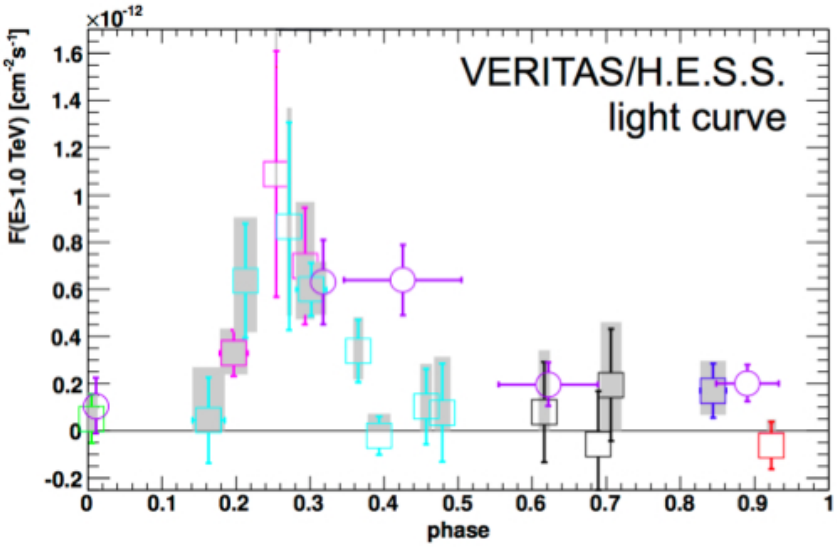

Figure A.6.: TeV γ-ray light curve of HESS J0632+057 as function of the orbital phase provided by Swift [MS11b]. The data points originate from H.E.S.S. observations (circular markers) and VERITAS observations (square markers, different colors represent different observation periods).

B. Auxiliary Information

B.1. Detailed Information on the Spectrum Fits in the New Analysis of HESS J1825–137

In the analysis of HESS J1825–137 published in 2006 as well as in the one presented in this thesis the energy spectra have been extracted for different wedges. The definition of these wedges can be found in Tab. 4.1. To each data set a power-law has been fitted. A very compact representation of the fit results has been shown in Fig. 4.17. Here, in this appendix, a more detailed account of the fit results is given. The Figures B.1, B.2, and B.3 show the best fitting power-laws for each wedge, as well as the forward folded spectrum points. In the lower panels the corresponding residuals in reconstructed energy are presented. Moreover, the insets summarize all values needed to reconstruct the spectra and to rank the quality of the fits.

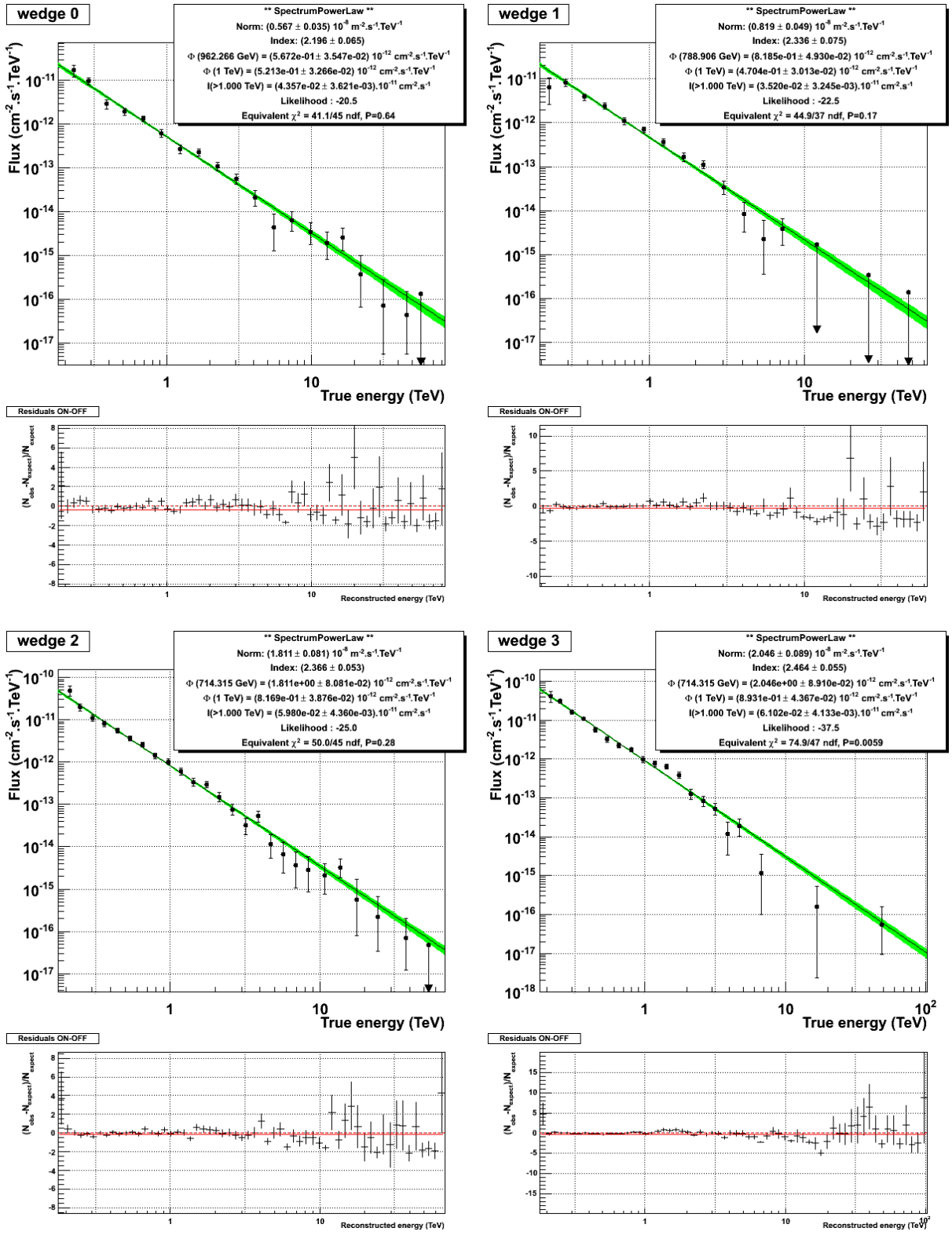

Figure B.1.: New H.E.S.S. spectra and fit results of the four innermost wedge regions.

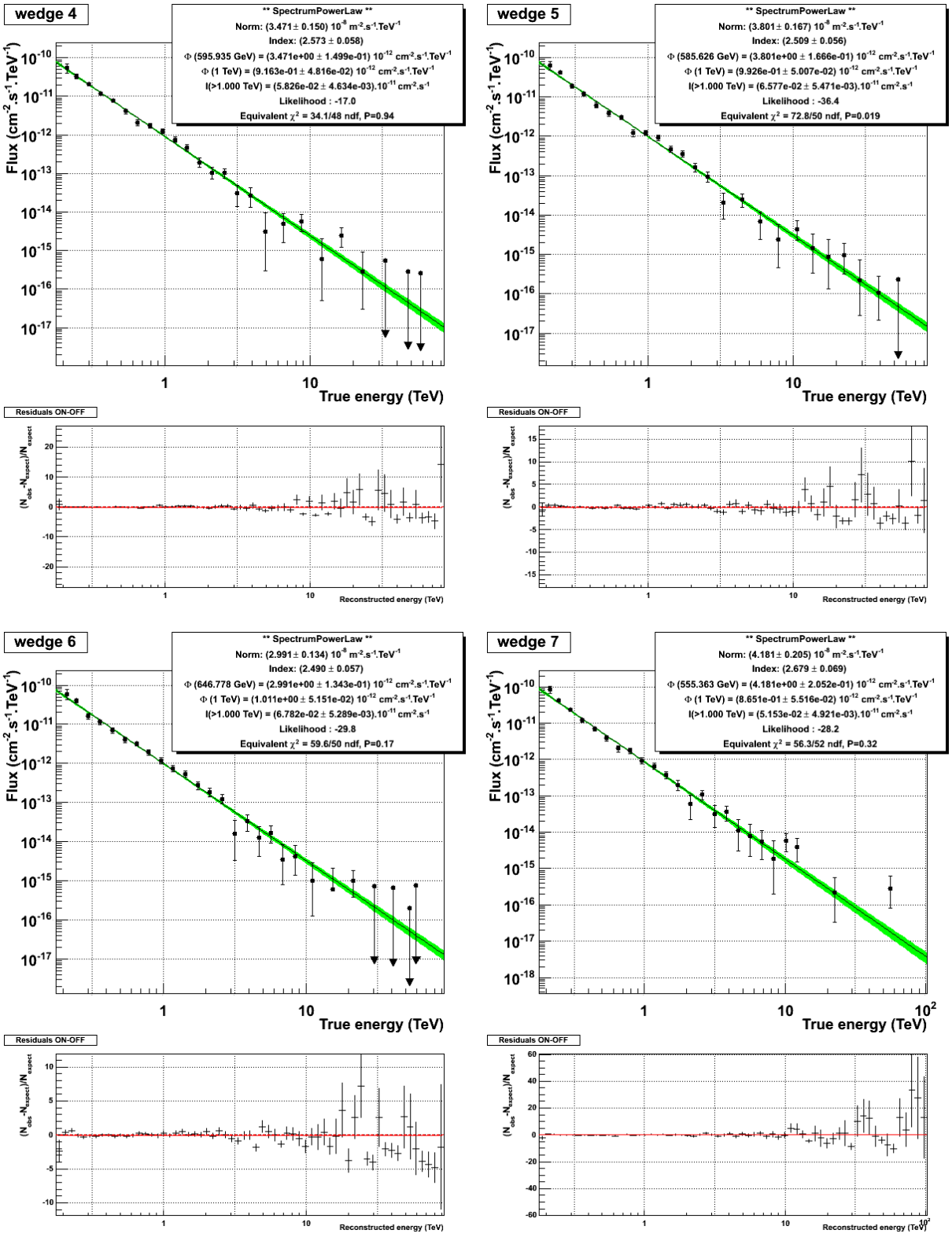

Figure B.2.: New H.E.S.S. spectra and fit results of the four central wedge regions.

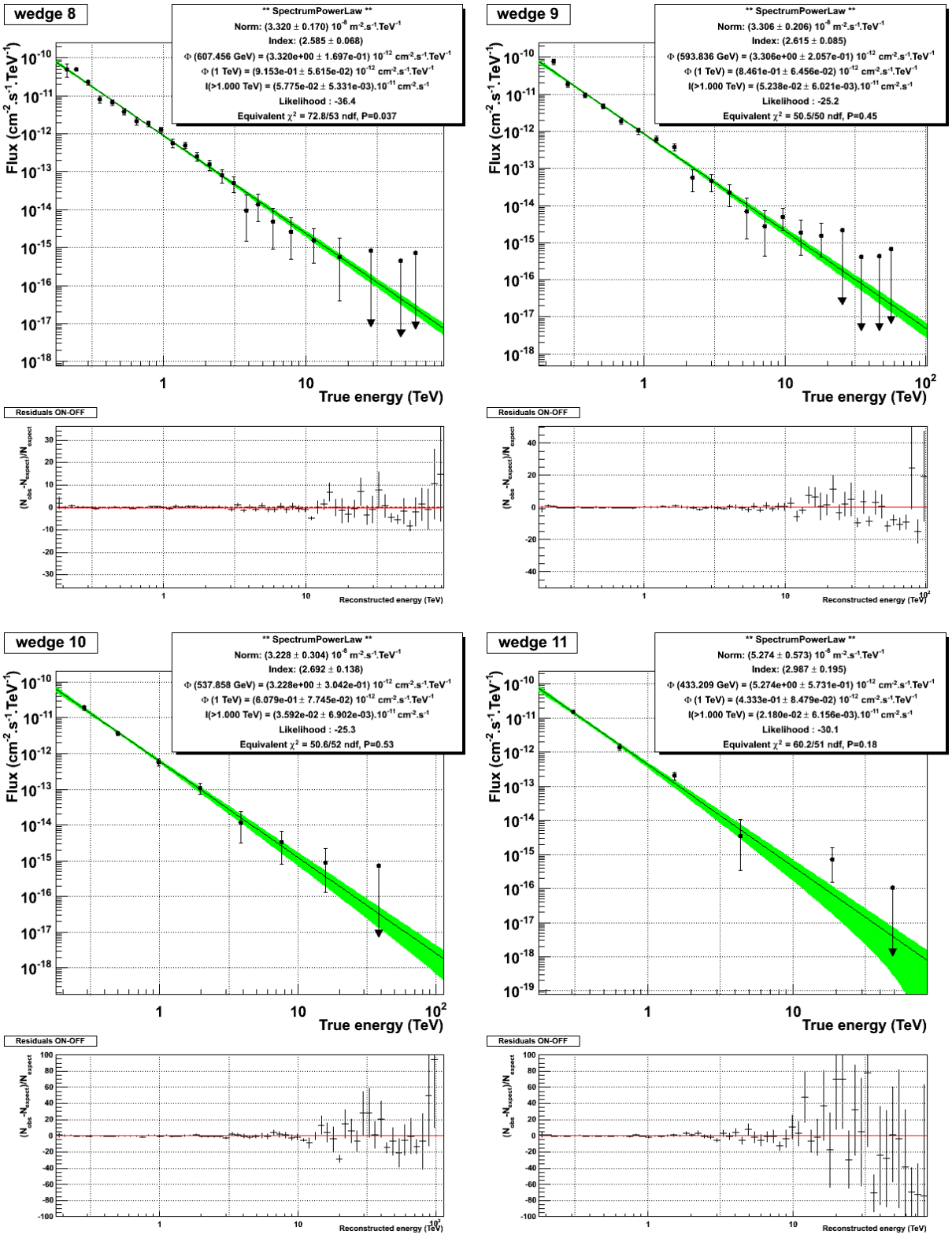

Figure B.3.: New H.E.S.S. spectra and fit results of the four outermost wedge regions.

B.2. X^2 Distributions in the Vicinities of the Simplex Minimisation Minima

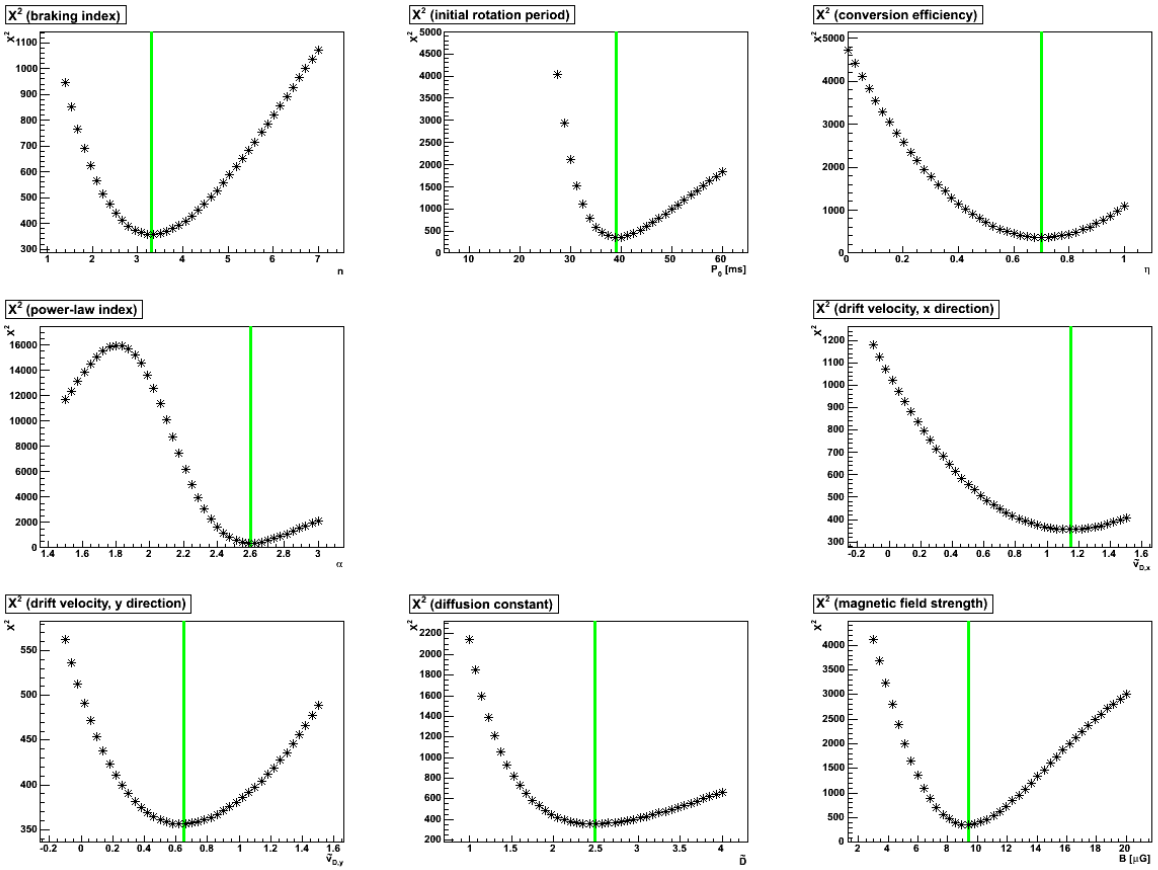

Figure B.4.: X^2 distribution in the vicinity of minimum 3.2.

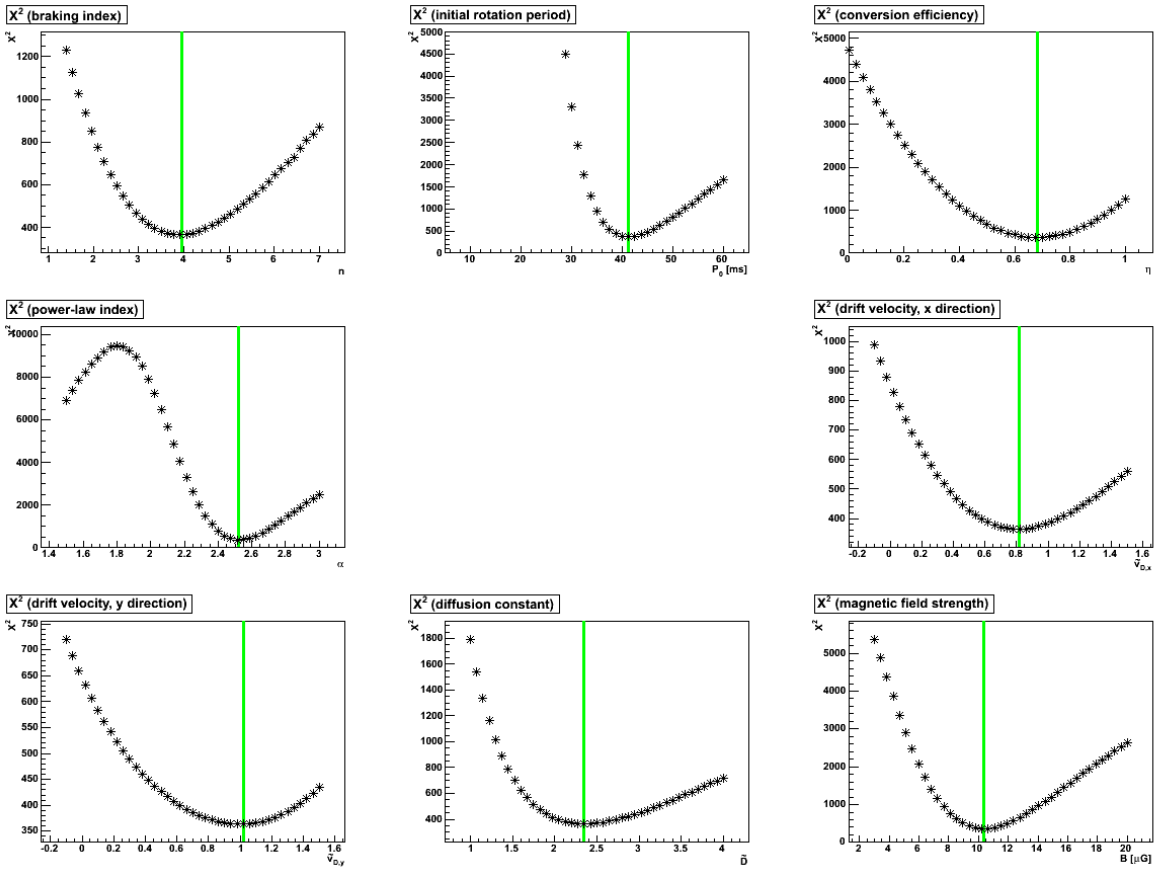

Figure B.5.: X^2 distribution in the vicinity of minimum 3.3.

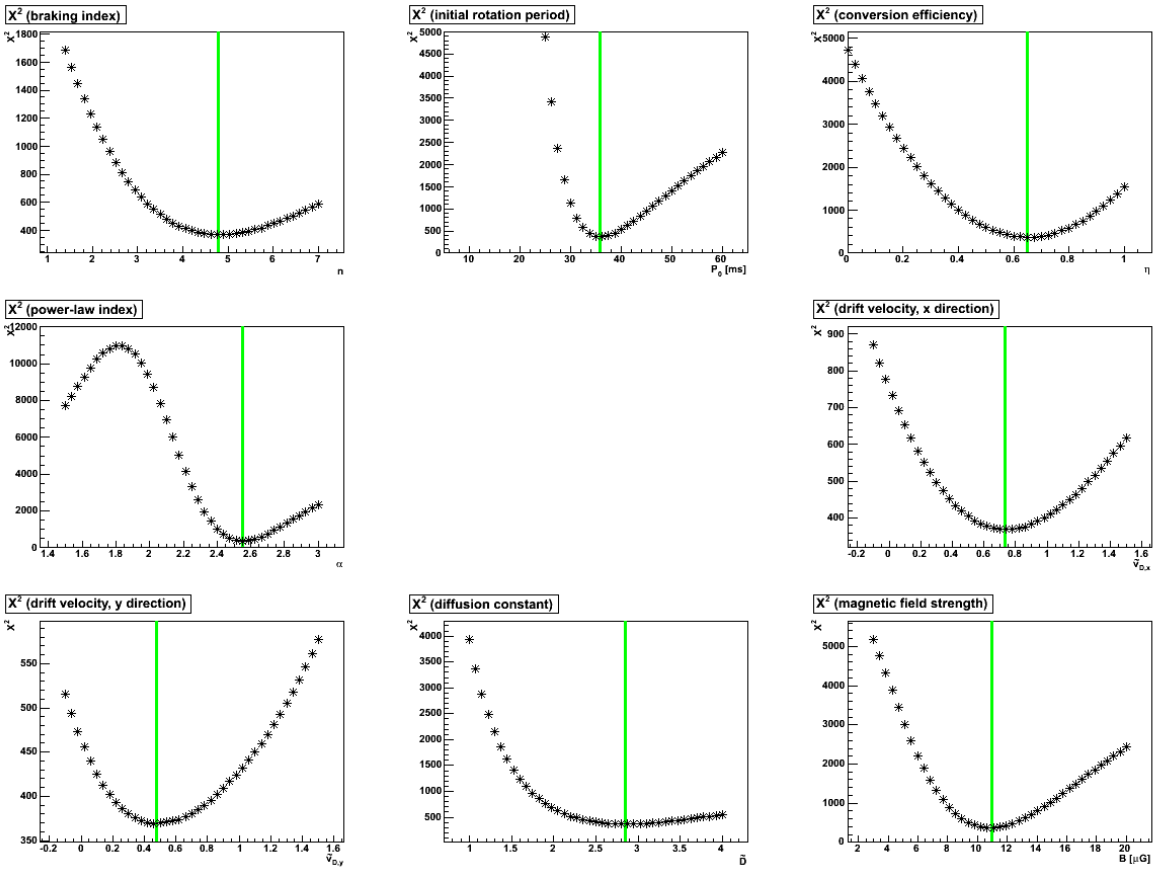

Figure B.6.: X^2 distribution in the vicinity of minimum 3.4.

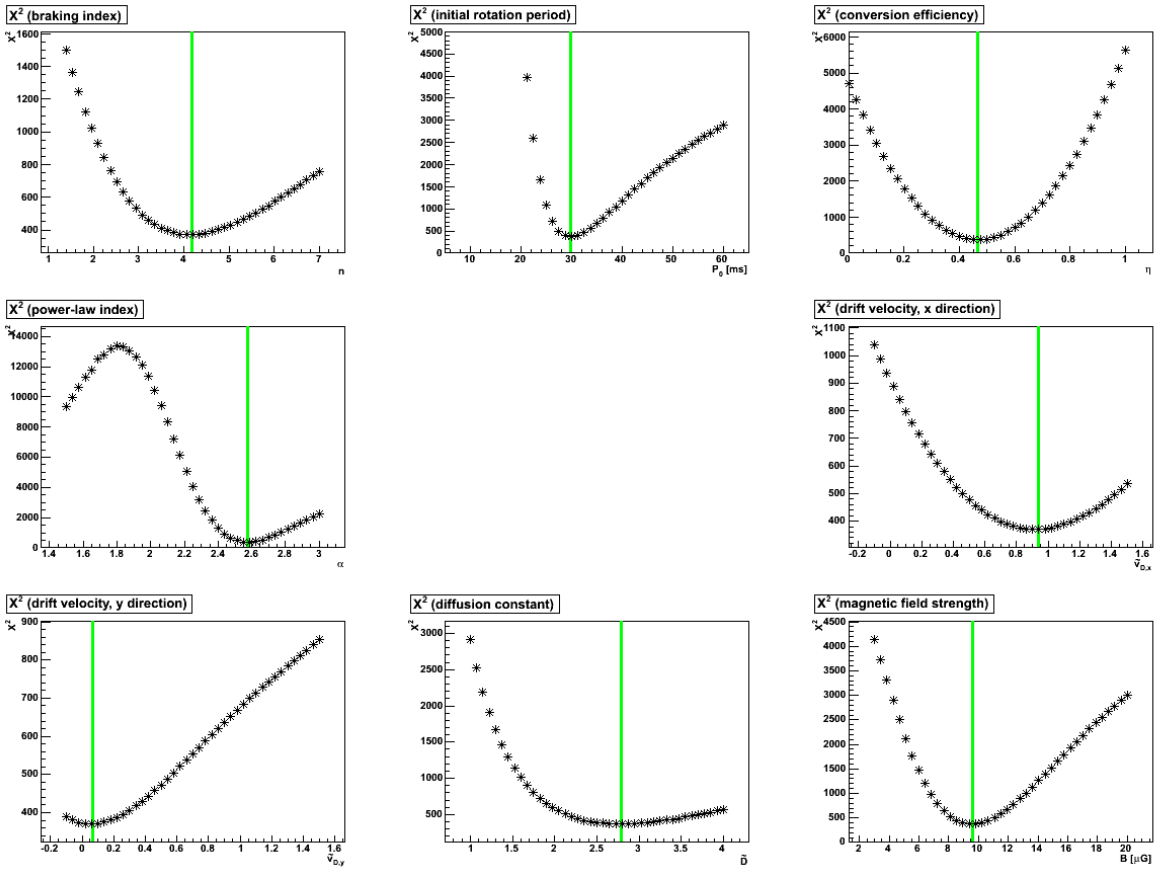

Figure B.7.: X^2 distribution in the vicinity of minimum 3.5.

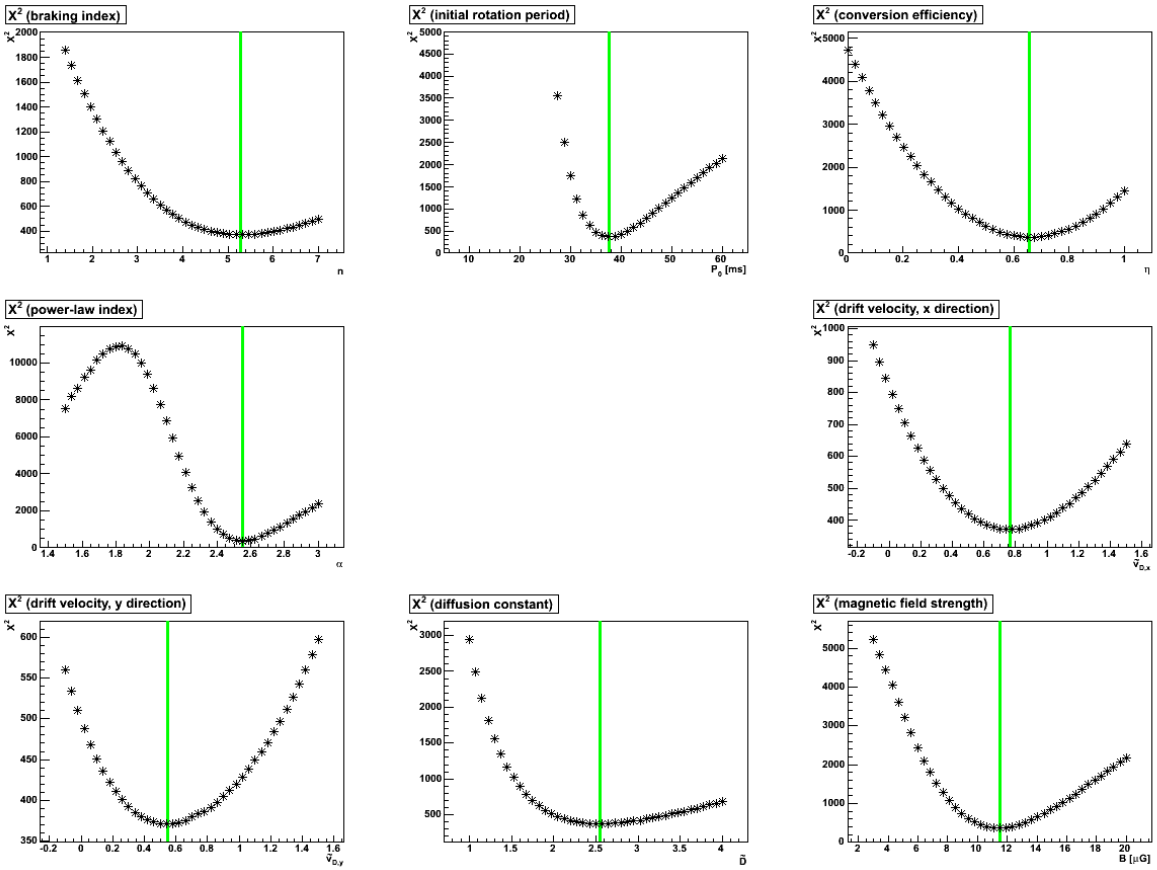

Figure B.8.: X^2 distribution in the vicinity of minimum 3.6.

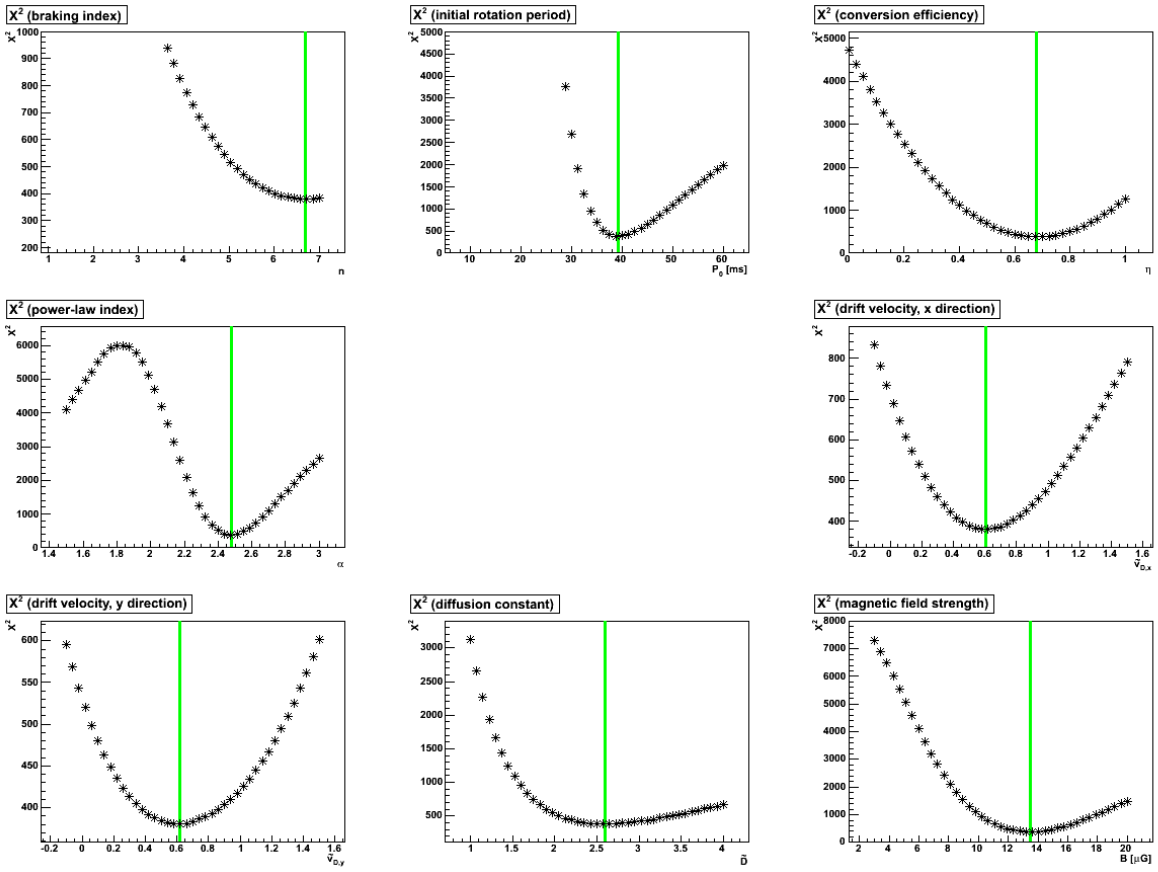

Figure B.9.: X^2 distribution in the vicinity of minimum 3.7.

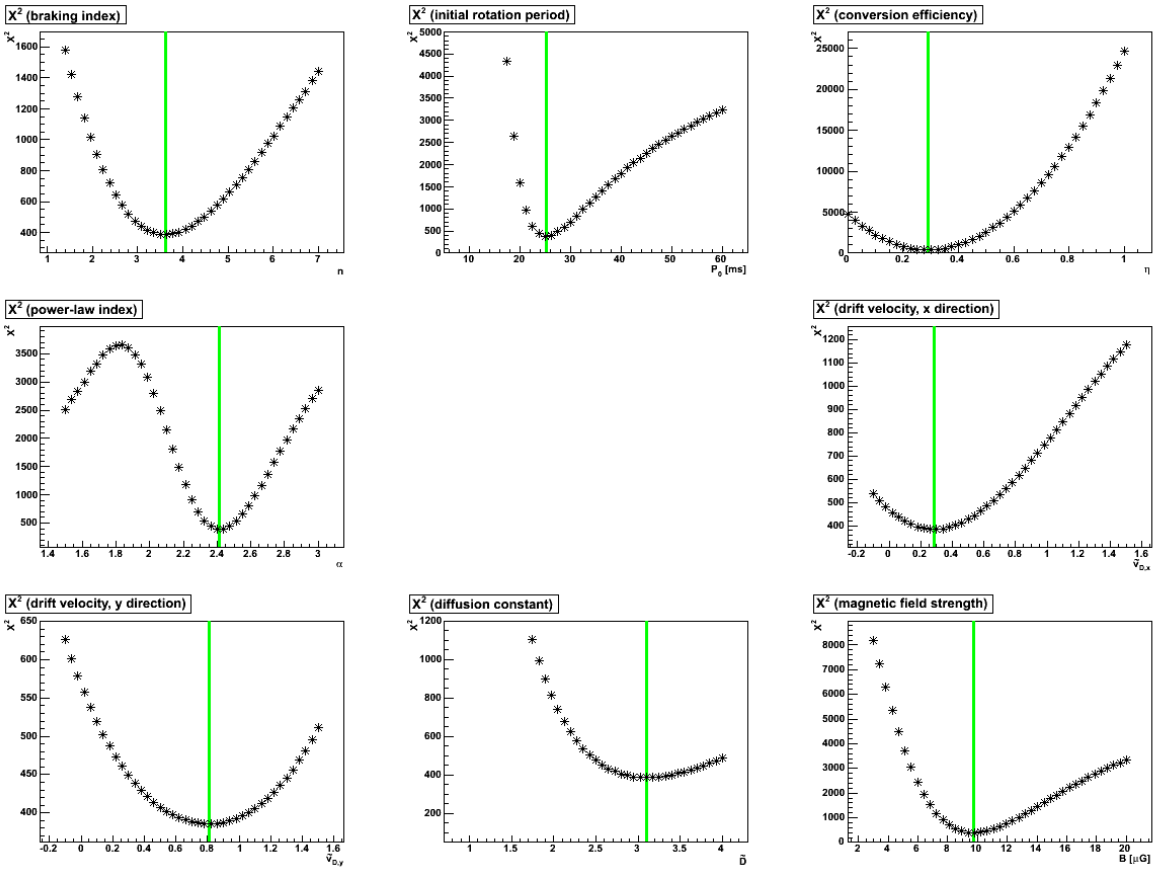

Figure B.10.: X^2 distribution in the vicinity of minimum 3.8.

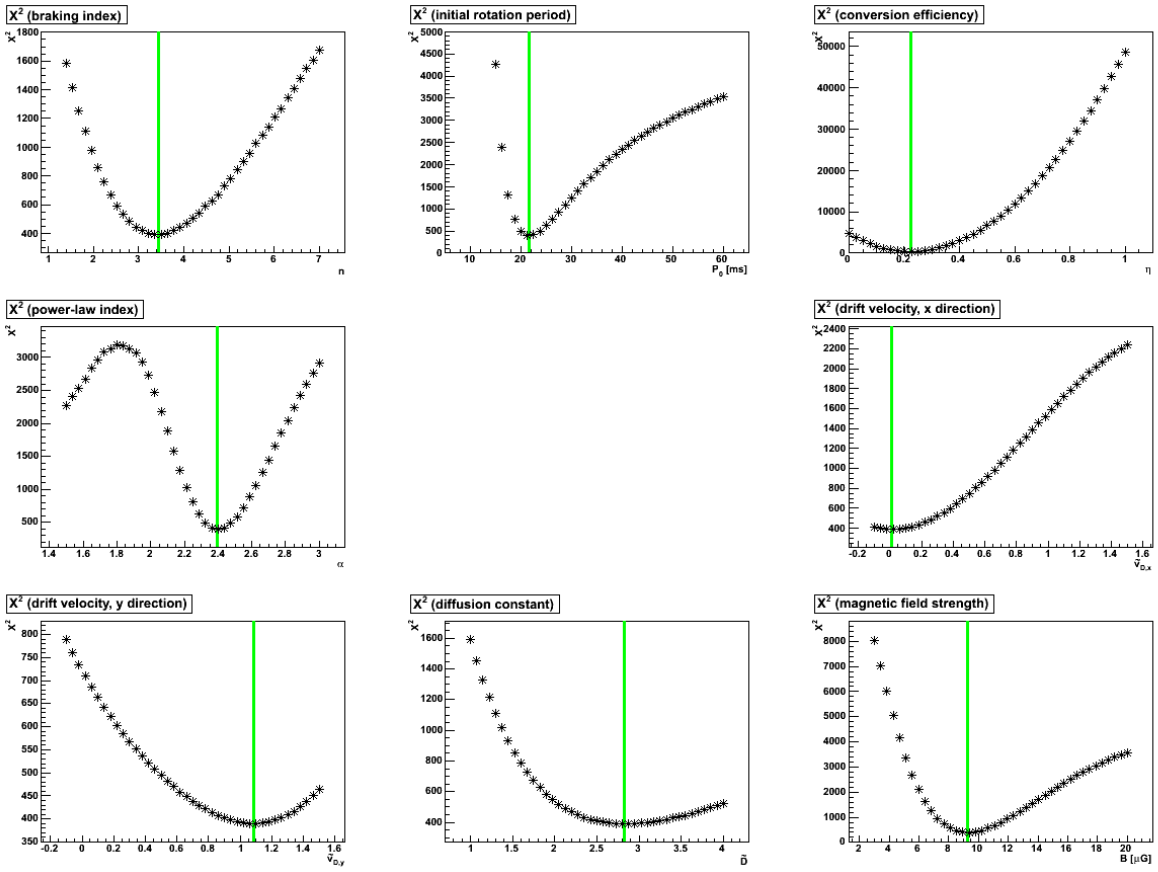

Figure B.11.: X^2 distribution in the vicinity of minimum 3.9.

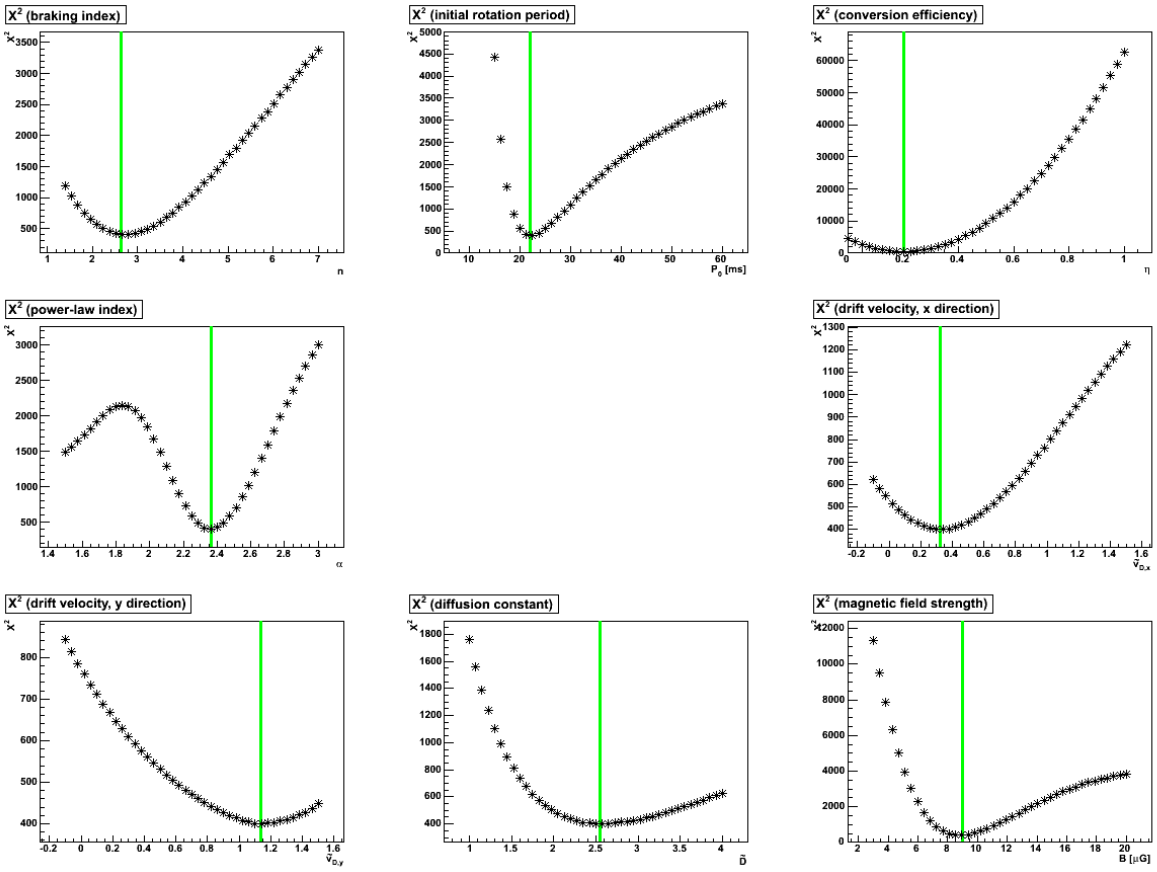

Figure B.12.: X^2 distribution in the vicinity of minimum 3.10.

B.3. $-LL_{\mathrm{sp}}$ Distributions in the Vicinities of the Simplex Minimisation Minima

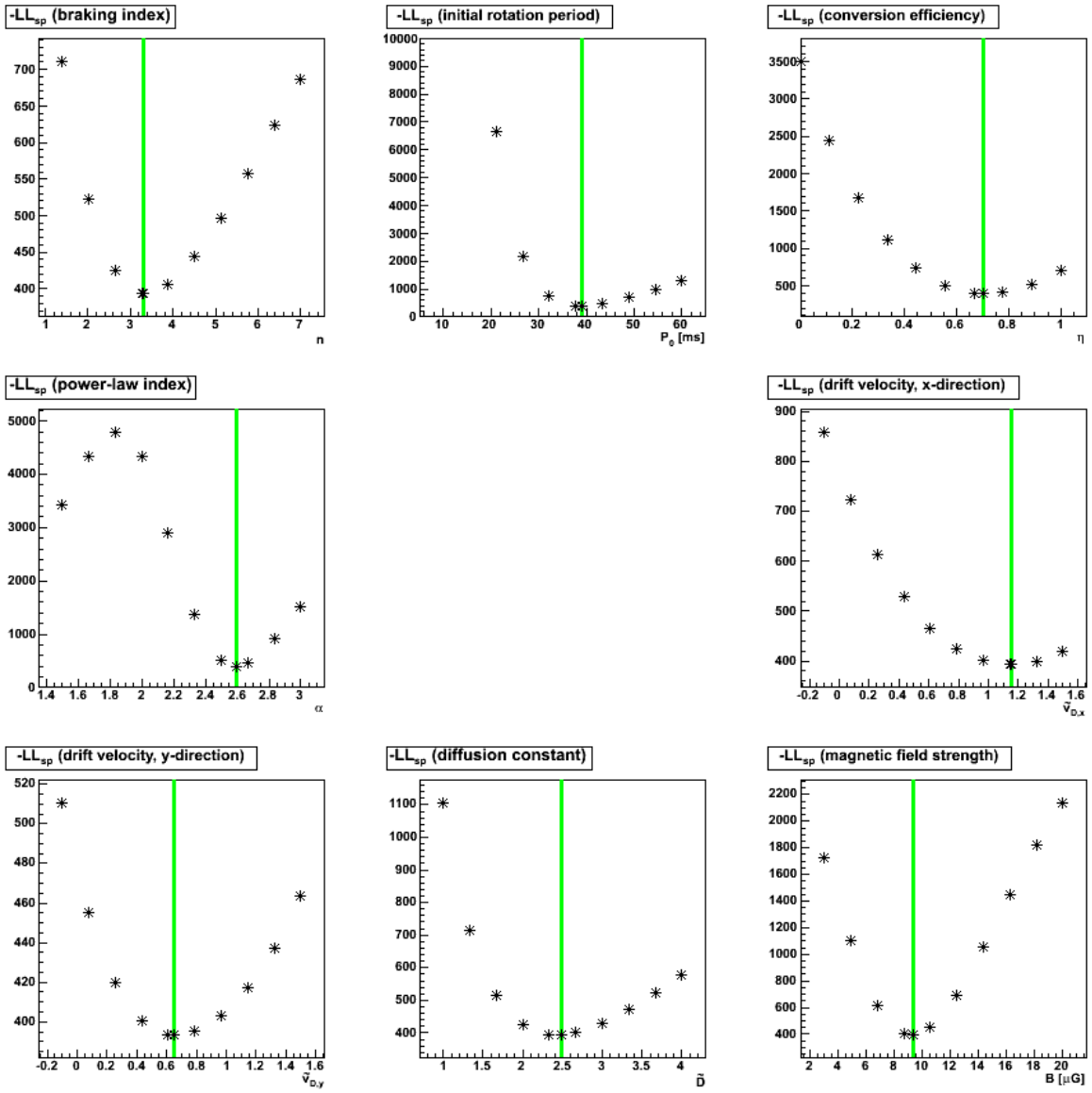

Figure B.13.: $-LL_{\mathrm{sp}}$ distribution in the vicinity of minimum 3.2.

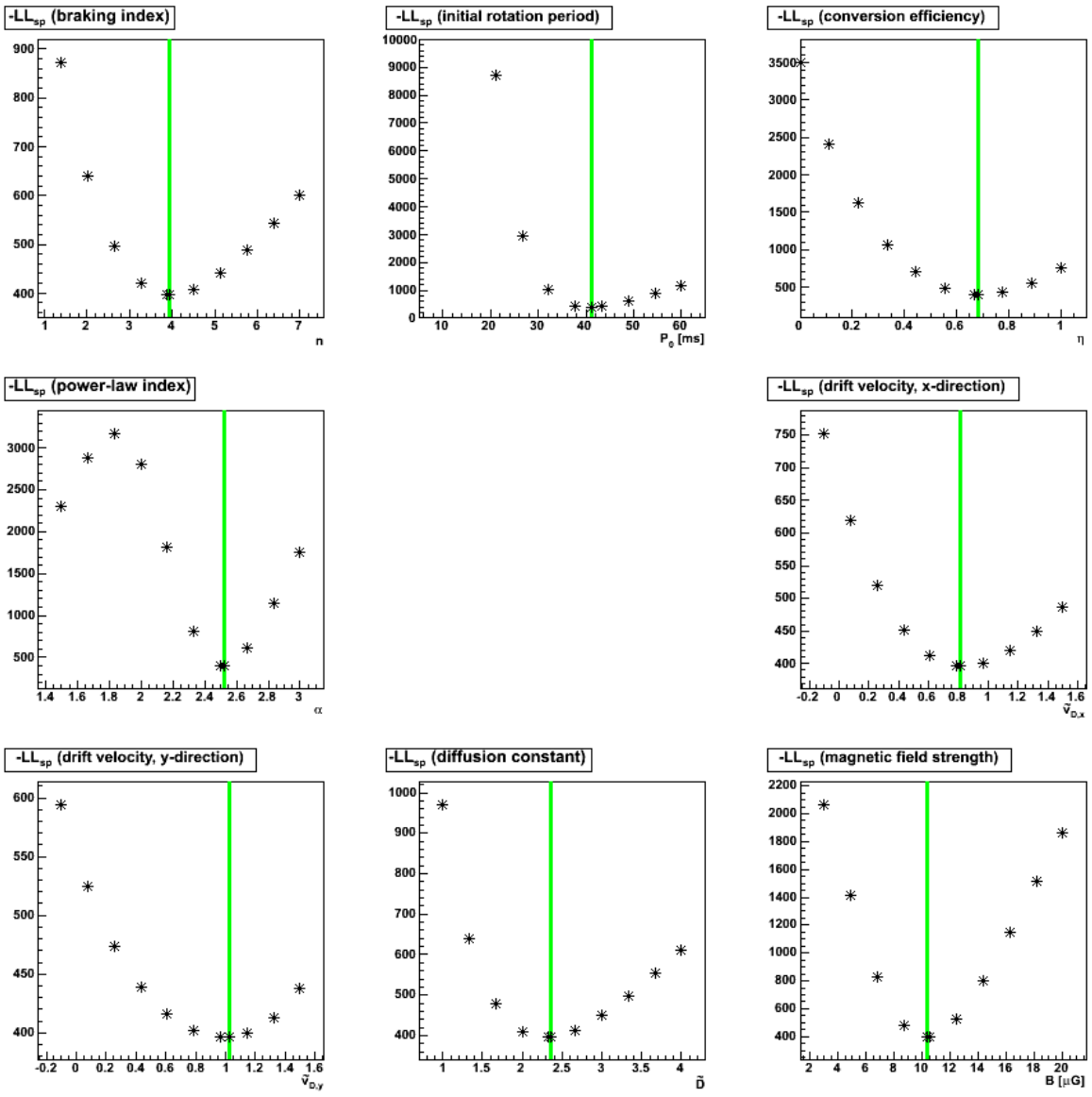

Figure B.14.: $-LL_{\mathrm{sp}}$ distribution in the vicinity of minimum 3.3.

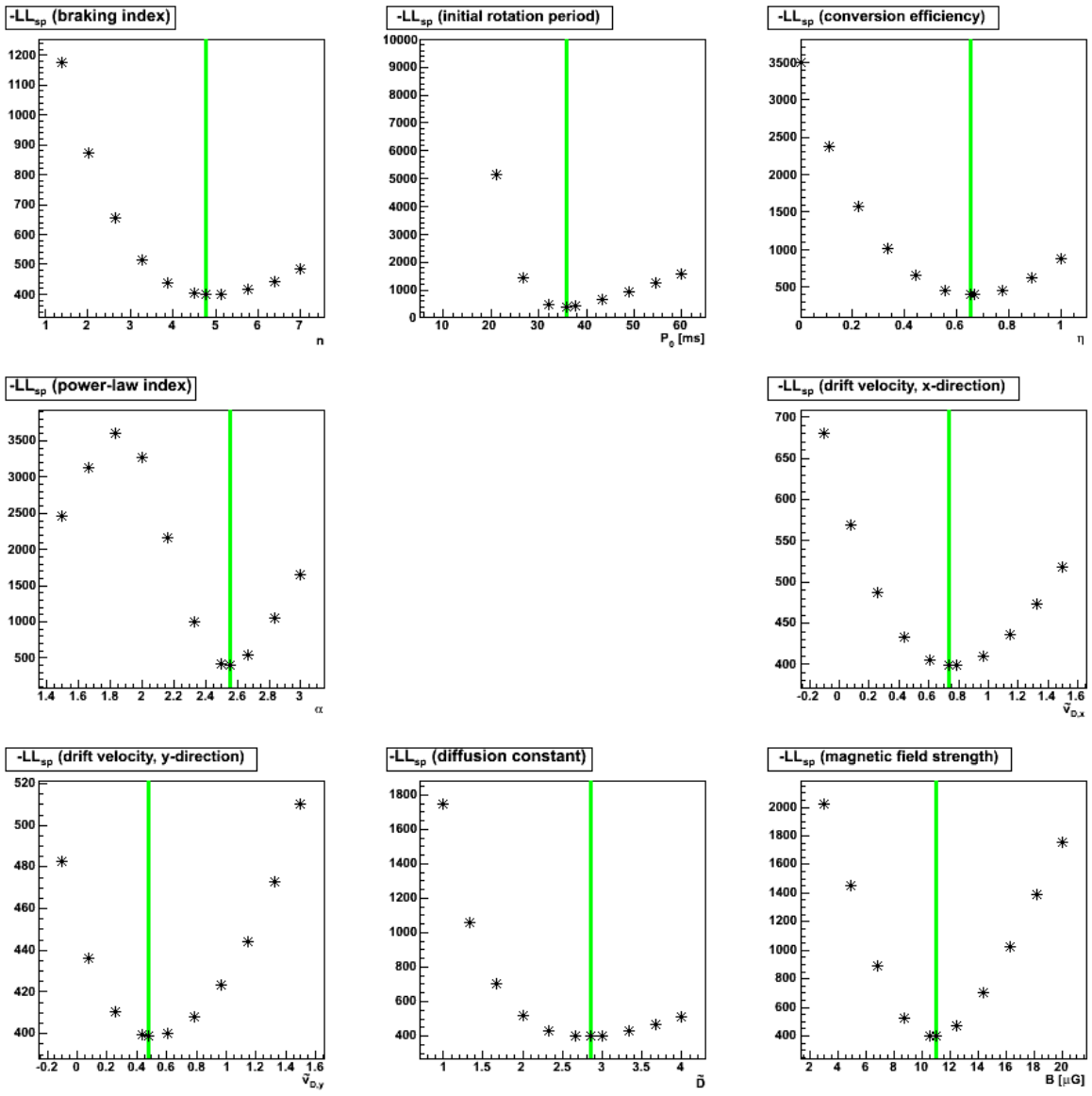

Figure B.15.: $-LL_{\mathrm{sp}}$ distribution in the vicinity of minimum 3.4.

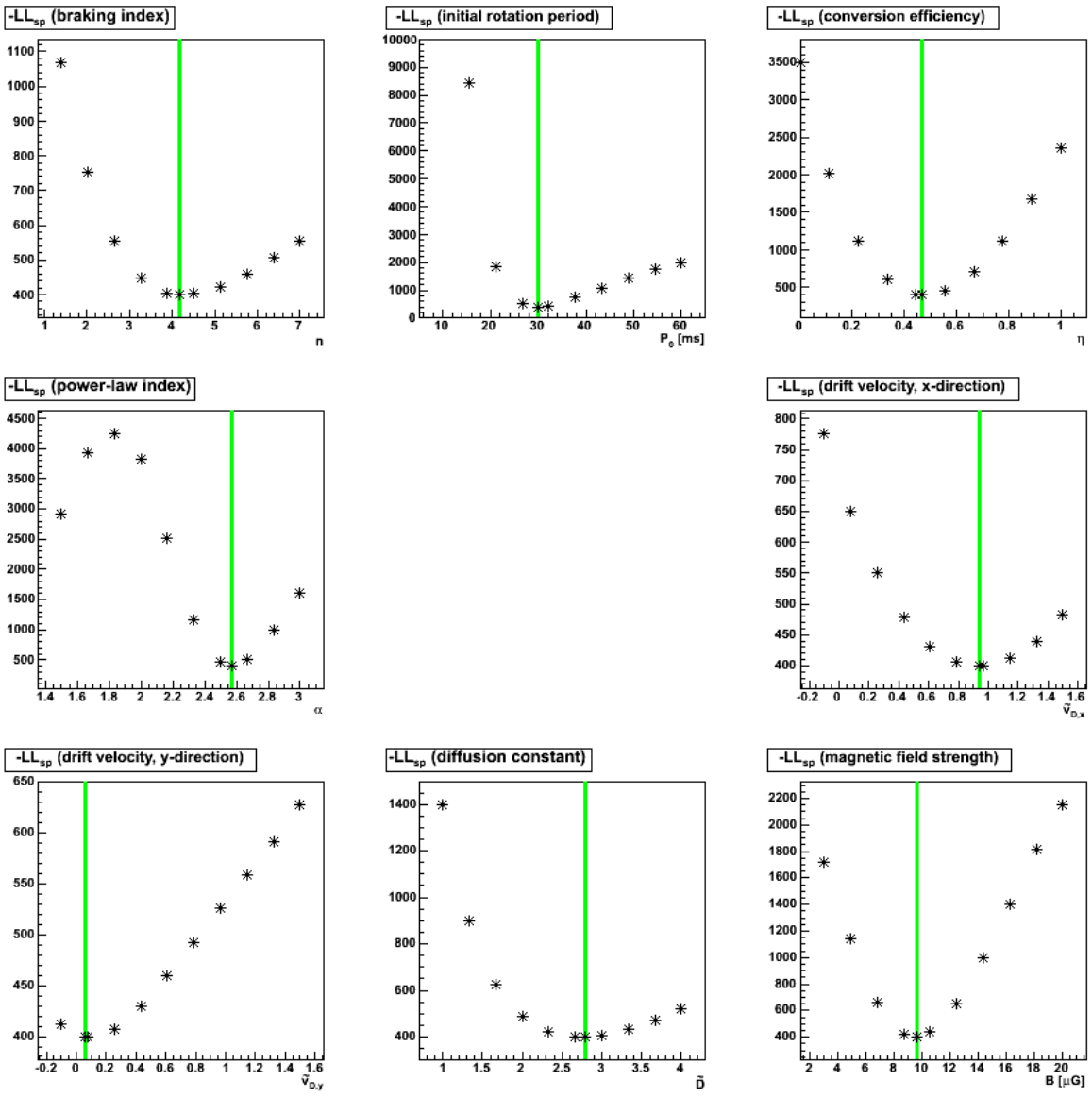

Figure B.16.: $-LL_{\rm sp}$ distribution in the vicinity of minimum 3.5.

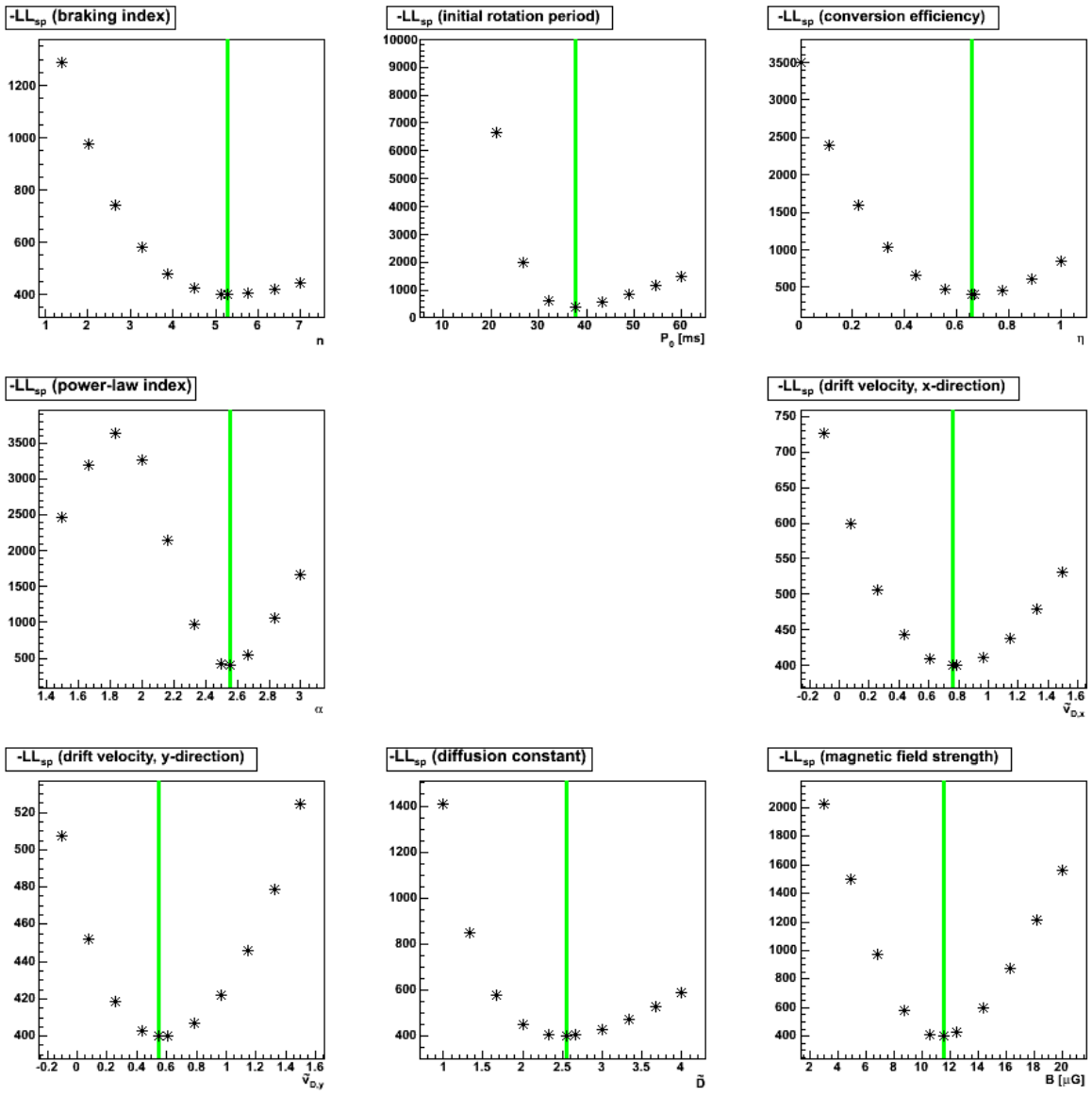

Figure B.17.: $-LL_{\mathrm{sp}}$ distribution in the vicinity of minimum 3.6.

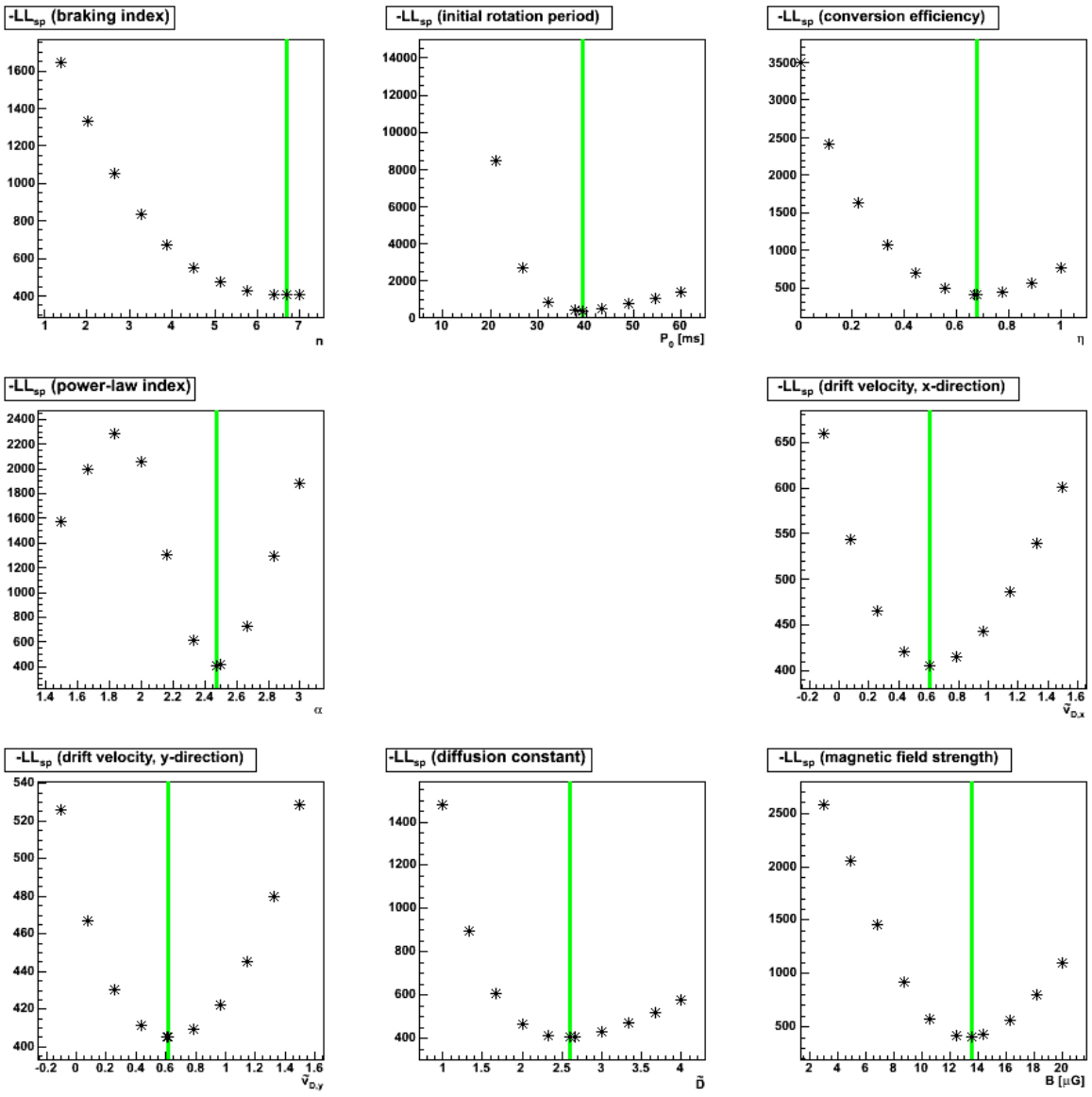

Figure B.18.: $-LL_{\rm sp}$ distribution in the vicinity of minimum 3.7.

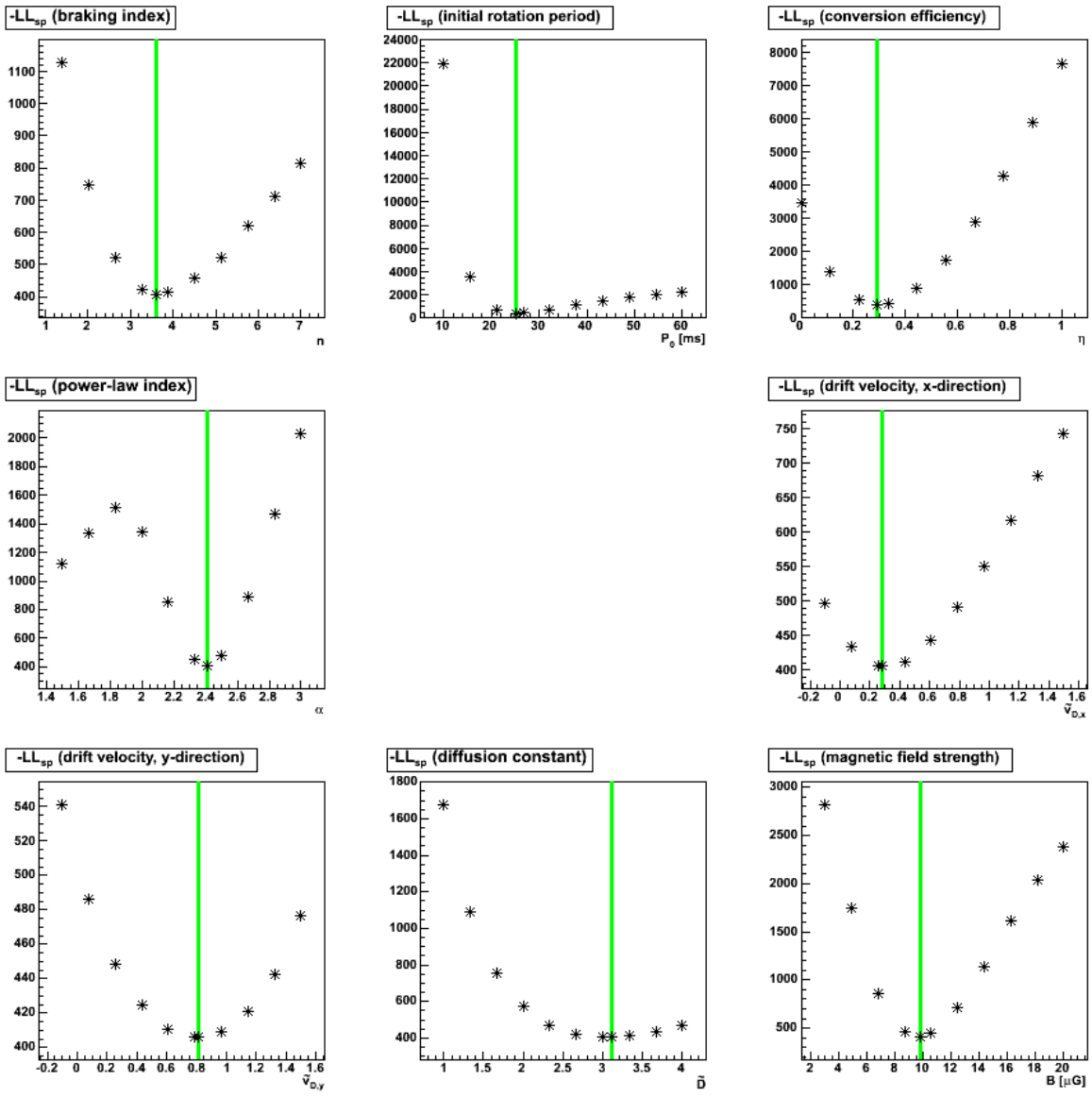

Figure B.19.: $-LL_{\mathrm{sp}}$ distribution in the vicinity of minimum 3.8.

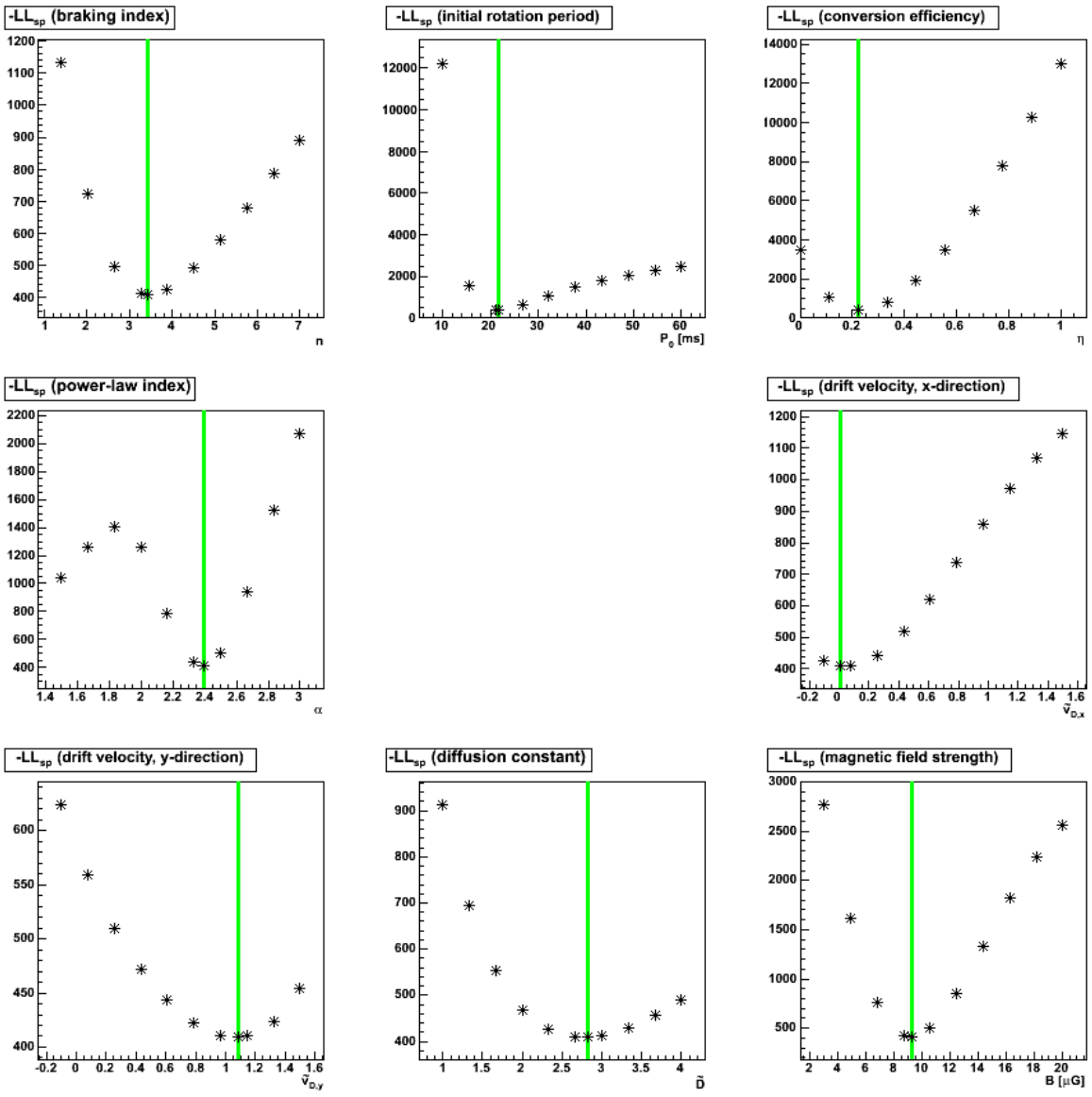

Figure B.20.: $-LL_{\mathrm{sp}}$ distribution in the vicinity of minimum 3.9.

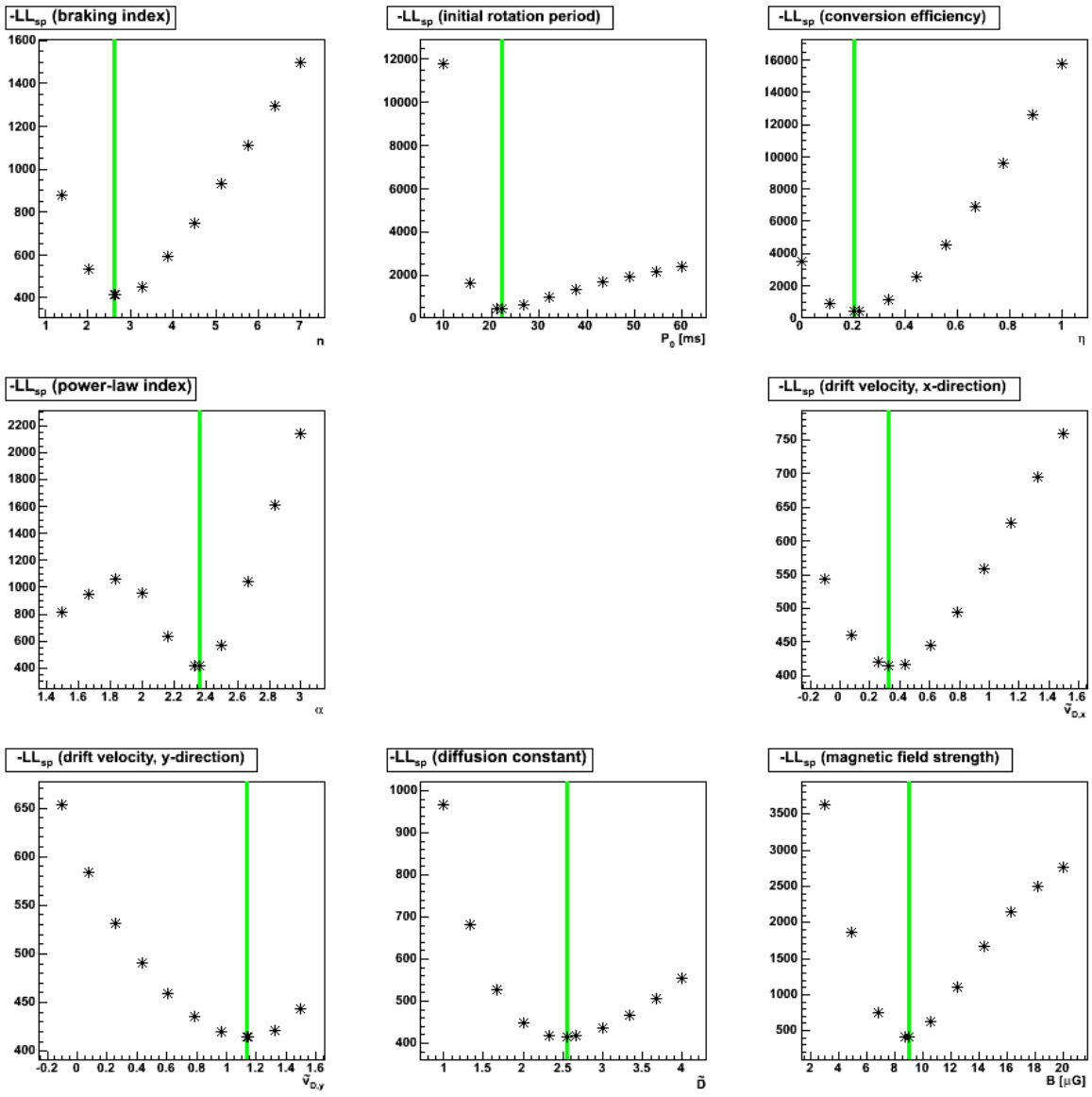

Figure B.21.: $-LL_{\mathrm{sp}}$ distribution in the vicinity of minimum 3.10.

B.4. $-LL_{\mathrm{sk}}$ Distribution in the Vicinity of the Simplex Minimisation Minima

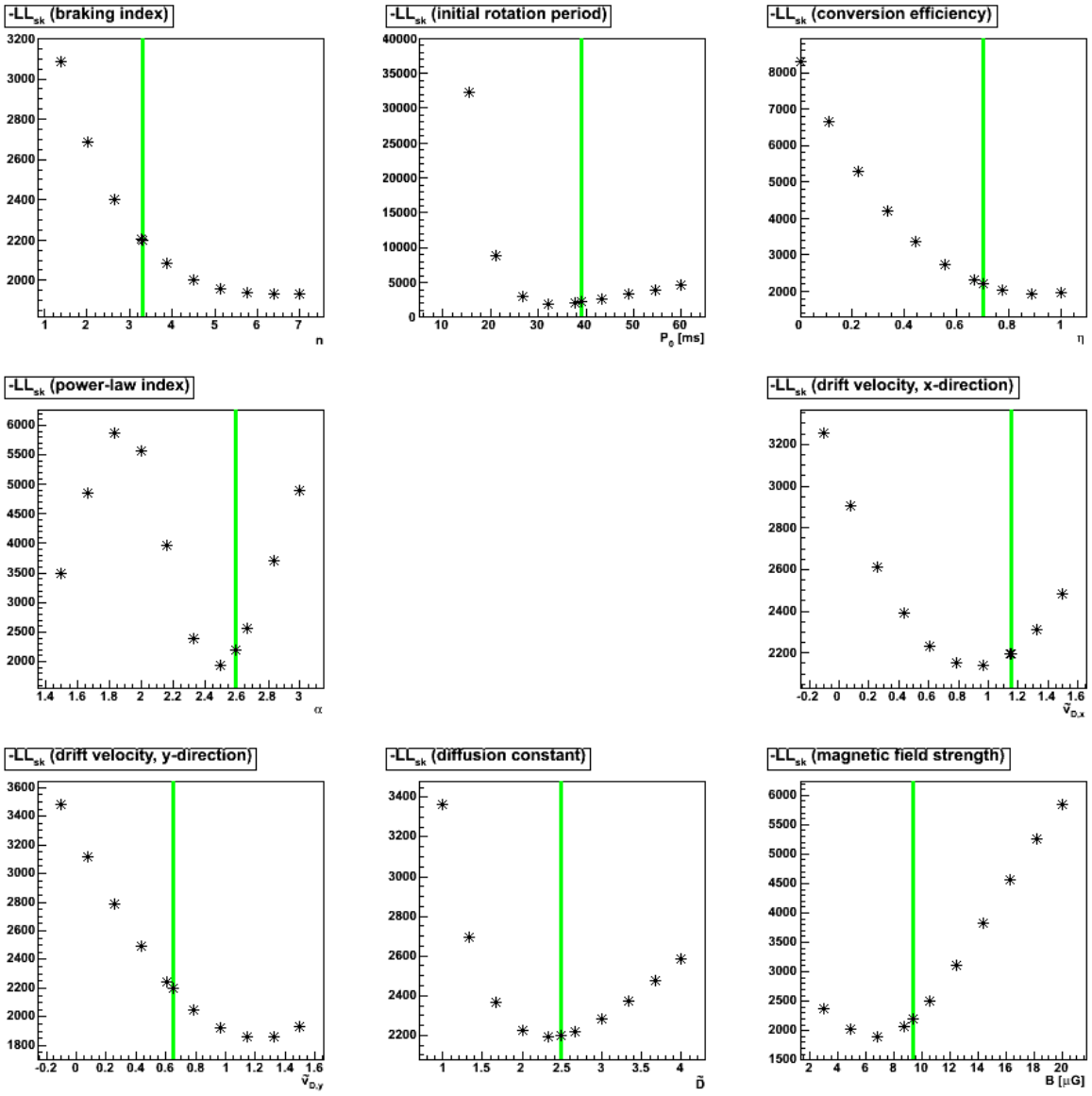

Figure B.22.: $-LL_{\mathrm{sk}}$ distribution in the vicinity of minimum 3.2.

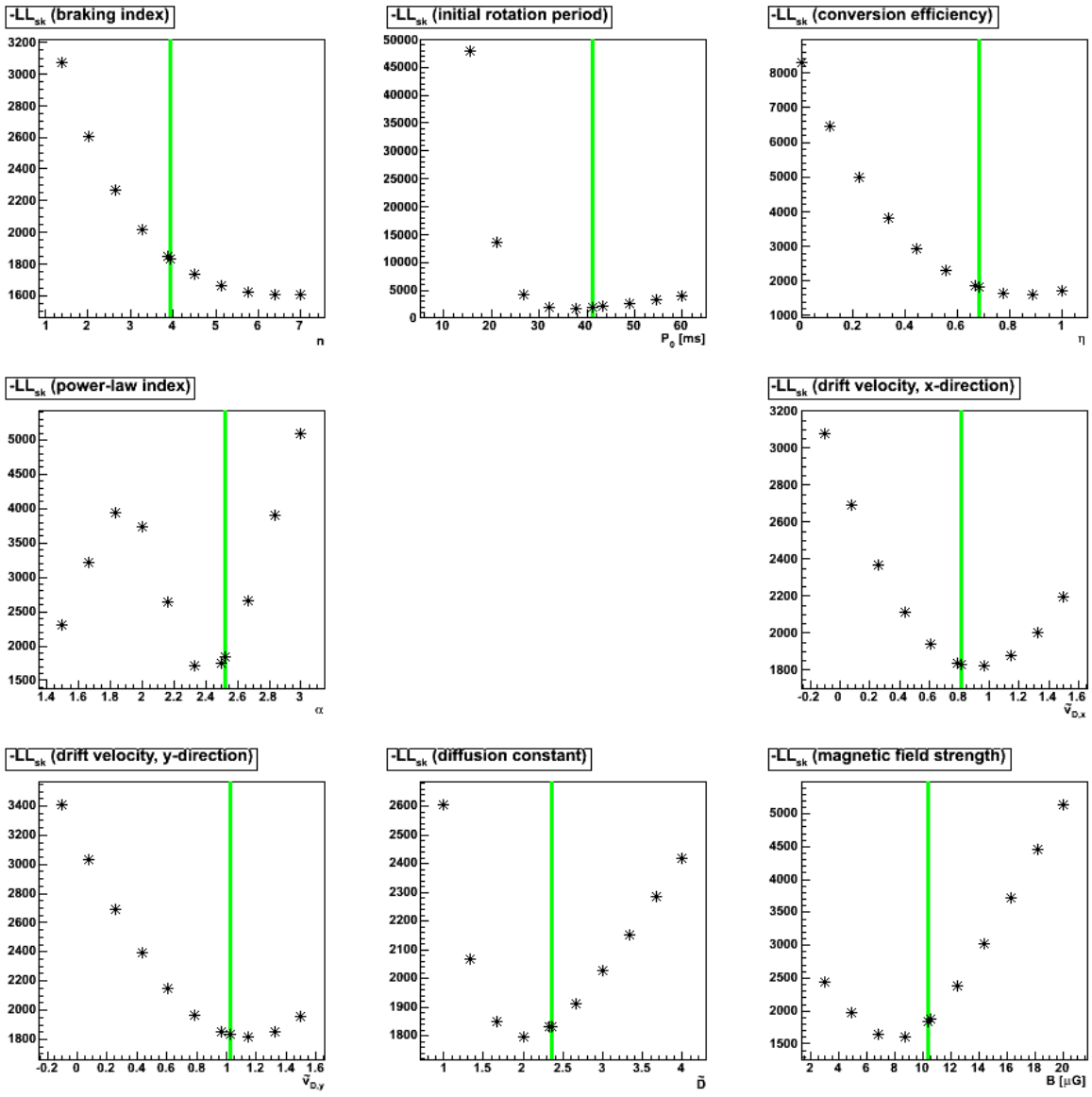

Figure B.23.: $-LL_{\mathrm{sk}}$ distribution in the vicinity of minimum 3.3.

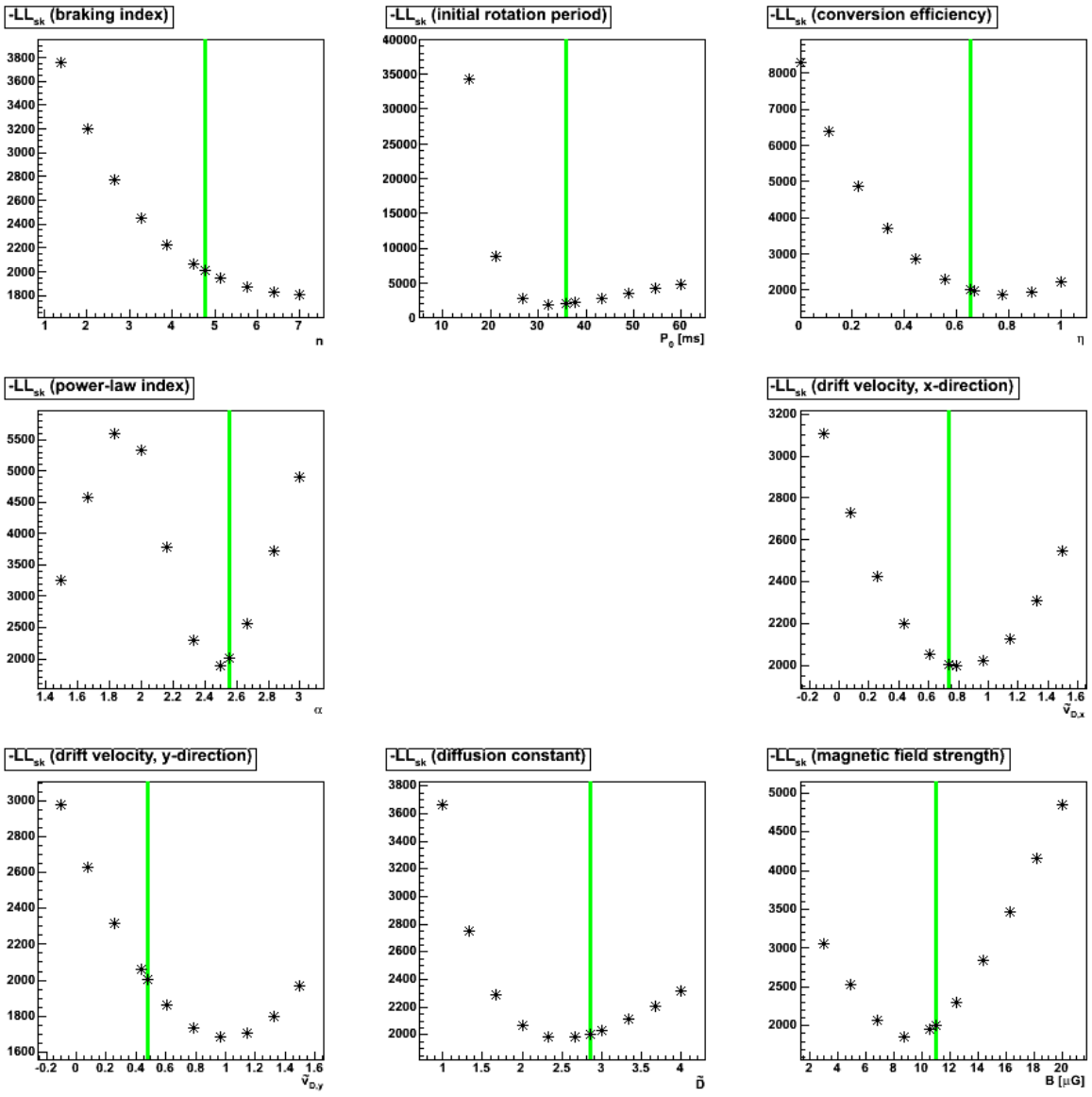

Figure B.24.: $-LL_{\rm sk}$ distribution in the vicinity of minimum 3.4.

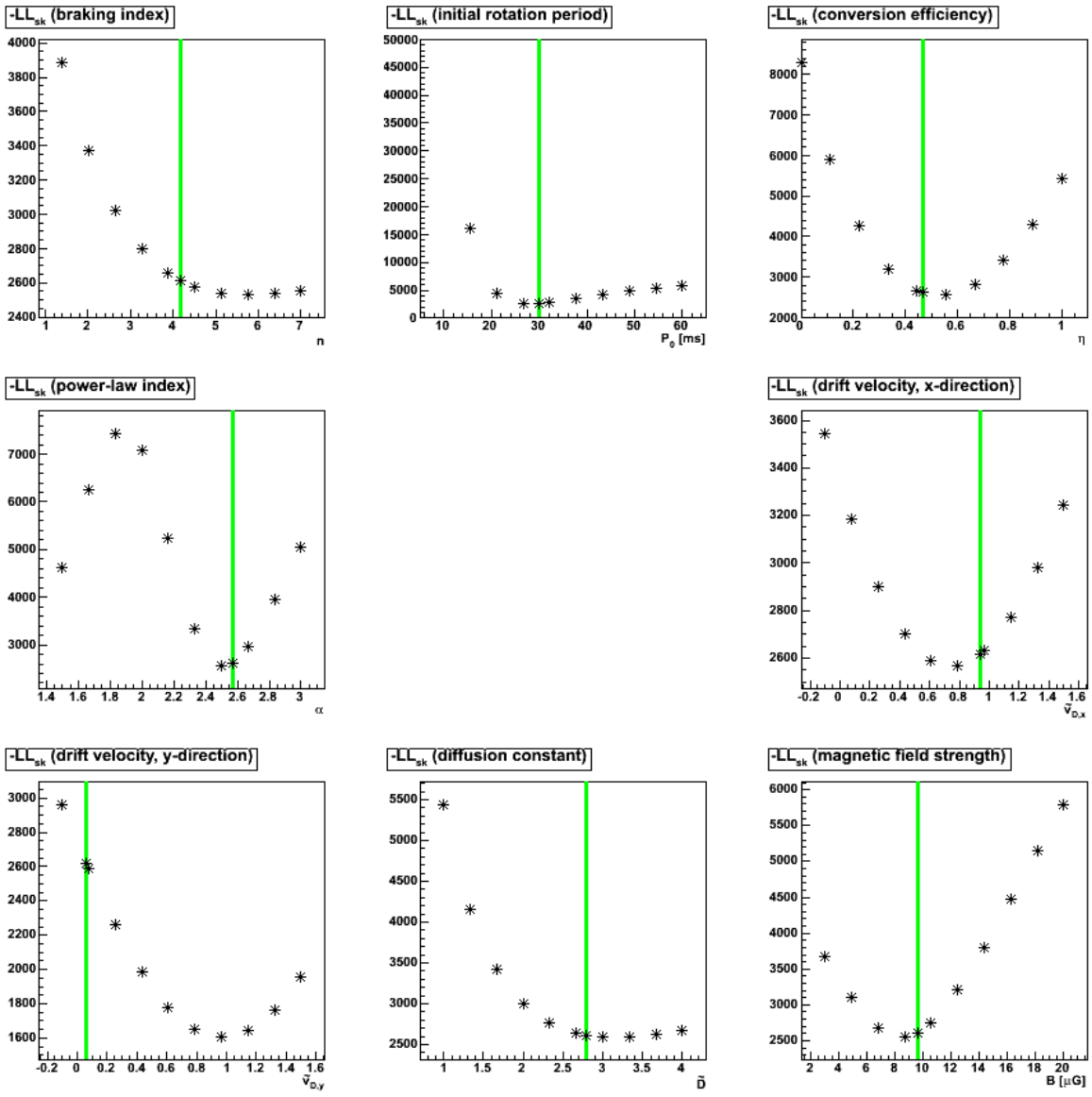

Figure B.25.: $-LL_{\mathrm{sk}}$ distribution in the vicinity of minimum 3.5.

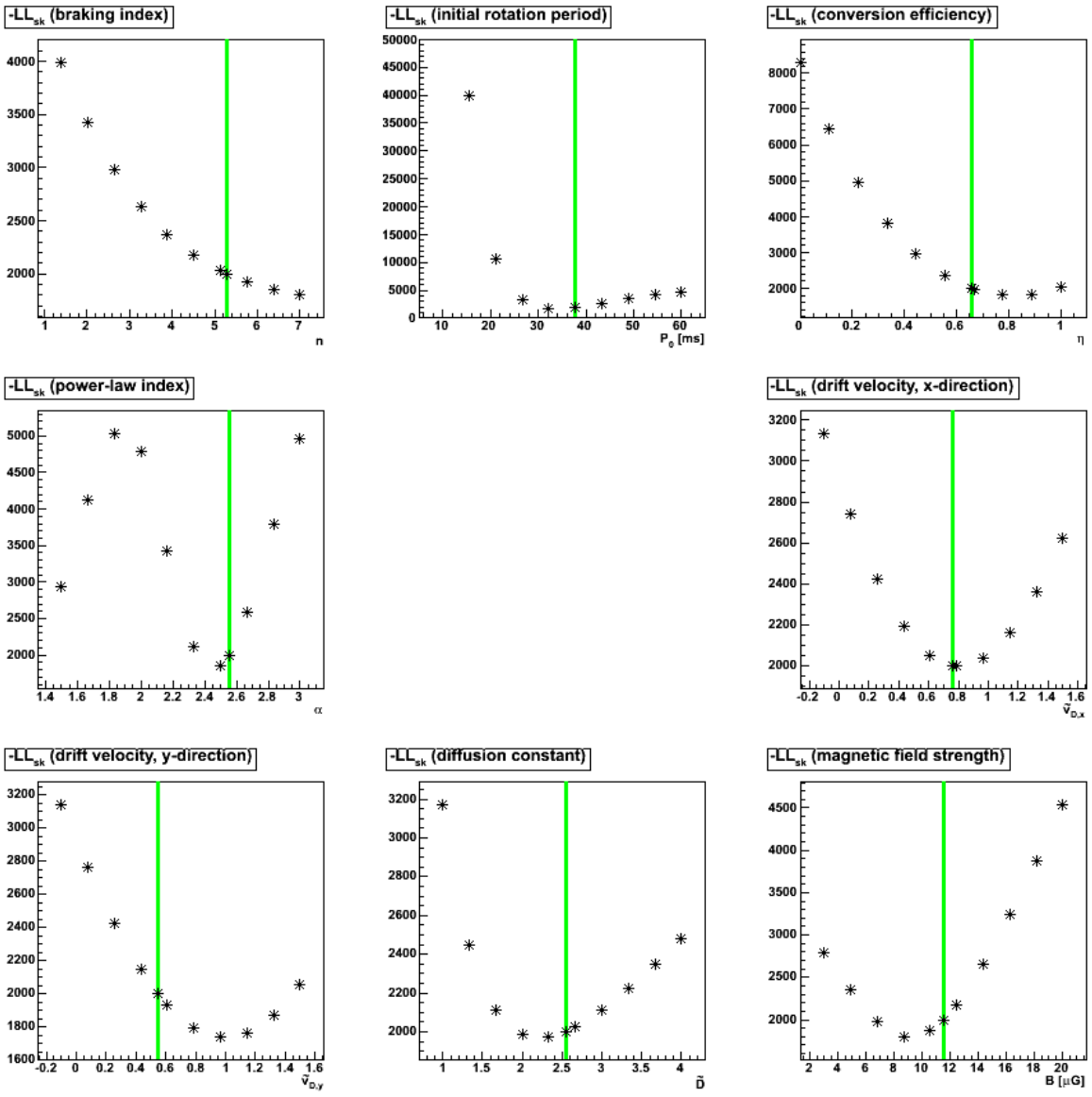

Figure B.26.: $-LL_{\mathrm{sk}}$ distribution in the vicinity of minimum 3.6.

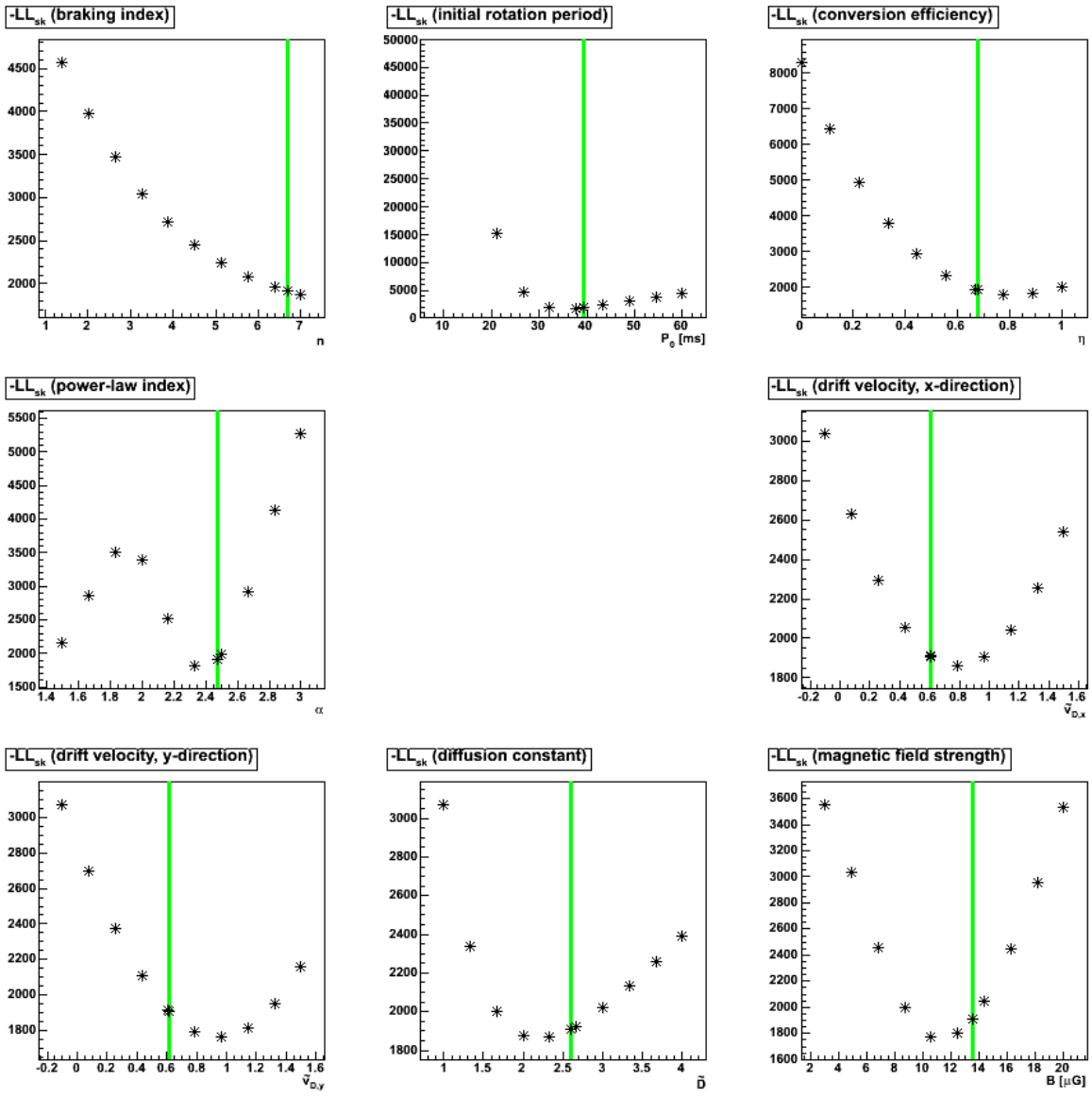

Figure B.27.: $-LL_{\mathrm{sk}}$ distribution in the vicinity of minimum 3.7.

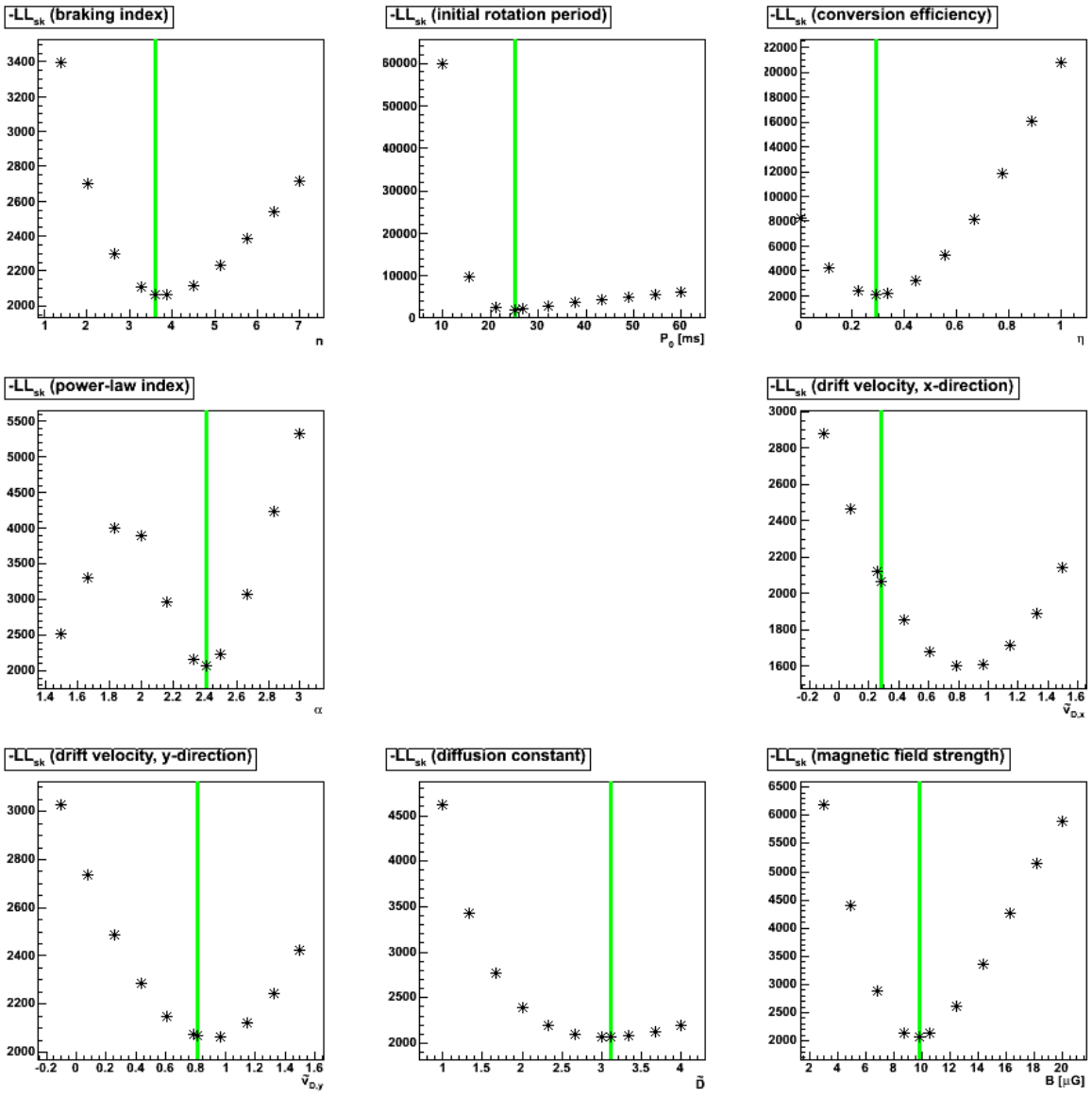

Figure B.28.: $-LL_{\rm sk}$ distribution in the vicinity of minimum 3.8.

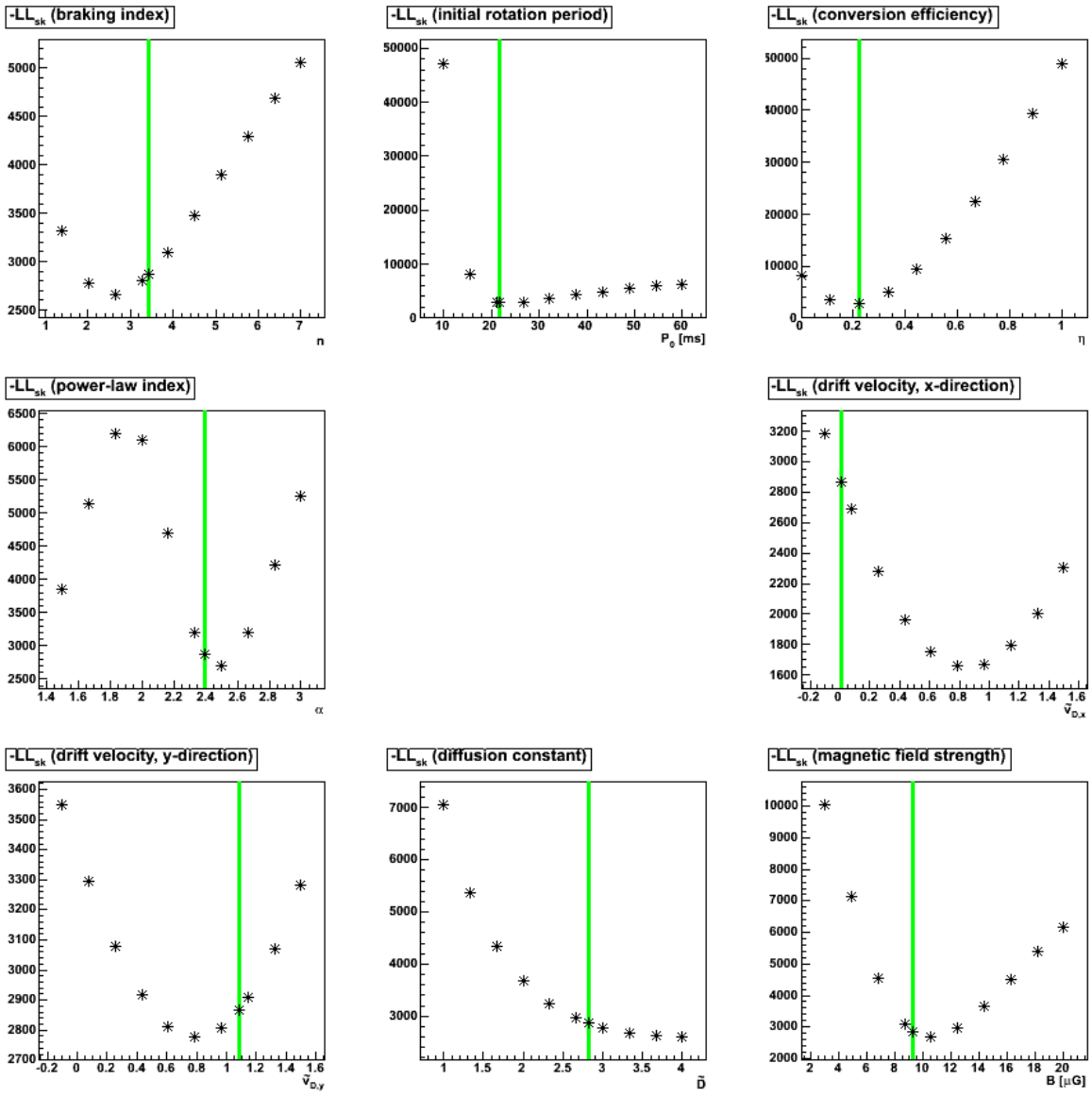

Figure B.29.: $-LL_{\mathrm{sk}}$ distribution in the vicinity of minimum 3.9.

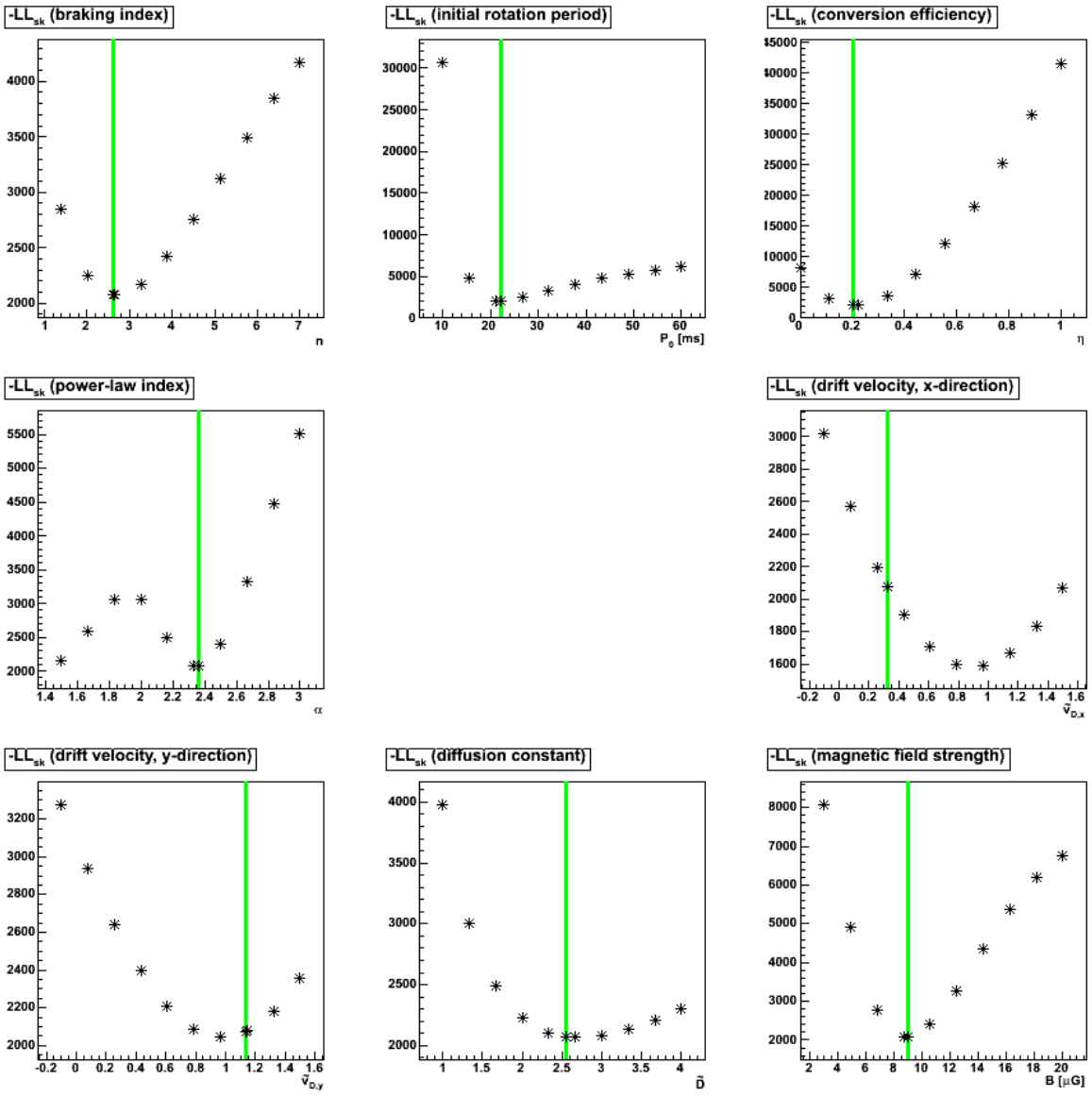

Figure B.30.: $-LL_{\mathrm{sk}}$ distribution in the vicinity of minimum 3.10.

Glossary

Jodrell Bank observatory Radio telescopes at the University of Manchester. The most prominent telescope is the Lovell Telescope, which has a steerable dish with a diameter of 76 m and which is designed to observe at wavelengths smaller than 5 GHz. The Lovell Telescope has been put into operation in 1955. See `http://www.jb.man.ac.uk`.

Nanshan radio telescope 25-meter radio telescope in Urumqi, China, takes part in very long baseline interferometry (VLBI) observations. In operation since 2002.

Very Large Array (VLA) Radio interferometry observatory in New Mexico, USA. The observatory consists of 27 radio telescopes, each of which has a dish with a diameter of 25 m. The telescopes can be moved along the 21 km long arms of a Y-shape so that the observatory can be used in different configurations. All in all, a frequency range from 74 MHz to 50 GHz is covered and an angular resolution up to 0.05″ is reached. The observatory has been in operation since 1980 and has recently undergone major upgrades. It is also part of the Very Long Baseline Array. See `http://www.vla.nrao.edu`.

ROentgen SATellite (ROSAT) X-ray satellite which had been in operation between 1990 and 1999. The X-ray telescope was designed for the energy range between 0.1 and 2.0 keV and provided a FOV up to 2° and an angular resolution smaller than 5″. See `http://www.dlr.de/dlr/en/desktopdefault.aspx/tabid-10424`.

Advanced Satellite for Cosmology and Astrophysics (ASCA) Japanese X-ray satellite which had been in operation between 1993 and 2000. ASCA had four X-ray telescopes on-board which were operated either in conjunction with a gas imaging spectrometer (GIS) or a solid-state imaging spectrometer (SIS). In conjunction with the GIS the 0.8–12 keV energy range was covered, the FOV had a diameter of 50′ and the spatial resolution was in the order of 30″ for 5.9 keV. For the SIS detector the accessible energy range was 0.4–12 keV, the FOV had an extent of $22' \times 22'$ and the spatial resolution was in also the order of 30″. In comparison to ROSAT ASCA was better suited for spectral studies. See `http://heasarc.gsfc.nasa.gov/docs/asca/asca.html`.

X-Ray Multi-Mirror Mission - Newton (XMM-Newton) X-ray observatory of the European Space Agency (ESA), which was launched in 1999. Three X-ray telescopes are operated on-board of the satellite, each of which is equipped with a European Photon Imaging Camera (EPIC). Two of the cameras use Metal Oxide Semiconductor (MOS) CCD arrays, while the third one uses a PN CCD arrays. The cameras cover the energy range 0.2–12 keV and a FoV with a diameter of 30′. In

average a spectral resolution of $E/\Delta E \approx 20$–50 and an angular resolution of $6''$ (full width at half maximum, FWHM) is achieved. See `http://xmm.esac.esa.int`.

Energetic Gamma-Ray Experiment Telescope (EGRET) One of the experiments onboard the Compton Gamma Ray Observatory (CGRO), which had been in operation between 1991 and 1999. EGRET could detect γ rays in the 20 MeV–30 GeV energy range. The large field of view had a diameter of about 80°. The angular resolution depended strongly on the energy as well as on the location within the FoV: at 5 GeV and on-axis an angular resolution of approximately 0.5° was achieved. Moreover, on-axis the effective area was about $1000\,\mathrm{cm}^2$, while the energy resolution was in the order of 20 %. See `http://heasarc.gsfc.nasa.gov/docs/cgro/egret`.

Chandra X-ray observatory (Chandra) NASA X-ray telescope, launched in 1999, which was designed for the 0.1–10 keV energy range. In comparison to preceding X-ray telescopes Chandra exhibits a spatial resolution, which had been improved by an order of magnitude. There are two focal plane instruments available: the High Resolution Camera (HRC) and the Advanced CCD Imaging Spectrometer (ACIS). While the HRC is optimised for images with an angular resolution smaller than $0.5''$, the ACIS has a slightly worse angular resolution, but an improved spectral resolving power. The FoV depends on the focal plane instrument: in case of the HRC it is $30' \times 30'$ and for ACIS it is $16' \times 16'$. See `http://chandra.harvard.edu`.

Fermi Gamma-ray space telescope (Fermi) Gamma-ray observatory, launched in 2008, which is the successor of EGRET. The observatory comprises two instruments: the Large Area Telescope (LAT) and the Gamma-Ray Burst Monitor (GBM). The LAT has been optimised to detect γ rays between 30 MeV and 300 GeV. Since the FoV covers about 20 % of the sky, Fermi-LAT is well suited for all-sky surveys. The PSF strongly depends on the location within the FoV and the energy of the γ ray: for a 100 MeV on-axis photon the 68%-containment radius is approx. 3°. See `http://http://fermi.gsfc.nasa.gov`.

Suzaku satellite Japanese X-ray satellite which has been launched in 2005. Since the X-ray spectrometer (XRS) failed shortly after the launch, the X-ray telescopes are only operated in conjunction with X-ray Imaging Spectrometers (XIS), which consist of CCD cameras. These cameras cover the energy range from 0.2 to 10 keV. The FoV of Suzaku has an extent of $18' \times 18'$ and the angular resolution of the telescopes is in the order of $2'$ (half-power diameter, HPD). See `http://www.nasa.gov/mission_pages/astro-e2/main/index.html`.

Bibliography

[A+04a] F. A. Aharonian et al., Astroparticle Physics **22** (2004), no. 2, 109.

[A+04b] K.-M. Aye et al., AIP Conference Proceedings, vol. 745, 2004, 724.

[A+05a] F. A. Aharonian et al., Science **307** (2005), no. 5717, 1938.

[A+05b] F. A. Aharonian et al., Astronomy and Astrophysics **442** (2005), no. 3, L25.

[A+05c] F. A. Aharonian et al., Astronomy and Astrophysics **435** (2005), no. 1, L17.

[A+05d] F. A. Aharonian et al., Astronomy and Astrophysics **442** (2005), no. 1, 1.

[A+05e] F. A. Aharonian et al., Science **309** (2005), no. 5735, 746.

[A+06a] F. A. Aharonian et al., Astronomy and Astrophysics **460** (2006), no. 3, 743.

[A+06b] F. A. Aharonian et al., Astronomy and Astrophysics **460** (2006), 365.

[A+06c] F. A. Aharonian et al., Astronomy and Astrophysics **448** (2006), L43.

[A+06d] F. A. Aharonian et al., Astronomy and Astrophysics **457** (2006), no. 3, 899.

[A+07] F. A. Aharonian et al., Astronomy and Astrophysics **469** (2007), no. 1, L1.

[A+08a] J. Albert et al., The Astrophysical Journal **684** (2008), no. 2, 1351.

[A+08b] E. Aliu et al., Science **322** (2008), no. 5905, 1221.

[A+09a] A. A. Abdo et al., Science **325** (2009), no. 5942, 840.

[A+09b] V. A. Acciari et al., The Astrophysical Journal **698** (2009), no. 2, L94.

[A+10] A. A. Abdo et al., The Astrophysical Journal **713** (2010), 146–153.

[A+12a] A. Abramowski et al., Astronomy & Astrophysics **545** (2012), L2.

[A+12b] M. Ackermann et al., Science **335** (2012), no. 6065, 189.

[AA96] A. M. Atoyan and F. A. Aharonian, Monthly Notices of the Royal Astronomical Society **278** (1996), no. 2, 525.

[AA04] E. Amato and J. Arons, The Astrophysical Journal **653** (2004), 325.

[AB03] F. A. Aharonian and S. V. Bogovalov, New Astronomy **8** (2003), 85.

[ABK12] F. A. Aharonian, S. V. Bogovalov, and D. Khangulyan, Nature **482** (2012), 507.

[Aha04] F. A. Aharonian, Very High Energy Cosmic Gamma Radiation, World Scientific, 2004.

[AI75] P. W. Anderson and N. Itoh, Nature **256** (1975), no. 5512, 25.

[AS79] J. Arons and E. T. Scharlemann, The Astrophysical Journal **231** (1979), 854.

[B+98] S. Le Bohec et al., Nuclear Instruments & Methods in Physics Research, Section a-Accelerators Spectrometers Detectors and Associated Equipment **416** (1998), 425.

[B+03] K. Bernlöhr et al., Astroparticle Physics **20** (2003), no. 2, 111.

[B+11] S. D. Bongiorno et al., The Astrophysical Journal **737** (2011), no. 1, L11.

[Bar04] M. G. Baring, Advances in Space Research **33** (2004), 552.

[BCF01] J. M. Blondin, R. A. Chevalier, and D. M. Frierson, The Astrophysical Journal **563** (2001), no. 2, 806.

[Bed07] W. Bednarek, Astrophysics and Space Science **309** (2007), 179.

[Ben05] W. Benbow, Proceedings of 7th Workshop on "Toward a Network of Atmospheric Cherenkov Detectors", dec 2005, 163.

[Ber06] D. Berge, A detailed study of the gamma-ray supernova remnant RX J1713.7-3946 with H.E.S.S., Ph.D. thesis, Ruperto-Carola University of Heidelberg, 2006.

[Ber08] K. Bernlöhr, Astroparticle Physics **30** (2008), no. 3, 149.

[BFH07] D. Berge, S. Funk, and J. Hinton, Astronomy and Astrophysics **466** (2007), no. 3, 1219.

[BG70] G. R. Blumenthal and R. J. Gould, Reviews of Modern Physics **42** (1970), 237.

[BGL89] R. Braun, W. M. Goss, and A. G. Lyne, The Astrophysical Journal **340** (1989), 355.

[Bla48] P. M. S. Blackett, Proceedings of Rep. Gassiot Committee of the Royal Society of London, 1948, 34.

[BPP69] G. Baym, C. Pethick, and D. Pines, Nature **224** (1969), no. 5220, 673.

[BR+05] V. Bosch-Ramon et al., The Astrophysical Journal **628** (2005), no. 1, 388.

[Bru07] J. Brucker, Investigation of H.E.S.S. skymaps by means of Minkowski Functionals, diploma thesis, Friedrich-Alexander-Universität Erlangen-Nürnberg, 2007.

[BZ34] W. Baade and F. Zwicky, Proceedings of the National Academy of Sciences of the United States of America, vol. 20, 1934, 254.

[C+92] T. R. Clifton et al., Monthly Notices of the Royal Astronomical Society **254** (1992), 177.

[C+00] F. Camilo et al., The Astrophysical Journal **541** (2000), 367.

[C+03] R. Cornils et al., Astroparticle Physics **20** (2003), no. 2, 129.

[C+05] J. Casares et al., Monthly Notices of the Royal Astronomical Society **364** (2005), no. 3, 899.

[CBO10] A. E. Chukwude, A. A. Baiden, and C. C. Onuchukwu, Astronomy and Astrophysics **515** (2010), A21.

[CDH08] B. Cerutti, G. Dubus, and G. Henri, SF2A-2008, November 2008, 187.

[Che77] R. A. Chevalier, Supernovae, ed. D. N. Schramm, Reidel Dordrecht, 1977.

[CHR86] K. S. Cheng, C. Ho, and M. Ruderman, The Astrophysical Journal **300** (1986), 500.

[CL02] J. M. Cordes and T. J. W. Lazio, arXiv:astro-ph/0207156v3 (2002).

[CL03] J. M. Cordes and T. J. W. Lazio, arXiv:astro-ph/0301598v1 (2003).

[D+01] T. M. Dame et al., The Astrophysical Journal **547** (2001), 792.

[Dal10] M. Dalton, Presentation at the TeV Particle Astrophysics (2010), `http://irfu.cea.fr/Meetings/TeVPA/slides/21_07_pm_Dalton.pdf`.

[dH92] O. C. de Jager and A. K. Harding, The Astrophysical Journal **396** (1992), 161.

[dJDA09] O. C. de Jager and A. Djannati-Ataï, Neutron Stars and Pulsars, vol. 357, ch. Implications of H.E.S.S. Observations of Pulsar, p. 451, Astrophysics and Space Science Library, Springer Verlag, 2009.

[ER11] A. Van Etten and R. W. Romani, The Astrophysical Journal **742** (2011), 62.

[F+04] S. Funk et al., Astroparticle Physics **22** (2004), 285.

[F+10] A. D. Falcone et al., The Astrophysical Journal Letters **708** (2010), L52.

[Fer49] E. Fermi, Physical Review **75** (1949), 1169.

[Feu12] B. Feuerstein, Informationsdienst Wissenschaft, press release: Cold wind of the Crab pulsar produces very-high-energy gamma-ray pulses, 2012, `http://idw-online.de/en/news463661`, visited on July 15th 2012.

[FHdJ08] S. Funk, J. A. Hinton, and O. C. de Jager, Proceedings of the 30th International Cosmic Ray Conference, vol. 2, 2008, 605.

[Fie95] J. M. Fierro, Observations of spin-powered pulsars with the EGRET gamma ray telescope, Ph.D. thesis, Stanford University, 1995.

[FSP96] J. P. Finley, R. Srinivasan, and S. Park, The Astrophysical Journal **466** (1996), no. 2, 938.

[G+03] B. M. Gaensler et al., The Astrophysical Journal **588** (2003), 441.

[G+11] M.-H. Grondin et al., The Astrophysical Journal **738** (2011), 42.

[Gal07] Y. A. Gallant, Astrophysics and Space Science **309** (2007), 197.

[GJ69] P. Goldreich and W. H. Julian, The Astrophysical Journal **157** (1969), 869.

[GO70] J. E. Gunn and J. P. Ostriker, The Astrophysical Journal **160** (1970), 979.

[Gol68] T. Gold, Nature **218** (1968), no. 5143, 731.

[Gol69] T. Gold, Nature **221** (1969), no. 5175, 25.

[GS06] B. M. Gaensler and P. O. Slane, Annual Review of Astronomy & Astrophysics **44** (2006), 17.

[GSZ09] J. D. Gelfand, P. O. Slane, and W. Zhang, The Astrophysical Journal **703** (2009), no. 2, 2051.

[Guy03] J. Guy, Premiers résultats de l'expérience HESS et étude du potentiel de détection de matière noire supersymétrique, Ph.D. thesis, Universities of Paris VI, 2003.

[H+68] A. Hewish et al., Nature **217** (1968), 709.

[H+99] R. C. Hartman et al., The Astrophysical Journal Supplement Series **123** (1999), no. 1, 79.

[H+05] G. Hobbs et al., Monthly Notices of the Royal Astronomical Society **360** (2005), no. 3, 974.

[H+09] J. A. Hinton et al., The Astrophysical Journal Letters **690** (2009), no. 2, L101.

[H+11] J. A. Hinton et al., The Astrophysical Journal Letters **743** (2011), no. 1, L7.

[H+12] M. Holler et al., Astronomy and Astrophysics **539** (2012), A24.

[Hah10] J. Hahn, Modelling the Inverse Compton Emission from Pulsar Wind Nebulae, 2010, Diploma thesis, Faculty of physics and astronomy, University of Heidelberg.

[Har08] A. K. Harding, The Astrophysical Journal **680** (2008), 1378–1393.

[H.E12] H.E.S.S. Collaboration, H.E.S.S.-The High Energy Stereoscopic System, 2012, `http://www.mpi-hd.mpg.de/hfm/HESS`.

[Hei54] W. Heitler, Quantum Theory of Radiation, Oxford University Press, 1954.

[HG90] A. K. Harding and T. K. Gaisser, The Astrophysical Journal **358** (1990), 561.

[HH09] J. A. Hinton and W. Hofmann, Annual Review of Astronomy & Astrophysics **47** (2009), 523.

[Hil82] A. M. Hillas, Journal of Physics G: Nuclear Physics **8** (1982), 1461.

[Hil85] A. M. Hillas, Proceedings of the 19th International Cosmic Ray Conference, vol. 3, aug 1985, 445.

[Jag96] O. C. de Jager, The Astrophysical Journal **457** (1996), 253.

[JR75] F. James and M. Roos, Computer Physics Communications **10** (1975), 343.

[Jun03] I. Jung, Entwicklung der Spiegelmechanik, Eichung der Kamera und erste Ergebnisse zum Nachweis hochenergetischer γ-Strahlung aus Richtung des Krebsnebels und PKS 2155–304 mit dem ersten H.E.S.S.-Teleskop, Ph.D. thesis, Ruperto-Carola University of Heidelberg, 2003.

[K$^+$99] P. Kaaret et al., The Astrophysical Journal **523** (1999), no. 1, 197.

[KC84a] C. F. Kennel and F. V. Coroniti, The Astrophysical Journal **283** (1984), no. 2, 694.

[KC84b] C. F. Kennel and F. V. Coroniti, The Astrophysical Journal **283** (1984), no. 2, 710.

[KDT03] C. Kouveliotou, R. C. Duncan, and C. Thompson, Scientific American, February Issue (2003), 35.

[KLP09] J. G. Kirk, Y. Lyubarsky, and J. Petri, Astrophysics and Space Science Library, ed. W. Becker **357** (2009), 421.

[KRU06] R. Kothes, W. Reich, and B. Uyanıker, The Astrophysical Journal **638** (2006), 225.

[KS94] M. P. Kertzman and G. H. Sembroski, Nuclear Instruments and Methods in Physics Research A **343** (1994), 629.

[L$^+$96] A. G. Lyne et al., Nature **381** (1996), 497.

[Lat04] J. M. Lattimer, Science **304** (2004), no. 5670, 536.

[Lev44] K. Levenberg, Quarterly of Applied Mathematics **2** (1944), 164.

[LEV92] B. Link, R. I. Epstein, and K.A. Vanriper, Nature **359** (1992), no. 6396, 616.

[LGS05] A. Lyne and F. Graham-Smith, Pulsar Astronomy, vol. Third Edition, Cambridge University Press, 2005.

[LK01] Y. Lyubarsky and J. G. Kirk, The Astrophysical Journal **547** (2001), 437.

[LK04] D. R. Lorimer and M. Kramer, Handbook of Pulsar Astronomy, Cambridge University Press, 2004.

[LM83] T.-P. Li and Y.-Q. Ma, The Astrophysical Journal **272** (1983), 317.

[LM97] R. C. Lamb and D. J. Macomb, The Astrophysical Journal **488** (1997), no. 2, 872.

[Lon94] Longair, M. S., High Energy Astrophysics, Stars, the Galaxy and the interstellar medium, second ed., vol. 2, Cambridge University Press, 1994.

[Lor05] D. R. Lorimer, Proceedings of the NATO ASI "The electromagnetic spectrum of neutron stars", Baykal et al., Springer, 2005, `http://www.jb.man.ac.uk/~drl/publications/lor05.pdf`.

[LP01] J. M. Lattimer and M. Prakash, The Astroparticle Journal **550** (2001), 426.

[LPG93] A. G. Lyne, R. S. Pritchard, and F. Graham-Smith, Monthly Notices of the

Royal Astronomical Society **265** (1993), 1003.

[LTDA05] A. Lemiere, R. Terrier, and A. Djannati-Ataï, Proceedings of the 29th International Cosmic Ray Conference, vol. 4, 2005, 105.

[LVM68] M. I. Large, A. E. Vaughan, and B. Y. Mills, Nature **220** (1968), 340.

[M+01] R. S. McGary et al., The Astronomical Journal **121** (2001), no. 2, 1192.

[M+05] R. N. Manchester et al., The Astronomical Journal **129** (2005), no. 4, 1993.

[M+08] F. Mattana et al., American Institute of Physics Conference Series (F. A. Aharonian, W. Hofmann, and F. Rieger, eds.), American Institute of Physics Conference Series, vol. 1085, December 2008, 308.

[M+12] M. Mayer et al., arXiv:1202.1455v2 (2012).

[Man77] Manchester, R. N. and Taylor, J. H., Pulsars, Freeman, 1977.

[Mar63] D. Marquardt, SIAM Journal on Applied Mathematics **11** (1963), 431.

[Mir12] I. F. Mirabel, Science **335** (2012), no. 6, 175.

[MPR98] J. Marti, J. M. Paredes, and M. Ribo, Astronomy and Astrophysics **338** (1998), no. 3, L71.

[MPS06] I. V. Moskalenko, T. A. Porter, and A. W. Strong, The Astrophysical Journal **640** (2006), L155.

[MS11a] G. Maier and J. L. Skilton, Presentation at the 32th International Cosmic Ray Conference, Beijing, China, 2011, `http://indico.ihep.ac.cn/getFile.py/access?contribId=268&sessionId=34&resId=0&materialId=slides&confId=1628`.

[MS11b] G. Maier and J. L. Skilton, Proceedings of the 32th International Cosmic Ray Conference, 2011, arXiv:1111.2155v1.

[N+96] H. I. Nel et al., The Astrophysical Journal **465** (1996), 898.

[N+03] P. L. Nolan et al., The Astrophysical Journal **597** (2003), no. 1, 615.

[N+12] M. De Naurois et al., Paris Analysis Documentation, 2012, internal web documentation `http://lpnhess.in2p3.fr/~denauroi/protected/Doc/parisanalysis/`, visited on September 25th 2012.

[Nau11] M. De Naurois, Advances is Space Research (2011), `http://dx.doi.org/10.1016/j.asr.2011.04.009`.

[Nau12] M. De Naurois, L'astronomie gamma de très haute énergie de H.E.S.S. à CTA. Ouverture d'une nouvelle fenêtre astronomique sur l'Univers non thermique, Habilitation, Université Pierre et Marie Curie - Paris VI, 2012, `http://hal.archives-ouvertes.fr/tel-00687872/`.

[NM65] J. A. Nelder and R. Mead, The Computer Journal **7** (1965), 308.

[NR09] M. De Naurois and L. Rolland, Astroparticle Physics **32** (2009), no. 5, 231.

[P+00] J. M. Paredes et al., Science **288** (2000), no. 5475, 2340.

[Pac67] F. Pacini, Nature **216** (1967), no. 5115, 567.

[Pac68] F. Pacini, Nature **219** (1968), no. 5150, 145.

[PDW03] D. Porquet, A. Decourchelle, and R. S. Warwick, Astronomy and Astrophysics **401** (2003), 197.

[PKB08] G. G. Pavlov, O. Kargaltsev, and W. F. Brisken, The Astrophysical Journal **675** (2008), no. 1, 683.

[PL07] J. Pétri and Y. Lyubarsky, Astronomy & Astrophysics **473** (2007), 683.

[Poh11] M. Pohl, Lecture Notes: Astroparticle Physics – Synchrotron Radiation, 2011, `http://www-zeuthen.desy.de/~pohlmadq/teach/582/ch6+7.pdf`, visited on June 14th 2012.

[Por05] Porter, T. A., Strong, A. W., Proceedings of the 29th International Cosmic Ray Conference, 2005, 101.

[PS73] F. Pacini and M. Salvati, The Astrophysical Journal **186** (1973), 249.

[R+69] V. Radhakrishnan et al., Nature **221** (1969), no. 5179, 443.

[R+07] M. S. E. Roberts et al., Proceedings of the 363. WE-Heraeus Seminar on Neutron Stars and Pulsars 40 years after the discovery, jan 2007, 24.

[R+11] P. S. Ray et al., The Astrophysical Journal Supplement Series **194** (2011), no. 2, 17.

[RC69] D. W. Richards and J. M. Comella, Nature **222** (1969), no. 5193, 551.

[RC84] S. P. Reynolds and R. A. Chevalier, The Astrophysical Journal **278** (1984), 630.

[RG74] M. J. Rees and J. E. Gunn, Monthly Notices of the Royal Astronomical Society **167** (1974), 1.

[RGB12] S. P. Reynolds, B. M. Gaensler, and F. Bocchino, Space Science Reviews **166** (2012), 231.

[Rob09] M. S. E. Roberts, Presentation at "Supernova Remnants And Pulsar Wind Nebulae In The Chandra Era", Boston, july 2009, `http://cxc.cfa.harvard.edu/cdo/snr09/pres/Roberts_Mallory.pdf`.

[RRK01] M. S. E. Roberts, R. W. Romani, and N. Kawai, The Astrophysical Journal Supplement Series **133** (2001), no. 2, 451.

[RS75] M. A. Ruderman and P. G. Sutherland, The Astrophysical Journal **196** (1975), 51.

[RT11] N. Rea and D. F. Torres, The Astrophysical Journal Letters **737** (2011), no. 1, L12.

[Rud71] M. Ruderman, Physical Review Letters **27** (1971), no. 1, 1306.

[S+01] I. Sakurai et al., New Century of X-ray Astronomy, ASP Conference Proceedings, vol. 251, 2001, 408.

[S+04] P. Slane et al., The Astrophysical Journal **616** (2004), 403.

[S+09] J. L. Skilton et al., Monthly Notices of the Royal Astronomical Society **399** (2009), no. 1, 317.

[Sch10] F. Schöck, A detailed Study of the Pulsar Wind Nebula MSH 15–5*2* in X-rays and TeV γ-rays, Ph.D. thesis, Friedrich-Alexander-Universität Erlangen-Nürnberg, 2010.

[Sla08] P. O. Slane, AIP Conference Proceedings, vol. 1085, 2008, 120.

[SMP07] A. W. Strong, I. V. Moskalenko, and V. S. Ptuskin, Annual Review of Nuclear and Particle Science **57** (2007), 285.

[SR68] D. H. Staelin and E. C. Reifenstein, Science **162** (1968), no. 3861, 1481.

[T+08] A. P. S. Tang et al., The Astrophysical Journal **676** (2008), no. 1, 562.

[T+09] M. Tavani et al., Nature **462** (2009), no. 7273, 620.

[TC93] J. H. Taylor and J. M. Cordes, The Astrophysical Journal - Part 1 **411** (1993), 674.

[TOUD07] R. H. D. Townsend, S. P. Owocki, and A. Ud-Doula, Monthly Notices of the Royal Astronomical Society **382** (2007), no. 1, 139.

[TT10] S. J. Tanaka and F. Takahara, The Astrophysical Journal **715** (2010), no. 2, 1248.

[U+09] H. Uchiyama et al., Publications of the Astronomical Society of Japan **61** (2009), 189.

[v+01] E. van der Swaluw et al., Astronomy and Astrophysics **380** (2001), 309.

[VB09] H. J. Völk and K. Bernlöhr, Experimental Astronomy **25** (2009), no. 1-3, 173.

[vDK04] E. van der Swaluw, T. P. Downes, and R. Keegan, Astronomy and Astrophysics **420** (2004), 937.

[vdSW01] E. van der Swaluw and Y. Wu, The Astrophysical Journal **555** (2001), L49.

[VJ06] C. Venter and O. C. de Jager, Proceedings of the 363. WE-Heraeus Seminar on "Neutron Stars and Pulsars", ed. W. Becker & H. H. Huang, 2006.

[Vla04] N. Vlahakis, The Astrophysical Journal **600** (2004), 324.

[W+89] T. C. Weekes et al., The Astrophysical Journal **342** (1989), 379.

[W+08] I. Wenig et al., AIP Conference Proceedings, vol. 1085, 2008, 698.

[W+09] K. P. Watters et al., The Astrophysical Journal **695** (2009), no. 2, 1289.

[WH12] S. Wakely and D. Horan, TeVCat, 2012, TeVCat - Online Gamma-Ray Catalog, `http://tevcat.uchicago.edu/`, visited on July 5th 2012.

[WP78] K. W. Weiler and N. Panagia, Astronomy & Astrophysics **70** (1978), 419.

[Y+10] J. P. Yuan et al., Monthly Notices of the Royal Astronomical Society **404** (2010), 289.

[ZC98] L. Zhang and K. S. Cheng, Astronomy and Astrophysics **335** (1998), 234.

[ZCF08] L. Zhang, S. B. Chen, and J. Fang, The Astrophysical Journal **676** (2008), 1210.

List of Figures

List of Tables